A Search for Extended Gamma-Ray Emission from the Galactic Center with VERITAS

Dissertation

zur Erlangung des akademischen Grades

doctor rerum naturalium
(Dr. rer. nat.)

im Fach: Physik
Spezialisierung: Experimentalphysik

eingereicht an der
Mathematisch-Naturwissenschaftlichen Fakultät
der Humboldt-Universität zu Berlin

von
M.Sc. Nathan Kelley-Hoskins

Präsident der Humboldt-Universität zu Berlin:
Prof. Dr.-Ing. Dr. Sabine Kunst

Dekan der Mathematisch-Naturwissenschaftlichen Fakultät:
Prof. Dr. Elmar Kulke

Gutachter: 1. Dr. Gernot Maier
2. Prof. Dr. Martin Pohl
3. Prof. Dr. Christopher van Eldik

Tag der mündlichen Prüfung: 3. Dezember 2019

Acknowledgments

To my parents, for relentlessly supporting me, even from 6,792 kilometers away.

Contents

List of Figures

List of Tables

Abstract

Dark matter accounts for 24% of the universe's energy, but the form in which it is stored is currently unknown. Understanding what form this matter takes is one of the major unsolved mysteries of modern physics. Much evidence exists for dark matter in the measurements of galaxies, dwarf galaxies, galaxy clusters, and cosmological measurements. One theory posits dark matter is a new undiscovered particle that only interacts via gravity and the weak force, called a *weakly interacting massive particle* (WIMP). One WIMP candidate is a supersymmetric particle called a neutralino. The objective of this thesis is to search for these dark matter particles, and attempt to measure their mass and cross section.

Dark matter particles appear to concentrate in most galaxy-scale gravitational wells. One region of space that is both nearby and assumed to have a high density of dark matter is the center of our own galaxy. The neutralino is expected to annihilate into Standard Model particles, which may decay into photons. Therefore, a search for gamma rays near the Galactic Center may uncover the presence of dark matter.

108 hours of VERITAS gamma-ray observations of the Galactic Center are used in an unbinned likelihood analysis to search for dark matter. The Galactic Center's low elevation results in VERITAS observing gamma rays in the 4–70 TeV energy range. The analysis used in this thesis consists of modeling the halo of dark matter at the Galactic Center, as well as the spectrum of gamma rays produced when two WIMPs annihilate. A point source is added to model the non-dark-matter gamma-ray emission detected from the Galactic Center. Background models are constructed from data of separate off-Galactic-Center observations.

No dark matter signal is found in the 4–100 TeV mass range. Upper limits on the WIMP's velocity-averaged cross section have been calculated, which above 70 TeV result in new limits of $\langle \sigma v \rangle < (6.6 - 7.6) \times 10^{-25} \frac{\mathrm{cm}^3}{\mathrm{s}}$ at the 95% confidence level.

Abstract

Dunkle Materie bindet etwa 24 % der gesamten Energie im Universum. Bis heute ist jedoch dessen Ursprung nicht bekannt. Dies ist eines der größten ungelösten Rätsel in der modernen Physik. Untersuchungen von Galaxien, Zwerggalaxien, Galaxienhaufen und kosmologischen Messungen deuten auf Dunkle Materie hin. Ein Kandidat für Dunkle Materie ist das sogenannte Weakly Interactive Massive Particle (WIMP), welches nur der Schwerkraft und der schwachen Wechselwirkung unterliegt. Eines dieser supersymmetrischen Teilchen ist das Neutralino. Das Ziel dieser Arbeit ist es, nach Dunkler Materie in dieser Form zu suchen und deren Eigenschaften, wie Masse und Wechselwirkungsquerschnitt, zu untersuchen.

Dunkle Materie verdichtet sich im Bereich von starken Gravitationsfeldern. Aufgrund seiner Nähe sowie der hohen Dichte an Dunkler Materie bietet das Zentrum unserer Galaxie besondere Möglichkeiten zur Suche nach diesen Teilchen. Es wird vermutet, dass Neutralinos miteinander wechselwirken, dabei in Teilchen des Standard Modells zerfallen und so Photonen mit hohen Energien entstehen. Die Suche nach hochenergetischen Gammastrahlen in der Nähe des Galaktischen Zentrums kann folglich das Rätsel der Dunklen Materie lösen.

Das Gammastrahlenobservatorium VERITAS hat das Galaktische Zentrum für etwa 108 Stunden beobachtet. Diese Daten wurden mittels einer unbinned Likelihood-Analyse auf die Existenz von Dunkler Materie untersucht. Da VERITAS das Galaktische Zentrum bei geringer Elevation beobachtet, können nur Gammastrahlen in einem Energiebereich zwischen 4 und 70 TeV detektiert werden. Die in dieser Arbeit benutzte Analysemethode besteht zum einen aus der Modellierung des Galaktischen Zentrums inklusive dessen Dunkle-Materie-Halo. Zum anderen wird das Gammastrahlenspektrum, welches bei der Wechselwirkung zweier WIMP-Teilchen entsteht, untersucht. Der Beitrag der Gammastrahlen, welcher nicht von Dunkler Materie erzeugt wird, ist mittels einer punktförmigen Quelle modelliert. Zum Schluss wird der Untergrund mit realen Daten außerhalb des Galaktischen Zentrums abgeschätzt.

Im Energiebereich zwischen 4 und 100 TeV wurde keine Signale der Dunklen Materie gefunden. Obere Grenzwerte für den Wechselwirkungsquerschnitt der WIMPs ergeben $\langle \sigma v \rangle < (6.6 - 7.6) \times 10^{-25} \frac{\mathrm{cm}^3}{\mathrm{s}}$ oberhalb von 70 TeV in einem 95-prozentigen Erwartungsintervall.

1 Introduction

How much mass is contained within a given volume of space? Within a galaxy? Within a cluster of galaxies? Within the observable Universe?

These questions have been asked repeatedly since the 1930s [1]. However, a variety of assessment techniques consistently result in very different mass measurements. Observing cosmological features like the cosmic microwave background, the distribution of galaxies, and gravitational lensing around galaxy clusters results in a larger mass, while observing the quantity of light produced results in a smaller mass. These observations occur over several different length scales, and are discussed in Chapter 2.

Dwarf galaxies, discussed in Section 2.1.1, are gravitationally bound groups of stars that orbit their center of mass at a wider distribution of velocities than is expected from their luminous mass. Galaxy scale evidence is discussed in Section 2.1.2, explaining how galaxies rotate faster than their baryonic mass alone would predict. Evidence on galaxy cluster scales is discussed in Section 2.1.3. Galaxy Clusters have two clouds of mass, one of hydrogen gas observable via X-ray observations, another observable via the gravitational lensing of visible light. Collisions between two galaxy clusters cause these two pairs of clouds to pass through each other, dragging and slowing each other down at different rates. The differences in drag hint that the gravitationally-lensed mass has a smaller cross section than the hydrogen gas cross section. In Section 2.1.4, Universe-scale evidence is discussed. In it, the observed spectrum of the cosmic microwave background matches predictions, but only when there is much more mass present in the Universe than is currently interacting with light.

All of this heavily implies that there is missing mass, missing *stuff*, unaccounted for by the existing model of physics and our Universe. As this mass prefers to only interact gravitationally and seemingly ignores the electromagnetic spectrum, it has earned the (in)conspicuous title of *dark matter*.

1.1 Motivation

This thesis will demonstrate that, by detecting gamma-rays from the Galactic Center with the VERITAS observatory, a search for dark matter can be conducted. Dark matter is proposed to be a particle that annihilates with itself into standard model particles. If dark matter particles form a spherical cloud (referred to as a halo) around the center of our galaxy, and if the annihliation of these particles produces (either directly or through secondary interactions) a detectable quantity of gamma rays, the density profile of this dark matter halo can be measured. If instead the gamma-ray flux is below detection limits, then observations and knowledge of VERITAS's sensitivity can help place an upper limit on the cross section of the dark matter particle.

1.2 Dark Matter

From measuring the cosmic microwave background, the WMAP [2] satellite found that dark matter makes up 24% of the energy of the Universe [3]; therefore understanding the nature of dark matter is fundamental to understanding our Universe. A leading explanation is that dark matter is a new particle, not included in the standard model of particle physics. As many particle models predict dark matter to either a) couple weakly to other particles, b) interact via the Weak force, or c) both, it is referred to as a Weakly Interacting Massive Particle, or WIMP. The Standard Model, and the WIMP's place in it, are discussed in Section 2.2.1.

From both cosmology and particle physics, the WIMP is predicted to have a mass in the range of GeV to TeV, and a velocity-averaged self-annihilation cross section $\langle \sigma v \rangle$ of around $\sim 3 \times 10^{-26}\,\mathrm{cm}^3\mathrm{s}^{-1}$. In Chapter 3, the production of gamma rays from dark matter is discussed. WIMPs may directly annihilate or decay into gamma rays, or they may first produce quarks or leptons, which would then produce gamma rays through secondary interactions. These gamma rays would then have energies similar to the original WIMP mass, around the TeV scale. This potential for WIMP dark matter to produce TeV gamma rays makes it an attractive science target for gamma-ray observatories like VERITAS. A description of the VERITAS observatory and gamma-ray-detecting hardware is discussed in Chapter 4. The method of reconstructing a gamma ray's position and energy are discussed in Chapter 5.

Then, the question becomes, where should we point our gamma-ray observatories? From gravitational and optical measurements, it is well documented that halos of dark matter augment the gravitational wells of most dwarf galaxies, regular galaxies, and galaxy clusters. Dwarf galaxies tend to have fewer background gamma-ray sources, but also have lower quantities of

dark matter, making them weaker sources of gamma rays from dark matter annihilations. Galaxy Clusters, while more massive (and thus more emissive), have a non-negligible redshift, which introduces more model parameters. The Galactic Center, on the other hand, possesses higher densities of dark matter mass than any dwarf galaxy, while also being closer than any dwarf galaxy, making it an excellent target for a dark matter search.

1.3 Galactic Center and Gamma Rays

At the center of our galaxy there is a supermassive black hole, with a mass of $4 \times 10^6\,\mathrm{M}_\odot$ [4]. As dark matter appears to accompany most baryonic gravitational wells, it is expected there is a halo of dark matter particles at the Galactic Center. Studying this halo is difficult, however, as our galaxy's large gravitational well has accreted a large amount of dust, as well as there being a large number of stars and supernova remnants nearby.

When there are multiple overlapping sources of gamma rays, it becomes difficult to discern which gamma rays came from which emission sources. The dust, supernova remnants, and the Galactic Center itself all emit gamma rays, making detection of a dark matter halo difficult. The dust operates as a collision target for high-energy protons from other galaxies, whose interactions produce π_0 particles, which then decay into gamma rays. These dust-induced gamma rays are collectively referred to as diffuse emission, and appear as a disk of gamma rays along the galactic plane. The supernova remnants accelerate electrons (e^-) and protons (p) outward, which then collide with the surrounding dust and gas forming a shockfront. This shockfront produces a spherical shell of gamma rays. Several of these shells (labeled with 'SNR') can be seen in Figure 1.1, a radio-frequency image of the Galactic Center. Several other angular scales are also shown in this figure, including the moon and the VERITAS field of view. The black hole Sgr A* at the Galactic Center also produces gamma rays in a point-like shape (point-like relative to the other sources), though the mechanism by which it does this is not well understood [6].

These effects all obscure the target of this analysis, the gamma ray emission from a dark matter halo. This spherically-symmetric halo of gamma rays would surround the Galactic Center, decreasing in intensity the further from the center. The halo's spectrum would also be different from the surrounding diffuse emission.

Once these gamma rays have been emitted, they would travel to Earth, where humans can detect them. This is done by using a telescope to observe the particle shower that occurs when each gamma ray hits the Earth's atmosphere. The VERITAS telescope has been observing gamma rays from the Galactic Center since 2010. The data from these observations is used in this analysis.

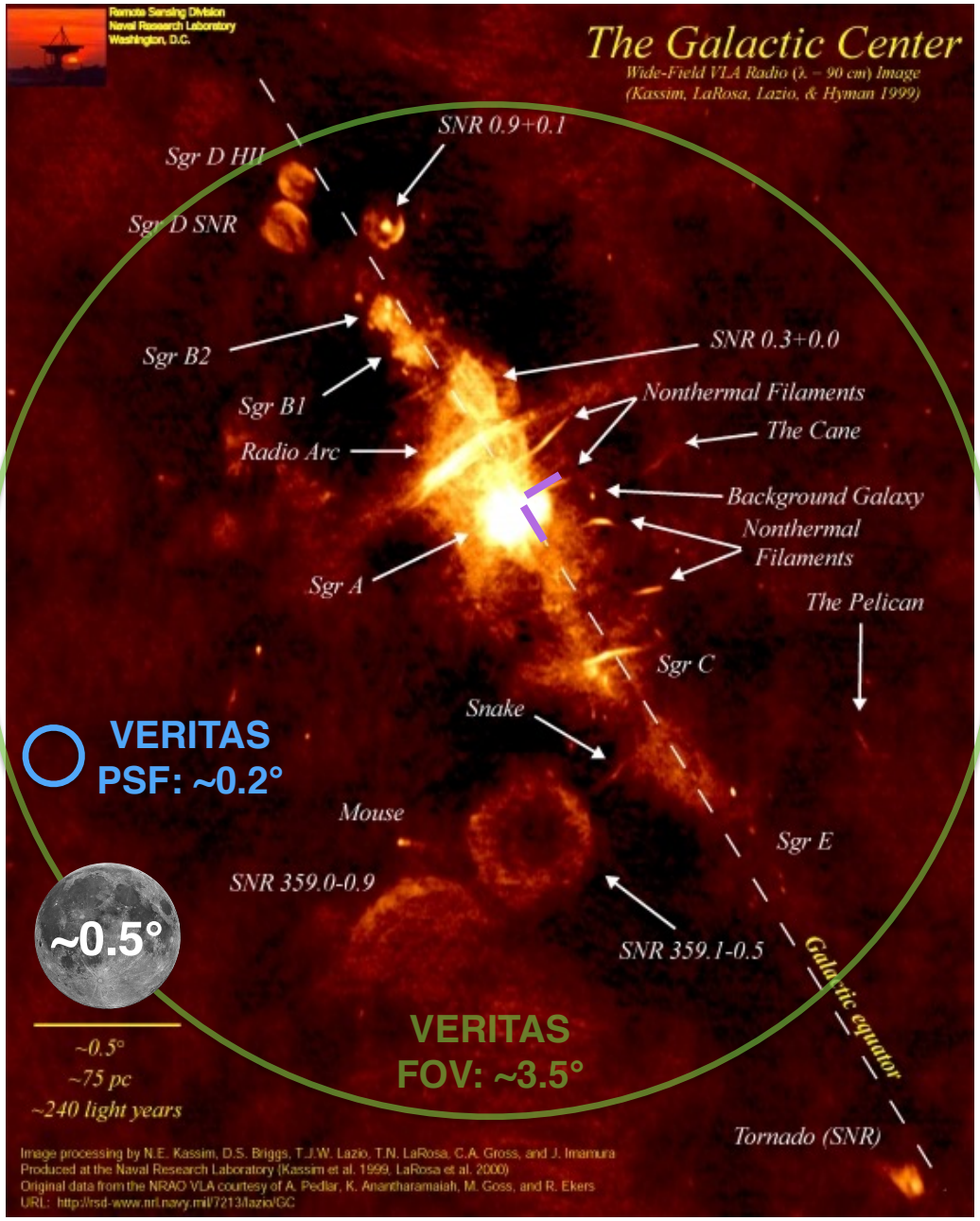

Figure 1.1: The center of our galaxy, viewed at a radio wavelength of $\lambda = 90$cm. The dashed white line roughly represents the galactic plane, and the purple marks indicate the center of our galaxy. Supernova remnants and dust are visible in the view. The VERITAS field of view, the VERITAS point source spread (68% containment), and the moon are shown for angular scale. Radio flux image is from Ref. [5].

1.4 Halo Analysis

After several years of operation, VERITAS has accumulated 108 hours of Galactic Center data, analyzed in Chapter 6. To analyze these observations, an unbinned likelihood analysis is used, described in Section 6.2. With this analysis, the Galactic Center region is modeled with nine different dark matter halos, where the magnitude of each halo is scaled to best fit the observations. For the spatial shape of the dark matter halo, a cuspy Einasto profile is chosen, as discussed in Section 3.3.3. For the spectral shape, only the $b\bar{b}$ annihilation channel is used, as discussed in Section 3.3.2. Each of the nine dark matter halos is modeled with a different dark matter mass m_χ, which changes the spectrum of gamma rays produced in each $\chi\chi$ annihilation.

From this analysis, Section 6.5.3 discusses how no dark matter signal was found at any of these masses. With this null result, the next step is to calculate the upper limit on the velocity-averaged cross section of this WIMP, discussed in Section 6.6. From these upper limits, new limits can be placed on the WIMP velocity-averaged cross section at 100 TeV.

2 The Dark Matter Paradigm

Dark matter makes up 26.5% of the Universe's energy and 81.5% of its mass [7]. It has had a significant impact on the development of the Universe, shaping its present day distribution. This, as well as the astrophysical evidence for dark matter, will be discussed in this chapter. In addition, an outline will be given of the current cosmological paradigm of ΛCDM and the Standard Model, as well as arguments for why dark matter may be in the form of a new, unknown particle.

2.1 Astrophysical Evidence for Dark Matter

The effects currently attributed to dark matter can be grouped into four different length scales. On the smallest length scales, groups of several thousand stars can be seen revolving around their center of mass. By measuring the Doppler shift of their spectral lines, they are observed to be moving at wider distribution of speeds than one would expect from the visible amount of matter. At larger scales the optical light from galaxies, as well as hydrogen lines, can be used to measure the galaxies' mass and rotational velocity. At even larger scales, galaxy velocities can be measured and compared, X-ray telescopes can monitor the amount of hot gas, and mass-heavy areas of space will gravitationally lens background galaxies. At the largest scale, the measurement of oscillations in the cosmic microwave background can be used to determine the amount of dark and baryonic matter. These effects can all be generalized to observations of gravity pulling on electromagnetic emitters, gravity bending background light, and the Universe's total energy budget.

Throughout this chapter, astrophysical objects are measured in units of the Sun's mass $M_\odot$, and the Sun's luminosity $L_\odot$. For these conversions, nominal values are $M_\odot = 1.9885 \times 10^{30}\,\text{kg}$ and $L_\odot = 3.828 \times 10^{26}\,\text{W}$, though different authors may use slightly different values depending on the year of publication [8]. The amount of dark matter in an object is then expressed in terms of the ratio $\frac{M_\odot}{L_\odot}$. For example, a ratio of $7\,\frac{M_\odot}{L_\odot}$ indicates that for every $1\,M_\odot$ worth of mass producing light (at a rate similar to the Sun), there is another $6\,M_\odot$ of mass in a dark form.

Figure 2.1: The Sculptor dwarf galaxy [10], with a $\frac{M_\odot}{L_\odot}$ ratio of 15.3 ± 6.9 [11], imaged by the MPG/ESO telescope [12].

2.1.1 Scales of 10^{19} m : Dwarf Galaxies

At scales of ~10^{19}m, dwarf galaxies, groups of thousands of stars, orbit full-size galaxies like our own. These dwarf galaxies are strong evidence for dark matter because their luminous matter is not enough to gravitationally bind them. An example of two dwarf galaxies are shown in Figures 2.1 and 2.2. Figure 2.1 is the Sculptor dwarf galaxy, imaged in the optical frequencies by the MPG/ESO Telescope, while Figure 2.2 is the Fornax dwarf galaxy, from the ESO Digitized Sky Survey II [9].

Measuring the mass of these dwarf galaxies has been done in two ways. In the first one, telescopes observed the individual spectra of these stars, allowing for their line-of-sight velocity to be calculated [13]. The width of the distribution of the velocities is called the velocity dispersion. By looking at this velocity dispersion, the total mass of the dwarf galaxy can be inferred [14, 15]. What makes this possible is that the velocity dispersion of a group of stars is proportional to the total mass of the gravitational well.

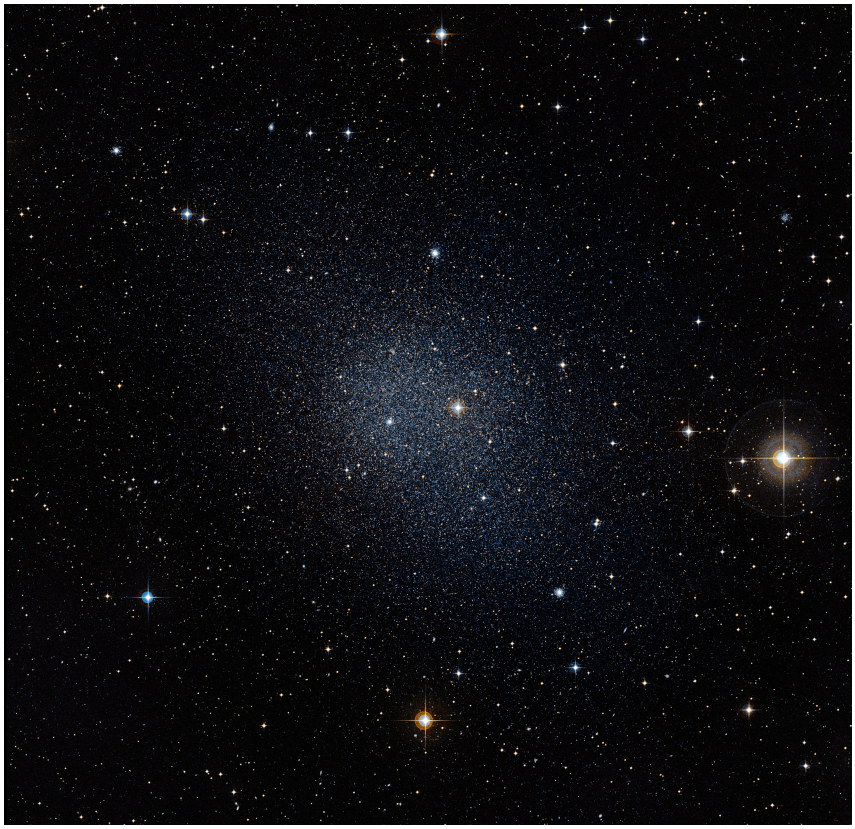

Figure 2.2: The Fornax dwarf galaxy, with a $\frac{M_\odot}{L_\odot}$ ratio of 8.8 ± 3.8 [11], from the ESO Digitized Sky Survey II [9].

This proportionality comes from the spherical Jean's equation [16],

$$\frac{d}{dr}\left(v\sigma_r^2\right) + \frac{2\beta}{r} v\sigma_r^2 + v\frac{d\Phi}{dr} = 0\,, \tag{2.1}$$

where r is the distance from the center of mass, $v(r)$ is a 3D distribution of stars, $\Phi(r)$ is a gravitational potential, $\sigma_r(r)$ is the distribution of radial velocities, and $\sigma_\theta(r)$ is the distribution of velocities orthogonal to the r direction. The parameter $\beta = 1 - \frac{\sigma_\theta^2}{\sigma_r^2}$ characterizes how different the two velocity distributions ($\sigma_r(r)$ and $\sigma_\theta(r)$) are. A solution to this equation can be used to calculate the measurable line-of-sight velocity distribution σ_{los} as a function of the projected angle from the center-of-mass of the dwarf R,

$$\sigma_{\text{los}}^2(R) = \frac{2}{I(R)} \int_R^\infty \left(1 - \beta(r)\frac{R^2}{r^2}\right) \frac{r}{\sqrt{r^2 - R^2}} \frac{1}{f(r)} \int_r^\infty f(s) \frac{v(s) G M(s)}{s^2}\, ds\, dr\,, \tag{2.2}$$

with

$$f(r) = f_{r'} \exp\left[\int_{r'}^{r} \frac{2\beta(t)}{t}\, dt\right]. \tag{2.3}$$

In these two equations, $I(R)$ is the surface brightness of the dwarf galaxy, $v(s)$ is the density profile of its luminous component, $M(s) = 4\pi \int_0^s \rho_{\mathrm{DM}}(r) r^2\, dr$ is the enclosed dark matter mass, and $\beta(r)$ is the velocity anisotropy profile. The calculated $\sigma_{\mathrm{los}}(r)$ velocity distribution in Equation 2.2 can then be compared to the radial velocity measurements of stars within dwarf galaxies to estimate the total mass (dark + baryonic) [14, 17, 18]. As stellar velocity measurements rely on Doppler-shifted spectral lines, and not the star's absolute brightness, any derived mass estimates are fairly robust with respect to changes in observed brightness. These changes in brightness can be from atmospheric variations during telescope observations or changes in the amount of light-absorbing dust in the line-of-sight.

The second way to measure galaxy masses is by measuring the total brightness of a galaxy, and dividing by the luminosity of the Sun $L_\odot$. This then indicates the number of solar masses $M_\odot$ contained in the galaxy, a measure of its baryonic (i.e. 'bright', not dark) mass.

The first way measures the *total* mass from the rotational profile, while the second only measures the mass of its *luminous* parts. The ratio of the total mass divided by the luminous mass is called the mass-to-light ratio, which indicates the amount of dark matter present in the galaxy [19]. Dwarf galaxies have mass-to-light ratios of around 5-100 $\frac{M_\odot}{L_\odot}$, but can reach up to ~1000 $\frac{\mathrm{M}_\odot}{\mathrm{L}_\odot}$ [20]. These high values are considered strong evidence for the presence of dark matter. A random assortment of Local Group dwarf galaxies and their $\frac{M_\odot}{L_\odot}$ is shown in Table 2.1.

Object	$\left[\frac{\mathrm{M}_\odot}{\mathrm{L}_\odot}\right]$	Object	$\left[\frac{\mathrm{M}_\odot}{\mathrm{L}_\odot}\right]$	Object	$\left[\frac{\mathrm{M}_\odot}{\mathrm{L}_\odot}\right]$	Object	$\left[\frac{\mathrm{M}_\odot}{\mathrm{L}_\odot}\right]$
IC 10	0.1	NGC 147	7.1	Sagittarius	22	Leo I	3.1
NGC 185	2.5	NGC 205	12	Ursa Minor	60	Fornax	4.8
LGS 3	21	IC 1613	1.4	Draco	58	Sculptor	11
Carina	30	Antlia	7.4	Sextans	34	GR 8	8.3

Table 2.1: Ratios of $\frac{M_\odot}{L_\odot}$ for various dwarf galaxy objects [21].

Additional evidence for dark matter was found in dwarf galaxies near the Perseus cluster. From the gravitational potential of their baryonic mass alone, these dwarf galaxies should be ripped apart by the tidal disruption of the Perseus cluster. Instead, these dwarf galaxies remain intact, leading to the conclusion that dark matter is providing extra gravitational force [22].

2.1.2 Scales of 10^{20} m : Galaxies

At scales of ~10^{20}m, some effects of dark matter on galaxies are also observable. Within galaxies, the amount of light observed in a sector predicts a lower amount of mass, while observing the line-of-sight velocity predicts a higher amount of mass.

In the first prediction technique, the total amount of light produced by a quadrant of a galaxy is measured with optical telescopes. Then, as in Section 2.1.1, the amount of light produced can be compared with the Sun as a standard mass-to-light ratio, allowing for a prediction of the amount of mass contained in that sector. Known mass-to-light ratios can then be used to calculate the total amount of mass within that quadrant. For example, in a survey of 25 galaxies in Ref. [23], most possessed a mass-to-light ratio of 1 to 10.

In the second prediction technique, a galaxy's emission spectrum is observed at many positions around its disk (center, outer edges, etc). By comparing the orientation of the disk with the Doppler-shifted position of well-known spectral lines, one can calculate the average velocity at which each section is traveling around the center of its galaxy, forming a rotation curve [24–26]. Newton's law of gravity can then be used to calculate the mass contained within a sphere of that same radius. This calculation results in a larger amount of mass than the one found simply from the total amount of light observed.

In Figure 2.3, a rotation curve from M33 observations is shown. The observed velocity curve (the data points) continues to increase at larger radii. If the galaxy was only made of stars, then the rotation curve would follow the short dashed line. If the galaxy was only made of gas, then the rotation curve would instead follow the long dashed line. Since these two major components do not combine to form the observed rotation curve, dark matter has been suggested to account for the difference, shown as the dashed-dotted line [27].

Table 2.2: Ratios of $\frac{M_\odot}{L_\odot}$ for various galactic-scale objects [19].

Object	$\left[\frac{M_\odot}{L_\odot}\right]$	Object	$\left[\frac{M_\odot}{L_\odot}\right]$
M31 (Andromeda)	7.6	NGC 801	2.4
M33	4.5	NGC 2403	5.5
M51	3.3	NGC 2841	10.6
M81	8.5	NGC 4324	5.5
M83	2.3	NGC 6822	0.58

A random sample of galaxies from Ref. [19] are shown alongside their mass-to-light ratios in Table 2.2. Our own Milky Way galaxy is measured to have a mass to light ratio of 1.2–1.5 $\frac{M_\odot}{L_\odot}$ [28].

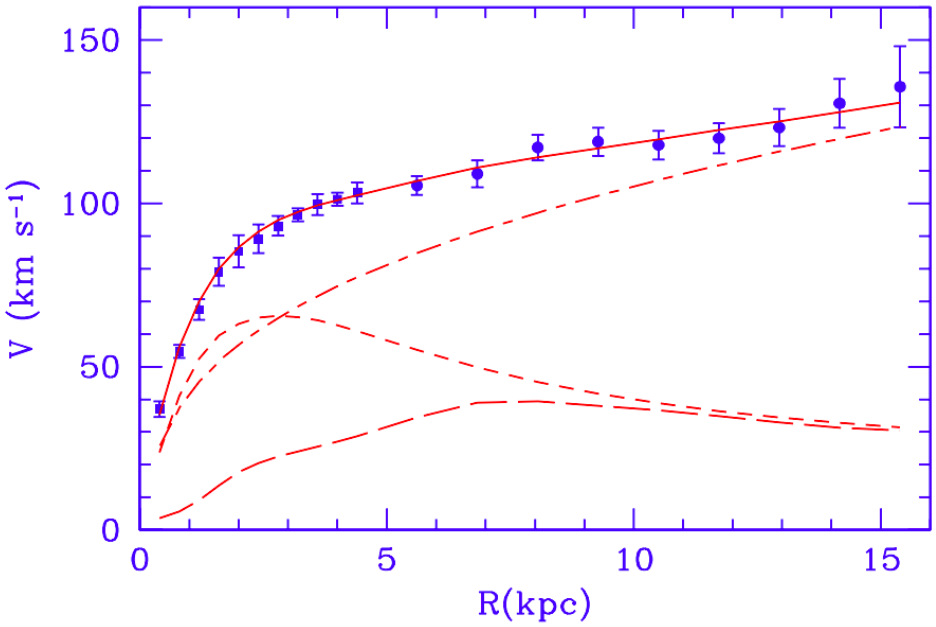

Figure 2.3: The rotation curve from M33 [27]. The solid line is the best fitting model to the observed velocity measurements. The short dashed line is the stellar disk contribution, the gas contribution is the long dashed line, and the dashed-dotted line is the dark matter contribution.

Further evidence of dark matter can be deduced through additional weak gravitational lensing [29]. Lensing elliptical galaxies can constrain mass profiles, as the amount of lensing indicates the total amount of mass, which in turn limits the amount of dark matter present at different radii [30].

Galaxy lensing can be used to estimate the size of the substructure of a lensing galaxy. In the case of Galaxy 0047-281 in Figure 2.4, the galaxy's mass bends light from a background quasar. This creates 4 images of the background quasar [31]. The spectra of the four lensed images vary in brightness and distortion. These variations can be seen by looking at the ratio of the widths of different spectral lines. These ratios of different lensed images indicate that variations exist in the mass density in the lensing galaxy. These variations are best fit by randomly distributing spheres of lensing mass throughout the lensing galaxy, each having a mass of $10^6\,M_\odot$. Spheres of this mass are consistent with the scale of dark matter substructure predicted by CDM.

2.1.3 Scales of 10^{23} m : Galaxy Clusters

At scales of ~10^{23}m, dark matter's effects on galactic clusters become observable with several techniques. In one technique, the mass-to-light ratio can be measured for galaxy clusters. This is done in the same way as with dwarf galaxies; luminous mass is derived from the brightness of the cluster, while total mass is measured from the velocity dispersion of individual galaxies within the cluster. From measurements of several hundred galaxy clusters, it was found that galaxy clusters have mass-to-light ratios of 10–1000 $\frac{M_\odot}{L_\odot}$ [32], indicating a very high amount of dark matter is present in these objects. Several galaxy clusters and their $\frac{M_\odot}{L_\odot}$ ratios are shown in Table 2.3.

Table 2.3: Ratios of $\frac{M_\odot}{L_\odot}$ for various galaxy clusters [32].

Object	$\left[\frac{M_\odot}{L_\odot}\right]$	Object	$\left[\frac{M_\odot}{L_\odot}\right]$	Object	$\left[\frac{M_\odot}{L_\odot}\right]$
Abell 85	445	Abell 2426	80	Abell 3695	180
Abell 458	401	Abell 3122	960	Abell 3921	175
Abell 999	100	Abell 3126	491	Abell 4008	227
Abell 1228	37	Abell 3354	94	Abell 4053	421

Another technique for measuring the total mass is by examining the amount of gravitational lensing caused by a cluster. When a massive galaxy cluster has a galaxy directly behind it,

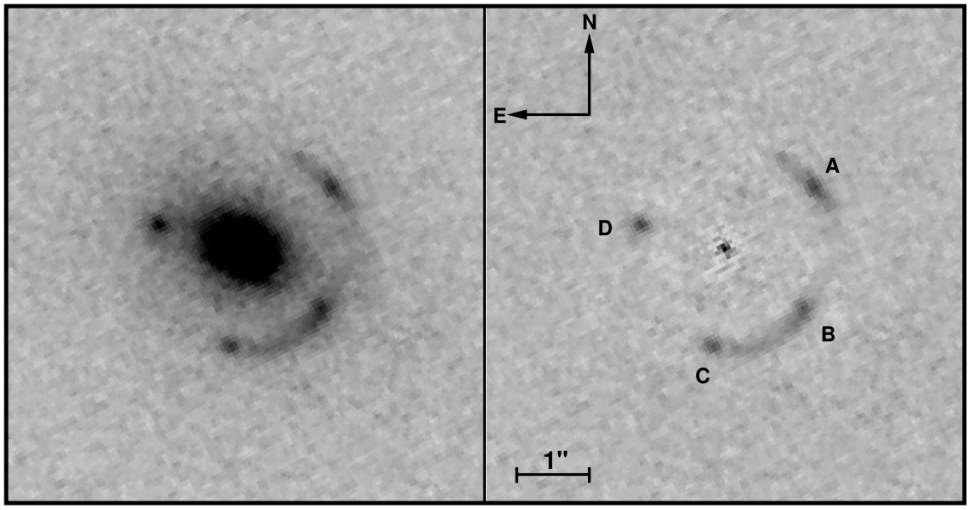

Figure 2.4: Galaxy 0047-281 imaged by the Hubble Space Telescope, from Ref. [30]. Left: Original image. Right: Same as original but with the central foreground galaxy subtracted, leaving behind 4 lensed images A, B, C, and D of a background galaxy.

the image of the background galaxy is distorted. The shape of the distorted image can then be used to infer the amount of total mass in the galaxy cluster. Then comparing this total mass to the luminous mass provides an estimate for the amount of dark matter contained in the galaxy cluster. This was used with galaxy clusters Abell 370 and CL 2244-02 to estimate the amount of dark matter in each [33]. Lensing cluster Abell 370 and several distorted background galaxies are shown in Figure 2.5. This technique found that for both Abell 370 and CL 2244-02, a large amount of dark matter is required to fit the observed arcs, within the range of 200–1000 $\frac{M_\odot}{L_\odot}$.

Cluster Cl0024+1654 is another example of using gravitational lensing to measure dark matter mass. This galaxy cluster produces several lensed images of the same background galaxy, which are used to measure the total mass. This lensing is shown in Figure 2.6, where the blue arcs are the distorted background galaxy images. From all of these lensed images, the best fit amount of dark matter indicates this cluster has a mass-to-light ratio of $161\frac{M_\odot}{L_\odot}$[‡] [35–37].

Yet another way of measuring the total mass of a cluster is by examining X-ray measurements. In galaxy clusters, the majority of the luminous mass is stored in warm ($kT \simeq 5\,\text{keV}$) gas, rather than stars. This warm gas emits X-rays, which can be detected by satellites like Chandra [38]. By measuring the X-ray flux at the center of the galaxy cluster Abell 2029, the total mass of the cluster can be estimated. This is done by assuming the warm gas is in hydrostatic equilibrium, where the force of gravity towards the cluster center is equally balanced by the pressure of the warm gas. This implies that when moving outwards from the cluster center, the density and temperature of the gas is predictable. From this, the mass-to-light ratio can be inferred at several different radii from the cluster center. Within $28.5\,\text{kpc}^\dagger$ of the center, the ratio is $12\,\frac{M_\odot}{L_\odot}$, while beyond a radius of $286\,\text{kpc}^\dagger$ the ratio rises above $100\,\frac{M_\odot}{L_\odot}$, indicating a high amount of dark matter is present [39].

These previously mentioned techniques have been combined into an analysis of galaxy cluster 1E 0657-558 to provide a cardinal piece of evidence in favor of particle dark matter. This cluster consists of two subgroups of galaxies, a larger *target* cluster, and a smaller *bullet* cluster. Each cluster's mass is contained in two clouds; gas and stars that form the baryonic cloud, and the much more massive dark matter cloud. The baryonic cloud is visible through Chandra X-ray observations, which are able to image the warm ($kT \simeq 10\,\text{keV}$) gas and infer its density. The dark matter cloud is inferred through weak lensing observations, where the mass of the cluster distorts the images of background galaxies. In this pair of clusters, the bullet cluster has fallen through the target cluster. However, the two clouds of the bullet cluster dragged on the clouds of the target cluster, and dragged at different rates. This difference in drag over time resulted in a separation between the bullet and target's baryonic and dark matter clouds, visible in

[‡]This measurement scales with the Hubble constant, which here is assumed to be 70 km/s/Mpc

[†]This scales inversely with the Hubble constant, assumed here to be 70 km/s/Mpc

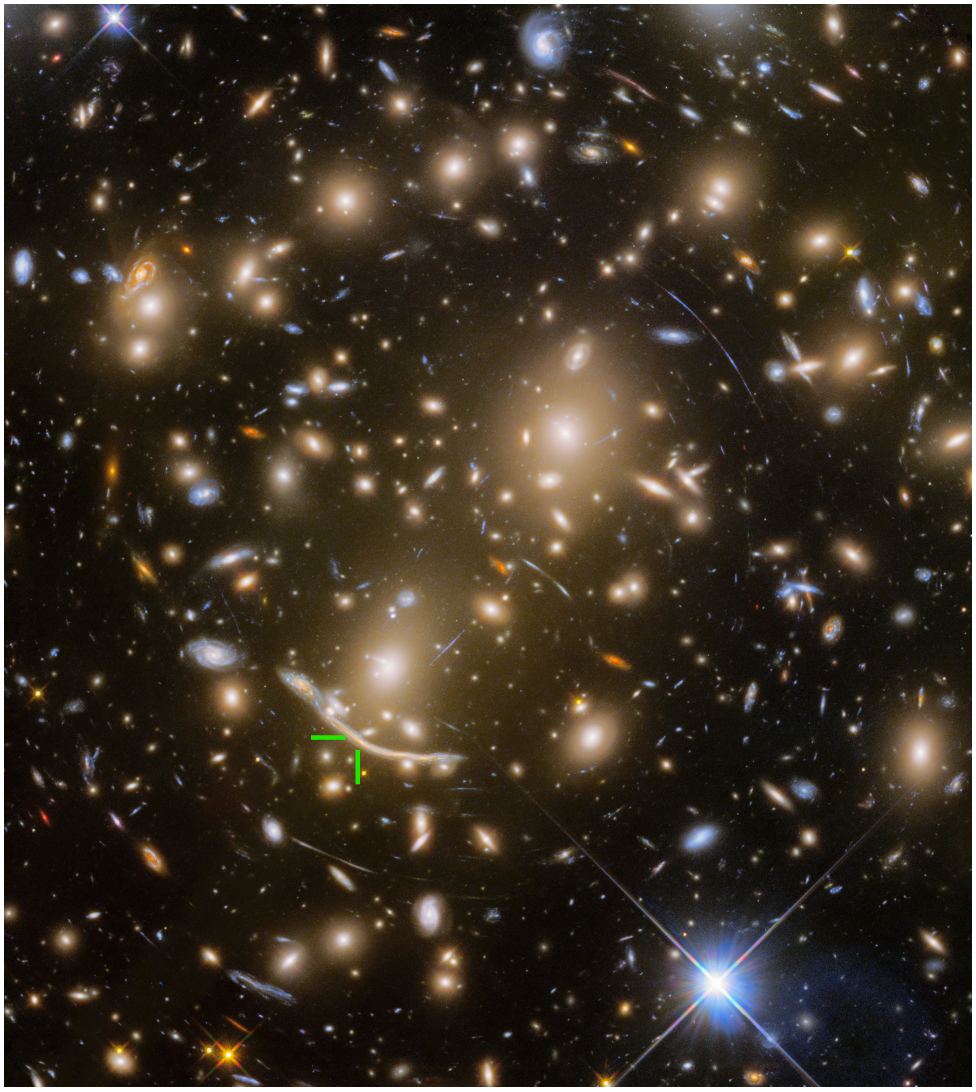

Figure 2.5: Galaxy cluster Abell 370 is shown here, along with many gravitationally lensed background galaxies. The large arc marked by the green lines is the distorted background galaxy image used to calculate the cluster's total mass [33]. Credit: NASA, ESA/Hubble, HST Frontier Fields [34].

Figure 2.7.

The pink clouds are X-ray observations of the cluster's warm gas, while the blue clouds are the weak lensing mass. The red triangle and blue oval show the approximate centers of mass of the Bullet cluster's two clouds. The difference in position between the two centers of mass allows for a constraint to be put on the dark matter particle's mass and cross section. This

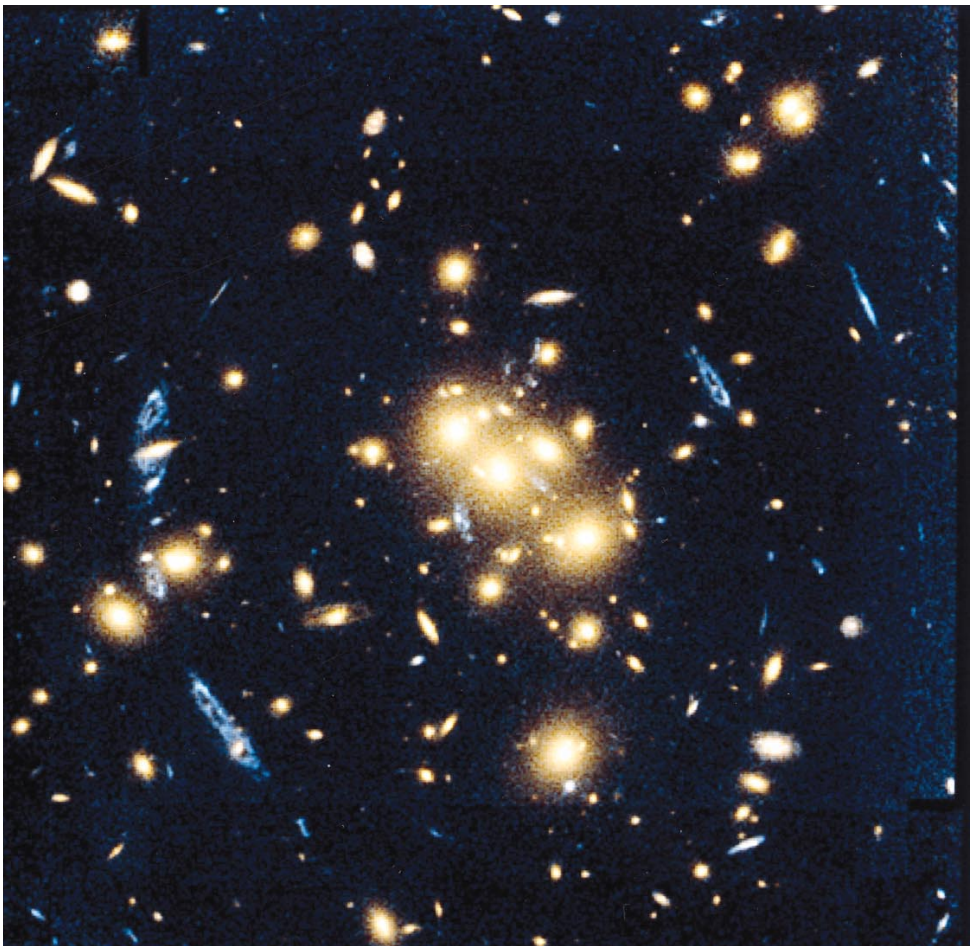

Figure 2.6: Strong lensing of a blue background galaxy by galaxy cluster Cl0024+1654 into multiple blue distorted images [35].

constraint is shown by

$$\frac{\sigma_\chi}{m_\chi} < 1\,\mathrm{cm}^2\,\mathrm{g}^{-1}\,, \tag{2.4}$$

where σ_χ is the dark matter particle cross section, and m_χ is the dark matter particle mass [41, 44], Further work on this combined 72 galaxy cluster collisions, improving the limit in Equation 2.4 to $0.47\,\mathrm{cm}^2\mathrm{g}^{-1}$ [45].

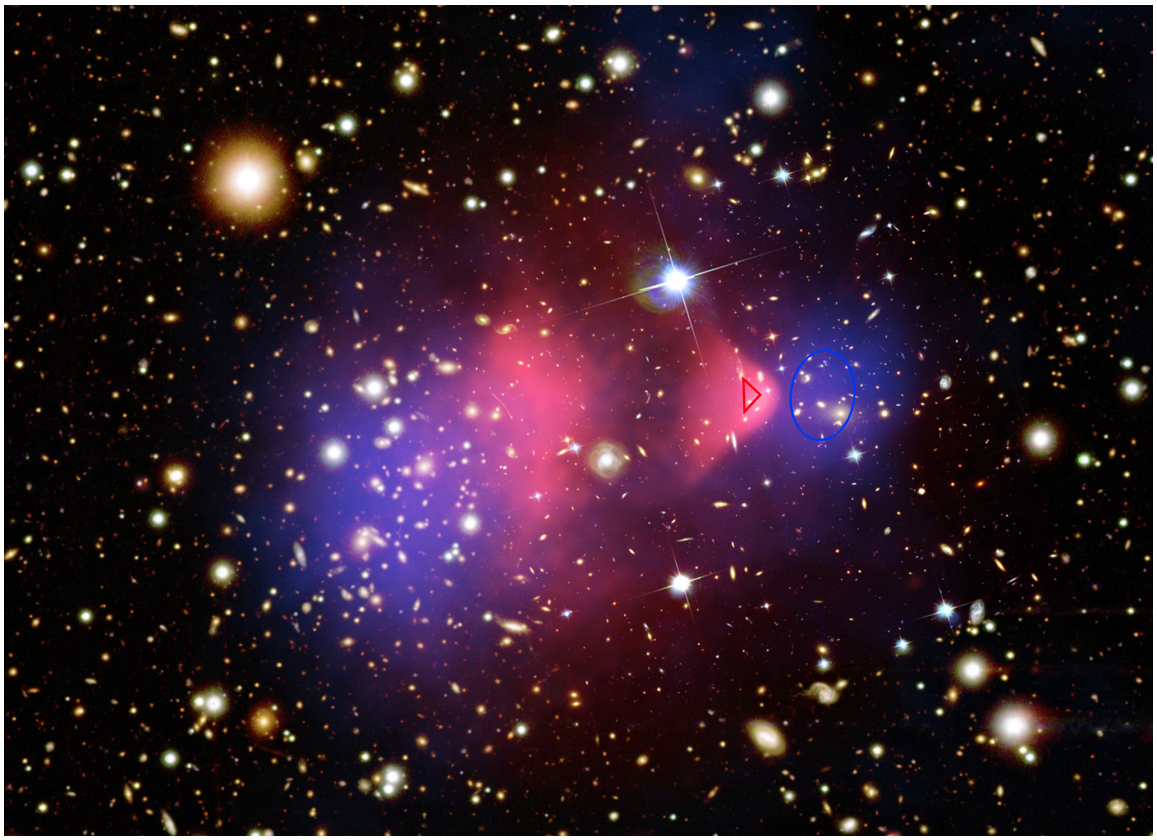

Figure 2.7: Galaxy cluster 1E 0657-558, also known as the Bullet Cluster [40]. The blue clouds indicate the gravitational lensing mass [41], the pink represents clouds of warm gas emitting X-rays [42]. The red triangle indicates the bullet's warm gas center-of-mass, and the blue oval marks the approximate center of the bullet's weak lensing (dark) mass. The remaining stars and galaxies are imaged in the optical spectrum [43].

2.1.4 Scales of 10^{26} m : The Observable Universe and ΛCDM Cosmology

At the Universe's largest scale, ~10^{26}m, the Cosmic Microwave Background (CMB) has been used to measure the total amount of dark matter in the Universe. The study of the structure of the CMB permits the Universe and its particle populations to be investigated, including how they developed and changed from the Big Bang to the present day. In order to understand dark matter's place in the evolution of the Universe, several important moments must be discussed.

The first moment of the Universe was Inflation, where a singularity with a temperature of $kT = 10^{17}$ GeV quickly expanded as a quark-gluon plasma while gradually cooling [46–49]. Once the average temperature had reduced enough, quarks began binding together to form baryons, in a stage known as baryogenesis. The time and temperature at which baryogenesis occurred

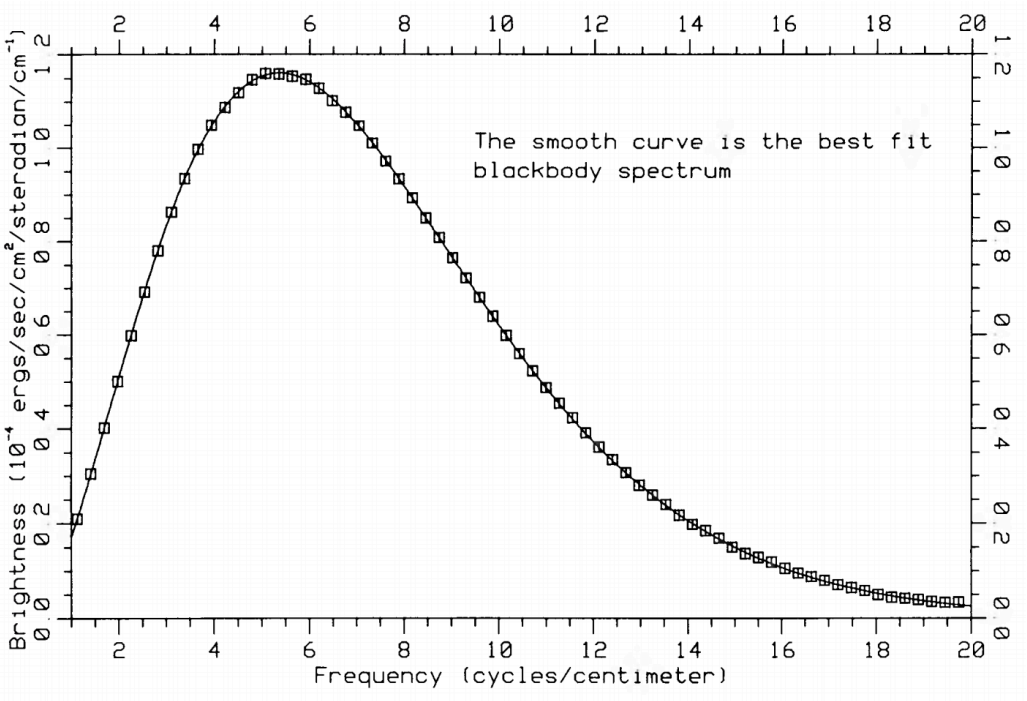

Figure 2.8: The black-body spectrum of the cosmic microwave background measured by the FIRAS instrument on the COBE satellite [55]. Error bars shown here are an assumed 1% error.

has not been determined. However, there are several competing theories that may explain how an unequal ratio of baryons to antibaryons were created [50, 51].

Later, when the Universe was ~380,000 years old and had expanded enough to cool to ~3000 K, another phase change occurred. Here, the Universe was a sea of free particles - photons (γ), electrons, and protons. Due to the numerous free electrons and protons, the mean free path of the photon was small, so the photons were in thermal equilibrium with the electrons and protons. Once the Universe expanded further, enough to cool below the electron-proton binding energy, protons began to capture electrons in great numbers. Since electrons and protons were forming electrically neutral hydrogen atoms (an event called recombination), the Universe became transparent to these photons, which were then free to travel the Universe [7, 52–54]. The spectrum of these photons follows a black-body spectrum, shown in Figure 2.8, and is now called the Cosmic Microwave Background.

However, the CMB spectrum varies a small amount from a pure black-body spectrum, roughly 1 part in 1000, in different parts of the sky. These variations are shown in Figure 2.9, and are due to Baryon Acoustic Oscillations (BAOs), which were imprinted when the electrons and protons recombined. This recombination was not instantaneous, and instead happened

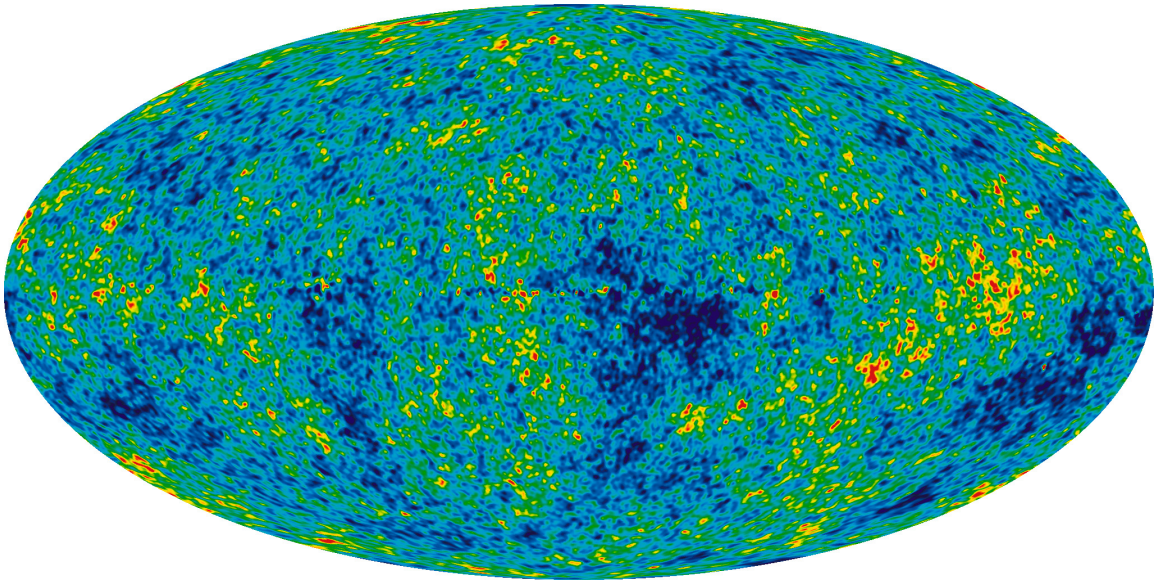

Figure 2.9: The cosmic microwave background temperature map of the Universe [56], from 9 years of WMAP observations [57]. The colors span a temperature range of $\pm 200\,\mu$Kelvin.

over time. During this gradual recombination, some baryons were gravitationally pulled into areas of higher mass densities. These high-density areas were formed in earlier times of the Universe, and were spread out evenly. The baryons would fall into these gravitational wells, until they became warmer, whereupon the baryons would emit more photons, which increased the photon pressure and drove the baryons out of the wells. After the matter escaped the wells, the photon pressure decreased and the gravitational force dominated, drawing the matter back into the wells again. After happening repeatedly, this created density waves (acoustic oscillations), which spread outwards, interfering with one another. These density waves, which had dense high-temperature areas, and sparse low-temperature areas, then emitted black-body photons at higher and lower temperatures, respectively. These higher and lower temperatures account for the spectrum of variations in the CMB's temperature in different parts of the sky.

Since the CMB is emitted by photons scattering off the baryons, the CMB spectrum only depends on the baryon temperature. However, since the baryons were pulled into the high density areas by gravity, the presence of dark matter increases the wavelength of these density ripples. This is similar to a simple spring pendulum, where adding an extra (dark) mass to an existing (baryonic) mass will decrease the oscillation frequency ($\omega = \sqrt{\frac{k}{m}}$), resulting in BAOs with longer wavelengths. In this way, the amount of dark matter in the Universe can be estimated from BAOs within the CMB correlations. The CMB correlation spectrum, measured by Planck, is shown in Figure 2.10.

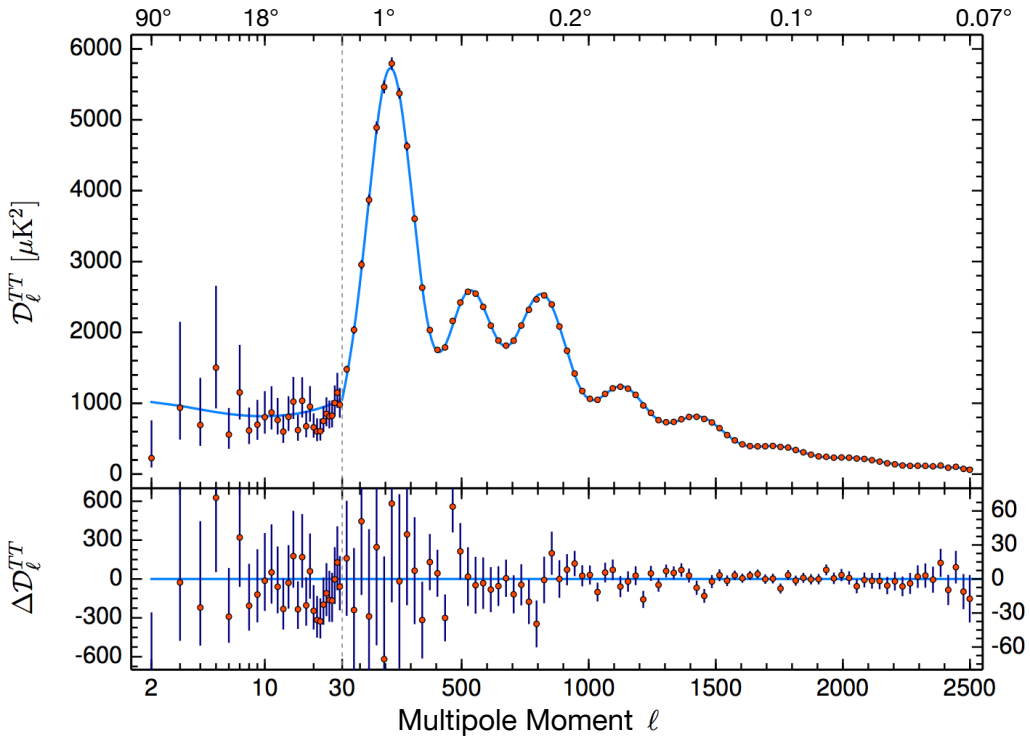

Figure 2.10: Correlation spectra from CMB temperature measurements with the Planck satellite [58]. The upper plot shows the spectra, the lower panel shows the residuals.

The BAOs in Figure 2.10 indicate that 68.6% of the Universe's energy is stored in *dark energy*, a repulsive force which causes almost all visible galaxies to accelerate away from each other. Another 4.9% of the Universe's energy is stored in baryonic matter, like protons and neutrons. The remaining 26.5% of the Universe's energy is contained in dark matter [7].

The measurements of the CMB contribute to the existing theory of how the Universe developed after the Big Bang, which is called ΛCDM. The Λ refers to the density of dark energy, while CDM refers to *cold dark matter*. This theory predicts how different particles fell out of their creation-annihilation equilibrium due to the expansion of space, leaving behind fixed or "frozen" particle populations.

From the CMB correlation spectrum in Figure 2.10, six parameters that describe the Universe can be modeled [58, 59]. These are shown in Table 2.4. The parameters Ω_b and Ω_c are the fraction of the Universe's energy stored in baryons and cold dark matter, respectively. The parameter θ_{MC} is the angular range that could be influenced during the BAOs produced after recombination. This is the comoving distance a sound wave could have traveled between the

	Value	Unit	Description
Ω_b	4.915 ± 0.033	%	Universe's energy in baryons
Ω_c	26.37 ± 0.264	%	Universe's energy in dark matter
θ_{MC}	$(1.04089 \pm 0.00031) \times 10^{-2}$	Radians	Angular size of the sound horizon
τ	$(5.40 \pm 0.74) \times 10^{-2}$	unitless	Thompson scattering optical depth (opacity)
A_s	$(2.097 \pm 0.029) \times 10^{-9}$	unitless	Seed density spectrum amplitude
n_s	0.9652 ± 0.0042	unitless	Seed density spectrum spectral index

Table 2.4: The best fit values for the six cosmological parameters using CMB measurements, from Ref. [58]

beginning of the Universe and recombination. The parameter τ describes how opaque the Universe became to photons during reionization, when the first stars started to reheat atoms and free electrons. The parameters A_s and n_s govern the amplitude and the spectral index of the initial seed perturbations in the early Universe. These Universe-scale parameters determine how the Universe evolved over time.

The observed quantities of deuterium in the early Universe also hint at dark matter's properties. During Big Bang nucleosynthesis, when the Universe was only a few seconds old, protons and neutrons started to combine into various isotopes, one of which is deuterium. However, like baryons, the amount of deuterium produced in the early Universe is heavily dependent on the initial baryon number density. So, any constraint on the deuterium fraction is also a constraint on the baryon fraction of the Universe [60, 61]. From the spectrum of deuterium and hydrogen lines from the quasar QSO Q0913+072, the baryon fraction was measured to be $\Omega_b h^2 = 0.0224 \pm 0.0005$ [62], indicating only 4.93% of the Universe's energy is stored in baryons. This suggests that only a small amount of matter in the Universe can be made of baryons, and the rest must instead reside in some non-baryonic form.

Another measurement that depends heavily on the presence of dark matter is the rate at which galaxies cluster together. In the Sloan Digital Sky Survey (SDSS), the positions of 1.6 million galaxies, quasars, and stars are mapped [63]. By simulating the distribution of similar objects as the Universe ages, the rate that galaxies cluster together can be measured, which depends on the total mass of all objects in the field of view. Only with extra mass from dark matter does the Universe form clumps that match SDSS observations.

Because dark matter is plausibly a new, undiscovered particle, a discussion of particle physics and the Standard Model is necessary to understand what properties a new dark particle may possess.

2.2 The Standard Model

The current paradigm of particle physics is called the Standard Model [64]. It consists of groups of particles called quarks and leptons, as well as the bosons that mediate interactions between these particles. Quarks combine to form mesons and hadrons, like protons and neutrons. Leptons consist of electrons, muons, tauons, and their neutrino companions. These particles have all been ruled out as dark matter candidates, so dark matter searches instead focus on extensions to the Standard Model. One important extension that may contain a dark matter WIMP is called supersymmetry [65], which is discussed in Section 2.2.1.

2.2.1 Particle Dark Matter

Early in the search for a candidate dark matter particle, Standard Model (SM) particles were first considered. One dark matter candidate was the neutrino, due to how many there are in the Universe and their lack of interaction with the strong and electromagnetic forces. This was generally referred to as *hot dark matter*, as neutrinos travel at relativistic speeds. However, it was eventually demonstrated that because of these relativistic speeds, neutrinos would diffuse out of their initial overdensities. This would result in large super-cluster-scale gravitational wells forming first, then cluster-scale wells, then galaxy-scale wells, called top-down structure formation. When observations are made of earlier times, the opposite is found: galaxy-scale gravitational wells form first, then cluster-scale wells, then super-cluster-scale wells in present times, called bottom-up formation. As this is the opposite of what is expected for relativistic dark matter, neutrinos were ruled out as a dark matter candidate [66].

In addition, limits on the mass of the neutrino ($\sum m_\nu = 0.194\,\text{eV}$, 95% C.L.) also rule it out since they are not numerous enough [7]. All other Standard Model particles have also been ruled out, usually for reasons of charge, mass, number density, or cross section. Since none of the Standard Model particles meet the conditions to be a dark matter candidate, theoretically predicted particles are now the focus of most searches.

One of the major expansions to the Standard Model that may contain a dark matter candidate is supersymmetry, or SUSY. There are several SUSY extensions, but the main one discussed here is the Minimal Supersymmetric Standard Model (MSSM) [67–69]. The basic idea of SUSY is that, just as Majorana fermions have a particle-antiparticle reflection, SUSY adds another reflection called R-parity for all particles. This R-parity is defined as

$$R = (-1)^{3B+L+2S}, \tag{2.5}$$

where B is the baryon number, L is the lepton number, and S is the particle spin.

This creates supersymmetric partner particles (superpartners) for each Standard Model particle, usually denoted by an 's-' prefix or an '-ino' suffix added to a particle name, and $\sim$ added atop the particle symbol ($e \rightarrow \tilde{e}$). Quarks become squarks, leptons become sleptons, and gluons become gluinos, etc. Standard model particles and fields have an R-parity of +1, while superpartners have an R-parity of -1.

When this SUSY reflection is performed, the superpartners develop some interesting properties. The spin of all the superpartners is reduced by $\frac{1}{2}$, so the fermionic electron with spin $\frac{1}{2}$ becomes a bosonic selectron with spin 0, and the bosonic gluon with spin 1 becomes the fermionic gluino with spin $\frac{1}{2}$. When the $W^{\pm}$ and weak hypercharge are reflected, they form the Bino and the Wino, respectively. When the Higgs field is reflected, two Higgsino fields result. The Bino, Wino, and two Higgsino fields then mix together to form 4 new particles called neutralinos. The lightest of these neutralinos has some properties that make it an excellent dark matter candidate, and is the WIMP candidate (χ) searched for in this thesis. Specifically, as it is the lightest neutralino, other neutralinos will decay into it. If R-parity is conserved, then this neutralino will also be stable, and not decay into anything else [70–72]. These two features would give the neutralino the stability to exist until the present day, and the numbers needed to match predictions from dark matter observations.

2.2.2 Relic Freeze-out and WIMP Miracle

The relic freeze-out refers to how dark matter may have behaved in the past. A population of dark matter particles (relic particles) existed during the early Universe, and at a later time the Universe expanded enough that their numbers stopped changing (the freeze-out).

This freeze-out is relevant because it hints at the self-interacting cross section of the WIMP. It has been theorized that early on when the Universe was still expanding, WIMPs were annihilating into SM particles, and SM particles were interacting and producing WIMPs. The number density and cross section of these two particle populations were such that that the number of WIMPs and SM particles remained constant; the two particle populations were in thermal equilibrium.

As the Universe expanded, both particle groups collided less and less. This meant that fewer particles were converted to the opposite population, meaning temperature changes in one population took longer and longer to propagate to the other population. Eventually the two populations became independent, sometimes called thermal decoupling. After this decoupling, WIMPs continued to annihilate occasionally, further reducing their numbers, until there were

so few left that they stopped encountering each other. As the population of WIMPs likely did not change much after that time, this transition is called a freeze-out.

The Boltzmann equation describing how the number of WIMPs evolves through this freeze-out is

$$\frac{dn}{dt} = -3Hn - \langle \sigma_A v \rangle \left(n^2 - n_{eq}^2 \right), \tag{2.6}$$

where n is the WIMP comoving number density, H is the Hubble expansion rate ($\frac{\dot{a}}{a}$), $\langle \sigma_A v \rangle$ is the effective velocity-averaged cross section for $\chi\chi$ annihilating into standard model particles [73]. The parameter n_{eq} is the equilibrium WIMP comoving number density.

Equation 2.6 is numerically solved and shown in Figure 2.11. It shows how the number of WIMPs evolve as the Universe ages, and its temperature decreases. The black equilibrium line indicates the number of WIMPs that would be left if they had a large ($\langle \sigma v \rangle \gg 2 \times 10^{-15} \mathrm{cm}^3 \mathrm{s}^{-1}$) cross section. This black line shows how the populations of SM particles annihilating into WIMPs and vice versa balance and replenish each other, forming an equilibrium number density. As the cross section decreases, fewer and fewer particles are annihilated, and more of the initial WIMP population survives to freeze out. This freeze-out can be thought of as the Universe expanding faster than the particles can annihilate.

The cross section of WIMPs can then be estimated from Equation 2.6. If the total amount of dark matter is known, and its mass estimated, this indicates the number density of WIMP particles present in the Universe. This number density combined with Equation 2.6 then indicates the cross section of a 100 GeV WIMP to be around $\langle \sigma_\chi v \rangle \approx 2 \times 10^{-26} \mathrm{cm}^3 \mathrm{s}^{-1}$ [74].

An interesting coincidence is that the weak cross section of a 100 GeV particle is approximately $10^{-25}\,\mathrm{cm}^3\mathrm{s}^{-1}$, only one order of magnitude away from the cross section found from the relic abundance [65]. This is quite surprising, as the cosmology of the relic abundance and the weak cross section come from very different physics. While this is not conclusive proof of the WIMP's existence, this *WIMP Miracle* is intriguing physics to search for.

Now that the motivation for dark matter searches is understood, a search can be prepared. The next question is "How does one search for dark matter?" If one has access to a gamma-ray observatory, it turns out gamma rays from dark matter annihilations may be detectable. The next chapter discusses how a cloud of dark matter around the Galactic Center might create an observable spectrum of gamma rays, and how those gamma rays can be detected on Earth.

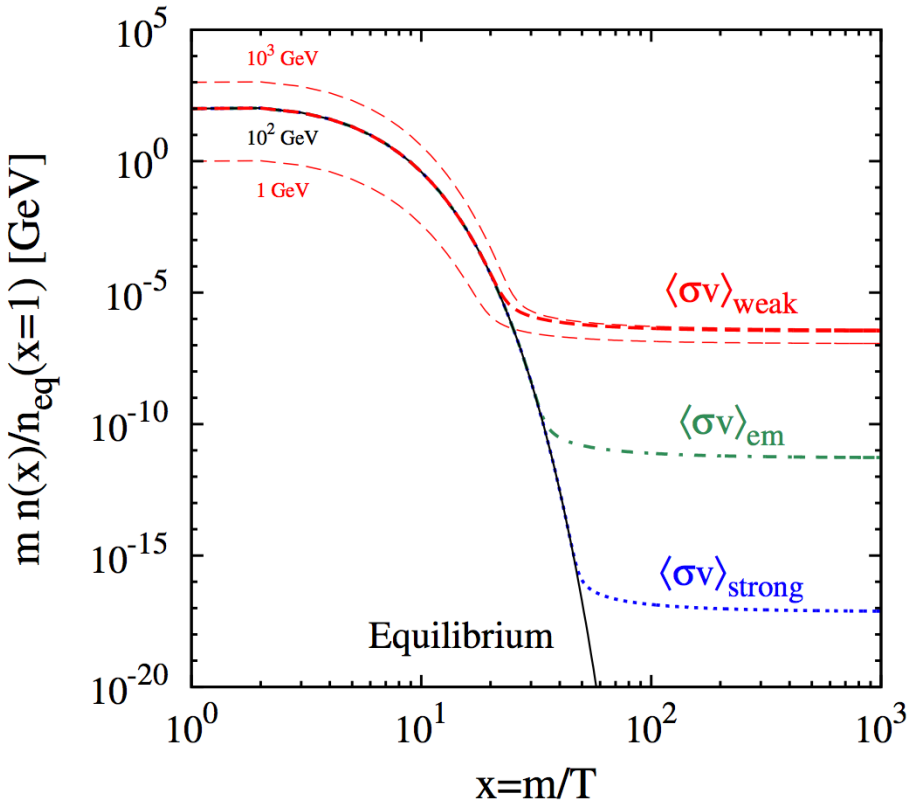

Figure 2.11: The relic abundance of WIMPs as a function of temperature, from Ref. [74], where m is the WIMP mass. The Universe's temperature is T, which decreases as the Universe expands. Therefore x is a proxy for time, increasing as one moves to the right along the x-axis. The number of WIMPs in a comoving volume is $n(x)$, $n_{\rm eq}(x)$ is the number of WIMPs at equilibrium, and the y values are scaled by $n_{\rm eq}(x=1)$. The weak, electromagnetic (em), and strong cross sections are shown for a 100 GeV WIMP, with additional lines for the weak cross section at 1 GeV and 10^3 GeV. The cross sections shown are:

$$\begin{aligned} \langle\sigma v\rangle_{\rm weak} &= 2\times10^{-26}\ {\rm cm}^3{\rm s}^{-1} \\ \langle\sigma v\rangle_{\rm em} &= 2\times10^{-21}\ {\rm cm}^3{\rm s}^{-1} \\ \langle\sigma v\rangle_{\rm strong} &= 2\times10^{-15}\ {\rm cm}^3{\rm s}^{-1} \end{aligned} \quad .$$

3 Gamma Rays and Dark Matter

This thesis searches for evidence of dark matter within gamma ray data, but the relationship between these two areas of physics is intricate. In this chapter three topics relevant to this relationship are discussed. The first is the astrophysical mechanisms that can produce TeV-energy gamma rays, a background for detecting dark matter gamma rays. The second is how dark matter around the Galactic Center can produce gamma rays. The third topic is how gamma rays induce air showers in the Earth's atmosphere.

3.1 Production of TeV Gamma Rays

There are several mechanisms that can produce photons with TeV energies. A gamma ray can start as a low-energy photon, then gain significant energy from electroweak interactions with electrons, referred to as a leptonic production. Alternately, a gamma ray can be created from a high-energy proton colliding with another proton, which produces neutral pions (π^0's) that decay into gamma rays. This is referred to as hadronic production. However, leptonic and hadronic production are separate from how gamma rays are produced by dark matter. Instead, two WIMP dark matter particles may annihilate (directly or indirectly) into gamma rays, and this is discussed in Section 3.3.2.

In leptonic production, electrons and low-energy photons collide, transferring energy to the photon. This interaction is called inverse Compton scattering (or occasionally upscattering) [75], and its Feynman diagram is shown in Figure 3.1.

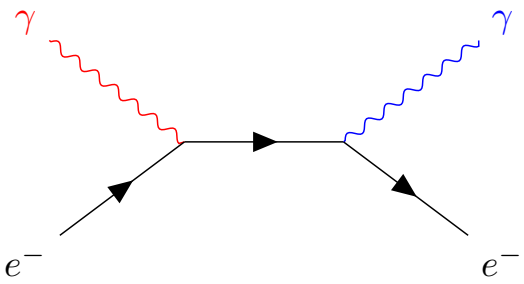

Figure 3.1: Feynman diagram of inverse Compton scattering, where an electron upscatters a low-energy photon (red) to produce a higher-energy (blue) photon.

In inverse Compton scattering [76, 77], a field of photons with an electron present will gain energy according to

$$\frac{dE}{dt} = \frac{4}{3}\,\sigma_t\,U\,c\,\gamma^2\,\frac{v^2}{c^2}\ , \tag{3.1}$$

where

- σ_t is the Thomson cross section, $\frac{8\pi}{3}\left(\frac{\alpha\hbar c}{mc^2}\right)$,
- c is the speed of light in vacuum,
- γ is the Lorentz factor,
- U is the energy density of the photon field in the rest frame of the electron (e.g. $Uc = N\hbar\omega c$), and
- v is the velocity of the electron in the laboratory frame.

The average energy E_{up} of photons upscattered this way can be calculated via

$$E_{up} = \frac{4}{3}\,\gamma^2\,E_0\,, \tag{3.2}$$

where the parameter E_0 is the energy of the original photon.

Astrophysical electrons have been detected at Earth at energies of 500 GeV [78, 79], and potentially as high as 20 TeV [80]. At energies of 500 GeV, the Lorentz factor is $\gamma = 10^6$. With this Lorentz factor, upscattered photons can increase their energy by up to* $\gamma^2 = 10^{12}$. For example, a green photon ($\lambda_{\text{green}} = 550\,\text{nm}$, $E_{\text{green}} = 0.3\,\text{eV}$) could be upscattered to as high as 467 GeV, becoming a gamma ray detectable by VERITAS.

In order to efficiently produce gamma rays via this method, a population of high-energy

*This is the maximum average energy gain when the upscattered photon is emitted back along its original trajectory.

electrons is needed. One environment that produces these electrons is pulsar wind nebulae. Because pulsars spin rapidly, they produce strong magnetic fields. For example, the pulsar at the heart of the Crab nebula has a surface magnetic field strength of 10^{12} G [81], much larger than Earth's $\sim$0.5 G [82]. These strong magnetic fields provide an environment for producing and accelerating charged particles. In these strong magnetic fields, ambient photons can convert into e^+e^- [83, 84]. The probability Υ $(0-1)$ of a photon pair-converting in a magnetic field is calculated by via

$$\Upsilon = \frac{E}{mc^2}\frac{H}{c}\frac{e\hbar}{m^2c^2}\,, \tag{3.3}$$

where E is the photon energy, H is the ambient magnetic field strength, e is the electron charge, and m is the mass of the electron [84]. The factor $\frac{e\hbar}{m^2c^2}$ acts as a threshold magnetic field strength, above which the conversion rate becomes significant. For electrons the threshold is $\frac{1}{4.4\times10^{13}\,\text{Gauss}}$, similar in scale to the pulsar's surface magnetic field strength.

Charged particles can also be accelerated by a pulsar's magnetic fields, in a process called magnetic reconnection, shown in Figure 3.2. In this mechanism, two oppositely oriented magnetic fields move towards each other (Figure 3.2.a), due to the field lines being frozen into the local plasma. As the magnetic field lines merge (Figures 3.2.b and c), induced current flows produce electric fields (Figure 3.2.d) that can accelerate charged particles [85–92].

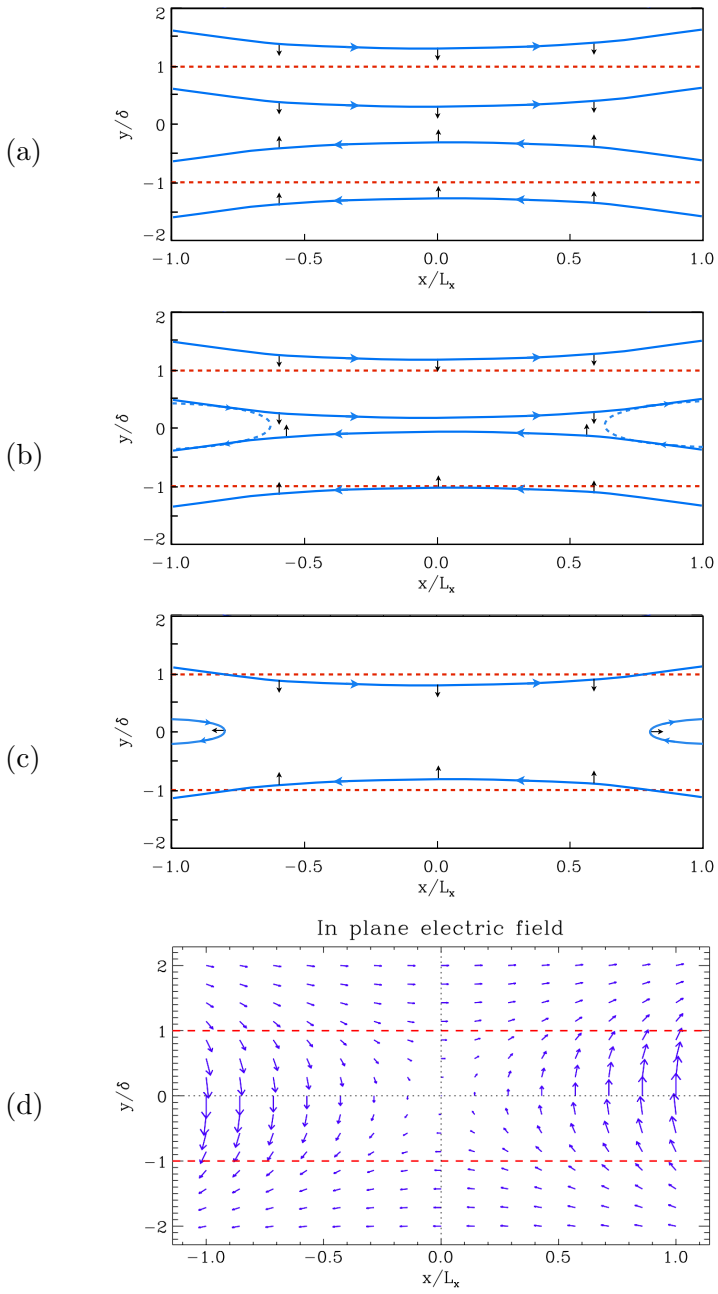

Figure 3.2: Reconnection of two magnetic fields. In (a), two oppositely-pointing magnetic fields move into each other. In (b), reconnection starts to occur. In (c), reconnection occurs, and plasma moves outwards along the $y = 0$ axis. In (d), the resulting electric fields from the moving plasma are shown in this scenario, from Ref. [85]. In these figures, δ and L_x are the distance parameters of the reconnection area.

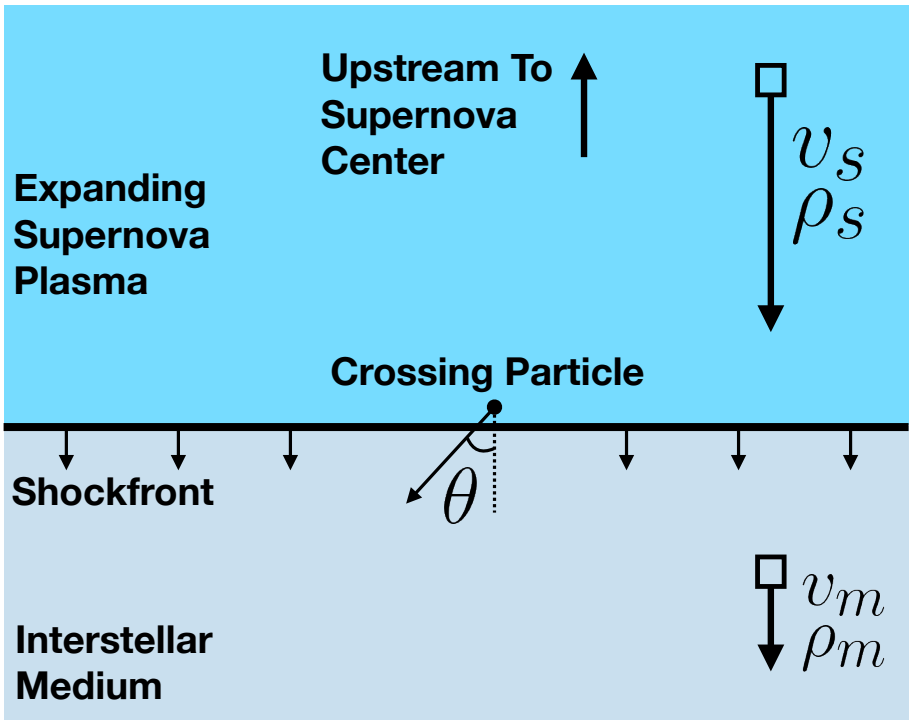

Figure 3.3: Diagram of supernova shockfront. Relative to some inertial observer, the supernova plasma expands at velocity v_s, while the ISM moves at velocity v_m.

Another mechanism that produces high-energy charged particles is Fermi acceleration [93, 94]. In general, this acceleration imparts energy to charged particles when they are reflected by an oncoming magnetic field.

One environment where this can happen often is in the shockfront of a supernova, where the process is called diffusive shock acceleration [95–99]. During and after a supernova's initial explosion, charged fermions are quickly heated. These heated particles then expand outwards, creating a moving shockfront at the boundary between the expanding particles and the surrounding Inter-Stellar Medium (ISM). These expanding particles bring their own magnetic fields due to Alfven's theorem [100, 101], which then reflect other charged particles. As the shockfront expands, it also runs into the ambient magnetic fields in the ISM, which can also reflect charged particles. This shockfront is shown in Figure 3.3.

At the shockfront, particles that cross it are reflected off the magnetic fields on the other side, gaining a small amount of energy each time. Over many crossings, charged particles can gain high energies, though the higher the energy of the particle, the more likely it is to escape the shockfront, since it's gyroradius increases as its energy increases. The amount of energy

gained is governed by a parameter β, in the equation

$$\beta = 1 + \frac{v_s}{c}\,. \tag{3.4}$$

This β parameter can be interpreted as the fractional energy gain per crossing, as in

$$E_{i+1} = \beta E_i\,, \tag{3.5}$$

where the E_i parameter is the average energy of a charged particle after it's i^{th} crossing. The energy gain β factor influences the energy spectrum of the escaping charged particles, but so too does P, the probability that the charged particle remains trapped at the shockfront after each crossing. This probability P can be calculated with

$$P = 1 - \frac{v_s}{c}\,. \tag{3.6}$$

With this probability P and the energy gain β, the energy spectrum of particles that permanently escape the shockfront can be calculated by

$$\frac{dN}{dE} \approx E^{\frac{\log P}{\log \beta} - 1}\,. \tag{3.7}$$

With Equations 3.4 and 3.6, the spectrum from Equation 3.7 can be simplified with the following substitution:

$$\begin{aligned} \log P &= \log\left(1 - \frac{v_s}{c}\right) \approx -\frac{v_s}{c} \\ \log \beta &= \log\left(1 + \frac{v_s}{c}\right) \approx +\frac{v_s}{c}\ . \end{aligned} \tag{3.8}$$

Using Equation 3.8, Equation 3.7 can then be simplified to

$$\begin{aligned} \frac{dN}{dE} &\approx E^{\frac{\log P}{\log \beta} - 1} \\ &\approx E^{\frac{-\frac{v_s}{c}}{+\frac{v_s}{c}} - 1} \\ &\approx E^{-1-1} \\ \frac{dN}{dE} &\approx E^{-2}\ . \end{aligned} \tag{3.9}$$

In Equation 3.9, the exponent is often referred to as the spectral index γ. From this diffusive shock acceleration, the spectral index of charged particles is approximately -2. This is quite close to the observed extragalactic cosmic ray spectral index range of -2.0 to -2.2, but additional effects (discussed in Ref. [102]) may soften this index to get to the observed galactic cosmic ray spectral index of ≈ -2.7. The spectral index's dependence on P and β is shown in two plots in Figure 3.4. The top plot in Figure 3.4 shows how changing β, the energy gain per shockfront crossing cycle, affects the escape probability. The bottom plot shows the differential spectra using the spectral indices from the top plot. From these two plots, it can be seen that increasing the energy gain per crossing cycle β creates a harder spectrum of particles with more higher energy particles, since they can reach escape energies in fewer cycles. It can also be seen that trapping more particles at the shockfront (higher P) also creates a harder spectrum of escaping particles, as particles can be contained for more cycles, gaining more energy before escaping [103].

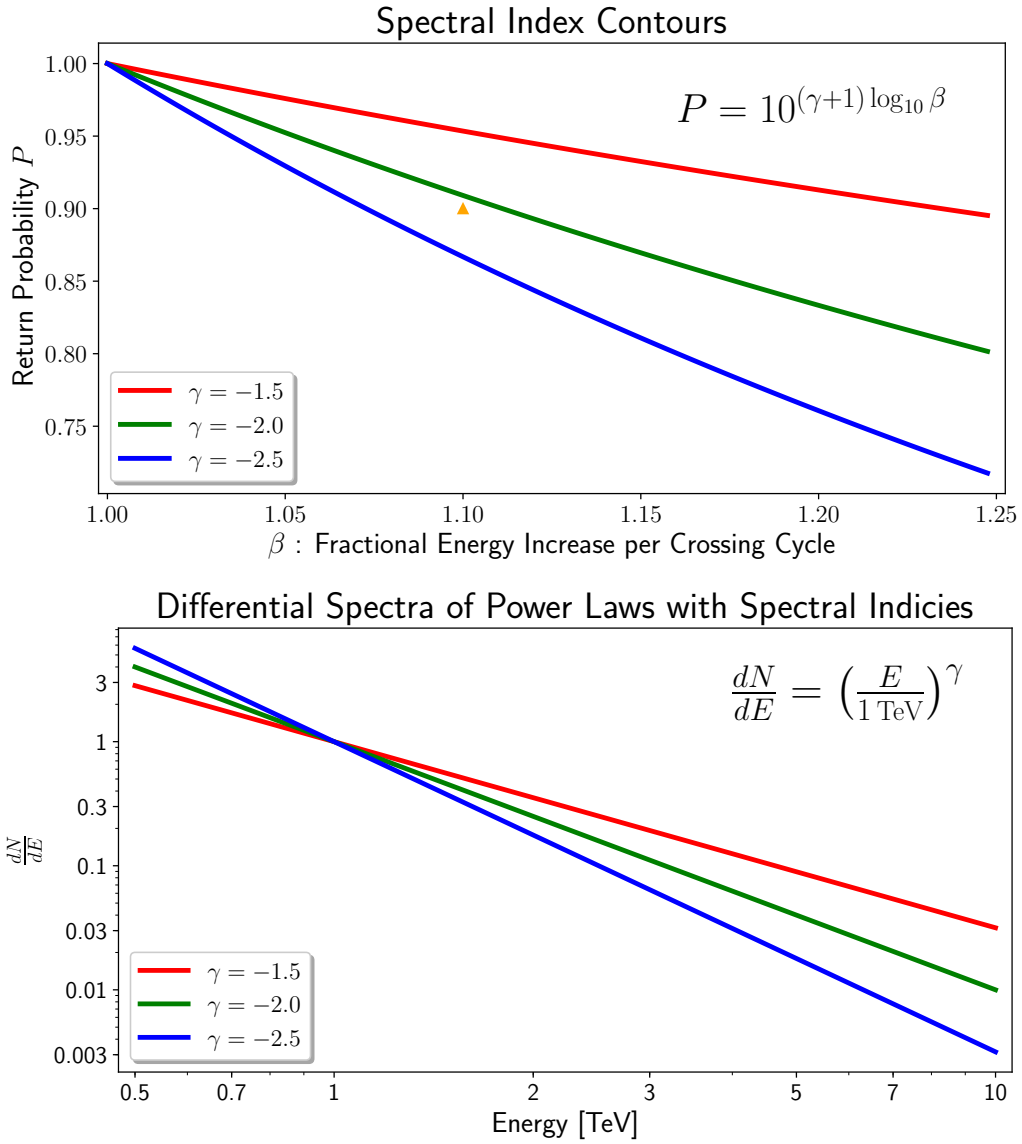

Figure 3.4: The top plot shows the spectral indices produced by various combinations of β, the fractional energy gained by a particle in one crossing cycle (upstream $\rightarrow$ downstream $\rightarrow$ upstream), and P, the average chance a particle is unable to escape the shockfront. The contours for three spectral indices γ are shown. For example, at the orange triangle, each crossing cycle increases a particles energy by a factor of 1.10, while it has a 90% chance of being permanently trapped, which produces particles with a spectral index of $\gamma = -2.1$. The bottom plot shows the differential flux produced by power laws with the three spectral indices shown in the top plot.

Both of these processes, magnetic reconnection and diffusive shock acceleration, can accelerate protons, electrons, or any other charged particles. When these processes produce electrons with high energies, these electrons can then upscatter ambient photons to TeV energies. Additionally, electrons spiralling through magnetic fields can produce synchrotron photons at X-ray energies, meaning fewer upscatters are needed to reach TeV energies [104].

In hadronic processes, protons can be accelerated (p_{accel}) by Fermi acceleration, by a supernova remnant [105], or as part of an active galactic nucleus jet [106, 107]. Then, upon striking an ambient proton ($p_{ambient}$), the interaction can, in some cases, produce $\pi^+\pi^+\pi^0$, and other particles X [108–110] with

$$p_{accel} + p_{ambient} \rightarrow \pi^+ + \pi^+ + \pi^0 + X\,.$$

The π^0 then quickly (8.5×10^{-17} s [111]) decays into two gamma rays. Because each pion resulting from the original pp interaction tends to receive roughly $\frac{1}{3}$ of the original proton's kinetic energy, and the π^0 decays into two gamma rays, each gamma ray ends up with ~15% of the original proton's kinetic energy. The X ends up possessing only a small amount of energy compared to the mass of the pions. For example, a proton with 10 TeV of kinetic energy will eventually produce two 1.5 TeV gamma rays.

While other products from the pp interaction may also produce gamma rays, the π^0 decay is the dominant production channel. Much of the diffuse gamma-ray component of the galactic disk is due to extra-galactic high-energy protons colliding with the protons of the galactic plane [112, 113].

Protons accelerated by these mechanisms form the majority of the showers detected by the VERITAS telescope, forming an irreducible background in the Galactic Center observations. This background is irreducible due to the fact that the Cherenkov images of proton and gamma-ray air showers have many similarities, and cannot be identified with perfect accuracy.

3.1.1 Dark Matter Interactions

The general dark matter particle searched for in this thesis is a WIMP. WIMPs may be detectable by three general search schemes, illustrated in Figure 3.5.

In collider searches, $SS \rightarrow \chi\chi$, missing transverse energy is sought as dark matter particles are not expected to interact with the detector. For direct searches, $\chi S \rightarrow \chi S$, sensitive particle detectors are built deep underground. When a WIMP scatters off of a nucleus within the detector, the nuclear recoil can be observed, through signals such as crystal phonons, excitation

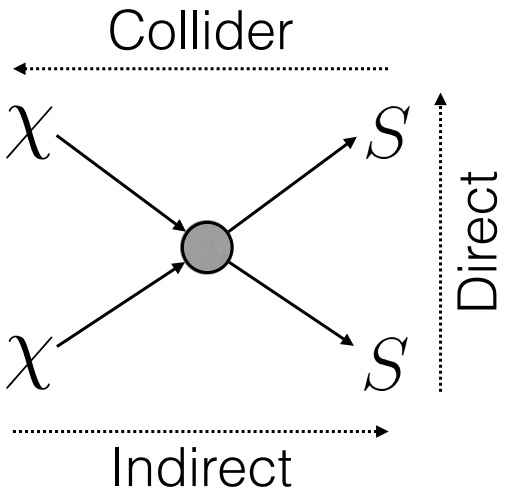

Figure 3.5: The three general search techniques for dark matter. The χ is a dark matter particle, while S is a standard model particle.

and release of photons, or ionization. Being underground shields the detectors from cosmic rays, which create background collisions that can mimic WIMP signals. For example, in liquid xenon detectors, WIMP particle collisions in the liquid produce UV photons and electrons, which are used to infer the presence of the WIMPS [114, 115]. Another type are cryogenic, which use pucks of germanium and silicon to measure WIMP collisions. These collisions produce detectable ionization and phonon signals, which are used to classify the incident particle [116]. A third example are scintillation detectors, which are built with crystals such as titanium-doped sodium iodine. When a WIMP collides with one of the nuclei within the crystal, that nucleus becomes excited, and then relaxes by releasing a photon [117]. However, to date no substantial dark matter signal has been detected with these methods [118].

For indirect searches, $\chi\chi \to ss$, dark matter particles may annihilate or decay into standard model particles. Observatories then search for excesses of these particles, excesses that cannot be explained by currently understood astrophysics. This analysis searches for an excess of gamma rays, as the center of our galaxy is believed to host a dark matter halo. This spherical halo would allow for many $\chi\chi$ annihilations, producing gamma rays with

$$\chi\bar{\chi} \to S\bar{S},$$

where $S\bar{S}$ can be any particle-antiparticle pair ($t\bar{t}$, $b\bar{b}$, $u\bar{u}$, $s\bar{s}$, $\mathrm{e}^-\mathrm{e}^+$, $\nu_\mathrm{e}\overline{\nu}_\mathrm{e}$, $\gamma\gamma$, gg, hh, etc). The particle-antiparticle pairs then annihilate or decay into different spectra of photons (γ). These different annihilation channels can produce different spectra of gamma rays, which will also vary based on the WIMP mass and cross section chosen. This is described further in Section 3.3.2.

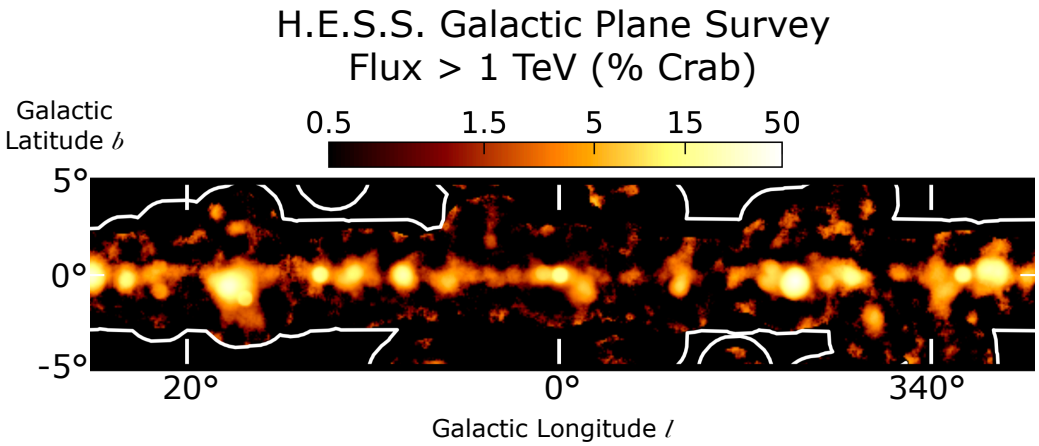

Figure 3.6: Flux map of the Galactic Center above 1 TeV, from the H.E.S.S. Galactic Plane Survey [123].

3.2 Galactic Center

The Galactic Center is a complex region of space, with many astrophysical sources of gamma rays. At its heart, kinematic observations of nearby stars have been used to infer the presence of a supermassive black hole, with a mass of $4 \times 10^6\,\mathrm{M}_\odot$ [4]. Around this black hole, gamma ray emission is observed [119–122], though the production mechanism is still debated. There are other gamma-ray sources as well, including dust along the galactic plane and supernova remnants. The TeV gamma-ray emission from a few of these sources is visible in Figure 3.6.

The VERITAS significance sky map of this Galactic Center region is shown in Figure 3.7. While a dark matter interpretation of this gamma-ray emission is intriguing [125, 126], there are several non-dark-matter models that might explain the observed features. One model that explains this TeV emission is that the supermassive black hole accelerates protons to PeV energies, which then collide with local atoms to produce π^0s, which then decay into TeV gamma rays [127]. The second possibility suggests a nearby population of pulsars may be accelerating electrons, which then upscatter local photons to TeV energies [128]. The debate between these two models is currently ongoing [129]. Due to their limited angular resolution, the current generation of gamma-ray telescopes can only resolve the Galactic Center's gamma ray emission as a point source [124, 119]. The Fermi telescope has observed a similar source of GeV gamma rays around the Galactic Center [130], though neither the dark matter or pulsar explanations are completely conclusive [131, 132].

In addition to this central source, there are also other sources of gamma rays in the vicinity. One of these sources is a disk of dust along the galactic plane, acting as an interaction medium for

proton cosmic rays [133]. These proton-proton collisions then produce neutral pions, which decay into gamma rays [127, 134, 135]. High energy electrons scattering off of nuclei can also produce gamma rays via Bremsstrahlung. Gamma rays around the Galactic Center can also be produced by inverse Compton scattering. This occurs due to the upscattering of optical, infrared, and cosmic microwave background photons. These photons are upscattered by electrons accelerated in nearby sources such as pulsar wind nebulae. Supernova remnants can also produce gamma rays, as their expanding shells interact with ambient dust. The extended emission from inverse Compton, pion decay, and supernovae processes are not modeled in this analysis. This is because the atmosphere's lack of uniformity overwhelms any diffuse emission in the residual sky maps[†].

3.3 Indirect Dark Matter Search

For this analysis, it is necessary to understand how a terrestrial telescope can detect the presence of dark matter. Imaging atmospheric Cherenkov telescopes like H.E.S.S., MAGIC, and VERITAS can indirectly search for dark matter. These observatories attempt to detect gamma rays that are emitted when two dark matter particles annihilate. Because the rate of annihilation depends on the local dark matter density, the gamma-ray emission rate is affected by the radially-dependent structure of the dark matter halo.

[†]These residual maps are discussed in Section 6.2.5.

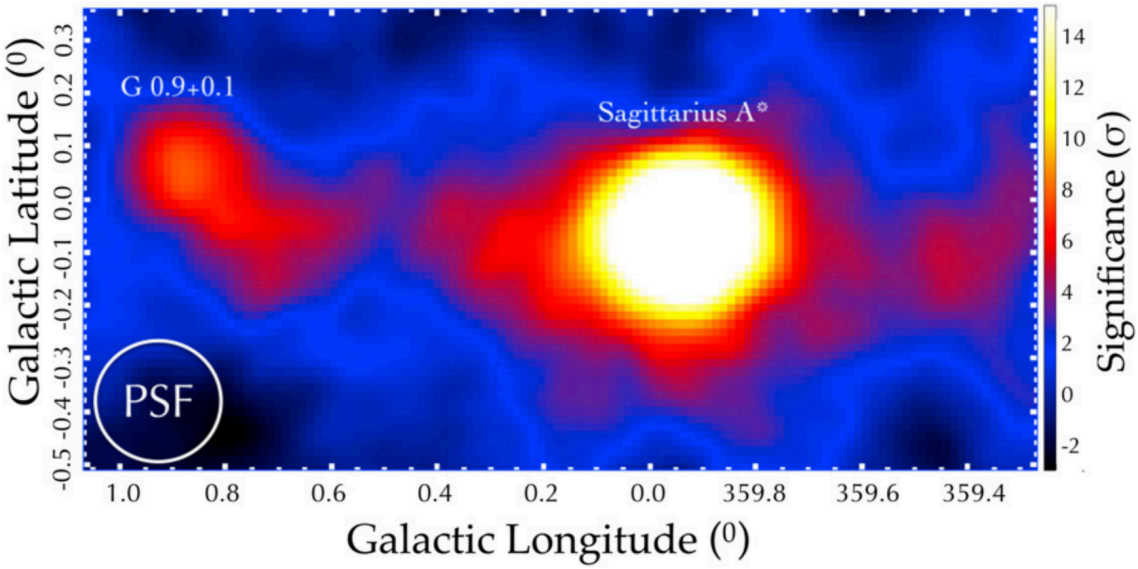

Figure 3.7: Galactic Center Ridge, from Ref. [124].

3.3.1 Dark Matter and Gamma Rays

Primarily, indirect searches focus on annihilating WIMPs, as the predicted decaying WIMP produces a lower flux of standard model particles than annihilation. WIMPs may annihilate into any standard model particle-antiparticle pair, but most studies examine a WIMP annihilating into a quark-antiquark or gamma-ray photon pair [111]. These different annihilations produce different spectra of final gamma rays. The final spectrum of gamma rays used in this analysis is calculated in Section 3.3.2. After the gamma-ray spectrum is understood, the spatial distribution of the annihilations is also discussed in Section 3.3.3. The expected flux of gamma rays from a halo can then be calculated by combining these spatial and spectral models.

3.3.2 Spectrum of Gamma Rays from WIMP Annihilations

In order to calculate the gamma-ray brightness of the dark matter halo, the produced gamma-ray energy spectrum from WIMP annihilations must be known. Different annihilation channels can produce different spectra. For instance, the $\chi\chi \to \gamma\gamma$ channel will produce a spectrum with a single spike at the WIMP's mass, while the $\chi\chi \to b\bar{b}$ channel will produce a curved power law spectrum of photons, shown in Figure 3.9. WIMP annihilations are expected to have multiple channels, where a population of WIMPs will annihilate into different channels with different probabilities. However, only the $\chi\chi \to b\bar{b}$ channel is considered for this analysis.

Three example Feynman diagrams of WIMP annihilations that produce a $b\bar{b}$ pair are shown in Figure 3.8, adapted from Ref. [65]. The particle $\tilde{f}$ is a supersymmetric fermion, the Z is the Z boson, and H is Higgs boson. The analysis in this thesis searches for a general $b\bar{b}$ signal, rather than the specific signal from one of these Feynman diagrams.

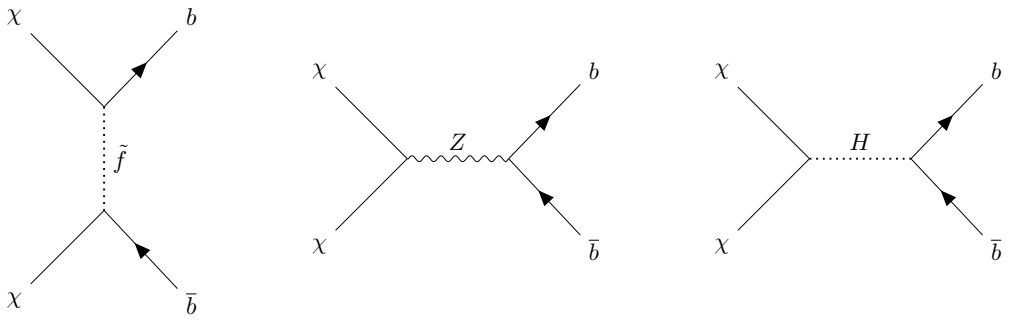

Figure 3.8: Three example Feynman diagrams of neutralino annihilations that produce a $b\bar{b}$ pair.

Source (Quarks)	Branching Ratio (%)	Products	PDG Chapter
$\bar{b}$	$\xrightarrow{\text{Hadronization}}$	B^+, B^0	b-Hadron Production
B^+ $(u\bar{b})$	$\xrightarrow{79\pm4}$	$\overline{\mathrm{D}}^0 + X$	Charged B Mesons
B^0 $(d\bar{b})$	$\xrightarrow{78\pm8}$	$\mathrm{K}^\pm + X$	Neutral B Mesons
B^0 $(d\bar{b})$	$\xrightarrow{47.4\pm2.8}$	$\overline{\mathrm{D}}^0 + X$	Neutral B Mesons
B^0 $(d\bar{b})$	$\xrightarrow{36.4\pm3.3}$	$\mathrm{D}^- + X$	Neutral B Mesons
$\overline{\mathrm{D}}^0$ $(u\bar{c})$	$\xrightarrow{45.7\pm2.8}$	$\mathrm{K}^+ + X$	Charm Mesons
D^- $(d\bar{c})$	$\xrightarrow{25.7\pm1.4}$	$\mathrm{K}^+ + X$	Charm Mesons
K^+ $(u\bar{s})$	$\xrightarrow{20.67\pm0.08}$	$\pi^0 + \pi^+$	Strange Mesons
K^- $(\bar{u}s)$	$\xrightarrow{20.67\pm0.08}$	$\pi^0 + \pi^-$	Strange Mesons
π^0 $\left(\frac{u\bar{u}-d\bar{d}}{\sqrt{2}}\right)$	$\xrightarrow{98.823\pm0.034}$	$\gamma + \gamma$	Neutral Pion

Table 3.1: Table of decay modes and products, indicating several ways photons are produced from $\bar{b}$ quarks. The X indicates other particles. Branching ratios and Particle Data Group (PDG) chapters are from Ref. [136].

After the desired channel is selected, the spectrum of photons produced by that channel is calculated. This is done by repeatedly simulating all the photons produced when the $b\bar{b}$ quarks hadronize and decay into other particles. Several of these decay processes are shown in Table 3.1. In the table, the $\bar{b}$ hadronizes into B^+ or B^0, which then decay into K and D mesons (plus some other particles X), and the D mesons also decay into K mesons. The K mesons can then decay into $\pi^\pm$ and π^0 mesons, and finally the π^0's decay into two photons. Though these pion decays are the dominant source of photons, these listed particles (as well as other unlisted ones) may produce additional photons through bremsstrahlung or annihilation mechanisms. All of the photons produced from pion decays, bremsstrahlung, and annihilations then make up a gamma-ray spectrum that is used in this analysis.

The software package CLUMPY [137] is used in this thesis to calculate the gamma-ray spectra for each annihilation channel. The spectral models that CLUMPY uses are based on the annihilation spectra in the PPPC 4 DM ID [138, 139]. These spectra are calculated using Monte Carlo simulations performed with PYTHIA [140] and HERWIG [141]. Figure 3.9 shows the resultant spectra from the annihilation of two WIMPs. Each line shows the spectrum from a different initial WIMP mass.

These spectra can be combined with the J-factor (Equation 3.12) to calculate the gamma-ray flux produced by the halo (Equation 3.11). It is important to note that mass-to-light ratios, and their derived J-factors are usually inferred from measuring star spectra. These measured J-factors can therefore suffer from large errors, as it can be difficult to determine which stars

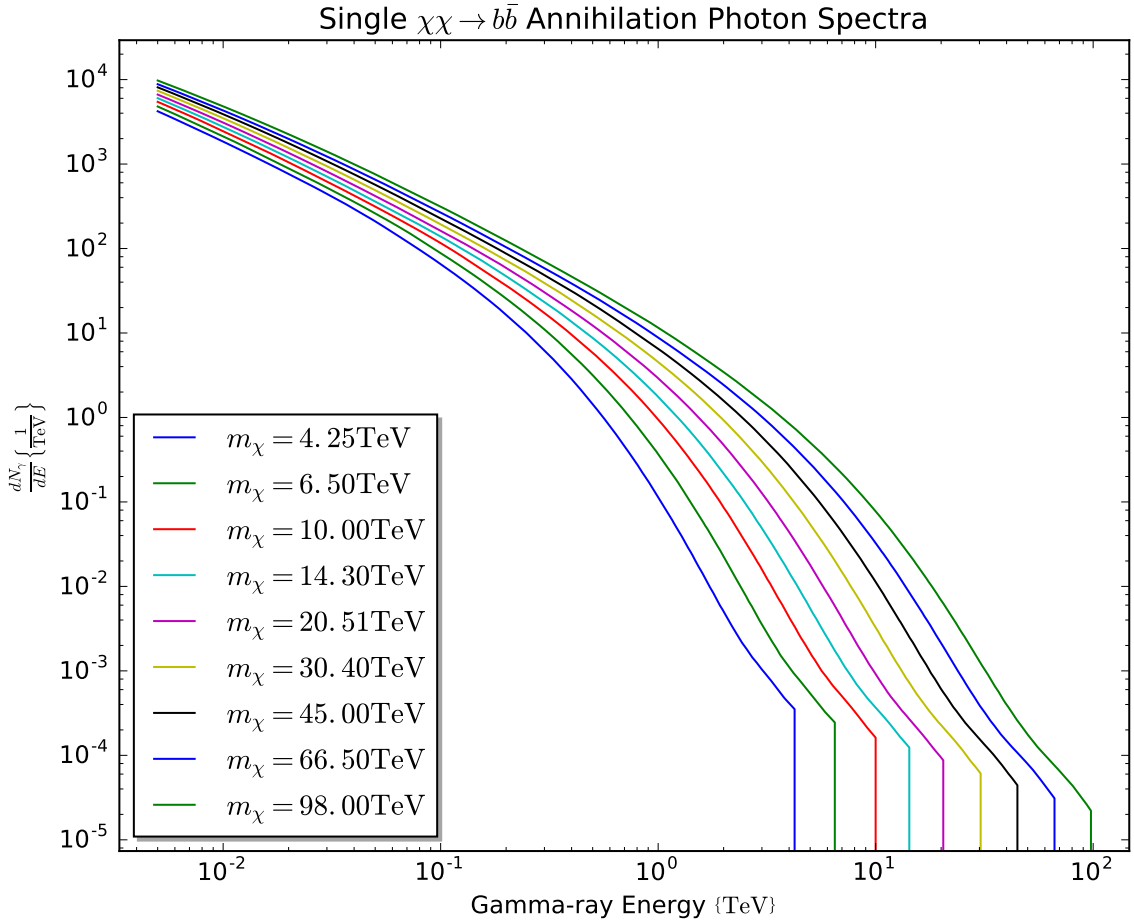

Figure 3.9: Resultant photon spectra from the annihilation of two WIMP particles solely into the $b\bar{b}$ channel. Each colored line represents a different WIMP mass.

are within a target gravitational well, and which ones are foreground or background stars [142].

By using estimated parameters with Equation 3.11, the flux of gamma rays from a dark matter halo can be estimated in order to understand how few events a dark matter halo produces. The flux of gamma rays from a dark matter halo can be estimated with Equation 3.11 to understand how just how few gamma rays can be observed from a dark matter halo. For this estimate, the dark matter mass is chosen to be 10 TeV, and the velocity-averaged cross section $\langle \sigma v \rangle$ is set at the relic cross section. Other chosen parameters are specified in Table 3.2, to align with the VERITAS telescope performance, or the parameters of the dark matter analysis performed in later chapters. For the table parameters, the dark matter halo would only produce a VERITAS-observable gamma ray between 4–10 TeV every 39 hours. This flux Φ is proportional

Estimated Parameters	
m_χ	10 TeV
Relic velocity-averaged cross section $\langle\sigma v\rangle$	$3\times10^{-26}\,\mathrm{cm}^3/\mathrm{s}$
Field of view	3°
Observable halo photon energy range	4–10 TeV[‡]
Observatory effective area	$287{,}000\,\mathrm{m}^2$
Annihilation channel	$\chi\chi\rightarrow b\bar{b}$
Dark matter halo shape	Einasto
Derived Values	
Integrated photon spectrum : $\int\frac{dN_\gamma}{dE}dE$	0.00536 photons per $\chi\chi$ annihilation
J-factor : $\int\int\rho^2 dl\,d\Omega$	$3.88\times10^{22}\,\mathrm{GeV}^2/\mathrm{cm}^5$
Halo flux Φ	2.5×10^{-11} photons/$(\mathrm{s}*\mathrm{m}^2)$
One halo photon detected every	39 hours

Table 3.2: Number of gamma rays from a dark matter halo. Field of view is the radial field of view of VERITAS. Observatory effective area is the VERITAS effective area at 29° telescope elevation (the average elevation of Galactic Center at VERITAS's latitude), 0.5° offset from GC, at the $\log_{10}$ mean energy (16.7 TeV) in the selected energy range. The Einasto halo shape parameters are chosen to be the same as in Section 3.3.3.

to the $\langle\sigma v\rangle$, so a factor of n larger particle cross section would produce a factor of n larger photon flux. Another way to increase the observed photon flux is by expanding the observable gamma-ray energy range. If the entire VERITAS energy range of 1.5–70 TeV is used, the observable halo photon energy range expands to 1.5–10 TeV, so the integrated photon spectrum increases, and the observed halo photon flux increases by a factor of 26.

3.3.3 Dark Matter Halo Structure

Observations allow most galactic dark matter halos to be modeled using a class of similar density profiles. A currently favored profile is the Einasto profile [143, 144]. This profile describes the mass-density of dark matter at a distance r from the halo center, $\rho(r)$. The Einasto profile is described by

$$\rho_{\mathrm{DM}}(r)=\rho_s Exp\left(-\frac{2}{\alpha}\left(\left(\frac{r}{r_s}\right)^{\alpha}-1\right)\right), \tag{3.10}$$

[‡]At 30° elevation, the VERITAS detectable photon energy range is 1.5–70 TeV. However, the analysis is limited to 4–70 TeV, and through conservation of energy, dark matter annihilations can't produce photons higher than the mass of the dark matter particle, 10 TeV in this example. Thus, the final observable energy range is 4–10 TeV.

where r_s is the scale radius of the halo, which specifies how wide the dark matter halo is. The parameter ρ_s is the scale density, which is the dark matter density at the scale radius. The parameter α is the power of the density profile's slope.

A larger α reduces the dark matter densities above and below the scale radius r_s. Both α and r_s are from the best fit values of the Aq-A-1 simulation in Table 2 of Ref. [145]. The r_s parameter is calculated via $r_s = r_{-2} = 15.14\,\text{kpc}$, where $r_{-2} = \frac{11.05}{h_{73}}\,\text{kpc}$ (in Ref. [145], Table 2) and $h_{73} = 0.73$ from Section 2.1 in Ref. [145]. In the model, the parameter α is fixed to 0.17, and r_s is fixed to 15.14 kpc. The distance to the Galactic Center is known to be $r_\odot = 8\,\text{kpc}$ [146–148]. The assumed Milky Way mass profile has a mass density of $\rho_\odot = 0.4\,\frac{\text{GeV}}{\text{cm}^3}$ [149, 150]. Since $r_\odot$ and $\rho_\odot$ are known, then in Equation 3.10 the dark matter density at the scale radius ρ_s is derived to be $0.12\,\text{GeV/cm}^3$. With these values, the Einasto profile in Equation 3.10 is shown in Figure 3.10. The distribution of dark matter follows an Einasto profile.

Most n-body simulations predict that density profiles steeply rise as $r \to 0$, forming a peak or *cusp* at their center. However, observations of dwarf galaxies usually show a flat density core within a given radius [151, 152]. This may be due to the presence of baryons in this core region, which can diffuse the central cusp of WIMPs into a core-like shape [153, 154]. As this flat core occurs in the innermost region covered by the gamma-ray observations in this analysis, the choice of a cusped or cored dark matter halo can have a significant impact. Specifically, if the true dark matter halo has a cored profile, but is modeled using a cusped one, then any derived upper limits on the dark matter cross section would be different. As a basic first step, only a cusped halo is used in this thesis.

When choosing which dark matter target to observe with a gamma-ray observatory, knowing the gamma-ray brightness of different sources can be useful. This Einasto density profile can be integrated to calculate the gamma-ray brightness, independent of the WIMP model being searched for. For annihilating dark matter, $\rho_{\text{DM}}(r)^2$ must be integrated along the line of sight.

The flux of gamma rays produced by these annihilations is given by

$$\frac{d\Phi}{dEd\Omega} = \frac{\langle\sigma v\rangle}{8\pi m_\chi^2}\frac{dN_\gamma}{dE}\int \rho^2 dl\,, \tag{3.11}$$

where the photon flux Φ is the number of gamma rays detected per area $\times$ time. The velocity-averaged cross section of the dark matter candidate is $\langle\sigma v\rangle$. Velocity-averaging is used because the cross section is velocity dependent, and the WIMPs that pass through a volume of space will have a distribution of velocities [155]. The average spectrum of photons produced by a single $\chi\chi$ annihilation is $\frac{dN_\gamma}{dE}$. The density integral in Equation 3.11 with the solid angle $d\Omega$

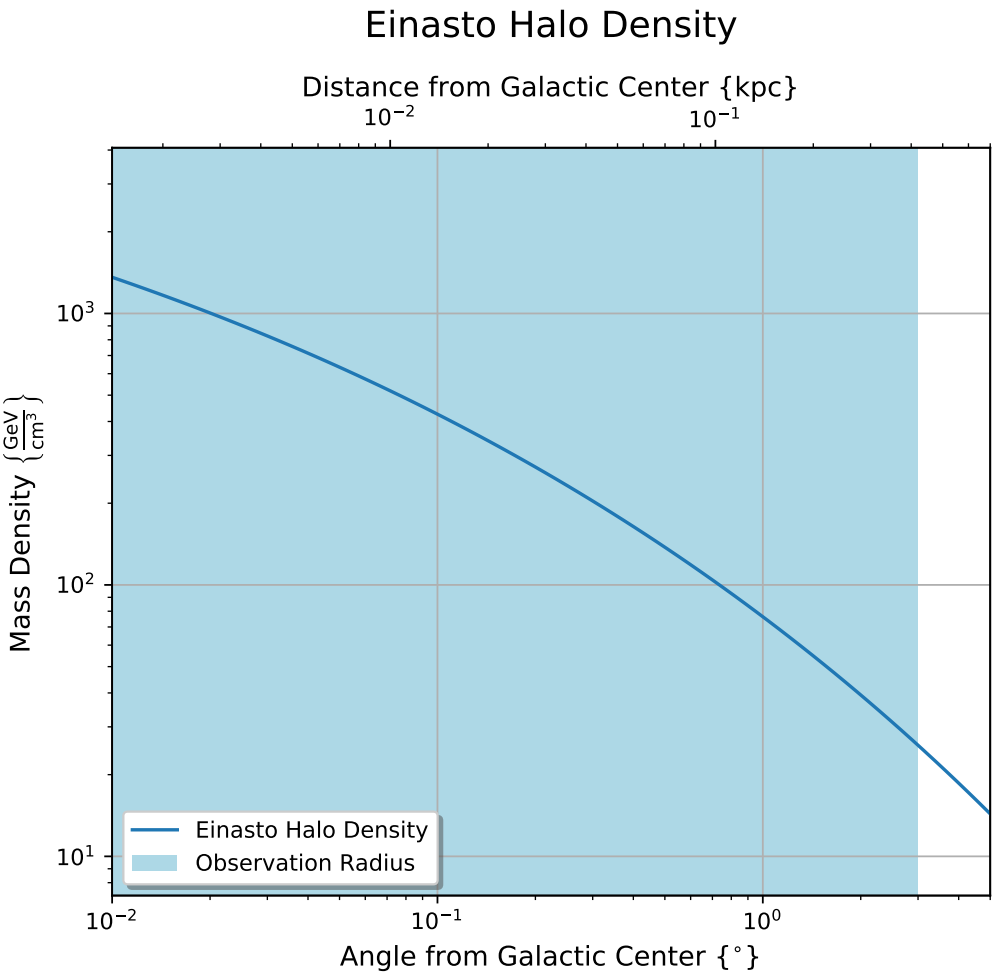

Figure 3.10: Mass density of the Einasto dark matter halo (Equation 3.10) used in this analysis. The bottom x axis shows the angle (as viewed from Earth) from the Galactic Center, while the top x axis shows the distance from the Galactic Center in kiloparsecs.

differential is often calculated separately, and is referred to as the J-factor,

$$J = \int \rho^2 dl\, d\Omega \ . \tag{3.12}$$

The J-factor is used to compare the relative gamma-ray brightness of different dark matter halos, which is a function of both dark matter density and observing distance. The Einasto density in Equation 3.10 can be integrated to calculate the J-factor at various radii, which is shown in Figure 3.11. In Figure 3.11, the profile shown is calculated with Equation 3.12, where

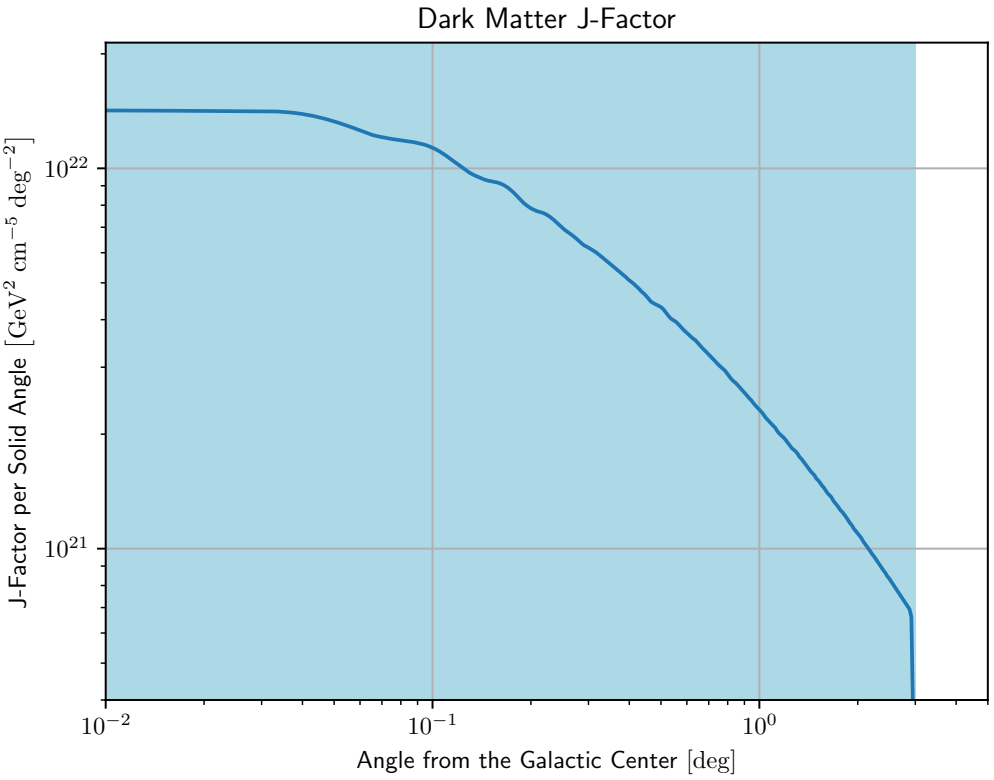

Figure 3.11: J-factor profile as a function of angle from the Galactic Center, calculated via Equation 3.12 with the Einasto density profile in Equation 3.10. The J-factor values are calculated by integrating 0.06° around each angle from the Galactic Center.

the $d\Omega$ integration limits span a radial angle of 0.06°. This J-factor profile then forms the spatial component of the dark matter halo, $M_{s,\text{halo}}$, used in Chapter 6. This profile is shown in a two-dimensional plot in Figure 3.12.

The halo structure in Figure 3.12 is a simple first step halo, one that does not account for more complex dark matter models. For example, a search for decaying dark matter would instead change the J-factor calculation to $\int \rho \, dl \, d\Omega$, spreading out the gamma-ray emission. More exotic WIMP models may slightly alter the gamma-ray brightness of the dark matter halo, compared to the previously mentioned WIMP model. For example, if dark matter WIMPs have an attractive force between them, their effective annihilation cross section is enhanced, increasing the gamma-ray emission from the halo. This effect is called Sommerfeld enhancement [157].

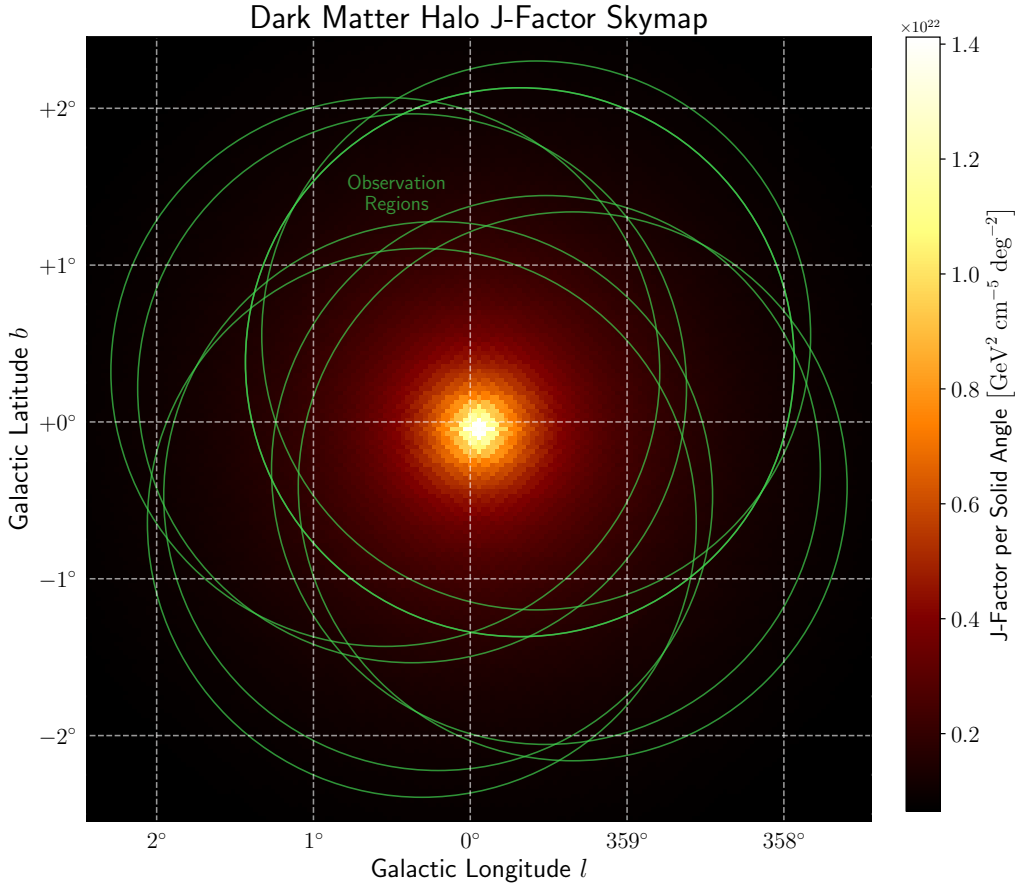

Figure 3.12: J-factor of the dark matter halo model used in this analysis. The green circles indicate the different observation regions. Note this is showing the same model as Figure 3.11, except here the J-factor axis is linear instead of logarithmic. The black corners result from the halo model only being calculated out to a radius of 3°, since there are no observations that extend past that. The halo center is positioned at Sgr A*, which is at

$$(l, b)_{\text{J2000}} = (359.944212°, -0.046013°)\,.$$

It is not positioned at the origin $(0,0)$ because the (l,b) coordinate system does not perfectly align with the Milky Way galaxy [156].

3.4 Cherenkov Photons

Cherenkov light and its production is discussed in this section, because the detection of gamma rays in Section 3.5 relies heavily on knowledge of Cherenkov light. Within the Earth's atmosphere (or any dielectric medium), the phase velocity of light $c_{atmosphere}$ is slightly slower than in a vacuum. Any charged particles travelling at velocity $v > c_{atmosphere}$ will induce the

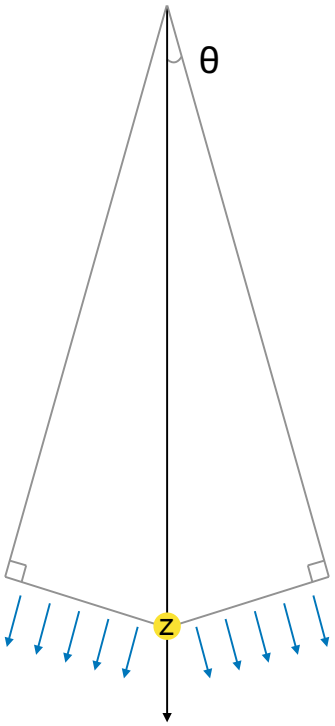

Figure 3.13: Cherenkov light (blue arrows) is emitted at angle θ, relative to the charged particle z's path.

atmosphere to produce Cherenkov photons [158]. From a single charged particle of constant velocity, Cherenkov photons form a conical wavefront shown in Figure 3.13. This wavefront is similar to a sonic boom shockwave, or the wake produced when a boat travels faster than the speed of the waves.

Cherenkov photons are emitted at an angle θ relative to the charged particle's path, determined by the index of refraction of the medium n, the speed of the charged particle v, and the speed of light in the medium c:

$$\theta = ArcCos\left(\frac{c}{n\,v}\right). \tag{3.13}$$

For the air showers used in this analysis, the Cherenkov angle θ is ~1°. In practice, air showers are more complex due to the number and distribution of charged particles and their velocities, energy losses, and Cherenkov photons repeatedly scattering off of the atmosphere. These effects tend to smear the theoretically-clean Cherenkov cones into a diffuse pool of light on the ground, shown in Figure 3.14.

The spectrum of photons produced by the Cherenkov effect can be calculated with the

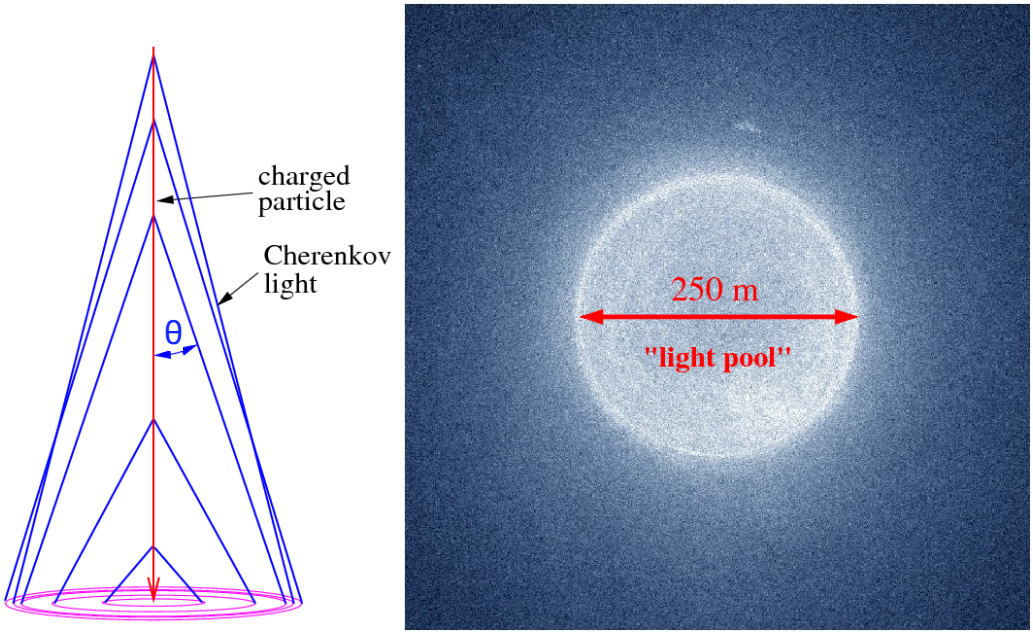

Figure 3.14: Cherenkov light from a gamma ray shower illuminating the ground. Due to the changing atmospheric density, the Cherenkov angle changes as the electromagnetic shower descends (left), concentrating the emitted light into a ring-like pool (right). The initial gamma ray in this simulated example had an energy of 1 TeV. Figure is from Ref. [159].

Frank-Tamm formula [160, 161],

$$\frac{dE}{dx\,d\omega} = \frac{(ze)^2\omega}{c^2}\left(1 - \frac{c^2}{v^2\,\epsilon(\omega)}\right), \tag{3.14}$$

where E is the energy emitted as Cherenkov radiation, x is the length of the charged particle path, ze is the charge of the particle, ω is the emitted Cherenkov photon frequency, c is the speed of light (phase velocity) in the medium, v is the speed of the particle, and $\epsilon(\omega)$ is the frequency-dependent permittivity.

In Figure 3.15, a visible example of Cherenkov photons is shown, produced in the Advanced Test Reactor at the Idaho National Laboratory. Neutrons emitted by the reactor collide with atoms in the water, freeing some electrons with enough kinetic energy to travel faster than the speed of light in water. These superluminal-in-water electrons then create the blue Cherenkov photons imaged here.

Section 3.5 covers how particles from outer space can produce Cherenkov photons. These UV- and visible-spectrum Cherenkov photons are then imaged and recorded by the VERITAS observatory, as discussed in Chapter 4.

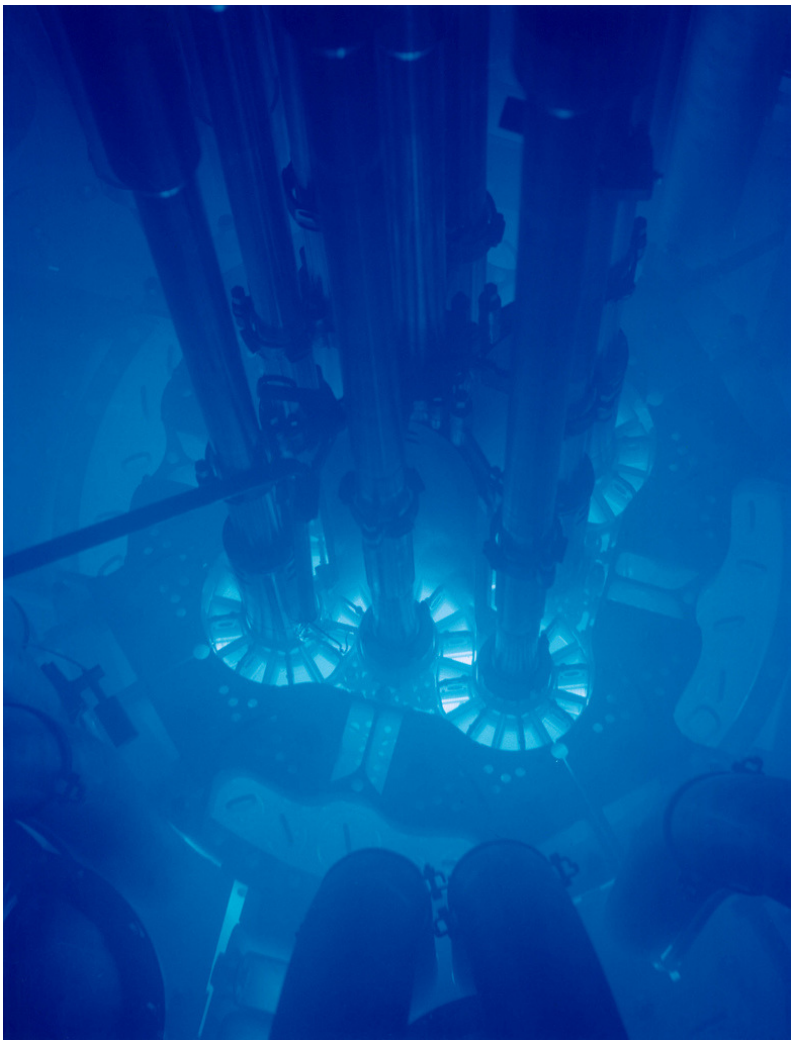

Figure 3.15: Blue Cherenkov light in the Advanced Test Reactor core, at the Idaho National Laboratory [162, 163].

3.5 Atmospheric Showers

When a particle (the primary) strikes an atom of Earth's atmosphere at GeV or higher energies, it sets off a cascade of energetic particles called an air shower [164, 165]. When the primary particle consists of one or more hadrons, like a proton or iron atom, it creates a hadronic shower. When the primary particle is a gamma ray or a charged lepton, it creates an electromagnetic shower. Electromagnetic showers produce a cascade of electrons, positrons (e^+), and photons, where each successive generation of particles tends to have more particles but less energy per particle than the last. To start the shower, the primary gamma ray will

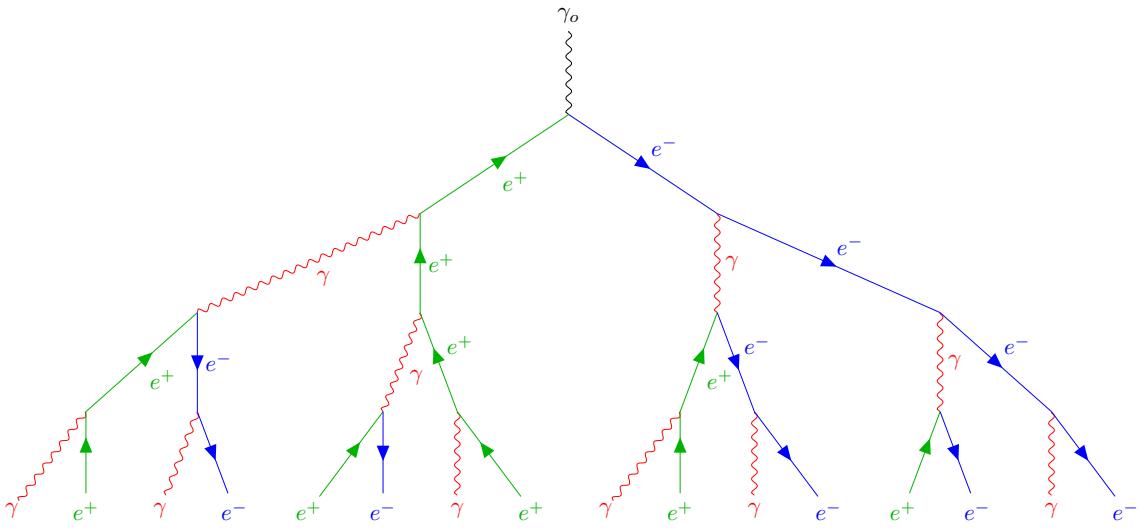

Figure 3.16: Diagram of the first few generations of an electromagnetic cascade as it descends downwards through the atmosphere, layered by interaction generation. At the top of the diagram, γ_o is the initial astrophysical gamma ray.

interact with an atmospheric atom, producing an e^-e^+ pair, each with roughly half the primary gamma ray's energy, as shown in Figure 3.16. The e^- and e^+ emit bremsstrahlung photons, and incite the atmosphere to emit Cherenkov photons, discussed further in Section 3.4. The higher-energy bremsstrahlung photons then produce e^-e^+ pairs, which go on to produce more bremsstrahlung and Cherenkov photons. As each newly created particle has less energy than its parent particle, eventually the particles in the shower lack the energy to produce additional child-particles. When electrons have around 80 MeV[§] or less of kinetic energy, energy losses due to ionization begin to dominate [167].

Of all detected air showers, ~99% are due to protons and electrons, rather than gamma rays. Protons produce hadronic showers which also produce Cherenkov light, like electromagnetic showers. In the initial collision, the astrophysical proton p_{cosmic} interacts with an atmospheric nucleon N. The proton-nucleon collision then may produce pions ($\pi^\pm$ and π^0), as well as other particles whose production rates vary with available interaction energy. These other particles include additional protons and neutrons, as well as kaons, other mesons, and additional baryons and nucleons. These all go on to interact and decay to produce further particles, as part of a hadronic cascade.

The π^0 decays into two gamma rays, which produce an electromagnetic cascade of electrons,

[§]This is the energy for which, for an electron, the loss of energy due to ionization is equal to the loss of energy due to bremsstrahlung [136, 166]

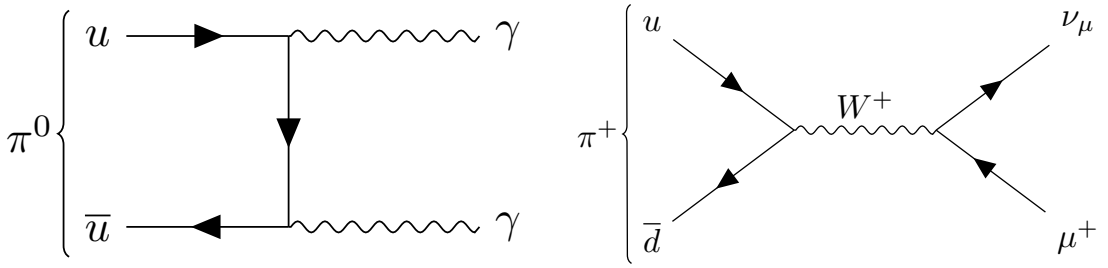

Figure 3.17: Left: Feynman diagram of a π^0 decaying into two photons. Right: Feynman diagram of π^+ decaying into a lepton pair.

positrons, and lower-energy photons. After each generation of the hadronic cascade, roughly 1/3 of the shower's energy is transferred into a new electromagnetic sub-shower. This π^0 decay is shown in Figure 3.17.

In hadronic showers, any produced π^+s and π^-s can travel far in the transverse direction, away from the main axis of the primary particle. The π^+s and π^-s then decay into $\mu^+\nu_\mu$ and $\mu^-\bar{\nu}_\mu$ pairs, respectively. The π^+ decay is shown in Figure 3.17. The π^0 quickly decays into a pair of gamma rays, each of which then start their own electromagnetic shower. The π^+ and π^- have longer lifetimes ($\pi^\pm \rightarrow 3\times10^{-8}$ s vs $\pi^0 \rightarrow 9\times10^{-17}$ s [167]), allowing them to carry energy farther away from the central shower axis. Both of these effects create sub-showers farther away from the primary particle axis, which tends to cause hadronic showers, and their resulting Cherenkov images, to be wider than a purely electromagnetic shower of the same length.

In order to accurately measure the gamma rays from an astrophysical source, the hadronic showers must first be removed. Because hadronic showers produce a slightly different image of Cherenkov light, many of them can be excluded from the analysis. The process of identifying and excluding these hadronic showers is referred to as gamma-hadron separation.

In Figure 3.18, the differences between a gamma-ray shower (left) and a proton shower (right) are shown. Darker areas indicate more Cherenkov photons are produced by charged particles in the shower. The gamma-ray shower produces most of its Cherenkov photons along the central vertical core of the shower, while the proton shower produces Cherenkov photons spread out in a wider, fan-like shape. In the proton shower, any produced π^0's decay into electromagnetic sub-showers in the interior of the shower. The net effect is that, when compared to a gamma ray, a proton must start with ~3 times the energy to produce a similar amount of Cherenkov photons, which are distributed in a wider pattern.

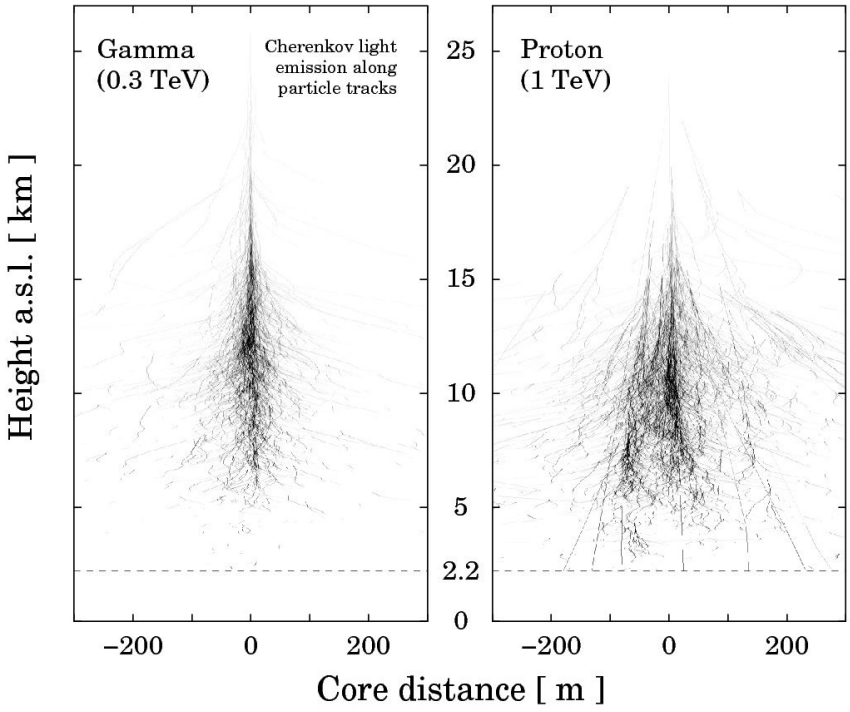

Figure 3.18: A gamma ray shower (left) alongside a proton shower (right) [168].

4 The VERITAS Observatory

Figure 4.1: The VERITAS observatory.

VERITAS, or Very Energetic Radiation Imaging Telescope Array System pictured in Figure 4.1, is a gamma-ray observatory operating in Arizona, USA, and is capable of detecting gamma rays with energies from 100 GeV to 70 TeV. The observatory consists of an array of four Imaging Atmospheric Cherenkov Telescopes (IACTs), spaced ~90 m apart. Each telescope carries an array of 345 mirrors, and a 499 photomultiplier tube (PMT) camera on a set of struts. When a gamma ray produces an air shower in the atmosphere, the shower emits blue-UV Cherenkov photons over a time span of nanoseconds. By focusing these photons onto the PMT camera with the mirrors, images of the shower can be taken, in which each pixel of the image consists of analog voltage pulses from each PMT.

In this chapter, the different hardware components are examined, in order of signal propagation. Section 4.1 details Telescope Pointing, including its monitoring and calibration. The mirrors are discussed in Section 4.2, including their properties and alignment. In Section 4.3, the PMTs are explored, including their performance and calibration. The trigger system is examined in Section 4.4, relating how candidate signal voltages are saved while discarding those sourced from noise. Section 4.5 discusses the different observatory epochs, as over time, changes and modifications have altered the observatory's performance.

4.1 Telescope Pointing

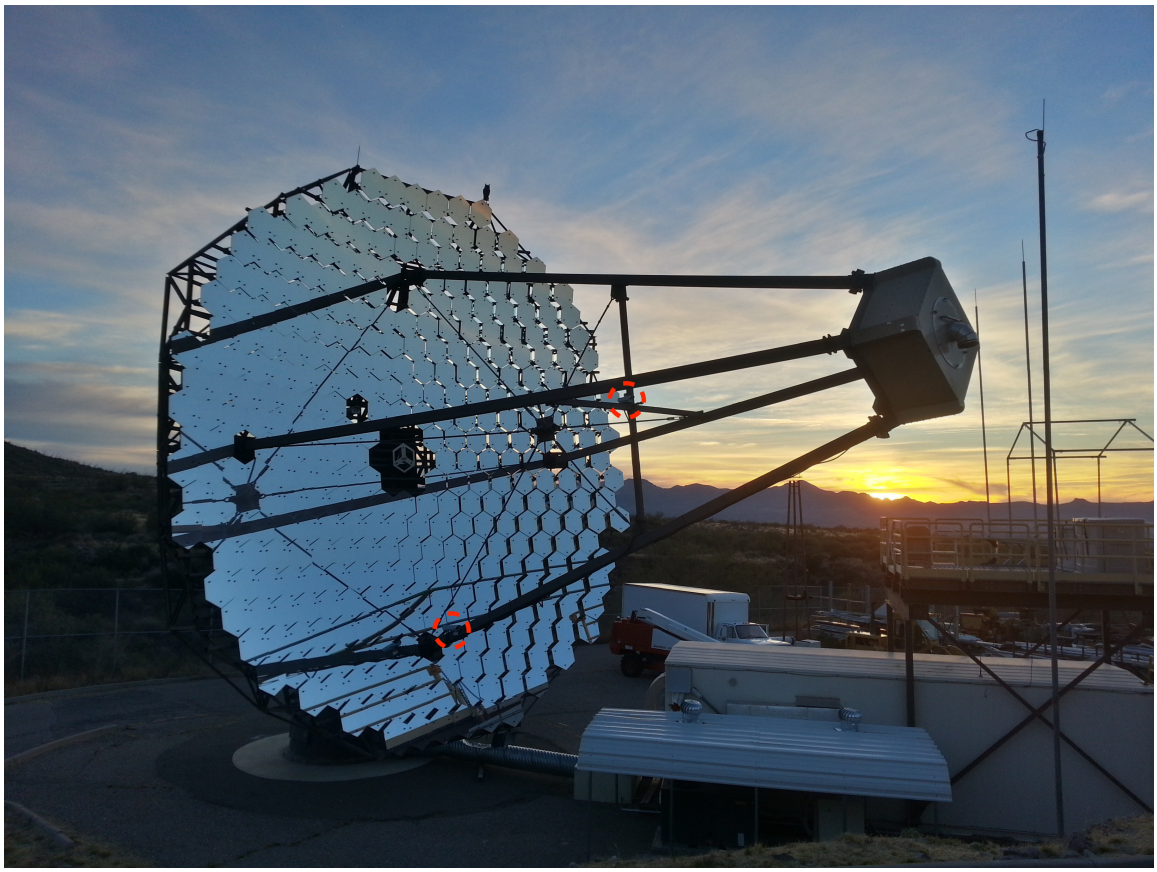

Figure 4.2: View of the 345 mirrors, the camera support structure, and the PMT camera housing at the end of the four supporting arms.

Like most telescopes, each VERITAS telescope has a fixed base and a pointable dish for collecting light. This dish can rotate in azimuth and in elevation, with enough range in both axes to point at any direction above the horizon that is not blocked by local mountains, though low elevations have reduced gamma-ray sensitivity. At their fastest, the telescopes slew at a rate of ~1° per second. To track where the telescopes are pointing, the motors that drive the azimuth and elevation movement have encoders that digitize the pointing direction of the dishes. These encoders are attached to the axes of the motors, and thus they are capable of tracking the azimuth and elevation over its entire range of motion. However, as the dishes are large metal structures, they bend and flex at different elevations and azimuths. This flexing also experiences hysteresis, in which the bending changes whether approaching a pointing target from a higher

or lower elevation. To account for this flexing, the encoder values are then given to a structural model called T-Point, which corrects for the dish structure bending at different azimuths and elevations. After applying this model, the telescope pointing can be tracked with an accuracy of ~0.02° [169].

As an improvement to the encoder measurements, a VERITAS Pointing Monitor (VPM) system is also in place. The VPM consists of two CCD cameras and 4 LED lights affixed to each telescope. The CCD cameras are oriented such that they can view the PMT camera and the background stars. The LED lights are attached to the PMT camera, next to the Winston cones detailed in Section 4.3. The first CCD camera is attached below the bottom mirrors, and images the stars in the field of view. The second CCD camera is attached to the support struts, roughly halfway between the mirrors and the camera, and images the focal plane of the telescope. Both cameras are marked by red dashed-line circles in Figure 4.2. During regular observations, these cameras take images of background stars and the focal plane LEDs every two seconds. By extrapolating the LED positions from the star positions, an improved pointing accuracy of ~0.007° can be achieved [170]. This improvement persists down to an elevation of 29°, where the data analysis in this thesis takes place.

4.2 Mirrors

When the Cherenkov light from a gamma-ray shower first interacts with the telescope array, it is reflected by some of the 345 mirrors. These mirrors face towards the incoming Cherenkov light, with the PMT camera facing the mirrors, as shown in Figure 4.2. When its spherical mirrors, spherical dish, and focal length ratio of ~2 are considered, this configuration is referred to as a Davies-Cotton telescope [171]. Each mirror has an area of $0.322\,\mathrm{m}^2$, and a spherical curvature radius of 24 m. The mirrors are each mounted along the optical support structure so that the total diameter of the telescope's mirror area is 12 m, with a total area of $111\,\mathrm{m}^2$ and a focal length of 12 m [172]. Figure 4.3 shows the mirrors' reflectivity as a function of wavelength. The VERITAS specifications state that the mirror reflectivity must be $\geq 85\%$, between 280–450 nm.

As the mirrors are exposed to the elements, they slowly accumulate dust and scratches. To combat this, they are cleaned and recoated every two years. Each mirror is attached to the optical support structure via three adjustable mounting points, allowing for adjustment of the mirror orientation to point directly at the camera, as detailed in [174]. This alignment is measured and adjusted at regular intervals, using background stars as a calibration source.

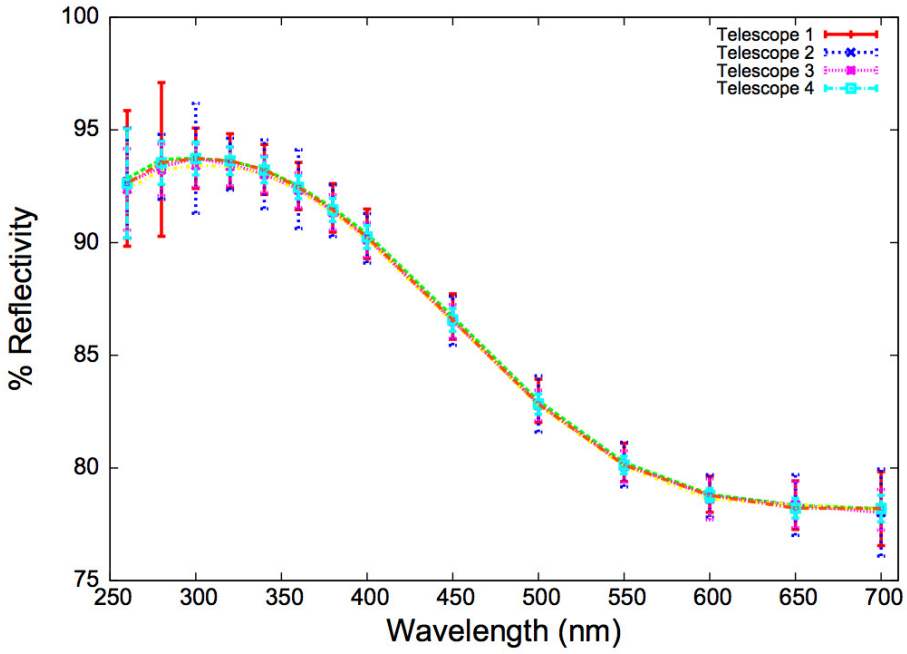

Figure 4.3: Mirror reflectivity as a function of wavelength for each telescope, from Ref. [173].

4.2.1 Star Point Spread Function

Photons that bounce off the mirrors are not reflected perfectly due to the Davies-Cotton design. This is because of how the mirrors are aligned with the focal point. When the mirrors' centers are aligned towards a focal point, the edges of these mirrors are inherently not aligned with the focal point [175]. The result is that a single point-like light source will appear blurred out on the focal plane. Minor imperfections in the surface of the mirrors, dust, and small mirror misalignments also contribute to this blurring.

This blurring is quantified by a fitted Gaussian function, usually called the Optical Point Spread Function* (OPSF). The OPSF is measured monthly by pointing a telescope at different stars and pointing CCDs at the focal plane. Figure 4.4 shows a calibration image from the first VERITAS telescope. The OPSF is roughly Gaussian-shaped but with longer tails and a 0.06° full width half maximum [172].

This point spread function is important, because it determines how accurately Cherenkov showers are imaged. A larger star point spread function means Cherenkov images are blurred out, which adds to the gamma-ray point spread function, discussed in Chapter 5.

*Please note that this is different from the PSF described in Chapter 5, which quantifies the spread in the reconstructed gamma-ray positions. The OPSF instead describes the spread of UV-Optical photons.

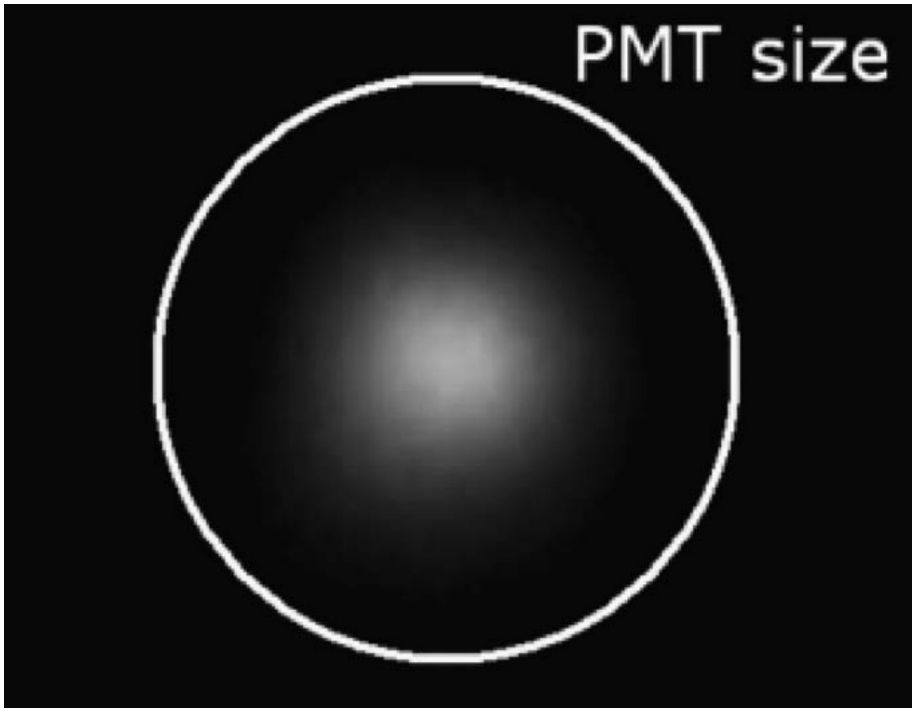

Figure 4.4: Image of Polaris after reflecting off the mirrors, demonstrating the shape of the OPSF, from [172]. The star has a full-width at half-maximum angle of 0.06°. The circle indicates the radius of a PMT.

4.2.2 Mirror Alignment

The mirror alignment procedure is performed by placing a CCD camera at the focal plane, facing towards the mirrors. The telescope is then pointed towards a magnitude 2 star at ~70° elevation. The pointing is known as a "raster" scan of the star, where each mirror's field of view is in turn centered on the star. By using the CCD to examine the position of the star in each mirror, the mirror's alignment can be calculated and corrected.

4.3 PMTs

Each telescope has a PMT camera on the end of four supporting arms, inside a protective housing. This camera consists of 499 Photo Multiplier Tubes (PMTs), each with a Winston cone to increase the light collection area for each PMT [176]. The PMTs are Hamamatsu's model R10560-100-20 MOD [177]. These Winston cones can be seen attached to the PMTs in Figure 4.5.

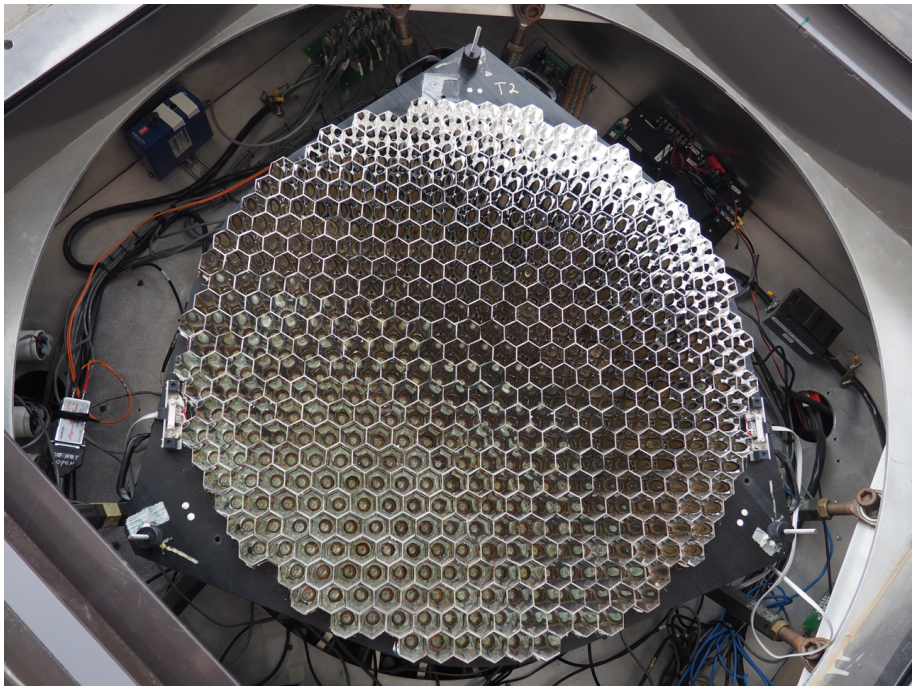

Figure 4.5: Hexagonal Winston cones over the circular PMTs, inside the camera housing. Image Credit: VERITAS Collaboration.

To operate, the PMTs are connected to high voltage, typically 900–1200 V. The PMTs' output signals are first sent through an amplifier, before travelling down a ~40 m cable to trigger and digitization electronics stationed near the telescope [178].

The first circuit that the signal passes through is a Constant Fraction Discriminator (CFD) circuit [179]. This circuit's behavior, shown in Figure 4.7, duplicates the signal voltage pulse from the PMTs, inverts and delays the duplicate pulse, and adds it back to the original pulse. This combined pulse is then sent to a Zero Crossing Discriminator (ZCD). When the input pulse crosses the zero-volts threshold, the ZCD emits a 10 ns trigger pulse.

The use of this circuit has two main benefits. The first is that the CFD circuit will trigger at the same position within the pulse, regardless of the pulse's size. If a simple voltage-threshold trigger were used instead, the time of the trigger would be earlier for faster-rising large pulses, and later for slower-rising small pulses. The CFD's zero threshold trigger is invoked when the signal voltage pulse reaches a predetermined fraction of its maximum value. For VERITAS, this fraction threshold is set at 75% of its maximum value. The second benefit of this circuit is that when it detects a voltage pulse larger than a given maximum threshold, it can emit an extra logic trigger, called a low-gain trigger. This extra low-gain trigger is then used by the Flash

Figure 4.6: The two PMT models used in the VERITAS cameras [177].

Analog-to-Digital Circuit (FADC) to read out either the high-gain and low-gain signal. The low-gain signal is not amplified as much before it is digitized. The high-gain trigger can only detect signals with at most 120 photoelectrons, while the low-gain trigger can detect signals up to 750 photoelectrons. This low-gain option increases the digitizable dynamic range of the entire system.

Stars and other sources of background light emit background visible photons (Night Sky Background or NSB photons) that can falsely trigger the CFD circuit, contaminating any Cherenkov signals. In order to reduce this contamination, the CFD circuit is set to ignore any pulses smaller than 45 mV. This threshold is adjusted during observations to account for varying rates of NSB photons.

After the CFD emits a trigger pulse, the signal voltage pulse is passed to the FADC circuit for digitization. This FADC circuit then, for each 2-nanosecond time bin, measures how large the voltage pulse is with a series of 255 voltage thresholds. The highest threshold that is crossed in a single time bin then determines the digital voltage value that is saved to the FADC buffer for that time bin.

For each voltage pulse, both the high-gain- and low-gain-amplified signals are digitized and saved to a single rolling buffer, with one at a delayed time in the buffer. Then, the FADC waits for higher level triggers to read out its buffers into a data file. If the low-gain trigger pulse was

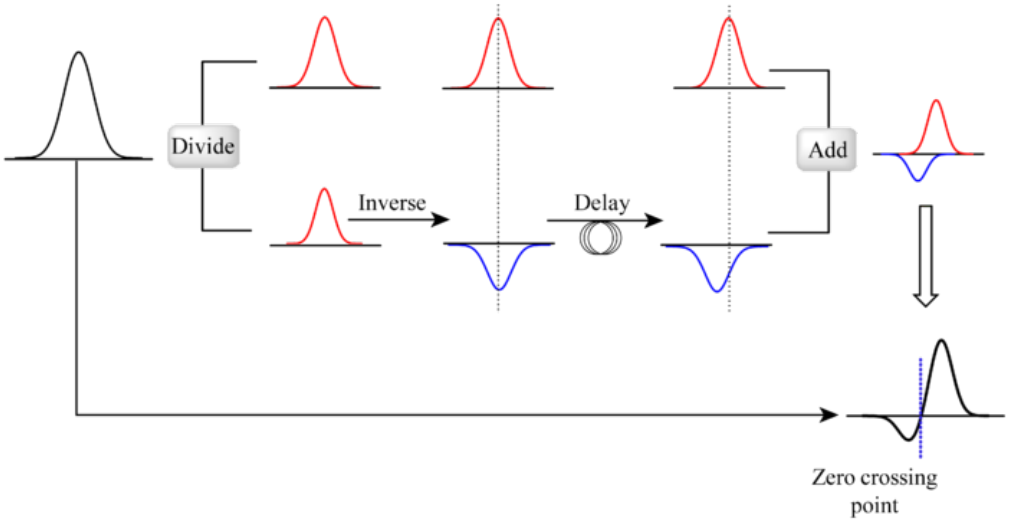

Figure 4.7: CFD signal processing, from Ref. [180]. An input signal on the left is manipulated to allow for constant fraction discrimination.

received by the FADC, then the segment of the buffer containing low-gain amplified signal is read out, otherwise the high-gain segment is read out instead [172, 181].

4.3.1 PMT Upgrade

In summer of 2012, all PMTs in the telescopes were replaced with improved PMTs. Specifically, the original Photonis XP2970 models were replaced with the Hamamatsu R10560-100-20 MOD. This was done because the R10560 collects 23% of incident Cherenkov photons, 35% more than the the XP2970. This higher collection rate means more photons from a shower are detected by the PMT, which makes VERITAS more sensitive to lower energy gamma rays. In addition, single-photoelectron studies indicate the R10560's voltage pulse's full duration at half maximum time is ~40% shorter than the XP2970, as shown in Figure 4.8. These shorter voltage pulses allow for easier discrimination between NSB fluctuations and Cherenkov signals [177].

The data used in this thesis was taken both before and after this upgrade, which means the telescope performance is different for these two time periods. This is accounted for by separate simulations for each PMT model, mostly resulting in different effective areas (discussed in Section 5.6.1) at the lower energies. These epochs are discussed further in Section 4.5.

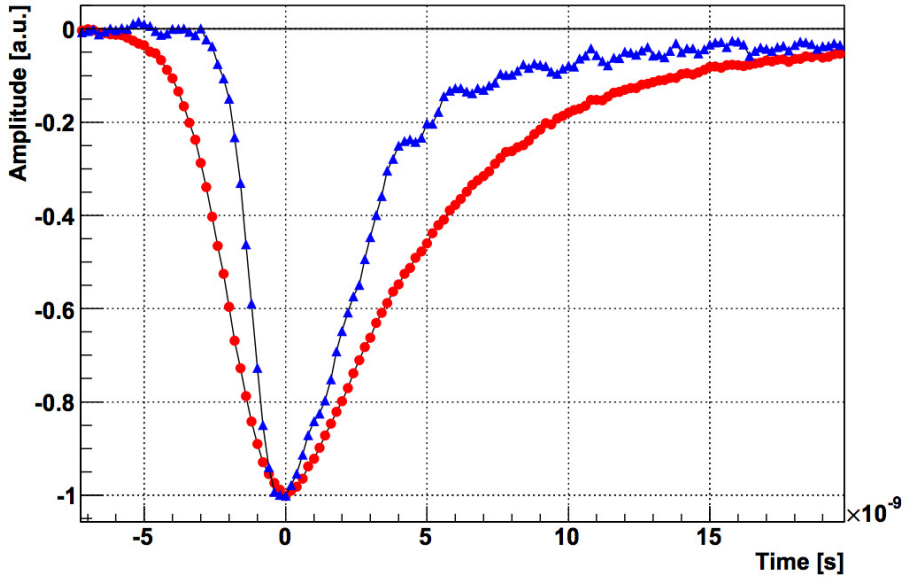

Figure 4.8: Pulse shapes of the old XP2970 PMTs (red circles) and the new R10560 PMTs (blue triangles). Plots are the average of many afterpulses, normalized to the maximum amplitude. Pulses shown include dispersion due to a ~40 m coaxial cable between the PMTs and the digitizer boards. [177]

4.3.2 PMT Calibration

While the VERITAS PMTs are all the same model, there are still differences from PMT to PMT that can impact any data taken. Primarily, these differences can cause the same number of incident photons to create differently-shaped output voltage pulses in each PMT. To account for these differences, a calibration procedure is applied nightly or semi-nightly. These are performed with a set of flashing LEDs, placed next to the mirrors such that they illuminate the PMTs.

Once per dark run, the single-photoelectron curves for each PMT are measured. A dark run is the roughly two-week-long period when the moon is below the horizon at night, providing optimally-dark observation conditions. This is done by placing an opaque (several-mm-thick metal) plate over the PMTs, with a mm-diameter hole drilled over the location of each PMT. The LEDs are then flashed repeatedly. Because the opaque plate has holes drilled over each PMT, each only receives on average 0–5 photons per flash. Large numbers of flashes can then be used to gather information on each PMT's distribution of pulse widths. By examining a histogram of the pulses' integrated charges, one can see Poisson-statistic peaks that are formed for integer numbers of photons. These peaks are then used to translate the integrated charges from the PMTs into their original number of photoelectrons. These calibration techniques are further detailed in Ref. [182].

4.4 Trigger System

The operation of VERITAS requires digitizing voltage pulses with voltage samples roughly once per two nanoseconds, per photomultiplier tube. This means that with 255 voltage levels, one second of all voltage measurements would require one terabyte of hard drive space. Since this is unfeasible with today's computing systems, only subsets of the raw pixel voltages are saved when certain trigger conditions are met. To complicate matters, photons from atmospheric muons and the night sky background can also cause voltage pulses similar to a gamma-ray shower's Cherenkov photons. Thus, VERITAS has a system of triggers that reduces the amount of raw data that is saved, while also partially filtering out non-gamma-ray events.

The trigger system consists of three levels. The L1 is the first and lowest level trigger. An L1 trigger (sometimes called a pixel trigger) is emitted when a PMT's CFD circuit detects a signal voltage above a given threshold, typically in the 10s of mV. This threshold voltage is varied throughout data taking by a rate-feedback system, which adjusts the trigger threshold according to the night-sky-background level.

Once L1 triggers have been emitted, they are passed to the L2 trigger system. The L2 image trigger is emitted when a group of L1 triggers meet two requirements. The first requirement is that multiple L1 triggers must fall within a certain time window. Multiple L1 triggers must be within 5–10 ns of each other, depending on the VERITAS hardware epoch. The second requirement is that multiple L1 triggers must all be from neighboring pixels. More specifically, any pixel with an L1 trigger and two neighboring pixels with L1 triggers (each pixel has 6 neighboring pixels) meets the pattern condition [183]. The pattern requirement helps reduce the number of triggers from non-gamma-ray sources. Night sky background photons are only able to trigger individual pixels, while muons tend to create ring-shaped images. Once one of these patterns occurs within a time window, the L2 system emits an L2 trigger, which is sent to the L3 array trigger system.

The L3 array trigger system looks for coincident L2 triggers that fall within a ~50 ns time window. This window is adjusted for each telescope based on the azimuth and elevation of the pointing, as these can introduce delays between images of up to hundreds of nanoseconds. During a typical observation period, the L3 trigger rate is around 200–300 Hz. Once an L3 trigger is invoked, a signal is sent to all telescopes that directs the digitized voltages for all pixels in the cameras to be read out from their buffers, and saved to memory. These pixel voltages can then be processed by the analysis software to reconstruct the gamma-ray events.

4.4.1 Dead Time

When the L3 trigger is invoked and the buffers are being read out, the FADCs are unable to store new PMT voltages in the buffers. Being unable to store new PMT voltages effectively reduces the amount of time spent observing gamma rays. This lost time is usually referred to as dead time. Since the dead time is a fixed time loss per event, the percent of time lost due to event readout rises the more frequently events are read out. For an L3 trigger rate of ~300 Hz, approximately 12% of the time is lost due to buffer readouts. Since the L3 rate varies over the course of a single 30 minute run, the dead time also varies, and is accounted for in the analysis in Chapter 6.

4.4.2 Time Zero Calibration

Because all PMTs and signal cables are not identical, there are differences in how long a voltage pulse takes to travel. More specifically, the time between a) when the photon strikes the PMT's photocathode and b) when the voltage pulse sets off its L1 trigger, can vary from pixel to pixel. This is usually measured by looking at the average arrival time of many events over all camera pixels. By looking at the average arrival time, pixels that are consistently early or late are accounted for, improving image identification.

4.5 Epochs

Since it was completed in 2007, VERITAS has evolved over several years as collaboration members have upgraded it to improve its performance. Each improvement in performance needs to be taken into account in the analysis chain. To organize these different observatory performances, in the data they are referred to as epochs 1, 2, 3, 4, 5, and 6, and are usually denoted as V1, V2, V3, V4, V5, and V6.

The four telescopes were built within a coordinate system where the origin is at 31.675N, 110.962W, the x axis points East, and the y axis points North. These local coordinates can be described by the format (X n, Y e), where X and Y are in meters. As the first three telescopes were constructed and brought online, data taken after each was considered part of the V1, V2, and V3 epochs. Telescope 1 was placed at (-37.6n, -23.7e), telescope 2 at (44.1n, -47.7e), and telescope 3 at (29.4n, 60.1e). In 2007, the fourth telescope was constructed at (-35.9n, 11.3e), and data taken between this point in time and the next major upgrade is considered the V4 epoch.

In September 2009, telescope 1 was moved to a new position (135.4n, -8.61e), after it was demonstrated with simulations that it would grant a ~30% improvement in sensitivity [184]. Data taken after this relocation is referred to as the V5 epoch.

In August 2012, the PMTs in all cameras were replaced with improved PMTs that had a higher quantum efficiency, improving the telescopes ability to resolve images [177], and is discussed in Section 4.3. Data taken after this upgrade is considered part of the V6 epoch.

Since these different epochs have different telescope configurations, the instrument response functions are different, meaning each epoch behaves in a quantifiably distinct manner. For the dark matter analysis described in this thesis, only data from the V5 and V6 epochs are used[†].

[†]This data is detailed further in Table 6.1.

5 Gamma-Ray Reconstruction Methods

Chapter 4 explained how the trigger system initializes the readout of PMT voltage traces. This chapter describes how gamma rays are reconstructed. In gamma-ray reconstruction, voltage traces induced by Cherenkov photons must be identified and combined to form an image of the original Cherenkov shower. Then the shower images from multiple telescopes can be used to reconstruct the original gamma ray's energy and direction.

Throughout the rest of this thesis, *Galactic Center* and *Sgr A** are used to describe the main analysis region. While in astrophysics *Galactic Center* refers to the several-degree-radius area around the center of our galaxy, *Sgr A** refers to the specific central gamma-ray point source ($<0.2°$ radius). VERITAS data observations that cover this point source are also referred to as *Sgr A** data, described further in Section 6.1.

5.1 Pedestal Variation

Before reconstructing any events, the pedestal and pedestal variations must be calculated. This is done by artificially triggering all pixels once per second during observations, in order to record events that contain only noise. The *pedestal* is the average of the digital counts (dc) of all noise events for each pixel. From this pedestal, the pedestal variations are then calculated for each pixel as the root mean square of all the dc counts in all noise events. In this context, noise events can be due to night-sky-background photons, or from electronic noise.

5.2 Pixel Identification

The first step to reconstruct events is to determine which pixels are part of a shower image. This is done by subtracting the dc pedestal from the entire trace, and then summing all trace bins within a fixed window, called the integration length, to get the total dc.

Most voltage traces have the same general shape: a quickly rising start of the pulse, followed by a longer, slowly falling tail. This can be seen in Figure 4.8 in the previous chapter. To act as a point of reference in each voltage pulse, the time when the voltage trace is at half of

its maximum value is called T_0. The trace is then integrated a second time using a smaller 14- or 24-ns-wide time window, starting at $T_0 - 30\%$, to reduce the inclusion of dc from NSB photons and electronic noise. This integration is the first of two passes, usually referred to as the double-pass method [185]. If a pixel's first-pass total dc is higher than 5 times the pedestal variation, then it is classified as an image pixel. If it is between 2.5 and 5 times the pedestal variation, it is considered a border pixel.

Once all pixels have been classified, isolated border pixels that have no neighboring image pixel are removed from the image, as they are more likely to be due to noise than Cherenkov photons. Then, the time gradient from the image and border pixels can be found by performing a linear fit of the T_0 times. This time gradient can then be used to place a third integration window with 30% of the window before each pixel's T_0, to more accurately measure the charge due to Cherenkov photons in the pixel. This third integration window is the second pass in the double-pass method.

From the image pixels, border pixels, and charge in each pixel, the shower's Hillas parameters [186] can be calculated. These parameters include the shower size in photoelectrons (or equivalent units), center of charge, angle, length, and width. The center of charge is the charge-weighted average of all image and border pixel positions. The angle of the shower determines how the image's major axis is oriented in the camera. The shower length and width are determined by the root mean square of the shower image along its major and minor axes, respectively, as shown in Figure 5.1.

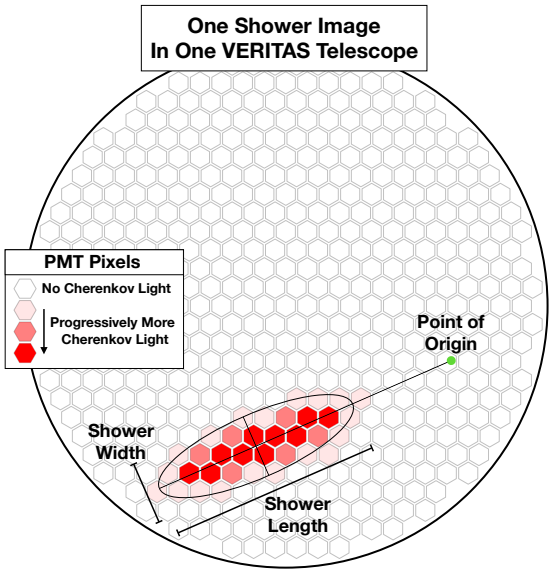

Figure 5.1: An example shower image in one VERITAS camera. The white hexagons are the locations of PMTs. Red hexagons are PMTs that have detected Cherenkov photons.

5.3 Position Reconstruction

By examining the images from multiple telescopes, the initial direction of the event can be determined. This is done by overlapping all telescope images in a single sky coordinate system, and projecting each image's major axis backward in time. These axes should intersect very close together, and the average of the intersection points determines the event's initial direction. The axes tend to not intersect perfectly due to the finite resolution of the camera pixels. Additionally, night sky background photons and atmospheric absorption can add and remove photons from the shower image.

When averaging the intersection points, weights can be applied to each intersection based on the angle between the two lines. This improves the reconstruction, because the intersection point from two images at 90° angles will be less sensitive to image fluctuations than two images at 160°, as shown in Figure 5.2. Additionally, the *disp* method is explored in Section 5.3.1 to provide improvements at lower telescope elevations. This would be beneficial as the Galactic Center is at a low (<50°) telescope elevation (see Figure 6.3).

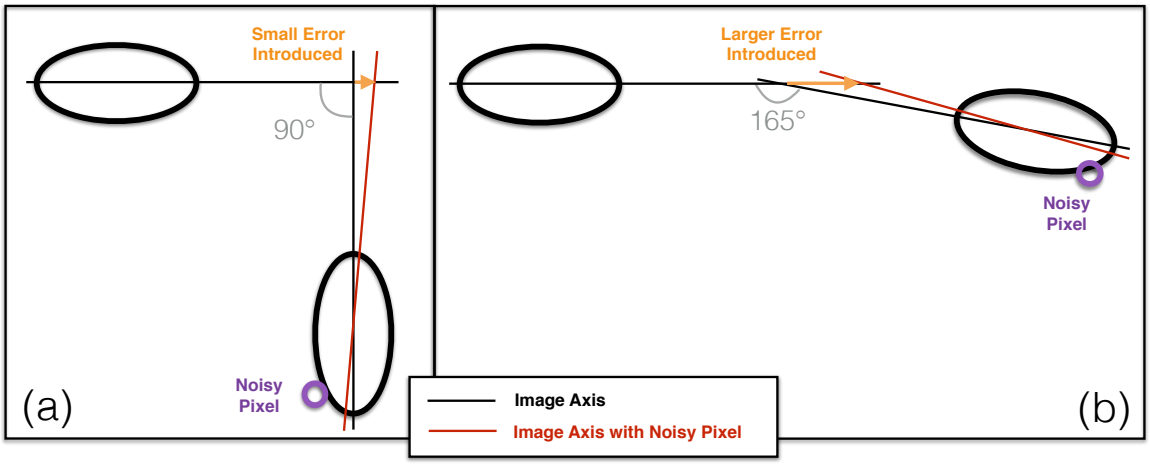

Figure 5.2: In diagram (a), when a noisy pixel is added to an image, the reconstructed position is only moved a small distance (the orange arrow). In diagram (b), due to the large angle between images, the error in the reconstructed position is much larger.

5.3.1 Angular Reconstruction with Boosted Decision Trees

At high elevations, shower images often form small intersection angles, because the telescopes are spread out in two dimensions, relative to the shower in the atmosphere. At low elevations near the Galactic Center, however, the telescope array flattens into one dimension, which makes the shower's impact parameter (the shortest distance between the telescope and the shower core axis) smaller for two of the telescopes. These two closer telescopes then have very short, almost circular images, which makes them more sensitive to noisy pixels or shower fluctuations, as shown in Figure 5.3. This also causes the remaining telescope images to have large intersection angles, which also reduces the accuracy of the position reconstruction.

To better handle these near-parallel image axes at low elevations, the reconstructed position can be determined from more parameters than just the weighted image axes intersection points. From simulations, the distance between the center of the Hillas shower image and the true position can be calculated, where the angular distance between the two is the disp parameter [187], shown in Figure 5.4. Then, this disp parameter can be provided to a machine learning algorithm [188], along with other image parameters detailed in Table 5.1.

These parameters for 17,000 simulated showers were used to train boosted decision trees (BDTs) that estimate the disp for a new shower's images. This estimated disp can then be combined with the image axes intersection points to more accurately reconstruct the original gamma-ray point of origin.

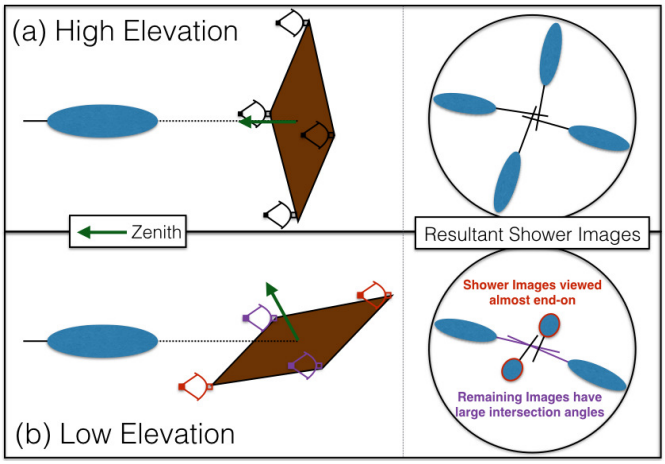

Figure 5.3: In Figure (a), high elevation showers produce long images in all four telescopes. In Figure (b), lower elevation showers produce shortened images in two telescopes, and the remaining images form larger intersection angles.

Table 5.1: Various image parameters and their descriptions.

Width	Image angular width
Length	Image angular length
Wol	$\frac{\text{width}}{\text{length}}$
Size	Total image dc
Ntubes	Number of pixels in the image
Loss	Fraction of image pixels at the edge of the camera
Asym	Distance between image center-of-dc and the pixel with the highest dc
Tgrad	The slope of the linear time fit to the pixel arrival times
Cross	Angular distance between the image center and the average intersection point of the image axes

Once the training is complete, it is tested on a separate set of 17,000 simulated events, whose true and predicted disps plotted in Figure 5.5. The x-axis describes the true disp value for each event, while the y-axis describes the disp value estimated by the BDT, with a black $x = y$ line marked, which represents a perfect 1:1 disp reconstruction. To examine how close the predicted disp is to the true disp, a residual plot is shown in Figure 5.6. It shows the $\frac{\text{Predicted disp}}{\text{True disp}}$ for each true disp bin, including $\pm$ 1 standard deviation error bars. From this residual plot, it can be seen that in nearly all bins the predicted disp is consistent with the true disp.

To examine the effect this disp method has on an analysis, the point spread functions (PSFs) are compared. The PSF describes how much a group of events from the same point source are spread out due to being imperfectly reconstructed. In general, PSFs are quantified by their 68% containment radius, the angular radius around a point source which contains 68% of the

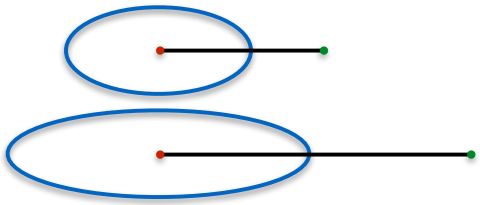

Figure 5.4: The disp parameter is the angular distance between the center (red dot) of a Hillas image (blue oval) and the true sky position (green dot). Generally, longer shower images have a larger disp angle.

reconstructed events. PSFs are discussed further in Section 5.6.2. The PSF containment radius is calculated from simulations, with both the disp reconstruction method and the regular geometric reconstruction method. The ratio of the $\frac{\text{disp PSF radius}}{\text{geometric PSF radius}}$ is shown in Figure 5.7. Because the PSF changes with telescope elevation, telescope azimuth and zenith, night sky background noise, atmosphere, and offset from the camera center, the average PSF at each gamma-ray energy is shown. This PSF is the average over the two data sets used in this analysis, the Crab Nebula and the Galactic Center, described further in Chapter 6. The average PSF for the Crab Nebula data is shown by a green line and a green 1-standard-deviation error band, and similarly the

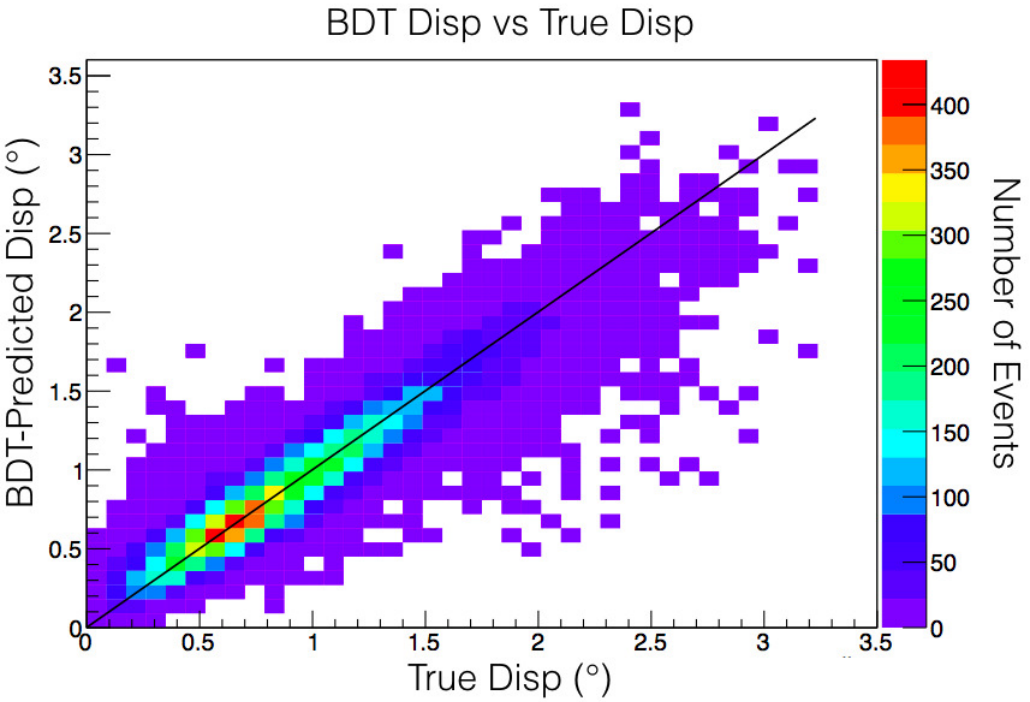

Figure 5.5: The true disp vs the BDT-predicted disp, for ~17,000 gamma-ray event images in T1, from 500 GeV to 200 TeV.

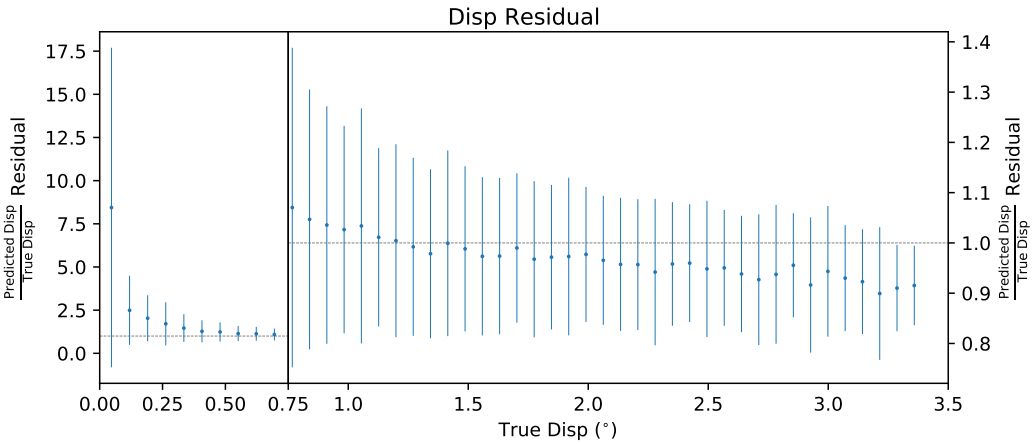

Figure 5.6: The predicted/true disp residual, from the bins in Figure 5.5. The error bars represent 1 standard deviation. The graph is split at $x = 0.75^\circ$ to keep the error bars visible.

Galactic Center is shown in blue.

Figure 5.7 shows the disp method does offer a minor improvement at low energies, but is worse at higher energies, though both are within the statistical uncertainties. The lack of improvement may be due to the use of boosted decision trees that were not optimized for this particular analysis. Nevertheless, the analysis described in Chapter 6 utilizes the disp method when reconstructing gamma-ray events.

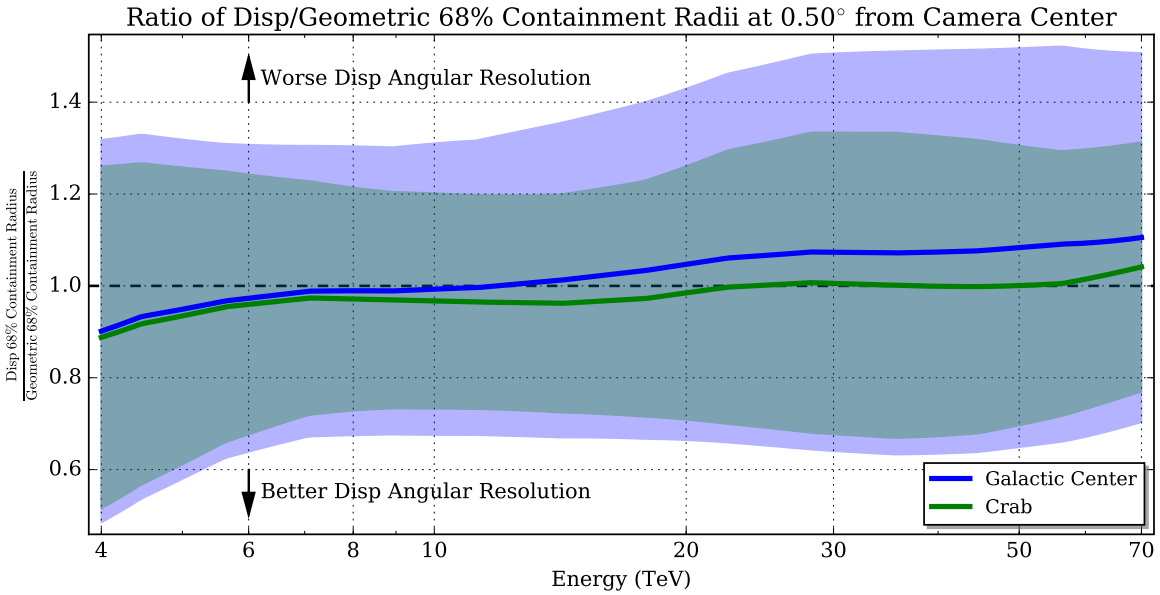

Figure 5.7: Comparison between the disp and geometric point spread function 68% containment radii. The lines represent the average ratio, with a 1 standard deviation error band. Green is from the Crab Nebula data, and blue is from the Galactic Center data. The average PSF shown is at a 0.5° offset from the camera center.

5.4 Energy Reconstruction

To reconstruct the energy of each shower, a lookup table of simulated showers is assembled. This database stores the median energy of the showers, as well as the spread of the distribution of shower energies. However, a shower's energy is strongly correlated with two measured parameters. The first is the shower's *image size*, the number of observed Cherenkov photons. The second is the *core distance*, the distance between the VERITAS array center and where the central shower axis intersects the ground. Showers are therefore divided into subgroups based on this size and distance, then the median energy and energy spread of each subgroup are stored in the lookup table.

The medians and spreads also vary based on the telescope, noise level, telescope azimuth and zenith angle, offset from camera center, and epoch, so additional showers are simulated at a variety of these parameters, and added to the lookup table. If any of these parameter space points were partially or completely combined, they would result in a larger error on the reconstructed energy.

One point in the parameter space of this lookup table is shown in Figure 5.8. In the left plot, the median energy is shown at at several shower core distances and image sizes. In the right plot, the spread in the energy distribution is shown at the same distances and sizes. By looking up a shower's size and distance in this table, the shower's true energy can be reconstructed.

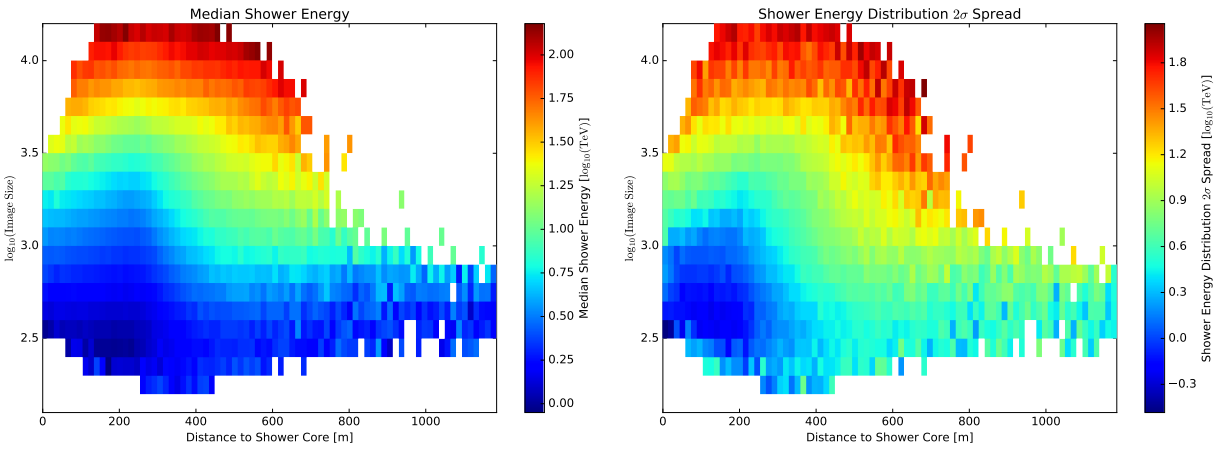

Figure 5.8: The median shower energy, and spread in energy, for several image sizes and core distances. The median shower energy is shown in the left plot, the right plot shows the 2σ spread in energy at the same parameter space points.

Once an energy has been estimated for each telescope's shower image, they are combined

with the weighted average in Equation 5.1, where E_i is the i^{th} telescope's energy and σ_x is the x^{th} telescopes energy distribution.

$$E = \frac{\sum_{i=1}^{N} \frac{E_i}{\sigma_i^2}}{\sum_{j=1}^{N} \frac{1}{\sigma_j^2}} \tag{5.1}$$

5.5 Gamma-Hadron Separation

After characterizing the direction and energy of each shower, the next step is to remove the considerable fraction (~1000:1) of showers that were induced by protons. This process is often referred to as Gamma-Hadron separation. When the lookup table in Section 5.4 is constructed, the medians and spreads of the showers' lengths and widths are stored alongside the energies. The length and width of one shower image are described in Figure 5.1. A group of these median widths are shown in Figure 5.9. These show how the shower width varies with core distance and image size.

These stored lengths and widths can then be used to create new parameters *mean reduced scaled length* (MRSL) and *mean reduced scaled width* (MRSW), calculated with

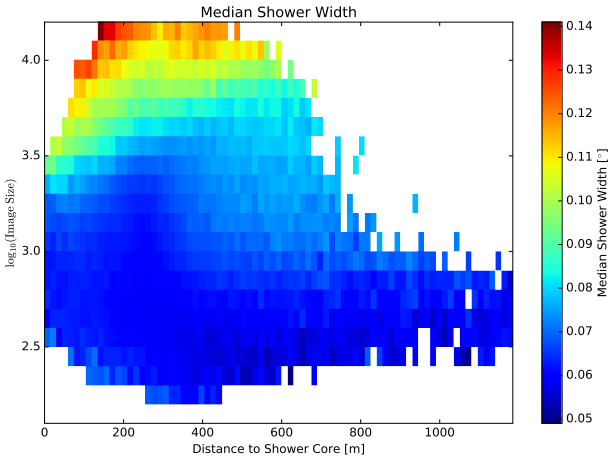

Figure 5.9: Plots of the shower widths from the lookup table. The median shower width is shown at several shower core distances and image sizes.

Equation 5.2 [189].

$$\begin{aligned} \mathrm{MRSL}_{\mathrm{shower}} &= \frac{1}{N_{\mathrm{images}}} \sum_{i}^{N_{\mathrm{images}}} \frac{l_i - l_{\mathrm{median}}}{l_{\mathrm{spread}}} \\ \mathrm{MRSW}_{\mathrm{shower}} &= \frac{1}{N_{\mathrm{images}}} \sum_{i}^{N_{\mathrm{images}}} \frac{w_i - w_{\mathrm{median}}}{w_{\mathrm{spread}}} \end{aligned} \tag{5.2}$$

In this equation, l_i and w_i are each observed image's length and width. Multiple images of the same shower can be combined to calculate the $\mathrm{MRSL}_{\mathrm{shower}}$ and $\mathrm{MRSW}_{\mathrm{shower}}$ for each shower. The parameters l_{median} and w_{median} are the median length and width from the lookup table. The parameters l_{spread} and w_{spread} are the spread in length and width distributions, also from the lookup table. The parameter N_{images} is the number of triggered telescope images. Gamma-ray showers and proton showers have different distributions of MRSL and MRSW (proton showers tend to be wider at a given length), so cuts are applied based on these two parameters to partially filter out the proton showers. In this analysis, only events that have a $\mathrm{MRSL} < 0.7$ and $\mathrm{MRSW} < 0.5$ are used.

These two distributions can be seen in Figure 5.10. In it, the MRSWs of events near the Crab Nebula are shown as a green histogram. The red histogram shows the MRSWs of events in several nearby regions which don't have any sources of gamma rays. The red histogram events are weighted by the number of off regions, so that both red and green distributions are scaled to the area of a single region. These off regions are the same size as the on region, and are radially-symmetric around the camera center. The excess of green events between $-2 < \mathrm{MRSW} < 0$ are the gamma-ray-like events from the Crab Nebula. The on region shows a slight peak that is not quite centered at $\mathrm{MRSW} = 0$, likely due to using simulations that were not tuned for these low elevations (see Section 6.1). See Ref. [190] for a more thorough discussion on gamma-hadron separation.

5.6 FITS Conversion for GammaLib and ctools

Once gamma rays have been reconstructed with Eventdisplay, they must be exported to GammaLib and ctools [191]. GammaLib and ctools are software that perform the likelihood calculation, which is described further in Section 6.2. This software possesses several useful features, including automatic model convolution with instrument response functions (IRFs) and easier comparison with results from other gamma-ray telescopes like H.E.S.S. and MAGIC. This

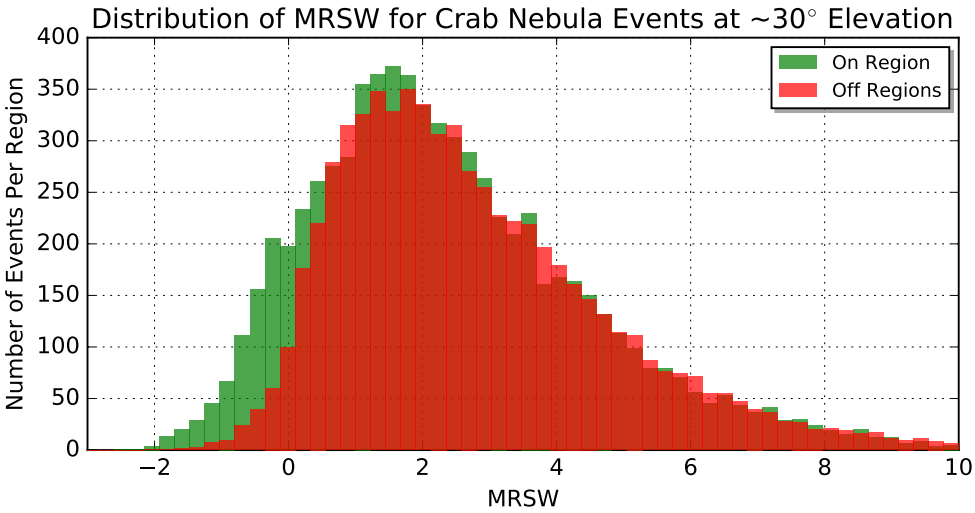

Figure 5.10: Plots of the MRSWs for events in the Crab Nebula analysis described further in Section 6.4. The green histogram is the MRSWs for events within 0.25° of the Crab Nebula, and should contain many gamma-ray events with a smaller MRSW. The red histogram is the MRSWs for events in several off regions, which should only contain proton-induced showers, which will have larger MRSWs, as proton showers tend to be wider than gamma-ray showers.

software is also one of the main high-level analysis tools to be used by the Cherenkov Telescope Array (CTA), making it easier to include VERITAS data into future CTA analyses.

Exporting gamma-ray data to this software involves converting the event list and IRFs to a FITS file format. The IRFs consist of the effective areas, the point spread functions, the background models, and the energy dispersion, defined in Sections 5.6.1-5.6.4. During the export, several decisions are baked into the event lists and IRFs. As this thesis revolves around an analysis at an elevation of ~29°, the IRFs may rapidly change with time. At this elevation, with VERITAS's field of view of 3.5°, the air mass column density (g/cm^2) is 13% higher at the bottom of the camera than at the top. Combined with the fact that an observing target can move several degrees over one 30 min observation, this means the air mass can change by several percent over a single 30-minute observation. This changing atmosphere would mean the IRFs at the beginning of an observation may be measurably different than at the end of an observation.

To reduce the impact of this, observations are broken up into 8-minute-long parts. For each of these 8 minute parts, IRFs are exported alongside the observation. A part's average elevation, azimuth, and night sky background rate are used to select the best-matching IRFs for that part.

The next subsections discuss each IRF individually. The effective areas are described in Section 5.6.1, the point spread function in Section 5.6.2, the background models in Section 5.6.3, and the energy dispersion in Section 5.6.4.

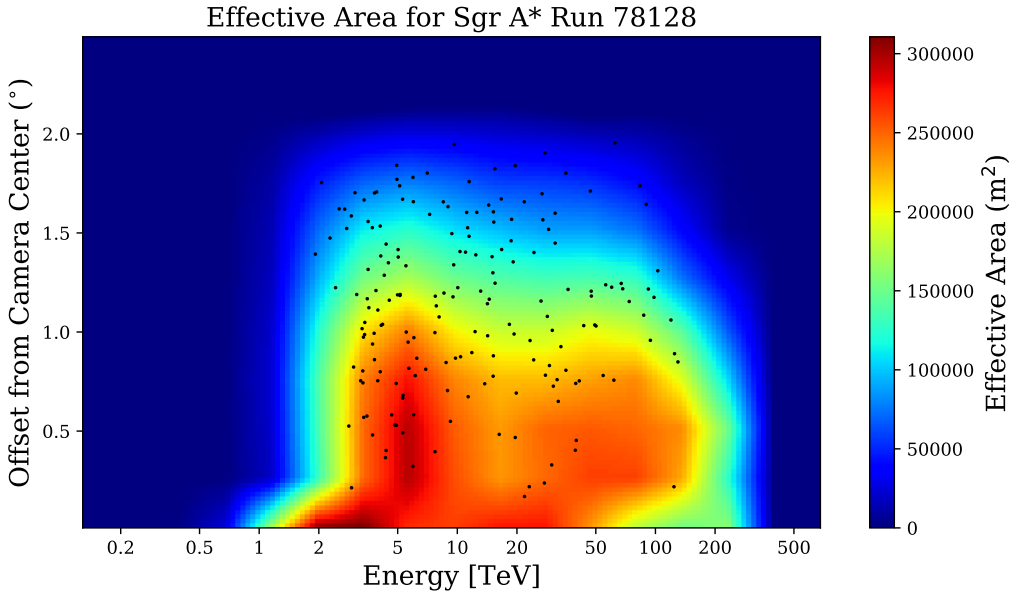

Figure 5.11: Effective areas at different points in the energy and camera offset parameter space for run 78128. Data is shown as the black points, indicating the position of some events from that run in the parameter space. The color axis indicates the effective area, calculated from simulations, at different gamma-ray energies and distances from the camera center.

5.6.1 Effective Area

Effective area is the measure of how large an observatory's collection area is, which determines how many gamma rays can be detected per unit time, solid angle, and energy. The effective areas are calculated with ~25 million Monte Carlo gamma-ray shower simulations for each point in the atmosphere/elevation/noise/offset parameter space. These simulations are created using the CORSIKA package [192]. This is done in the shower plane, the plane perpendicular to the line drawn between a pointing target and the center of the observatory. The effective area is then calculated via: $A = \pi R^2 \frac{N_{\text{survived}}}{N_{\text{simulated}}}$ where R is the radius of the area within which simulated showers are directed to fall, $N_{\text{simulated}}$ is the number of showers that were initially simulated into the area, and N_{survived} is the number of simulated showers that pass all cuts. This effective area is thus a measure of how much detection area the observatory would have if it had a 100% detection efficiency, which can then be used in calculating a source's flux. Figure 5.11 shows how the effective area peaks at $\sim 3 \times 10^5\,\text{m}^2$ for 3 TeV events at the camera center.

For the the Crab Nebula and Sgr A* data, the effective areas of all events are shown in

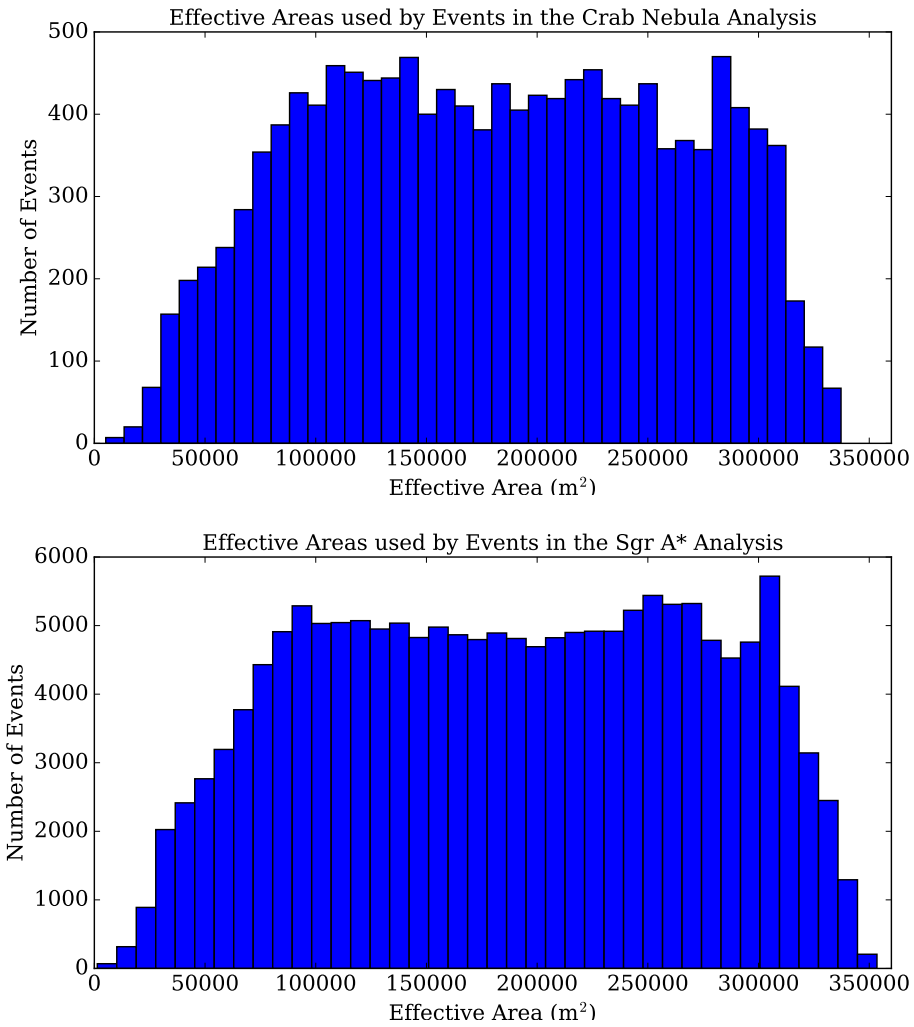

Figure 5.12: The effective areas used by all events in each analysis. From these plots, it is easy to check for events with anomalously high ($>$400,000 m^2) or low ($\sim$0 m^2) effective areas.

Figure 5.12. The Crab Nebula acts as a known *standard candle* source to test out the analysis, before attempting to search for dark matter within the Sgr A* data.

5.6.2 Point Spread Function

When reconstructing the source position of each gamma ray, it is necessary to know the uncertainty of the position. Errors in the position primarily come from the randomness of shower images. The same gamma ray may be reconstructed to have different energies or come

from different directions, due to the following:

- particles early in the shower receive different amounts of energy;
- shower particles scatter at different angles;
- different Cherenkov photons are scattered or absorbed by the atmosphere;
- different Cherenkov photons are reflected by the mirrors;
- different Cherenkov photons are converted into PMT photoelectrons.

In the image and position reconstruction, these all cause the same initial gamma ray to develop into a distribution of camera images and reconstructed positions. Inversely, this also means a single reconstructed gamma ray can come from a distribution of true gamma-ray positions.

This distribution of reconstructed positions is called the point spread function, and primarily affects the reconstructed shape of gamma-ray emission structures in the sky. A singular point source, nominally shaped by a Dirac function, is instead distributed according to the PSF. When searching for an extended source, like a dark matter halo, understanding the distribution of reconstructed positions is important. A large PSF on all events, for instance, will artificially expand the observed dark matter halo.

For VERITAS, the PSF is estimated by simulating many gamma rays, then measuring the distribution of true positions for each reconstructed position. The distribution of event positions are fitted with a King function [193] (see Equation 5.3), as this better models the longer PSF tails at lower elevations (Section 5.2.2 in Ref. [194]). The radially-normalized King probability density function is defined as

$$\mathrm{PSF}_{king}(r) = \frac{1}{2\pi\sigma^2}\left(1-\frac{1}{\gamma}\right)\left(1+\frac{r^2}{2\gamma\sigma^2}\right)^{-\gamma} , \tag{5.3}$$

where r is the angular distance from the reconstructed position, σ is analogous to the width of a Gaussian function, and γ governs how long the tails are. A King function fitting algorithm was added to Eventdisplay, that fits the γ and σ parameters to a set of simulated gamma rays. This fits well over almost all of the parameter space. In Figure 5.13, the PSF is shown for one Sgr A* run. In it, one can see how the PSF containment radius changes vs reconstructed energy and offset from the camera's center. Other runs, which have different elevations, azimuths and NSB noise levels will have different values at each point in the energy/offset parameter space.

For the Galactic Center and the Crab Nebula analyses, the distribution of 68% containment radii for all events is shown in Figure 5.14. The asymmetric structure is due to the varying effective area at different offsets and energies, which changes the distribution of events in the PSF table. The long tails are likely due to events at the edge of the observable energy and offset

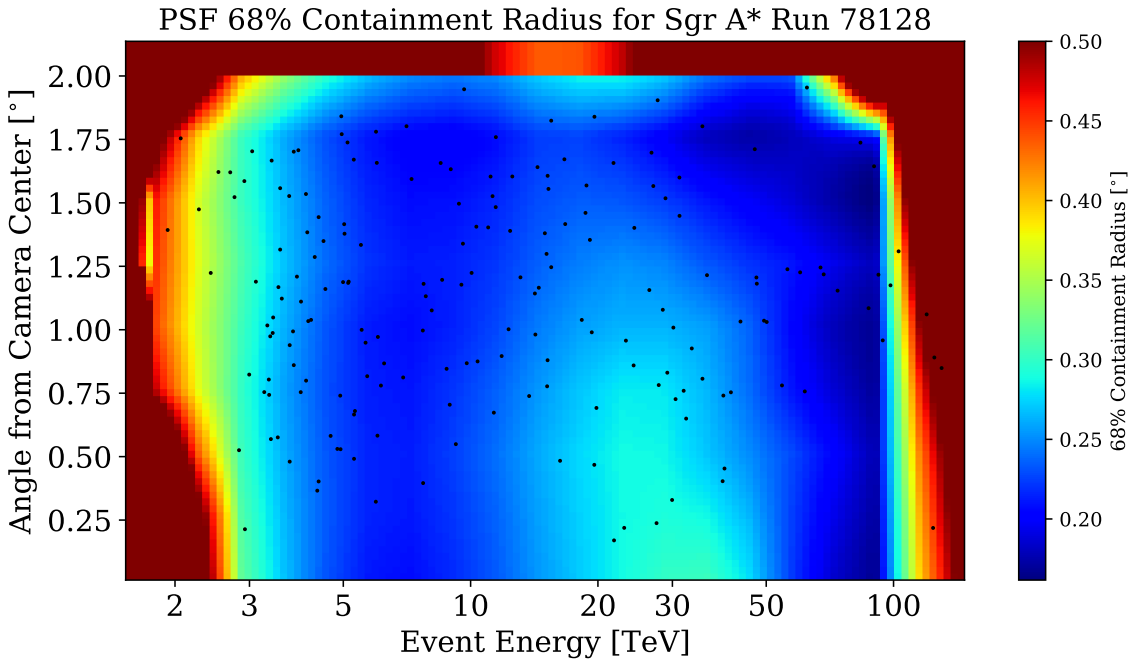

Figure 5.13: The 68% containment radius for the energy/offset parameter space for Sgr A* run 78128. The black points are from data, showing a subset of the event locations from run 78128 in the parameter space. The color axis is the containment radius, calculated from simulations. While events from all energies are shown in this figure, only events from 4–70 TeV are used in the analysis (see Section 6.4).

ranges, where the PSF gets worse.

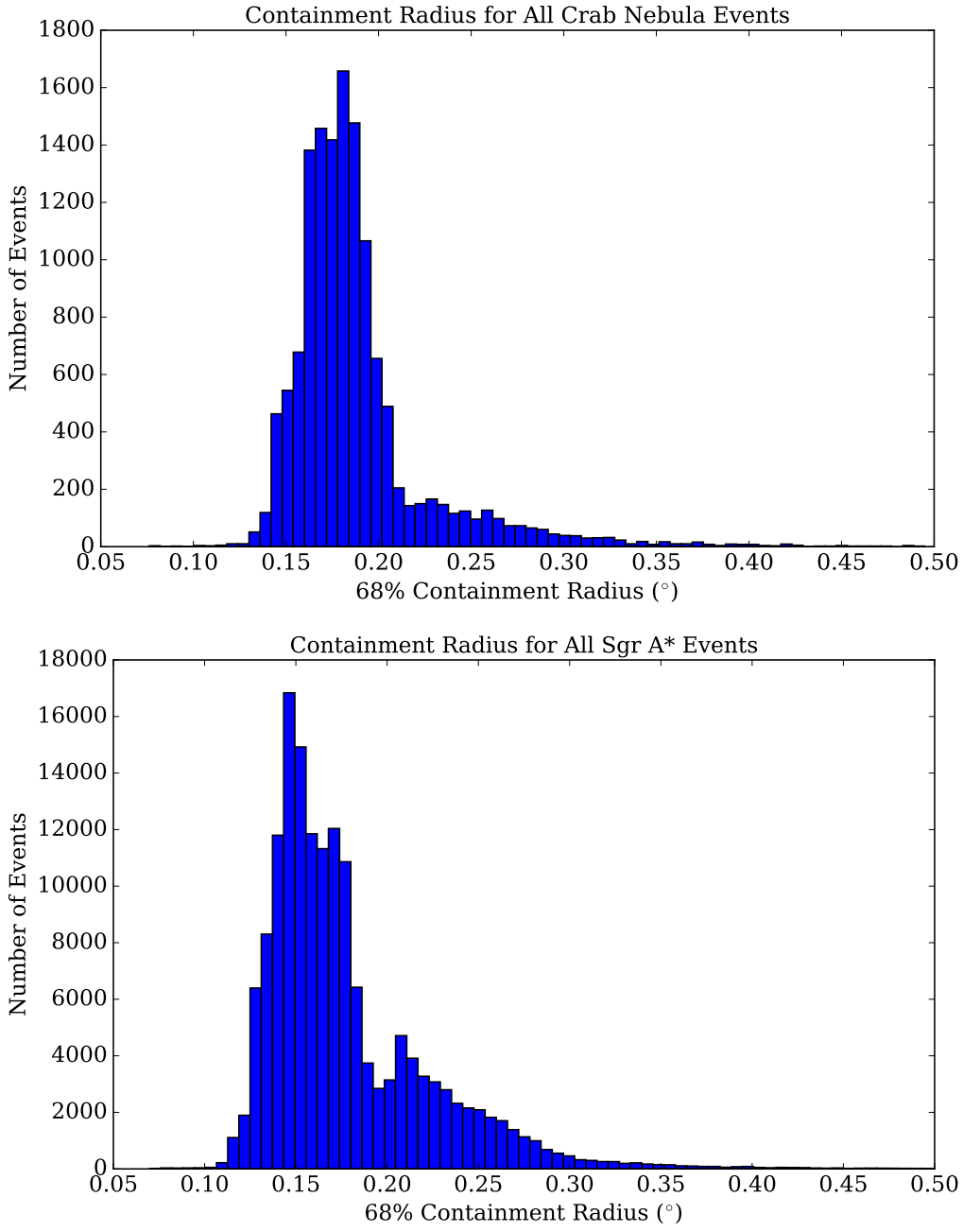

Figure 5.14: The 68% containment radius for all Crab Nebula and Sgr A* events used in this analysis.

5.6.3 Background Models

A background model is a three-dimensional function in camera x (a horizontal angle, parallel to azimuth), camera y (a vertical angle, parallel to elevation), and energy. Each background model is constructed from one of two templates, and the templates are built from dark run observations (see Figure 6.1). These background models calculate the number of expected background events in the camera, per unit solid angle, unit time, and unit energy. These background events are primarily proton-induced showers that are similar enough to gamma-ray showers that they pass all quality cuts. The background models are used to quantify how many counts are expected in different parts of the camera when observing any target. Understanding the background shape of the camera is crucial for properly studying extended sources, like dark matter halos, which may extend several degrees from the Galactic Center. Improperly estimating background models can result in fake structures appearing around an astrophysical target.

The background models used in this analysis are made from two background templates, one for each of the V5/V6 epochs (see Section 4.5). Once the templates are built, each chunk of data (a fraction of an observation run) is given an independent copy of its epoch-specific background template. The templates are constructed from dark observations, detailed later in Section 6.1. Each template is made by combining two independent binnings of the background events. The events are first binned radially to model the spatial behavior, then separately the same events are binned in energy to model the spectral behavior. Then an interpolating function is applied to each binning to produce smooth spatial and spectral components of the template. The spectral bins and interpolated function can be seen in Figure 5.15. The radial bins and interpolated function at two different energies is shown in Figure 5.16.

Finally, the spatial and spectral functions $M_s(e)$ and $M_e(x,y,e)$ are multiplied together, as in

$$f(e,x,y) = A \times M_e(e) \times M_s(x,y,e)\,. \tag{5.4}$$

The function $f(e,x,y)$ has units of $\frac{\text{Number of Counts}}{\text{MeV}\times\text{s}\times\text{sr}}$. The function $M_e(e)$ is an energy-dependent power law correction function, primarily used to account for variations in the acceptance of the background models at different elevations. The function $M_s(x,y,e)$ is a spatial template that varies with camera x, camera y, and energy e, built from Sgr A* Off data described in Section 6.1. The multiplied functions are then scaled with a constant A such that the total integral of the template (integrating across camera x, camera y, and energy) is equal

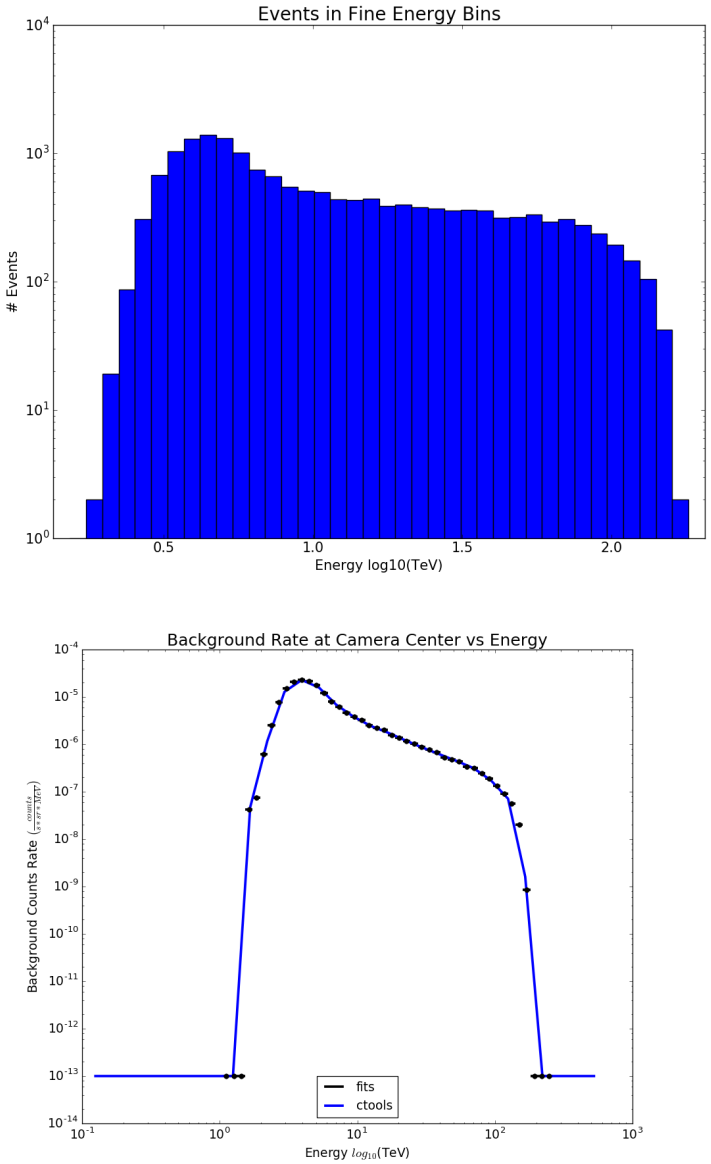

Figure 5.15: The V5 background's fine energy bins. The top plot shows the number of events in each energy bin from all background runs. The bottom plot shows the background rate, the number of background events divided by the observation time, solid angle, and energy span. The black points show the background rate in each energy bin, while the blue line shows the interpolated background rate.

to the original number of counts in the Sgr A* Off runs, as in

$$\text{Number of Background Events} = A \int M_e(e) \times M_s(x,y,e)\, dx\, dy\, de\,. \tag{5.5}$$

This function $f(e,x,y)$ is the background template in camera x and y. Each background template is used in the likelihood analysis as a model multiplied by two free parameters, a normalization factor, and the event energy exponentiated by the spectral index. This lets the likelihood fitter scale each run's background model up or down to best match the number of

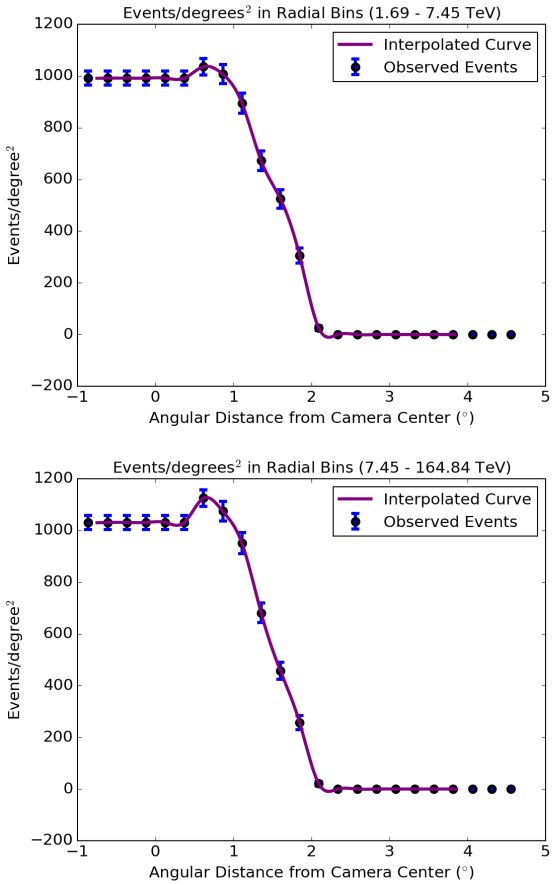

Figure 5.16: Radial bin profiles for the V5 backgrounds for low and high energies, to show how the shape varies with energy. The blue points are the counts per bin area, while the purple line is a spline interpolation with a 3rd order polynomial. The peak and plateau at 0°-1° is due to the background events not being radially symmetric in the camera, due to the changing atmospheric depth across the camera's field of view. For fitting the interpolated curve, the bin values at angles less than 0° are copied from the 0° bin. The same is done for bins beyond 2.5°, which are copies of the 2.5° bin value.

observed events. This means the analysis is less dependent on the background's absolute value, and more dependent on the relative values in different parts of the camera background or at different energies.

5.6.4 Energy Dispersion

As events are reconstructed imperfectly, it is important to understand what the distribution of reconstructed energies are for a given true energy. This *dispersion in energy* is quantified by an energy migration matrix $E_{i,j}$, where i denotes the i^{th} reconstructed energy bin, and j denotes the j^{th} true energy bin. A migration matrix is created by simulating many showers at a variety of true energies and binning them based on their true and reconstructed energies. Several matrices are then created, by grouping showers into bins based on their distance from the camera center.

Because simulations are computationally expensive, only a limited number can be produced for each migration matrix. At some places in the matrix, low simulation statistics can artificially alter the shape of the matrix. To reduce the effect of this, interpolation is applied to the matrix. The number of events at a particular place in the matrix is then found by interpolating from neighboring true energy, reconstructed energy, and angular offset bins in this table. This interpolated energy migration matrix can be used to account for two significant effects.

The first is that the reconstruction method introduces biases in the event energy, meaning an event at a given true energy can be reconstructed on average at a higher or lower energy. The second effect that is accounted for is the dispersion in the reconstructed energies. Gamma rays with the same energy will have their energies reconstructed as a distribution close to the true energy. These fluctuations can be due to randomness in air shower development or atmospheric absorption of Cherenkov photons. This has the effect of distributing events in each energy bin of a spectra. In the gamma-ray spectra of astrophysical sources, which often follow a power law, lower energy bins tend to have more events than higher energy bins. This results in lower-energy dispersion contributing more to the higher-energy bins than the higher-energy dispersion contributes to the lower-energy bins. When not accounted for, this energy dispersion will harden observed astrophysical spectra.

In Figure 5.17, an interpolated migration matrix is shown. Events at a given $\mathrm{E_{True}}$ are reconstructed at a spread of $\mathrm{E_{Reconstructed}}$. This spread is due to the variability in how air showers develop in the atmosphere. Small variations early in the shower can have a large impact on the shower's Cherenkov image, meaning the shower can appear as though it was from a higher- or lower-energy gamma ray. At the lowest $\mathrm{E_{True}}$ energies some showers fluctuate upwards

to produce more Cherenkov light, and consequently get reconstructed to higher $E_{Reconstructed}$ energies. At the highest E_{True} energies, showers may be so large that they fill the entire camera, leading to lost photons past the edge of the camera, which cause the shower's energy to be reconstructed lower than it actually is.

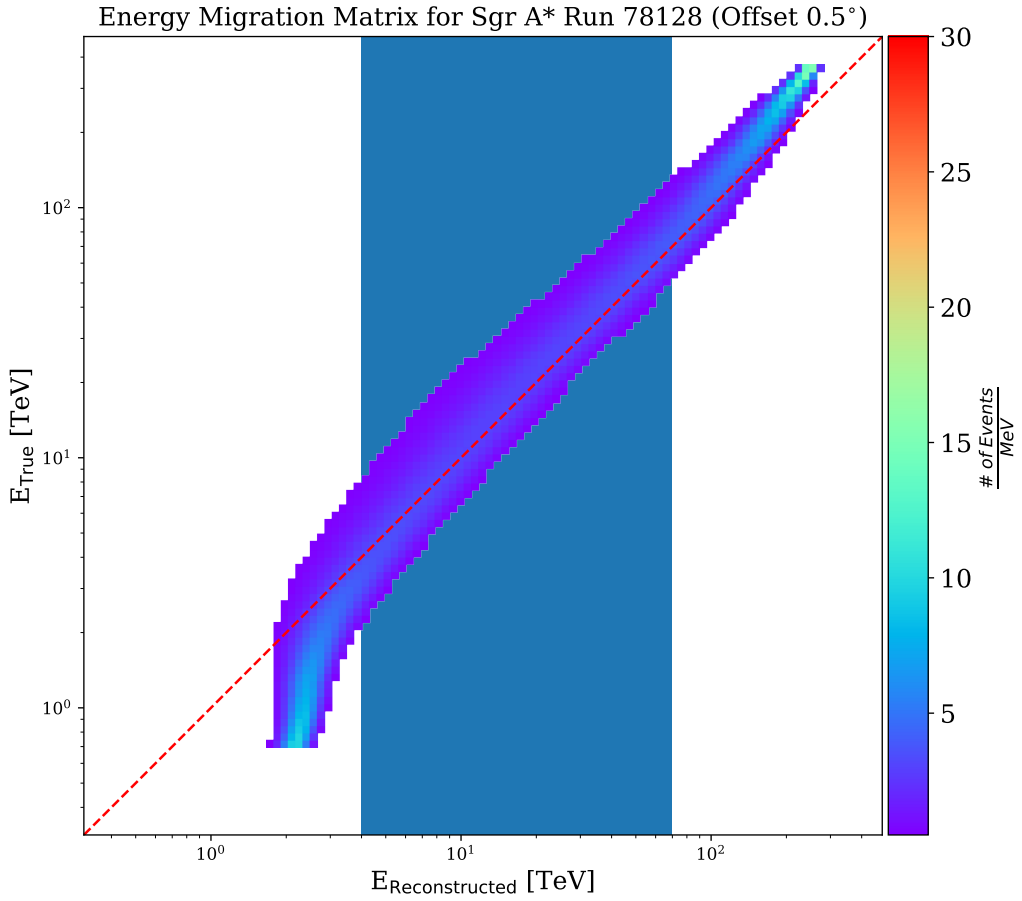

Figure 5.17: An energy migration matrix used with Sgr A* run 82288. The reconstructed energy is on the x-axis, and the true energy is on the y-axis. The z (color) axis denotes the interpolated number of simulated events that passed all cuts (see text for details). The dark-blue region from 4–70 TeV $E_{Reconstructed}$ is the range of energies used in this analysis.

Figure 5.17 shows one migration matrix, representative of all migration matrices used in this analysis. For all matrices in this analysis, the bias between 4–70 TeV is similar.

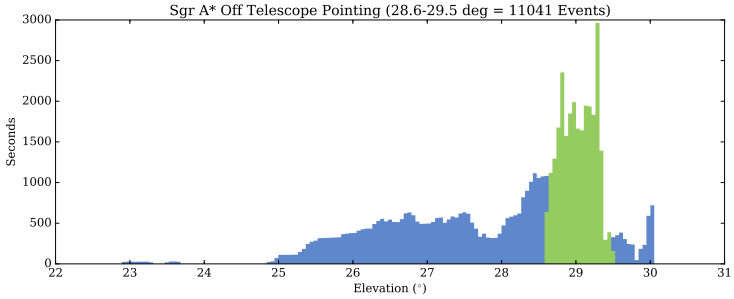

Figure 5.18: Time spent pointing the observatory at each elevation. Blue is all Sgr A* Off data, while green is the selected pointing elevations used in Figures 5.19 and 5.20.

5.7 Camera Studies

The objective of this thesis is to search for dark matter via the existence of a gamma-ray halo that is both extended and faint. The extension and faintness of the halo, plus the relatively large amount of noise near the Galactic Center, prioritize understanding how the VERITAS camera behaves in high-noise conditions. In order to better understand the camera's behavior in the reconstruction method, several studies were performed.

5.7.1 Background Structure at the Low Energy Threshold

To produce background models, events were binned according to their energy, telescope pointing elevation, and elevation and azimuth about the camera center. As a result of this detailed binning, some new effects were noted. First, Sgr A* Off data was reconstructed, which has no known gamma-ray source in its field of view. The time spent at each telescope elevation is shown in Figure 5.18. To reduce the effect of the varying telescope elevation, time cuts were applied to select data between 28.5° and 29.5° telescope elevations. This was done to reduce any effects of a large range of telescope elevations. Because the shape of the atmospheric interaction volume strongly depends on the telescope elevation, a small elevation range helps isolate atmosphere-dependent effects. Note that this is a cut on the telescope pointing, not on the actual event elevations.

Gamma-like events were then selected from this data, and binned in energy in Figures 5.19 and 5.20. The left histograms show the number of events at each energy. For each row, a different energy range is selected, shown in green in the left plot. The cuts to pointing-elevation and energy are applied, and the surviving events are then histogrammed in the right-hand plots according to their azimuth and elevation in the camera.

As a measure of how far the events deviate from the camera center, an orange dot and circle are also plotted. These indicate the average event position, and the 68% containment radius around that position. Figure 5.19 shows that at the lowest energies, events are reconstructed and pass cuts only in the top half of the camera. This is because at this low 29° elevation, the atmospheric column density is ~13% lower at the top of the camera than at the bottom. This allows lower-energy gamma rays and their showers' Cherenkov photons to get closer to the observatory, making them easier to detect. Below this energy, gamma rays do not produce enough Cherenkov photons to survive past the atmospheric scattering and PMT quantum efficiency. The bottom of the camera has more atmosphere, however, and can be considered opaque to gamma rays 2.5 TeV and lower. At higher energies a similar effect is also noted, where the events cluster in the bottom half of the camera more than the top half. As atmospheric column density is higher in that part of the camera, higher energy showers may be created farther away, where the observatory's fixed-angle opening views a much larger volume of the atmosphere, detecting more showers.

These effects are visible in the galactic (l,b) event maps from data. In Figure 5.21, the top plot shows the positions of all events from several hours of Crab Nebula data. The location of the Crab Nebula is marked in blue, while the red circle and point indicate the average event position and radius containing 68% of the events. The middle histogram shows the distribution of event energies, and the bottom plot shows the positions of events in a limited energy range, 1.5–3.25 TeV. The middle plot indicates a specific energy range used in the bottom plot. When events in this limited energy range are plotted in the bottom plot, the average event position (the red dot) shifts upwards by 0.32°. This is due to fewer events appearing in the bottom of the camera, due to the thicker atmosphere there.

When similar plots are made for the Galactic Center in Figure 5.22, the effect is much stronger, and rotated. In the top plot, events are radially symmetric around the source position. The red dot and circle are the average event position and the 68% containment radius. When only the events from 1.5–3.25 TeV are plotted, the average event position moves by 0.4°, due to a deficit in the lower right part of the plot. This area corresponds to the bottom of the low-energy camera plots in Figures 5.19 and 5.20. The rotation occurs when converting between camera x/y coordinates (Earth Elevation/Azimuth) and Galactic coordinates (l,b). The degree of rotation also changes from run to run, which further blurs this effect. For the Crab Nebula plots in Figure 5.21, the rotation is only a few degrees, while for Sgr A* in Figure 5.22, it is closer to 70°.

This effect is important to the analysis because it implies that, at the lowest energies, the background rate is not radially symmetric. Radial backgrounds (sometimes referred to as acceptances) are typically used in VERITAS, as no other camera x/y or energy dependence had

been demonstrated until now. Due to a limited amount of background data (see Table 6.1), only radially-dependent backgrounds are used in this analysis. To attempt to reduce the effect of the non-uniform atmosphere, the event energies were limited to 4–70 TeV. Even with this limited energy range, the atmospheric effect is still prominent, and studied further in Section 6.7.

Additional studies were performed to test if bright stars near the Galactic Center might affect a dark matter search, and are detailed in Appendix C. Bright stars were found to have a negligible effect, and were ignored in this analysis.

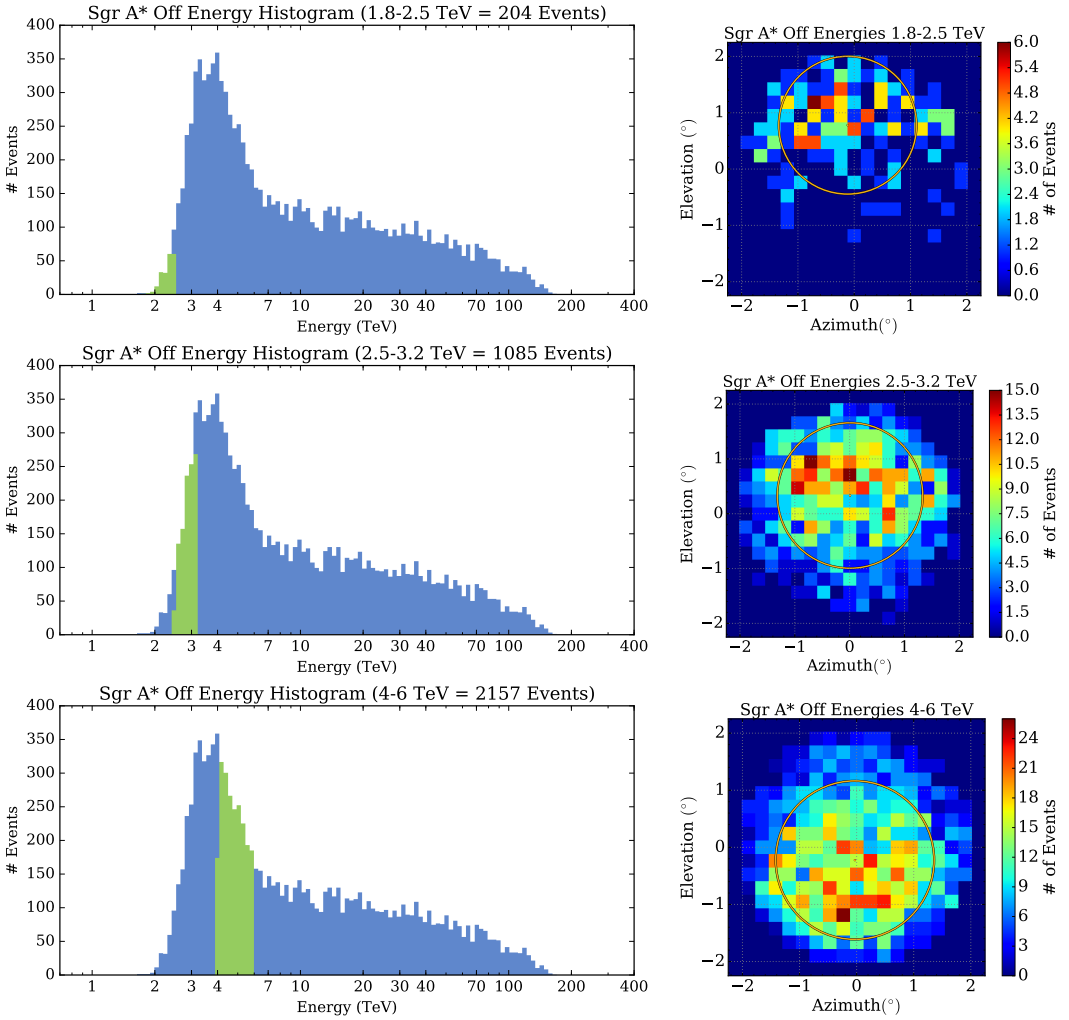

Figure 5.19: Event energies and camera backgrounds after the pointing elevation cut shown in Figure 5.18. In the left histograms, blue is all events while green is events in the selected energy range. The right shows 2D histograms, made from the camera azimuths and elevations using the green events selected in the histogram to its left. The orange dot and circle denote the average event position, and 68% containment radius for the events in the plot. The 1.8–3.2 TeV energy range shows events are detected more in the upper half of the camera. From 4–6 TeV, the mean even position has shifted to the bottom half of the camera.

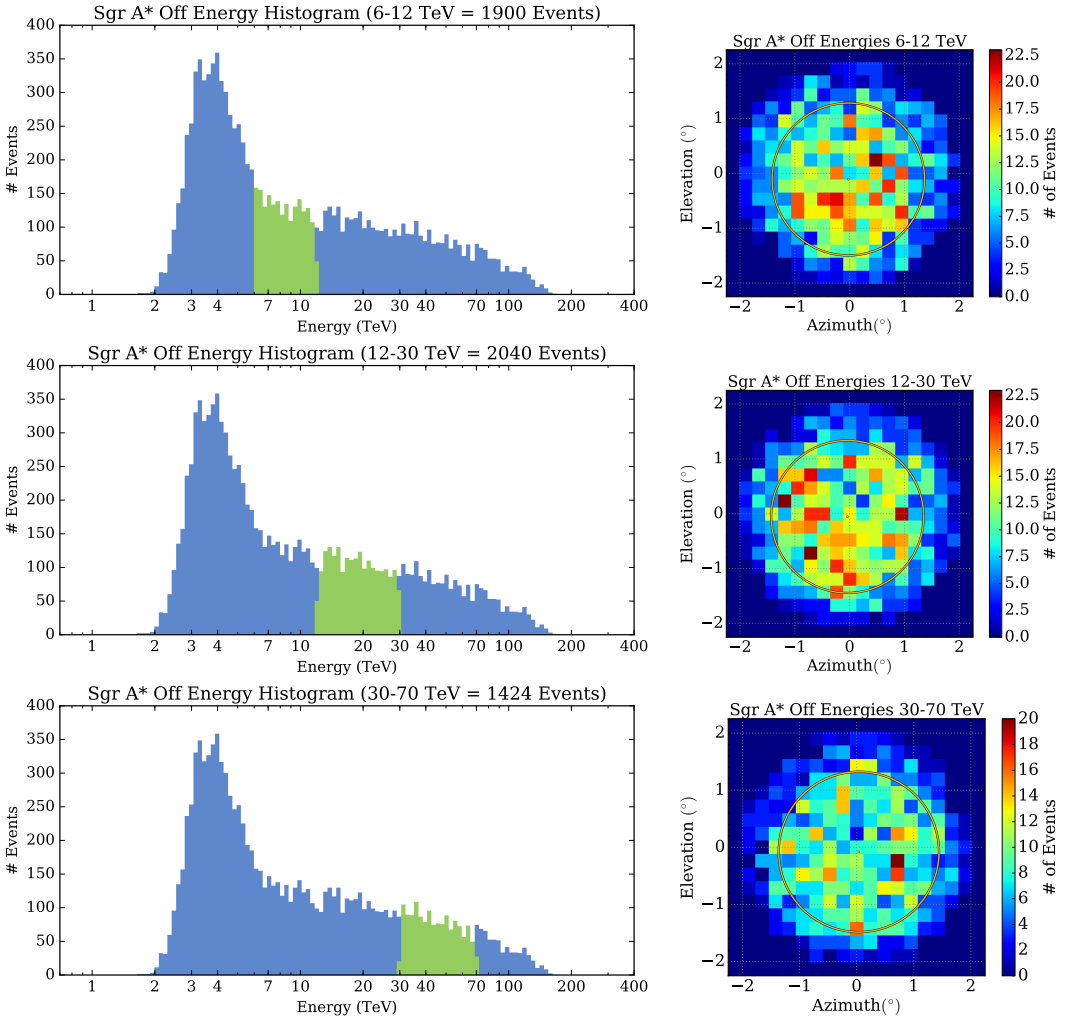

Figure 5.20: Event energies and camera backgrounds after the pointing elevation cut shown in Figure 5.18. In the left histograms, blue is all events while green is events in the selected energy range. The right shows 2D histograms, made from the camera azimuths and elevations using the green events selected in the histogram to its left. The orange dot and circle denote the average event position, and 68% containment radius for the events in the plot. In Figure 5.19 the lower energies are shown, while here the 6–70 TeV events are shown to be closer to the camera center.

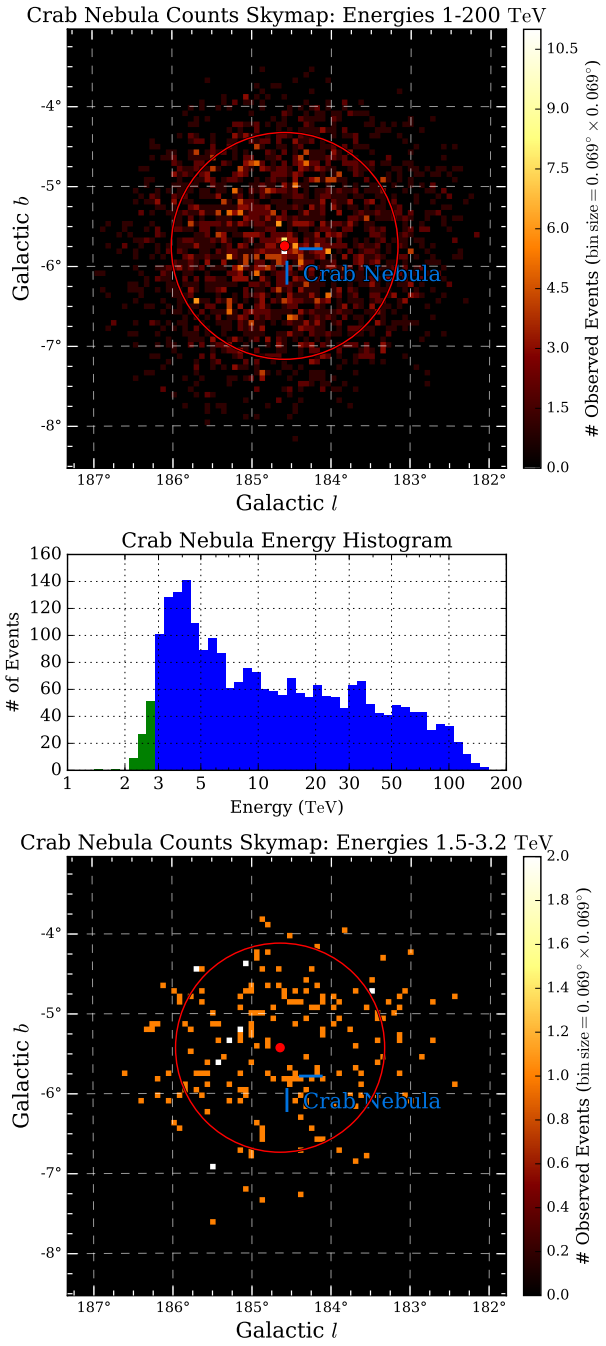

Figure 5.21: Plots of Crab Nebula observations. Top: Sky map of all events. Middle: Histogram of all events in energy. Bottom: Sky map of events from 1.5–3.25 TeV. Data is first filtered so that the telescope pointing is between elevations of 28.5° and 29.5°. Red dots and circles are the average event positions and the 68% containment radii.

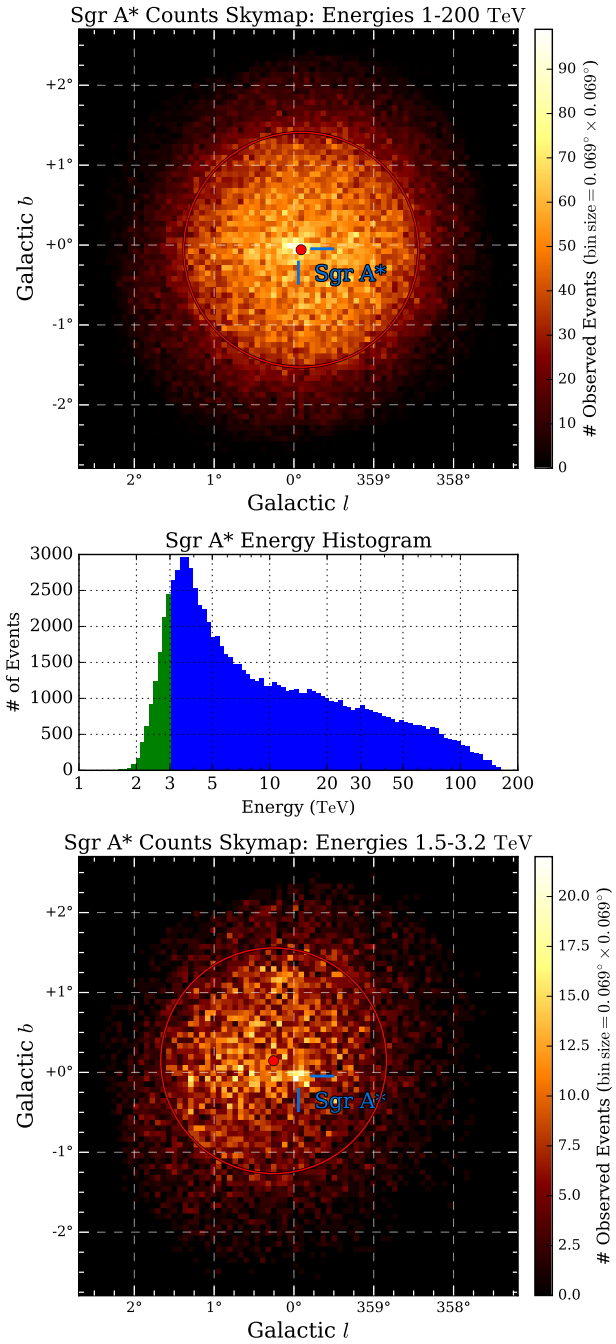

Figure 5.22: Plots of Sgr A* observations. Top: Sky map of all events. Middle: Histogram of all event energies. Bottom: Sky map of events from 1.5–3.25 TeV. Data is first filtered so that the telescope pointing is between elevations of 28.5° and 29.5°. Red dots and circles are the average event positions and the 68% containment radii.

6 A Likelihood Search for Dark Matter

6.1 VERITAS Data

The analysis in this thesis relies on three sets of VERITAS data. One set contains observations of the Crab Nebula, and a second of the Galactic Center. A third set contains observations of a dark region ~5° away from the Galactic Center. This dark region is referred to as Sgr A* Off, and is located at (l,b)=(357.3396°, 3.9984°). Sgr A* Off is located a few degrees away to avoid the bright diffuse gamma-ray emission caused by the galactic plane. The Galactic Center and Sgr A* Off observation regions are shown in Figure 6.1. To quantify the cosmic-ray background, observations are taken at 0.5° or 0.7° offsets from each observing target, in four different directions (wobbles) along right ascension/declination axes.

All three sets of data include observations from both the V5 and V6 epochs (see Section 4.5), where the number of hours are shown in Table 6.1. All used data was taken from April 2010 to June 2016. The specific VERITAS data run numbers are listed in Appendix B.

Table 6.1: Hours of Observations at Each Source/Epoch Combination

Epoch	**Crab Nebula**	**Sgr A***	**Sgr A* Off**
V5	3.3	46.3	13.0
V6	5.5	62.7	4.7

There are comparatively fewer Sgr A* Off observations because this source is only used for background estimation, and telescope time is in high demand. The small amount of Sgr A* Off observations results in a ~5% statistical uncertainty in the background models, which is not included in the Crab Nebula analysis in Section 6.4 or in the Dark Matter Likelihood Analysis in Section 6.5. There are also fewer Crab Nebula observations, as the majority of its data is taken at higher elevations, where the telescope has increased sensitivity to lower energies.

For all of these observations, quality cuts are applied. This includes monitoring the telescope hardware and cloud ceiling in the field of view. Two far-infrared pyrometers are used to measure the cloud ceiling height, by measuring the temperature of the sky. With the pyrometer, clouds (~−5°C) are measured to be significantly warmer than clear sky (~−50°C). Low-quality segments

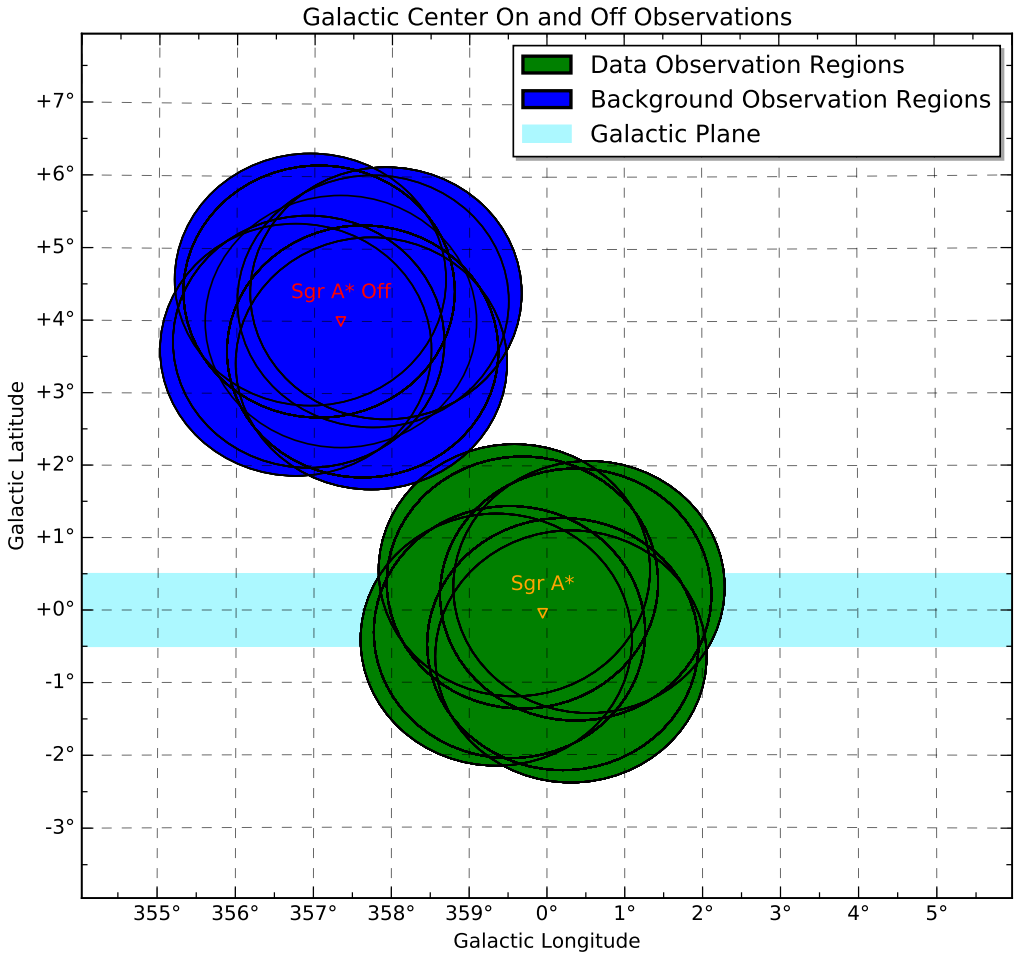

Figure 6.1: Fields of view for Galactic Center observations. Each circle marks the detection area of one telescope pointing. Green circles are Galactic Center observations, while dark blue circles are the Sgr A* Off observations used to construct the camera-background templates. The light blue band represents the galactic plane.

of data, where there are large (>20%) and/or rapid (<=30 s) changes in the L3 trigger rate or cloud ceiling height, are removed from the analysis [195].

Because each VERITAS epoch has a different hardware configuration, they also each have their own separate set of effective areas, point spread functions, energy migration matrices, and camera background models. In addition, specific IRFs were calculated for additional data dimensions, including the frequency of night sky background photons in the camera, the telescope elevation, the event energy, and each event's distance from the camera center. After this data is collected, it is used in a likelihood analysis, detailed in the next section.

6.2 Likelihood Ratio Test

A likelihood ratio test determines the likelihood of getting the observed data from two separate model groups. Once the likelhood is calculated, then the parameters of the model are varied until the maximum likelihood is found for each model. These two maximum likelihoods can then be used to calculate the test statistic (TS), which determines which model is statistically favored, and to what degree it is favored.

6.2.1 Likelihood Calculation

At its heart, a likelihood is a product of probabilities. With two events, the likelihood is (probability that event one happens) $\times$ (probability that event two happens). In a counting experiment like VERITAS, the likelihood L is determined via Poissonian statistics with

$$L = \frac{e^{-m} m^n}{n!}. \tag{6.1}$$

In this equation, n is the number of observed events, and m is the average number of events predicted by a model group.

For increased statistical power, the VERITAS data can be split into bins of energy, galactic l and b, and time. When combining multiple bins with index j, each bin's likelihood is multiplied together as in Equation 6.2. Future likelihood calculations may also include shower core position on the ground, or distance to the shower, or other observables.

The general formula for calculating a binned likelihood of Poissonian events is

$$L = \prod_j \frac{e^{-m_j} m_j^{n_j}}{n_j!}. \tag{6.2}$$

As events are grouped by bins, some information is lost, which generally results in a less powerful ratio test. The result in Equation 6.2 can be expanded into an unbinned likelihood through the following derivation. First, Equation 6.2 can be rearranged into

$$\begin{aligned} L &= \prod_j e^{-m_j} \prod_j \frac{m_j^{n_j}}{n_j!} \\ L &= e^{-\sum_j m_j} \prod_j \frac{m_j^{n_j}}{n_j!}. \end{aligned} \tag{6.3}$$

Then, the size of each bin can be shrunk until there are only 1 or 0 events in each bin. For empty bins (where $n = 0$), the product in Equation 6.3 becomes

$$n = 0 \rightarrow \frac{m_j^{n_j}}{n_j!} = \frac{m_j^0}{0!} = \frac{1}{1} = 1\,. \tag{6.4}$$

For bins with 1 event, the product in Equation 6.3 becomes

$$n = 1 \rightarrow \frac{m_j^{n_j}}{n_j!} = \frac{m_j^1}{1!} = \frac{m_j}{1} = m_j = m_i\,, \tag{6.5}$$

where i is the i^{th} event, and m_i is the number of predicted events at event i's sky position, energy, and time. In this derivation, m_j converts to m_i, because all the $n = 0$ bins are now 1 and can be ignored, and thus a loop over the j bins becomes a loop over the i events. Then Equation 6.3 becomes

$$L = e^{-\sum_j m_j} \prod_i m_i\,. \tag{6.6}$$

Here, $\prod_i m_i$ encodes the data events, while $\sum_j m_j$ encodes the model information.

When calculating L, certain computational problems can arise. Calculating the product of many small probabilities can result in extremely small numbers, beyond the binary storage limit of common variable types. Calculating derivatives of some of these numbers is also computationally expensive, so to solve these two problems, the a logarithm is applied to get the log-likelihood:

$$\mathcal{L} = \log(L)\,. \tag{6.7}$$

This is possible because both L and $\mathcal{L}$ are strictly increasing functions, so the maximum of both will be at the same position in the parameter space. The log-likelihood for a group of bins is then

$$\mathcal{L} = \log\left(e^{-\sum_j m_j} \prod_i m_i\right) = -\sum_j m_j + \sum_i \log(m_i)\,. \tag{6.8}$$

When the bin size is infinitely small, m_i becomes P_i, the value of the probability density

function (of all models combined) at the position of the event via

$$\mathcal{L} = \log\left(e^{-\sum_j m_j} \prod_i m_i\right) = -\sum_j m_j + \sum_i \log\left(P_i\right). \tag{6.9}$$

This unbinned equation shows how the log-likelihood is calculated in this analysis. The $\sum_j m_j$ term can be interpreted as the total number of events predicted by all models.

6.2.2 Models

Models are used in a likelihood analysis to predict the number of events that a particular source deposits into some bin j. In a likelihood analysis, each source of events gets its own model. Each model is described by a function M, and different sources will have different M functions. The function M has dimensional units of $\frac{N}{A\,T\,E\,\Omega}$. This function can be integrated over the energy, sky, and time region covered by a bin j to calculate the number of events predicted in that bin, as shown by

$$m_j = \int_{t\,\mathrm{bin}} \int_{E\,\mathrm{bin}} \int_{b\,\mathrm{bin}} \int_{l\,\mathrm{bin}} A * M(l,b,E,t)\; dl\; db\; dE\; dt\,. \tag{6.10}$$

Here, l and b are sky coordinates, E is energy, t is time, and A is the effective detector area. The basic models used in this analysis can be broken apart into their spatial, spectral, and temporal components, as in

$$M(l,b,E,t) = M_s(l,b,E,t)\;\; M_e(l,b,E,t)\;\; M_t(l,b,E,t)\,. \tag{6.11}$$

For this thesis, the sources being modeled are in equilibrium, so time-dependent effects are ignored by setting $M_t(l,b,E,t) = 1$.

For a basic point source, the spatial model function M_s is

$$M_{s,\mathrm{point}}(l,b) = \lim_{a\to\infty} \frac{1}{a\sqrt{\pi}} e^{-\left(\sqrt{(l-l_o)^2+(b-b_o)^2}/a\right)^2}. \tag{6.12}$$

In this equation, l_o and b_o specify the position of the point source in galactic sky coordinates, which can be model parameters. More complex M_s functions may also depend on energy E or time t, or may take on other shapes like an ellipse, a ring, or any other two-dimensional function. The energy spectrum can be similarly modeled by a basic power law. This basic power law is

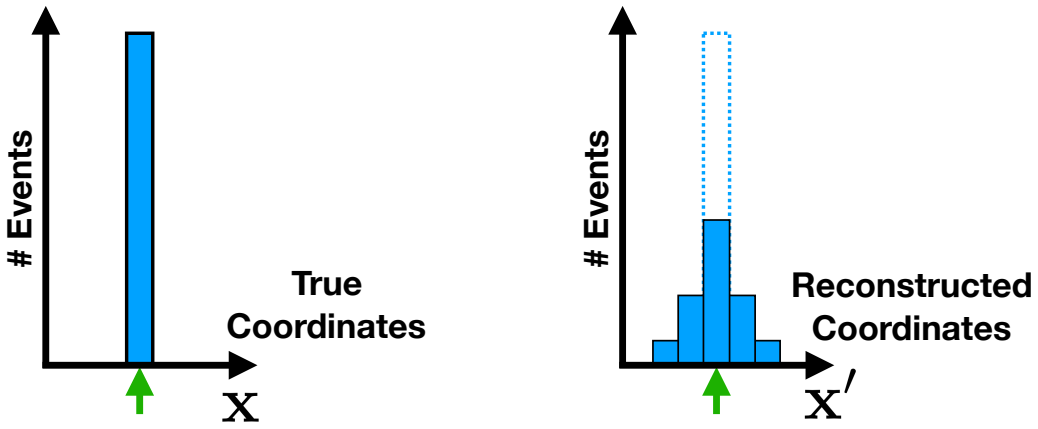

Figure 6.2: Left: Events from a source at the green arrow detected by a "perfect" detector, with bins in true coordinates. Right: The same events detected by a "real-world" detector, with bins in reconstructed coordinates.

defined by the model function

$$M_{e,\text{powerlaw}}(E) = N_o \left(\frac{E}{E_o}\right)^{-\gamma}. \tag{6.13}$$

Here, N_o is the flux normalization, E_o is the pivot energy, and γ is the spectral index, which are all be model parameters.

6.2.3 Instrument Response Function Folding

The average number of counts predicted by a model is calculated by integrating over the entire energy, sky, and time regions in the analysis. Because the reconstruction method is not perfect, all events from the astrophysical models are diffused according to the PSF and energy dispersion. Another way of understanding this is if a source is located in some sky bin j, events from that source can be reconstructed in neighboring bins $j+1$ and $j-1$. This increases the predicted number of events in those bins and decreases the number of events in bin j. The PSF is then a function that describes how many and how far events are diffused away from a sky position. This dispersion is illustrated in Figure 6.2. Similarly, energy dispersion will diffuse events out among neighboring energy bins. The effective area also alters the detector response, leading to more collection area at higher energies, due to being able to detect the brighter showers of high-energy gamma rays from further away. The PSF, energy dispersion, and effective area are collectively known as instrument response functions.

This leads to the need to define two distinct coordinate systems, x and x'. The coordinate x is

in true space (galactic l and b, energy E, and time t), *before* the IRFs are applied. Alternatively, x' is the coordinate in reconstructed detector space (l' and b', E', and t'), *after* the IRFs are applied. Another way this can be thought of is that x is the physical coordinate for events *before* they reach Earth's atmosphere, and x' is *after* the events have been reconstructed. Applying the IRFs is called *folding*, and is performed by an integration:

$$P_i\left(x'\right) = \int_x R\left(x', x\right) * M\left(x\right) dx\,. \tag{6.14}$$

Here, $P_i\left(x'\right)$ is the probability of detecting an event at detector coordinates $x' = \left(l', b', E', t'\right)$. The integration $\int_x$ takes place over the entire true space, time, and energy regions being studied. The function $M\left(x\right)$ is the number of counts predicted by the astrophysical models at coordinate x. The function

$$R(x', x) = A_{\text{eff}}\left(x\right) * PSF(x', x) * E_{\text{disp}}(E', x)\,, \tag{6.15}$$

is the instrument response function, which incorporates the effective area, PSF, and energy dispersion information, and is discussed further in Sections 5.6.1, 5.6.2, and 5.6.4. The functions A_{eff} , PSF, and E_{disp} are all interpolated from tables of stored values, which are derived from simulations.

The Crab Nebula point source in Section 6.4, the Galactic Center point source in Section 6.5.1, and the dark matter halo model in Section 6.5.2 all have this folding applied to the number of events they predict. An important distinction is that this folding is only applied to these astrophysical models, and not to the camera background models. This is because the background models are created with data from actual observations, and thus are already in x' space.

6.2.4 Combining Models into Hypotheses

When calculating the likelihood of a bin in Equation 6.1, the predicted number of counts in a bin may come from a combination of sources. Some fraction may come from a background model, another fraction from a specific source model, and some from other models. So in order to account for these multiple models, their predicted counts in a bin must be summed first, as in

$$m_j = \sum_k m_{k,j}\,, \tag{6.16}$$

before being used in Equation 6.9. Here, index k loops over the various models that contribute events at a position in the parameter space. The factor $m_{k,j}$ represents the number of counts predicted by model k, at the position of bin j.

In order to calculate the test statistic, the models must be grouped into two sets, called hypotheses. For a basic analysis, the null hypothesis consists of all models, except the specific one being searched for, called here H_{null}. Conceptually, the specific model being searched for should have its parameters set such that it contributes zero events, but this is mathematically the same as removing the model. The second hypothesis, called the alternate hypothesis, consists of all the models in the null hypothesis, plus the model being searched for, called here H_{alt}. Each observation would get its own camera background model, and then any additional astrophysical models are added separately. For example, if one has three observations of the Crab Nebula, this would mean there are three camera background models, plus a point source model for the Crab Nebula. The null hypothesis would be just the camera background models, while the alternate hypothesis would be the camera backgrounds plus the Crab Nebula model. Once these two hypotheses are assembled for an analysis, their maximum likelihood can then be sought.

6.2.5 Likelihood Maximization

The maximum likelihood is found by iteratively changing the parameters of a hypothesis's component models in directions that increase the likelihood. For example, take the alternate hypothesis used in Section 6.2.4, with three camera background models and one Crab Nebula point source. Each camera background model has a base template multiplied by a power law. The camera background models naively only need to fit the normalization, but the effect of using templates from one elevation with data at another elevation was uncertain, so the spectral index was also allowed to change. Each power law has two parameters, a normalization and a spectral index, so the background camera models have the parameters N_1, N_2, N_3, γ_1, γ_2, and γ_3. The Crab Nebula point source power law also has normalization and spectral index parameters N_c and γ_c. The Crab Nebula model also has location parameters l_c and b_c, but since these are fixed in this example (and thesis), the likelihood maximization can't vary them. Therefore this alternate hypothesis would have 8 free parameters, N_1, N_2, N_3, N_c, γ_1, γ_2, γ_3, and γ_c. For calculating the test statistic for the presence of the Crab Nebula, the null hypothesis is just the camera background models, with 6 free parameters N_1, N_2, N_3, γ_1, γ_2, and γ_3.

When finding the maximum likelihood for each hypothesis, these free parameters are varied, and the likelihood is recalculated. This procedure is repeated until a maximum likelihood is reached. While there are many maximization algorithms, this analysis uses the Levenberg-Marquardt method [196]. Once the maximum likelihood is calculated for both

hypotheses, then the test statistic can be calculated.

6.2.6 Test Statistic Calculation

In order to search for the presence of a source, the test statistic (TS) determines whether the null hypothesis is rejected. Once the maximum likelihood $\mathcal{L}_{\max}$ is found for these two hypotheses, the TS can be calculated with

$$\mathrm{TS} = -2 \log \left(\frac{\mathcal{L}_{\max}(M_{\mathrm{null}})}{\mathcal{L}_{\max}(M_{\mathrm{alt}})} \right) . \tag{6.17}$$

To convert this TS into a p-value, one has the option to simulate events using the null hypothesis probability density function multiple times. Then for each simulation, the TS is calculated. After many simulations, the resulting TS's will form a χ^2 distribution with n degrees of freedom, where n is the difference in number of free parameters between the two hypotheses. From this simulated TS distribution, an actual TS can be converted into a p-value. In simple situations where there is only one or two degrees of freedom, the significance of a specific model can be calculated as $\sqrt{\mathrm{TS}}$ according to Wilk's theorem [197], assuming the signal model has enough events. Due to time constraints, the p-value of this test statistic was not calculated with simulations, and only Wilk's theorem was used in the Crab Nebula analysis.

6.3 Background Models

The background models predict the number of background counts produced by a sky without gamma rays. This is used to model the probability density function of the background (primarily proton) events, which are several orders of magnitude more populous than the gamma rays. Background models are produced by binning events from observations of sky positions that have with weak or no gamma-ray emission. This results in a template of how the gamma-like background proton events are distributed in the camera. The construction of these models is described further in Section 5.6.3. For this low-elevation analysis the observations of the dark region Sgr A* Off, described in Section 6.1, were used to build these backgrounds.

To account for the difference between the V5 and V6 observatory configurations, the background observations are divided up based on their VERITAS hardware epoch, producing a unique background template for each epoch. These background templates depend on the event's position in the camera and the event energy. They are used in both the Crab Nebula analysis and the Galactic Center analysis. Because the templates are made from Sgr A* Off, which has

no sources of gamma-rays, the only expected detectable events are due to background cosmic rays.

6.4 Crab Nebula Likelihood Analysis

To verify the likelihood method is providing consistent results, the Crab Nebula was analyzed first, before any dark matter analysis was performed. As the Crab Nebula is the brightest gamma ray emitter in the sky, it has been observed extensively by VERITAS and other gamma ray telescopes. After searching for low-elevation Crab Nebula observations, a total of 17.1 hours of data were selected from the VERITAS data archives.

Since the Galactic Center only rises to around 29° elevation, low-elevation effects should be investigated. A plot of the telescope pointing elevation for the Crab Nebula, Galactic Center, and Galactic Center off data is shown in Figure 6.3. To uncover any low-elevation effects, time cuts were applied to this data to restrict the telescope pointing elevations to 27.5–32.5°, similar to the elevation of the later Galactic Center data. This resulted in 3.3 hours of V5 and 5.5 hours of V6 epoch data (see Table 6.1). In Figure 6.4, the position of all counts is shown in galactic l' and b'.

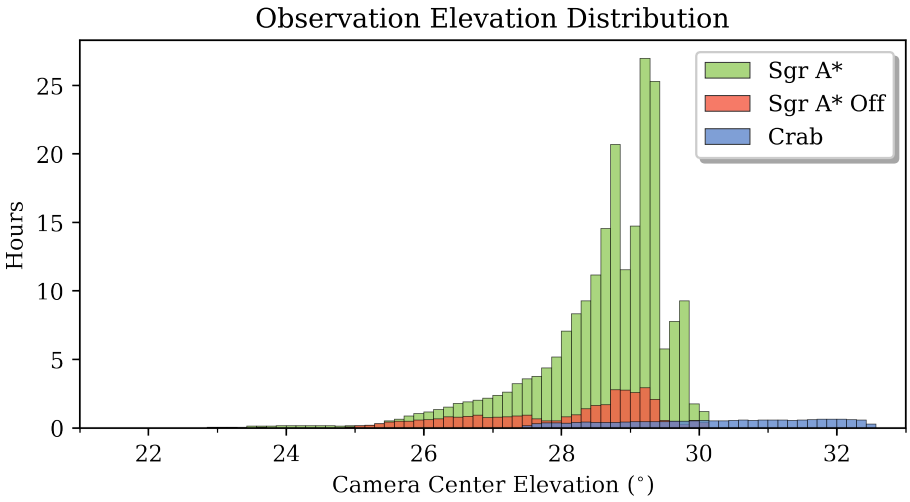

Figure 6.3: Camera center elevation for the three sets of data. The three peaks in the Sgr A* data are from the 4 wobble positions being at different elevations. The north wobble observations peak at elevation ~29.75°, east and west wobbles observations at ~29.25°, and south wobble observations at ~28.75°.

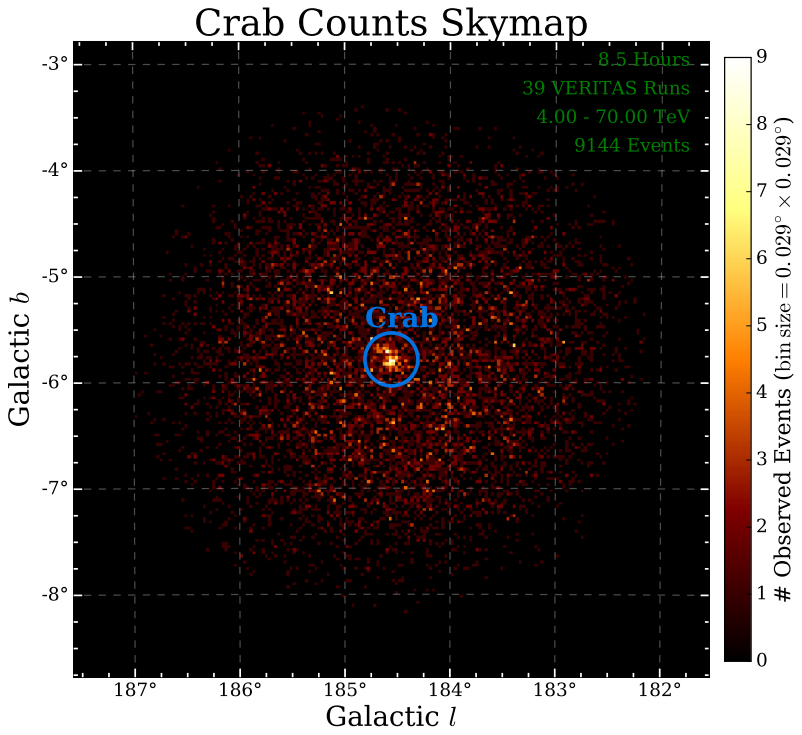

Figure 6.4: Sky map of event positions, (l',b'). No corrections are made for observing time or effective area.

The Crab Nebula is modeled by a point source with the simple power law spectrum,

$$M(x) = M_{s,\text{powerlaw}}(x) * M_{e,\text{point}}(x) = N_o \left(\frac{E}{E_o}\right)^{-\gamma} * \lim_{a\to\infty} \frac{1}{a\sqrt{\pi}} e^{-\left(\sqrt{(l-l_c)^2+(b-b_c)^2}/a\right)^2} . \quad (6.18)$$

These spatial and spectral shapes are both discussed in Section 6.2.5. The sky position of the point source is set to the Crab Nebula, at

$$(l_c, b_c)_{\text{J2000}} = (184.557600°, -5.784180°) \ .$$

This position is fixed, in order to reduce the complexity of the analysis. The pivot energy E_o of its spectrum is fixed at 16.73 TeV, while the normalization N_o and the spectral index γ are free to vary during the likelihood optimization.

Only events between 4–70 TeV are used in this test analysis. At an elevation of 25°, the reconstruction method is able to reconstruct events as low as 1.5 TeV. Below 4 TeV, however, the camera sensitivity starts to decrease in a poorly understood way, and IRFs in this region

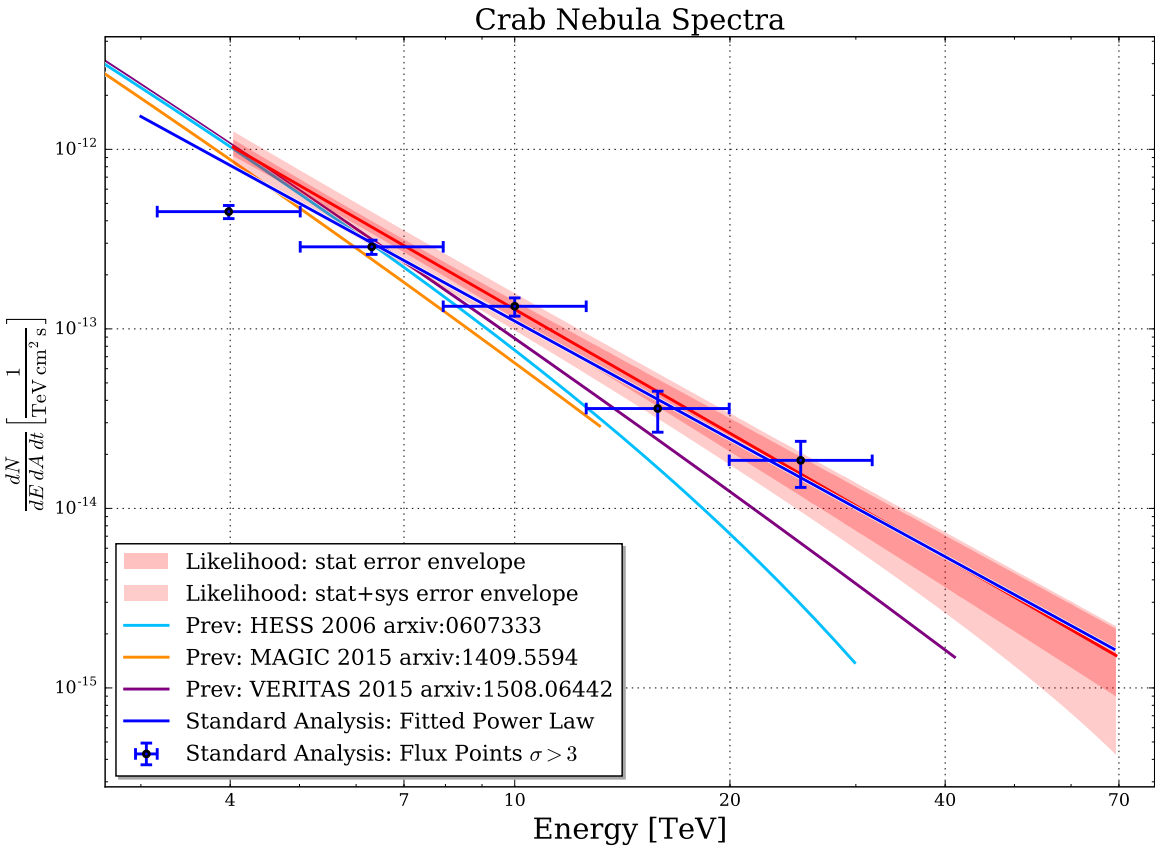

Figure 6.5: Crab Nebula spectra from various analyses and observatories. The solid red line is the best-fit spectra from the CTOOLS analysis described in this chapter, using only events from 4–70 TeV. The inner red envelope is the statistical fitting error on the solid red line. The outer red envelope is the combined statistical+systematic uncertainty. The dark blue line is the standard VERITAS Eventdisplay spectrum using the same set of observations. The dark blue data points are flux points for specific energy bins, from Eventdisplay. Light blue is a Crab Nebula spectrum from HESS [198]. Purple is a previously published spectrum from VERITAS [199]. Orange is a spectrum from MAGIC [200].

may not be accurate. Part of this decrease is explored in Section 5.7.1 (see Figures 5.21 and 5.22). The analysis range was limited to 70 TeV due to only having accurate IRFs up to that energy.

After fitting all model parameters to the events from 4–70 TeV, the best fit power law values are $N_o = (3.90 \pm 0.71) * 10^{-20} \frac{\text{photons}}{\text{cm}^2\,\text{s MeV}}$, $\gamma = 2.31 \pm 0.17$, with a test statistic of 408.8, corresponding to $\sim 20.2\,\sigma$.

In the standard VERITAS Eventdisplay analysis, the Crab Nebula is found to have a point source significance of $21.3\,\sigma$, shown in Table 6.2. However, the energy range of this Eventdisplay

Analysis Method	**Min Energy** TeV	**Max Energy** TeV	**FOV** # Events	**PSF** # Events	σ
ON/OFF Region	3.16	79.4	11197	145	21.3
Likelihood	4.00	70.0	9319	120	20.2

Table 6.2: Comparison between the two different Crab Nebula analyses, using the ON/OFF regions in Eventdisplay, and the likelihood analysis in ctools.

analysis was from 3.16–79.4 TeV, which contained a total of 11197 events in the field of view. The likelihood analysis was from 4–70 TeV, containing only 9319 events, ~17% fewer events. This ratio persisted when the events were limited to within 0.18° of the Crab Nebula, the approximate radius of the PSF at 10 TeV (145 vs 120 events). Thus, the likelihood test detects the Crab Nebula at a similar significance level, indicating this likelihood method provides results consistent with the standard analysis.

In Figure 6.5, the fitted Crab Nebula spectra is shown, along with literature results from earlier VERITAS, HESS, and MAGIC observations of the Crab Nebula. The fitted spectra from this work is shown as a red line, with a red statistical uncertainty band. A second larger red uncertainty band includes a ~20% systematic uncertainty on the flux, due to gamma rays of different energies producing similar-looking shower images in the VERITAS telescopes.

The fitted models can also be viewed as a check that the likelihood engine is fitting the models to the data. In Figures 6.6 and 6.7, the counts from the observations and models were integrated along a slice of galactic l and b. The counts from only the camera background models is shown in yellow, along with the counts from all camera backgrounds plus the point source in green. The difference between these two histograms is then the counts from the Crab Nebula point source model. In Figure 6.8, a profile is made at 1° north of the Crab Nebula in Galactic b. This shows how when no source is present, the background is still well modeled by the background models. In Figure 6.9, a similar plot is made, though integrated in a 0.6°×0.6° square around the Crab Nebula at different energies.

For the Crab Nebula, a sky map of the significances are shown in Figures 6.10. The significance of each sky bin is calculated with the equation

$$\text{Significance} = \text{sign}(D-M) \times \sqrt{2\left(D\ln\left(\frac{D}{M}\right)+M-D\right)}, \tag{6.19}$$

which is derived in Appendix D.

The bin values from Figure 6.10 are histogrammed in Figure 6.11. After removing all bins with zero observed counts, the histogram follows a Gaussian distribution. Simulations are shown

in red using the best-fit models, and the $\frac{\text{Simulated Models}}{\text{Data}}$ residual is shown in the bottom plot. Since most bins in the residual overlap the $\frac{\text{Simulated Models}}{\text{Data}} = 1$ line, it can be concluded that the models are not deficient in any particular area.

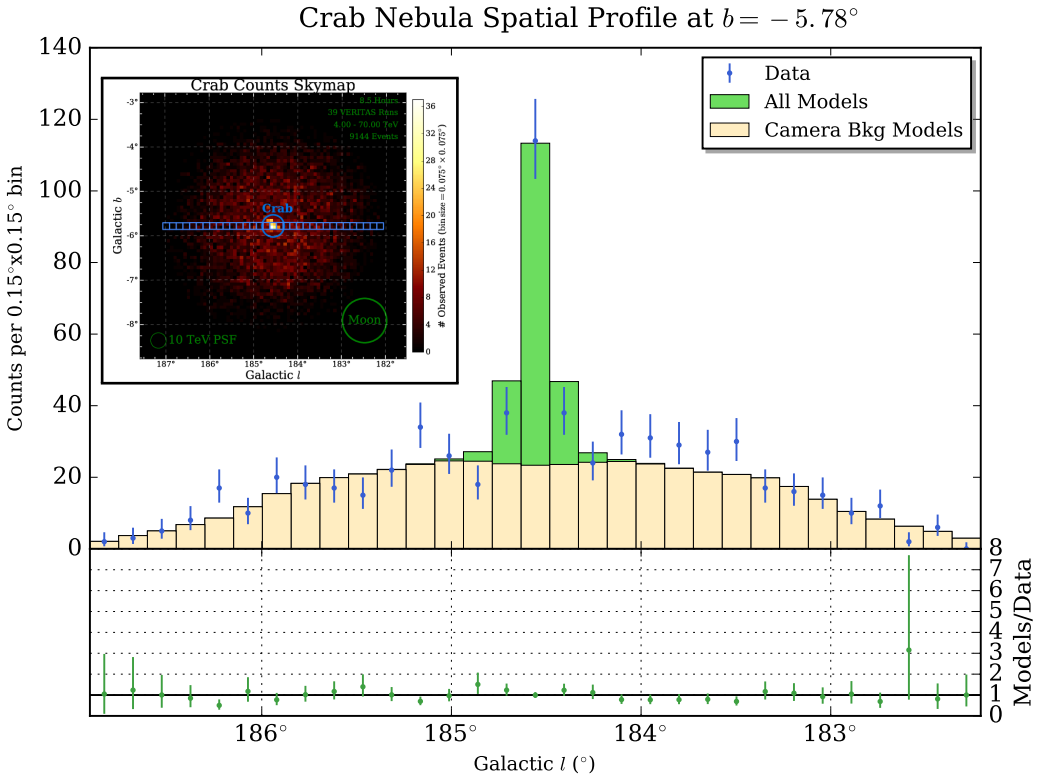

Figure 6.6: The top plot shows the number of counts along a 0.15°-wide-slice through Crab Nebula, along the galactic l axis. Blue points are the number of observed counts, with Poissonian error bars [201]. The green histogram bars are the number of counts predicted by all models. Yellow histogram bars are the number of counts predicted by only the camera-background models. The bottom plot shows the $\frac{\text{all models}}{\text{data}}$ residual as green points. The inset plot shows the counts map from Figure 6.4, with blue squares showing the profile bin locations.

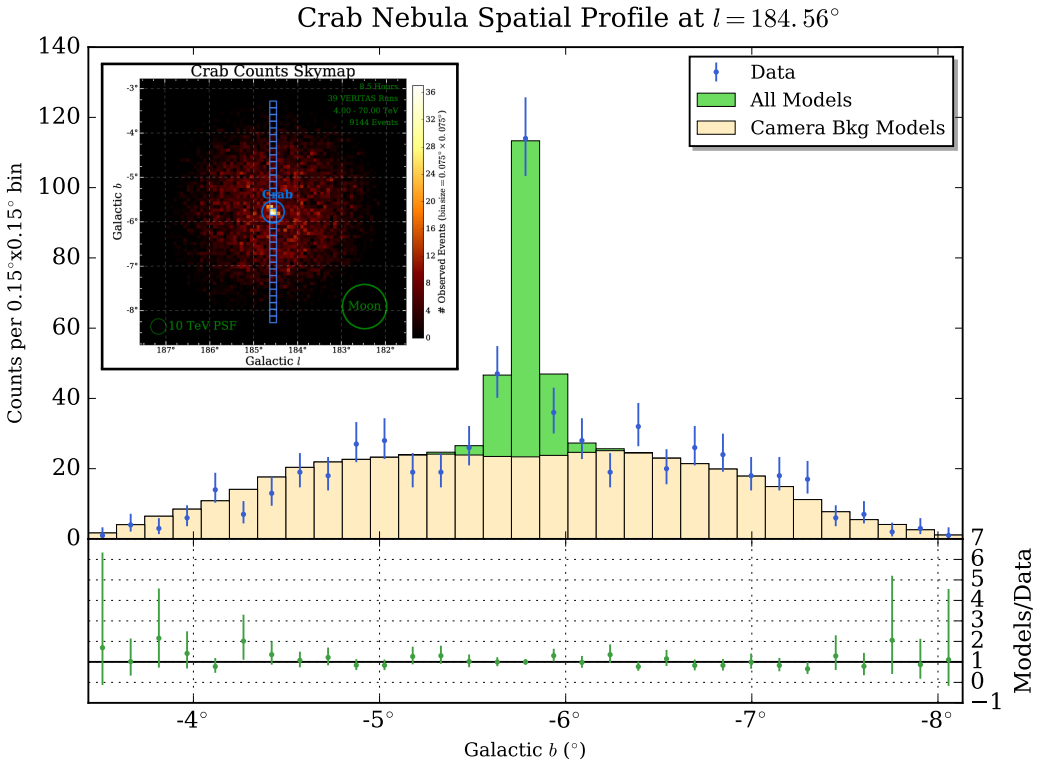

Figure 6.7: The top plot shows the number of counts along a 0.15°-wide-slice through the Crab Nebula along the galactic b axis. Blue points are the number of observed counts, with Poissonian error bars [201]. The green histogram bars are the number of counts predicted by all models. Yellow histogram bars are the number of counts predicted by only the camera-background models. The bottom plot shows the $\frac{\text{all models}}{\text{data}}$ residual as green points. The inset plot shows the counts map from Figure 6.4, with blue squares showing the profile bin locations.

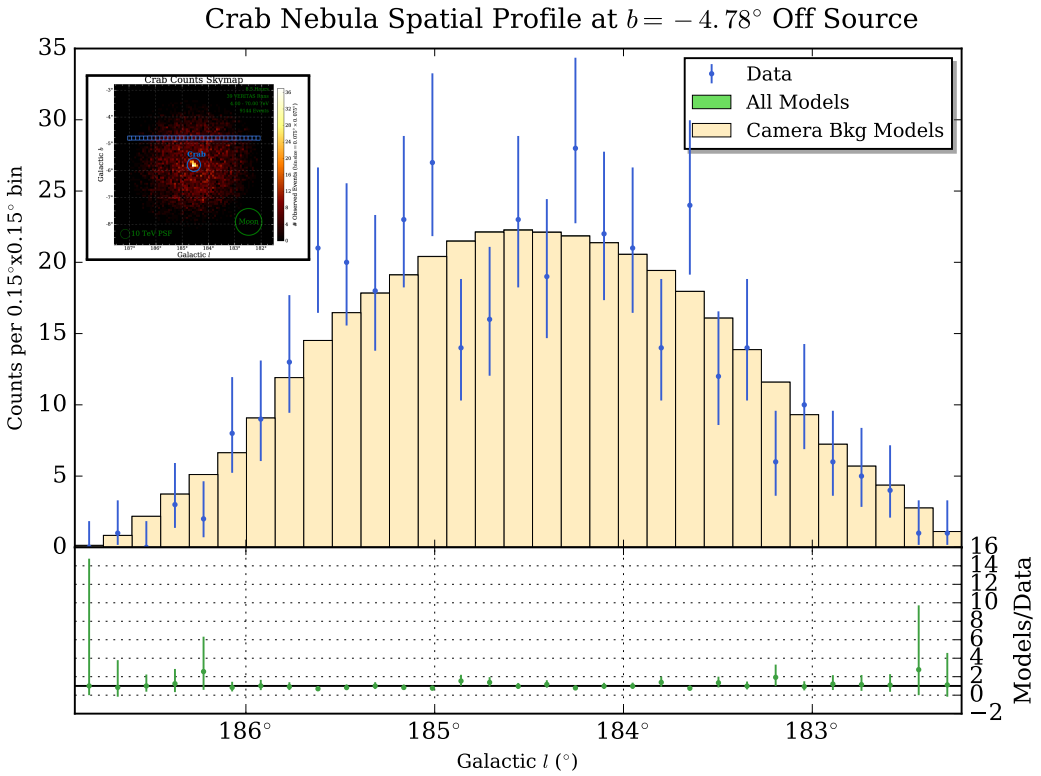

Figure 6.8: The top plot shows the number of counts along a 0.15°-wide-slice along the galactic l axis. This slice doesn't go through the Crab Nebula, but instead 1° higher in galactic b. As this doesn't include the Crab Nebula, this plot primarily demonstrates the camera background modeling. Blue points are the number of observed counts, with Poissonian error bars [201]. The green histogram bars are the number of counts predicted by all models. As the Crab Nebula doesn't contribute any events 1° to the north, the green histogram bars are identical (and behind) the yellow histogram bars. Yellow histogram bars are the number of counts predicted by only the camera-background models. The bottom plot shows the $\frac{\text{all models}}{\text{data}}$ residual as green points. The inset plot shows the counts map from Figure 6.4, with blue squares showing the profile bin locations.

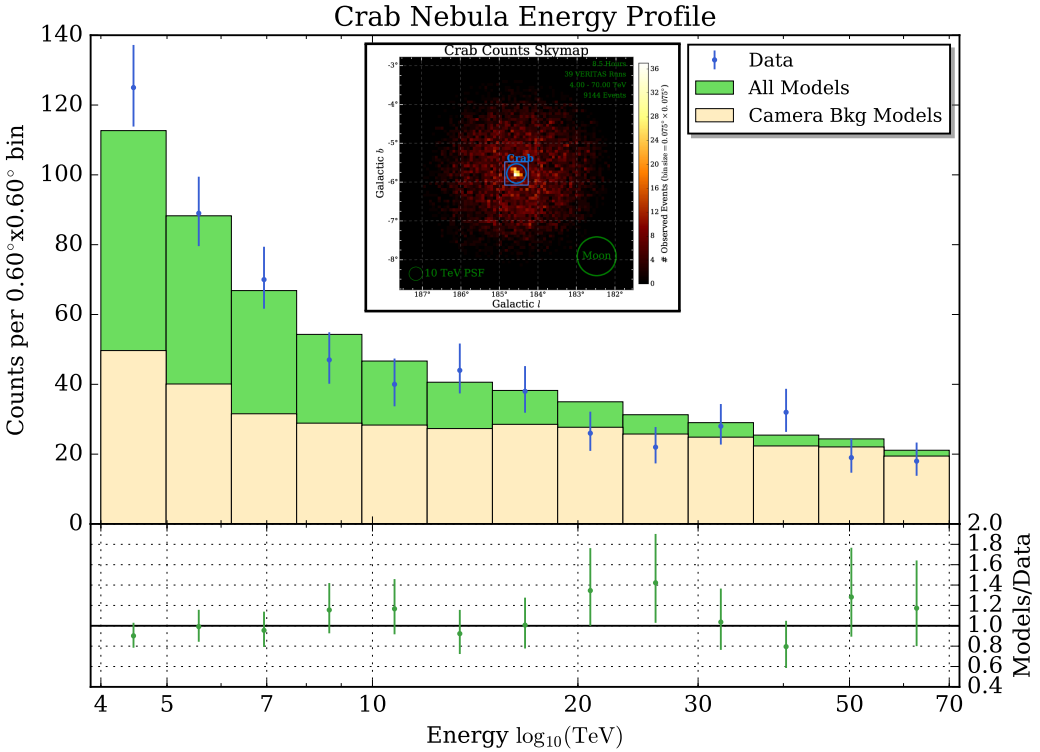

Figure 6.9: The top plot shows the number of counts in a 0.6° x 0.6° square centered on the Crab Nebula, vs energy. Blue points are the number of observed counts, with Poissonian error bars [201]. The green histogram bars are the number of counts predicted by all models. Yellow histogram bars are the number of counts predicted by only the camera-background models. The bottom plot shows the $\frac{\text{all models}}{\text{data}}$ residual as green points. The inset plot shows the counts map from Figure 6.4, with a blue square showing the profile bin location.

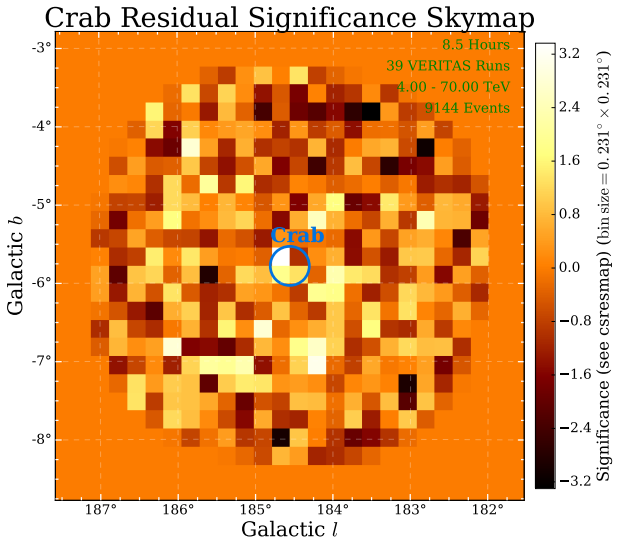

Figure 6.10: Sky map showing how significantly the models differ from the observations in each bin. This plot uses 0.23°-wide bins.

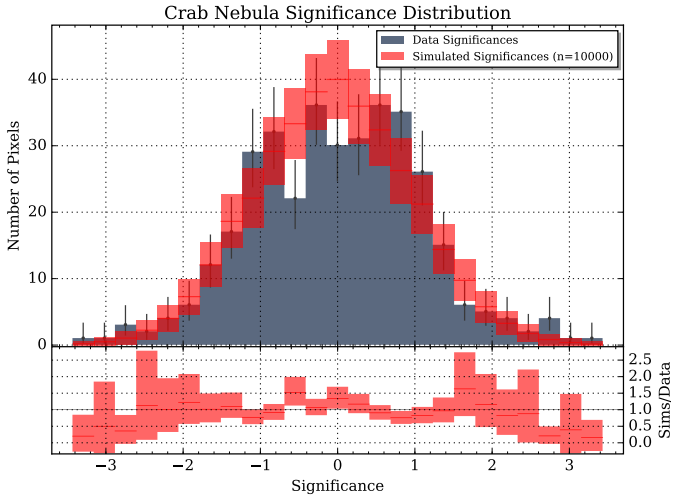

Figure 6.11: Data and simulated significance distributions from the significance sky map in Figure 6.10. In the top plot, the gray histogram bars indicate the data's significance distribution, with gray Poissonian error bars. The red lines and bars indicate the range of simulated significances, centered on the mean, and extending up and down by one standard deviation. The bottom plot shows the $\frac{\text{simulated}}{\text{data}}$ residual.

6.5 Dark Matter Likelihood Analysis

Since the test analysis on the Crab Nebula data shows results consistent with other VERITAS, H.E.S.S., and MAGIC studies, the main dark matter analysis can begin in earnest. The 108 hours of Galactic Center data used in this analysis is described in Section 6.1. A sky-map histogram of all observed events is shown in Figure 6.12. This sky map is uncorrected for exposure time or effective area; it is only a histogram of event positions. A histogram of all events' energies from 4–70 TeV is shown in Figure 6.13. As this histogram is uncorrected for effective area, it does not follow the standard power-law shape. Once the data is reconstructed, the next step is to set up the models. These include the camera background models, similar to the Crab Nebula analysis, as well as a point source at the Galactic Center, and a dark matter halo.

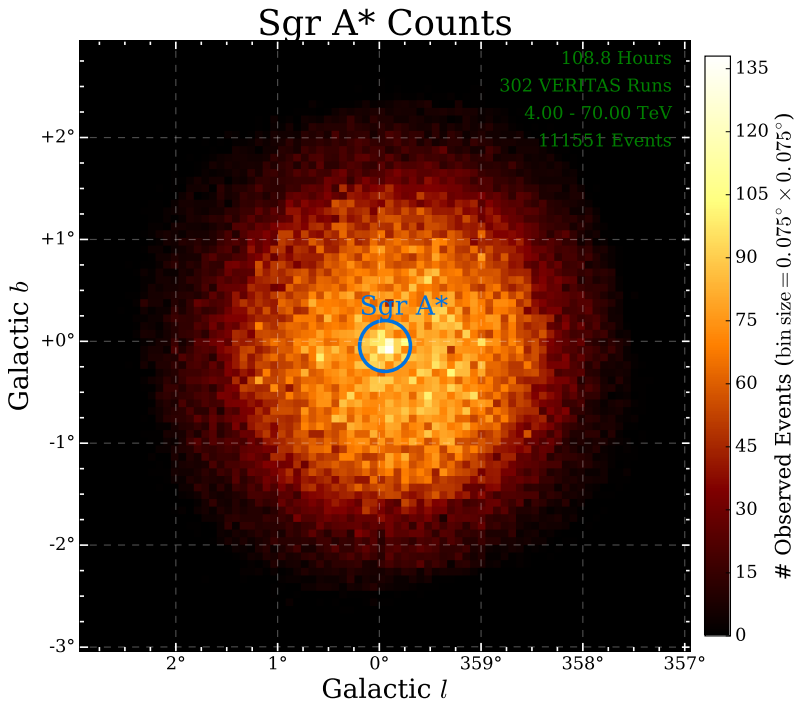

Figure 6.12: Sky map of all events used in this analysis. No adjustments are made here for effective area, observation time, or background rate.

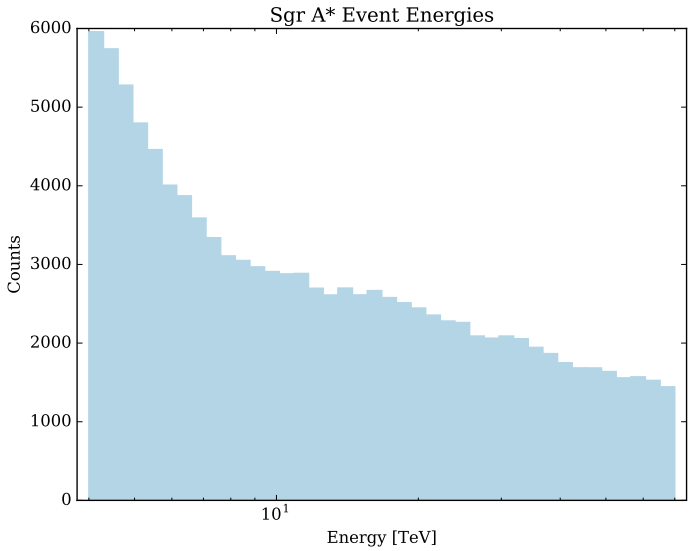

Figure 6.13: Histogram of all event energies (E') used in this analysis. No adjustments are made here for effective area, observation time, or background rate.

6.5.1 Non-Dark Astrophysical Models

For this analysis, a point source model was added at the position of Sgr A*, at

$$(l, b)_{\text{J2000}} = (359.944212°, -0.046013°)\,.$$

This was done because previous studies had detected a gamma-ray excess at Sgr A*, and it was found to be point-like. This excess may be produced by WIMPs annihilating, or it may be due to some other non-dark-matter mechanism (see Section 3.2). In this analysis, the excess from Sgr A* is considered as not coming from dark matter and a point source is added.

The point source's spectral shape is set by a broken power law,

$$M_e(x) = M_e(E) = N_o * \left(\frac{E}{E_{\text{pivot}}}\right)^{\gamma} e^{-\frac{E}{E_{\text{cutoff}}}}\,. \tag{6.20}$$

This was chosen because, in a previous VERITAS analysis of the Galactic Center, a broken power law was found to be a better fit than a simple power law [124].

Several parameters are fixed in the likelihood optimization. The values used in Equation 6.20 are from Ref. [124], where $E_{\text{pivot}} = 1\,\text{TeV}$, $E_{\text{cutoff}} = 12.8\,\text{TeV}$, and $\gamma = -2.1$. The normalization parameter N_o was initially set to $2.8 * 10^{-12}\,\text{cm}^{-2}\,\text{s}^{-1}\,\text{TeV}^{-1}$, but was free to change in the

likelihood optimization, while E_{pivot}, E_{cutoff}, and γ were all fixed. The dark matter limits may change if these parameters are instead left free, however with more free parameters the likelihood maximization process has a tendency to converge to non-physical values and fail, so in this first-step analysis these parameters are left fixed. The normalization N_o was left free to allow for the potential of some mixing between the point source events and any dark matter halo events. For example, a stronger dark matter halo gamma-ray flux would result in a weaker point source flux.

The galactic disk also produces its own gamma-ray emission, as the protons in the disk act as an interaction target for relativistic protons [202]. At these high energies, the contribution from the galactic diffuse emission is negligible compared to the atmospheric effects discussed in Section 6.7.

There is also evidence of diffuse TeV emission around the galactic center, possibly from PeV electrons [127]. The flux from this diffuse source is of a similar strength to the galactic center point source. In the dark matter search this is unmodeled, in order to simplify the analysis. Leaving this unmodeled will cause the background models to be fitted with slightly higher normalizations, which will reduce the number of gamma rays available for fitting the galactic center point source and dark matter models. This has the tendency to make any dark matter upper limits more conservative.

6.5.2 Dark Matter Models

Dark matter halos are modeled by a spherically-symmetric mass-per-volume density profile, combined with an annihilation spectrum. This is assembled with a simplified version of Equation 3.11:

$$M_{\text{dm}} = N \times M_{\text{e,halo}} \times M_{\text{s,halo}}\,. \tag{6.21}$$

In this analysis, an Einasto density profile is used for the spatial component function M_s of the dark matter halo model. See Section 3.3.3 for a discussion on the $M_{s,\text{halo}}$ function.

For the spectral component, each of the nine dark matter masses tested has their own spectrum function M_e produced with CLUMPY. These spectra are shown in Figure 6.14, and are discussed further in Section 3.3.2. The parameter N is the magnitude of the halo, which was left free in the likelihood fit.

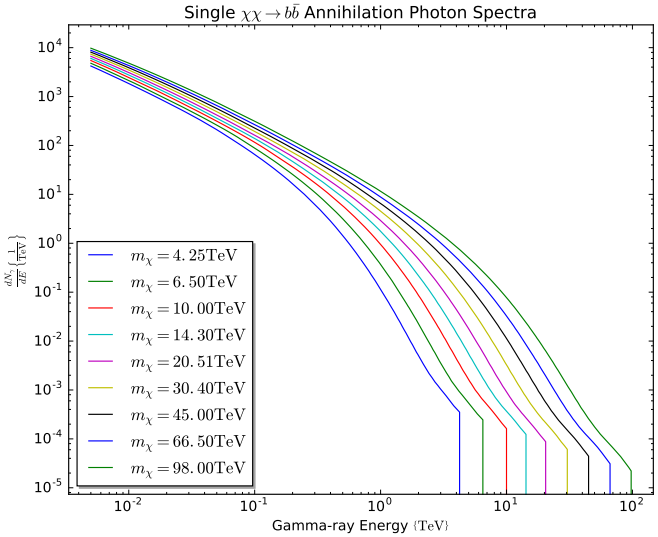

Figure 6.14: Resultant photon spectra from the annihilation of two WIMP particles purely into the $b\bar{b}$ channel. Each colored line represents a different WIMP mass.

6.5.3 Likelihood Maximization Results

The fully assembled likelihood analysis is described in the following section. 108 hours of VERITAS data have been organized into 948 observations. Each observation has a camera background model, with two free parameters, a normalization N_o and a spectral index γ_o. In this analysis as well, the backgrounds are a template multiplied by a power law, in case the spectrum changes due to the changing elevation of the observations. A point source has been added at the Galactic Center with a broken power law spectrum, where only its normalization N_o is a free parameter. The last model is then one of nine dark matter halo models, each with a cuspy Einasto spatial profile. The spectrum of this halo is from two WIMPs of mass m_χ annihilating into a $b\bar{b}$ pair. The dark matter halo's only free parameter is its normalization N_o. These models are then grouped into two hypotheses, where M_{null} consists of the 948 camera background models and the Galactic Center point source. Then M_{alt} is all the models in M_{null} plus the dark matter halo for one m_χ.

With these two hypotheses, the likelihood function was maximized to find the best-fit model parameters for each m_χ. In Table 6.3, the TS values from each dark matter mass are shown. Using Wilk's theorem [197] with one free parameter, a TS value greater than 20 would hint at the presence of a dark matter halo. The fact that all of these are less than zero shows that the null (no dark matter) hypothesis is statistically favored. The next steps are to examine

DM Mass m_χ [TeV]	Halo TS
4.250	-0.034
6.500	-0.184
10.000	-0.457
14.300	-0.055
20.512	-0.044
30.400	-0.009
45.000	-0.743
66.500	-5.894
98.000	-0.026

Table 6.3: TS values for each dark matter halo model likelihood ratio maximization fit.

what dark matter cross sections were ruled out with an upper limit calculation. This is done in Section 6.6. Before these upper limits are calculated, some verification can be done to check that the analysis was modeling the data properly.

As there are 948 camera background models in each likelihood analysis, each with a free normalization and spectral index, these are histogrammed as a sanity check in Figure 6.15. The spectral index distribution is centered on zero because the power law is applied to an existing (non-power-law) background shape. This means that on average the background models required little spectral hardening or softening. Because the spectral index is centered on zero, and the spread of spectral indices (~0.2) is comparable to the statistical uncertainty on the Crab Nebula spectrum fit (Section 6.4, $\gamma = 2.31 \pm 0.17$), this confirms that it is enough to only leave the normalization free.

To check that the other models are fitting the observed events, we can compare the observed vs modeled counts in different slices. In Figure 6.16, the observed counts are shown compared to the final, likelihood-optimized modeled counts. The histogram bins are located on 0.22°-wide slice along the galactic l axis, centered on Sgr A*'s galactic b coordinate. Yellow histogram bins are the modeled counts from only the camera background models. Green histogram bins are the total modeled counts from the camera background models, the Galactic Center point source, and the dark matter halo. Blue points with error bars are the observed counts in each bin, with Poissonian errors. The observed counts are higher on the left and lower on the right than the modeled histogram. This is likely due to unaccounted-for elevation effects in the camera background models. The impact of this elevation effect is tested later in Section 6.7.

Figure 6.17 is similar to Figure 6.16, except it slices through Sgr A* along the galactic b axis. The feature in which the observed counts are higher on the left and lower on the right

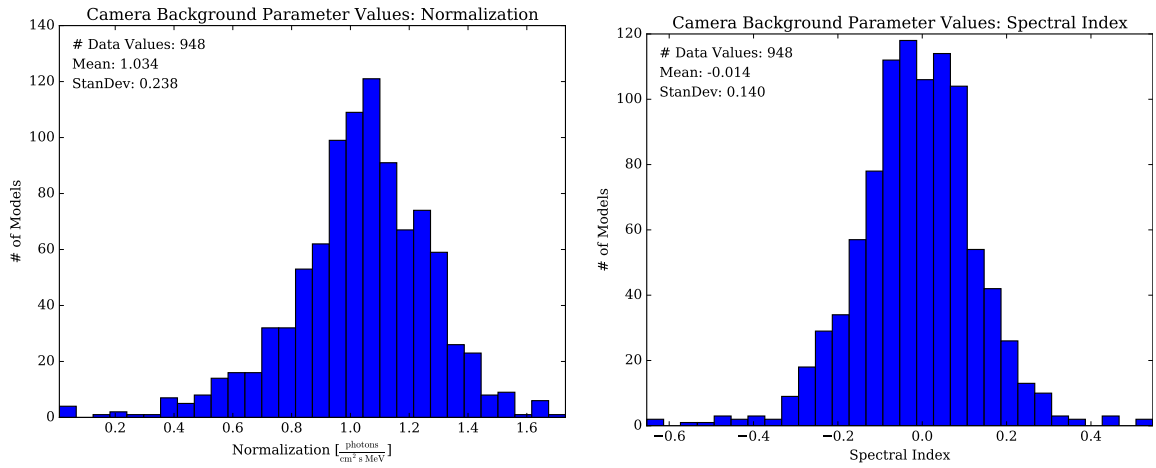

Figure 6.15: Histogram of the two free parameters in each of the 948 camera background models. Only the parameters from the $m_\chi = 45\,\text{TeV}$ likelihood fit are shown here.

is also visible here. Figure 6.18 shows a similar profile, except it is integrated over a $0.2°\times0.2°$ galactic (l,b) square centered on Sgr A*.

To check for any poorly modeled areas of the sky, the difference between the observed counts and models can be examined. The observed counts and models in this Galactic Center analysis are broken up into individual sky-map bins. Then, each bin's significance (how significantly the models differ from the data) is calculated with Equation 6.19 and shown in Figure 6.19. In this plot, the deficiency of the radially-symmetric camera background models is apparent. Lighter/darker areas indicate places where there were more/fewer observed counts than the best-fit models predicted. The darker upper-left and lighter lower-right areas are due to the gradient in the atmospheric air mass. This creates a gradient in the background that is not radially symmetric, which the radially-symmetric background models cannot properly fit. Several darker bins in a ring-like pattern around the edge of the field of view may be due to how the background models behave at the edge of the camera (see Figure 5.16), or how events near the edge of the camera may be poorly reconstructed at low telescope elevations.

The distribution of the pixel significances from Figure 6.19 is also shown in gray in Figure 6.20, along with a set of 10,000 simulated distributions in red. Before creating the histogram and simulations, all bins with zero observed counts are removed. If the source and background models were perfectly known, the gray bars would overlap the red simulations in most of the bins, and the residual will overlap the $\frac{\text{Simulated Models}}{\text{Data}} = 1$ line. Because only 12 of the 45 residual bins are consistent with 1, differences are observed between the models and the data. Specifically, there are more negatively-significant and positively-significant data pixels

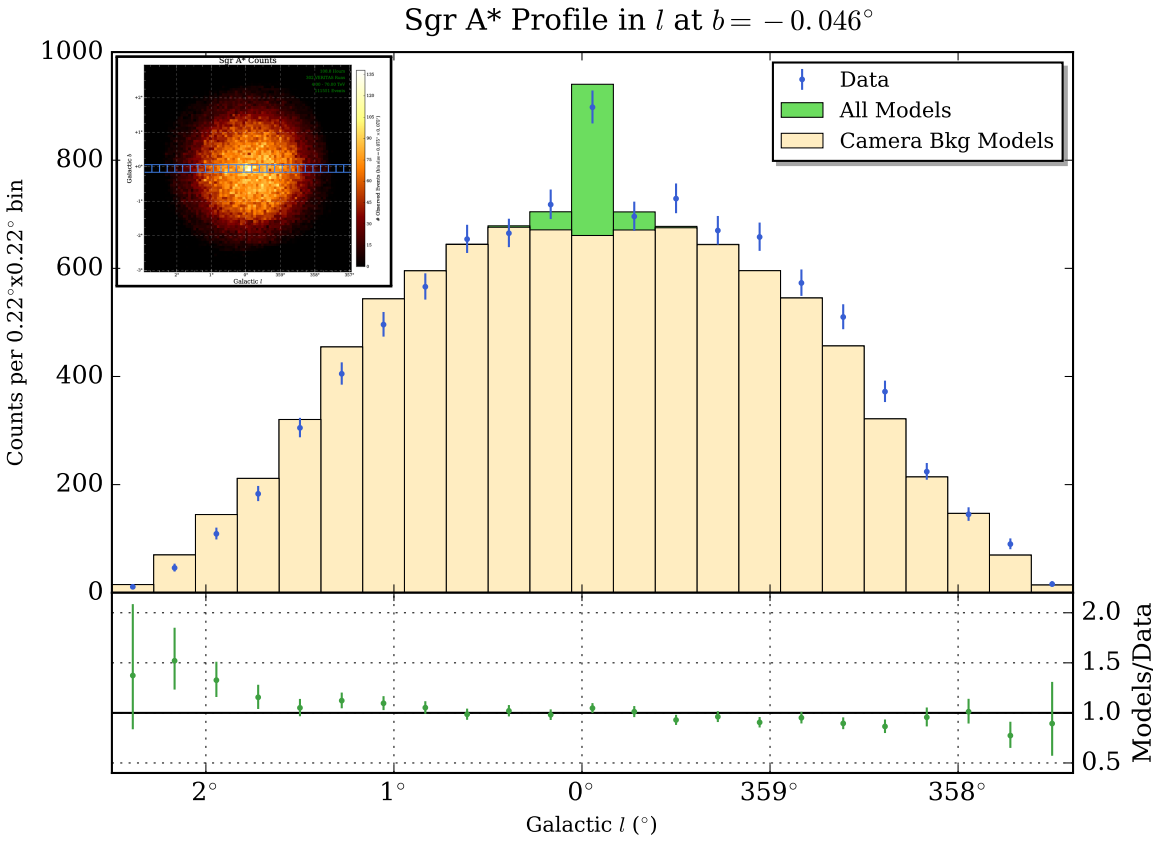

Figure 6.16: Observed vs modeled counts in a slice of the sky parallel to the galactic l axis at $b = -0.046°$. Modeled counts from camera background models are shown in yellow, total modeled counts are shown in green. Observed counts with Poissonian errors are shown in blue. The bottom plot shows the $\frac{\text{all models}}{\text{data}}$ residual as green points. The inset plot shows the counts map from Figure 6.12, with blue squares showing the profile bin locations.

than expected from the models, hinting that one or more features in the Galactic Center data are not being modeled properly. This is discussed further in Section 6.7.

The Galactic Center point source spectrum can be plotted as a check of the likelihood fitting. This spectrum is shown in Figure 6.21. This point source was detected with a test statistic of 224.25 (with one degree of freedom), with a normalization of $(4.764 \pm 0.402) \times 10^{-18} \frac{\text{photons}}{\text{cm}^2\,\text{s}\,\text{MeV}}$. A statistical uncertainty band is shown as a very thin red region, and a combined statistical plus systematic uncertainty is shown as a slightly thicker red band. The systematic uncertainty comes from showers of different energies forming similar images in the VERITAS telescopes, leading to a ~20% systematic uncertainty on the flux. The difference between the two spectra is likely due to the previous VERITAS being made from a combined fit with data from another telescope.

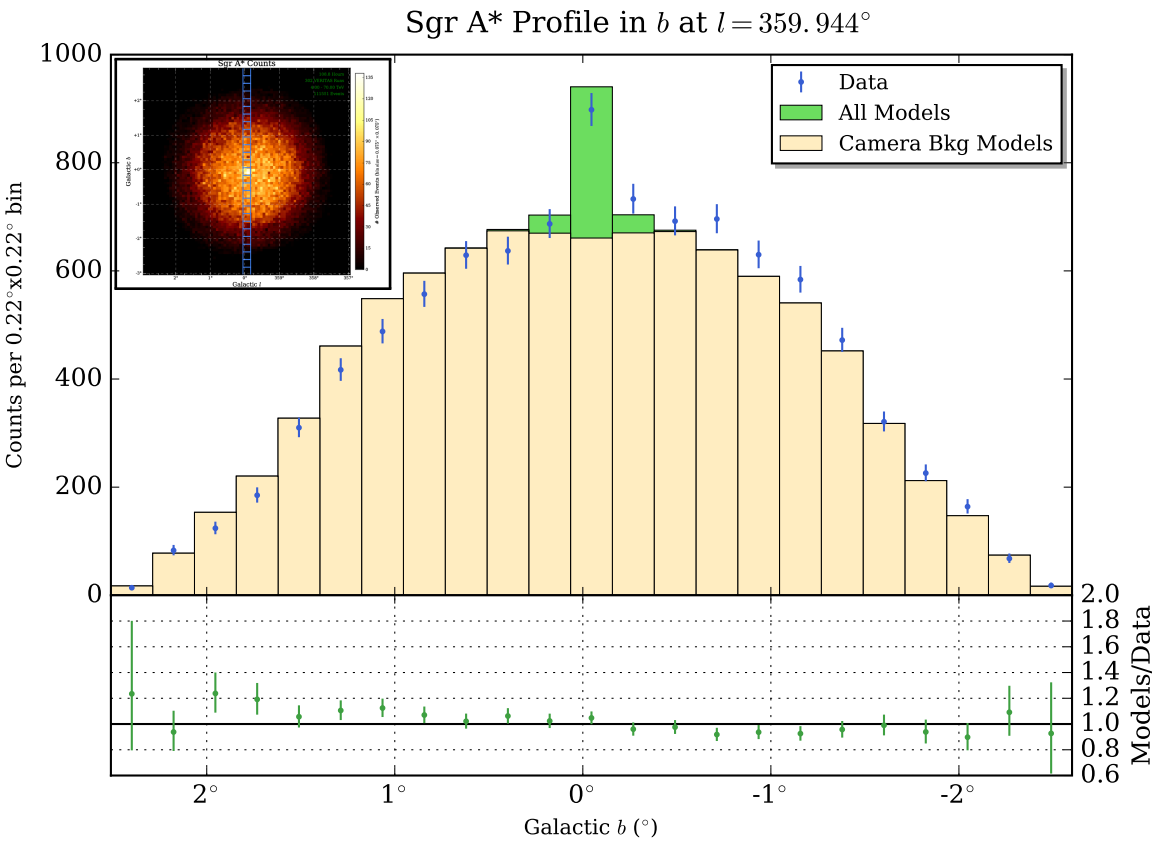

Figure 6.17: Observed vs modeled counts in a slice of the sky parallel to the galactic b axis at $l = 359.944^\circ$. Modeled counts from camera background models are shown in yellow, total modeled counts are shown in green. Observed counts with Poissonian errors are shown in blue. The bottom plot shows the $\frac{\text{all models}}{\text{data}}$ residual as green points. The inset plot shows the counts map from Figure 6.12, with blue squares showing the profile bin locations.

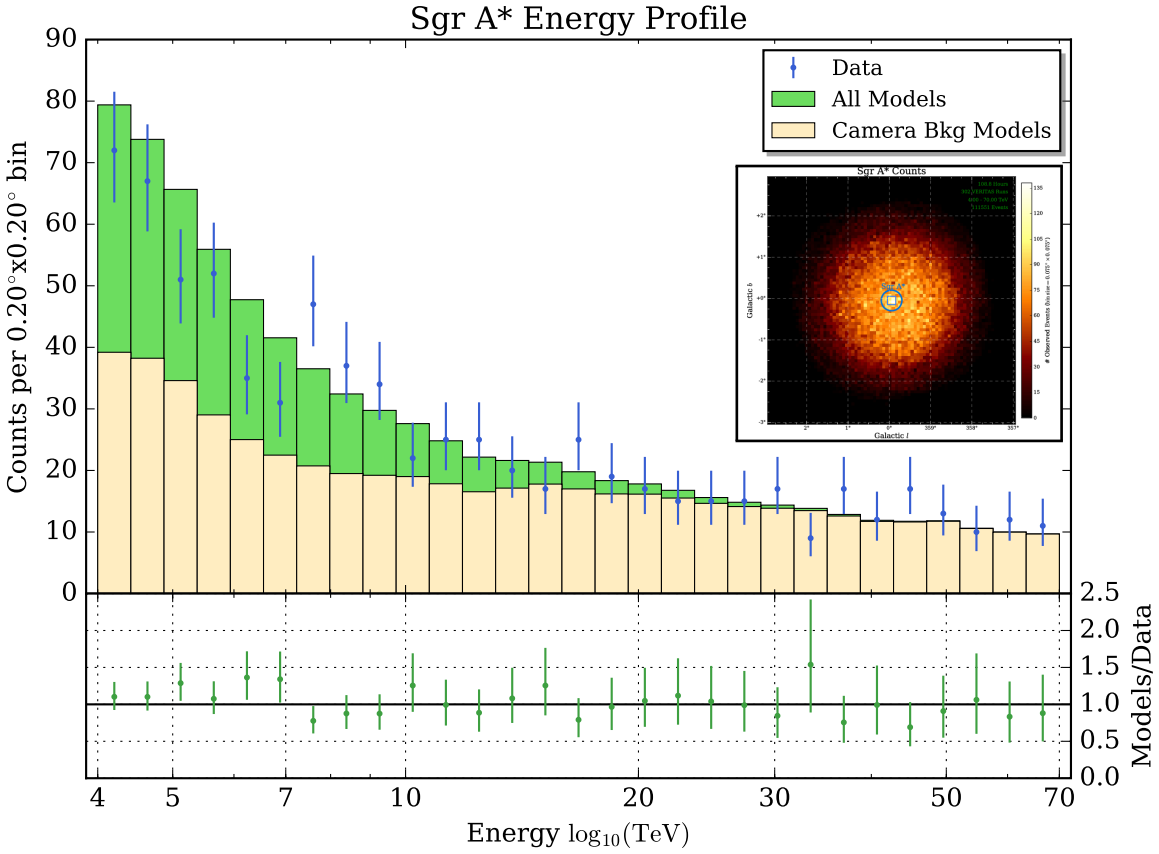

Figure 6.18: Observed vs modeled counts in a 0.2°×0.2° square bin centered on Sgr A* at energies from 4–70 TeV. Modeled counts from camera background models are shown in yellow, total modeled counts are shown in green. Observed counts with Poissonian errors are shown in blue. The bottom plot shows the $\frac{\text{all models}}{\text{data}}$ residual as green points. The inset plot shows the counts map from Figure 6.12, with a blue square showing the profile location.

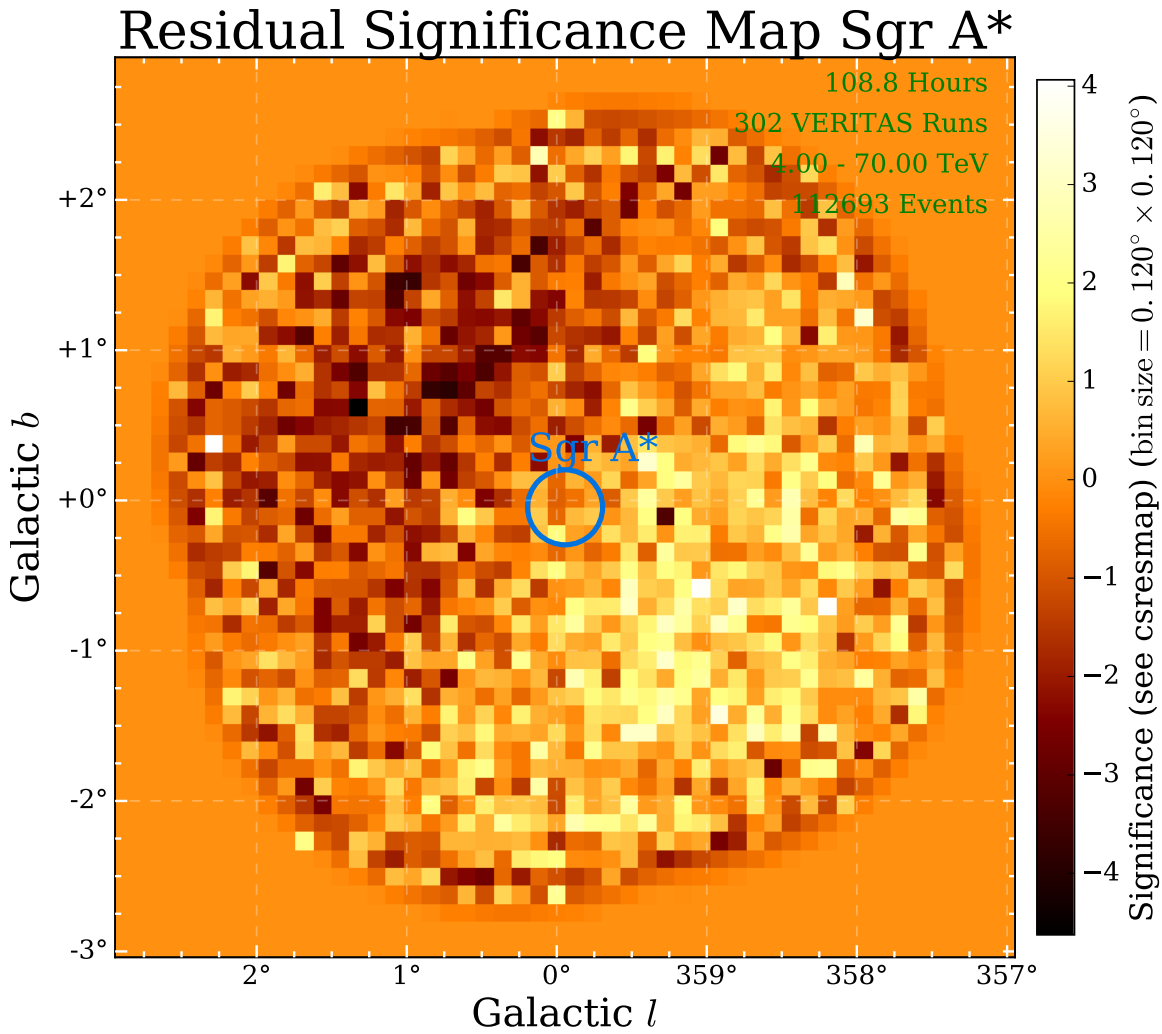

Figure 6.19: Significance of each sky-map bin's residual counts. See Equation 6.19 for details.

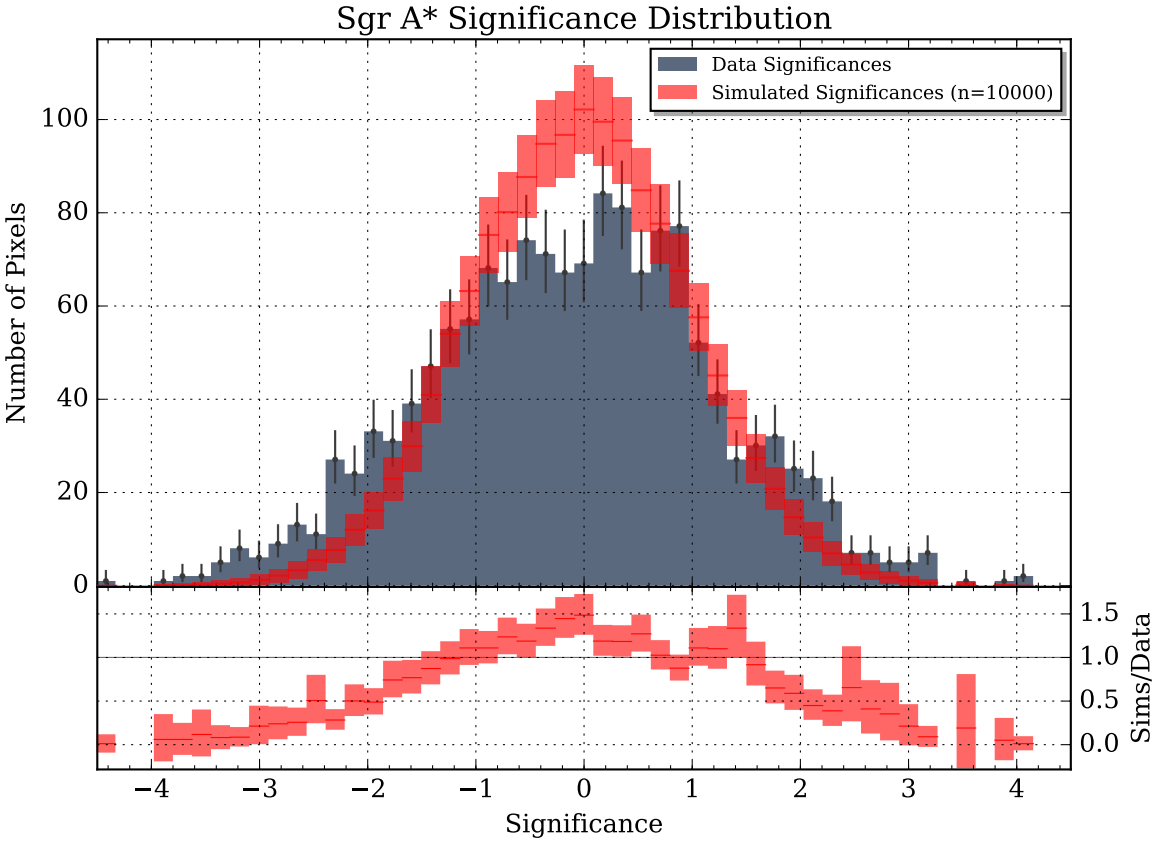

Figure 6.20: Histogram of the residual sky-map bin significances from Figure 6.19, calculated with Equation 6.19. In the top plot, the gray histogram bars indicate the data's significance distribution, with gray Poissonian error bars. The red lines and bars indicate the range of simulated significances, centered on the mean, and extending up and down by one standard deviation. The bottom plot shows the $\frac{\text{simulated}}{\text{data}}$ residual. Only sky-map bins within Sgr A*'s region of interest are histogrammed.

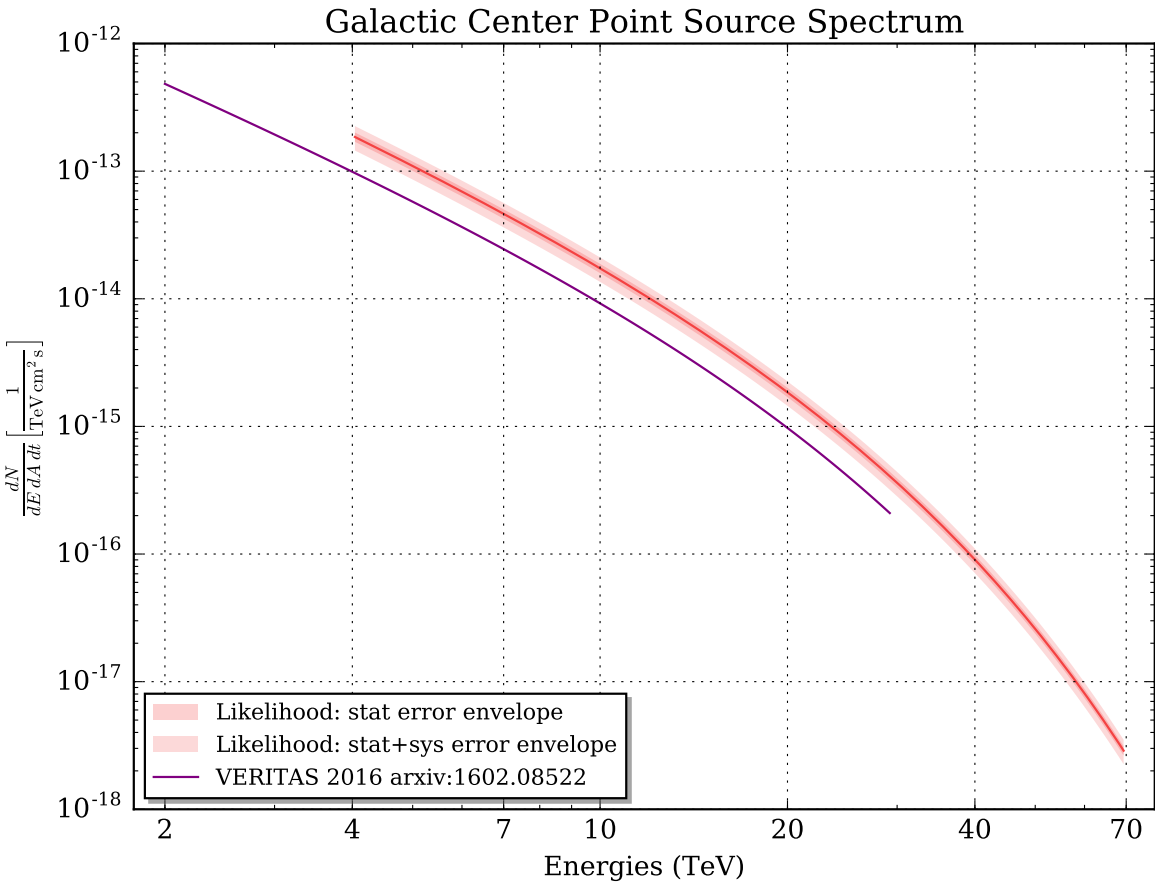

Figure 6.21: The spectrum of the fitted Galactic Center point source is shown in red, with statistical and combined statistical+systematic uncertainty bands. Only the normalization was free in the likelihood fit. The original VERITAS spectrum is shown in purple, from Ref. [124]. Note that the original VERITAS spectrum is part of a combined fit with another gamma-ray telescope.

6.6 Upper Limit

Because no dark matter signal was detected, the next step is to calculate what parts of the parameter space are ruled out. This is done by calculating an upper limit on the WIMP's velocity-averaged cross section $\langle \sigma v \rangle$. From the dark matter flux

$$\frac{d\Phi}{dEd\Omega} = \frac{\langle \sigma v \rangle}{8\pi m_\chi^2} \frac{dN_\gamma}{dE} \int \rho^2 dl \,, \tag{6.22}$$

(see Equation 3.11 for details), an upper limit on the observed gamma-ray flux can be derived. When all other variables in Equation 6.22 are fixed, a larger $\langle \sigma v \rangle$ always results in a larger gamma-ray flux. This means that the flux and cross section can both be replaced by their upper limits ($x \to x|_{\text{ul}}$), as in

$$\frac{d\phi}{dEd\Omega}\,|_{\text{ul}} = \frac{\langle \sigma v \rangle\,|_{\text{ul}}}{8\pi m_\chi^2} \frac{dN_\gamma}{dE} \int \rho^2 \, dl \,. \tag{6.23}$$

To calculate the upper limit, the parameter $\langle \sigma v \rangle$ is fixed and the maximum likelihood is found. Then, $\langle \sigma v \rangle$ is fixed to a slightly larger value, and a new maximum likelihood is found. Because no dark matter signal was found, increasing $\langle \sigma v \rangle$ increases the dark matter halo's flux, which decreases the maximum likelihood.

This procedure of increasing a parameter and rerunning the likelihood forms a *likelihood profile*. Naively, this profile can be approximated by a polynomial, as shown in Figure 6.22. Wilk's theorem then says that a decrease in likelihood will follow a Chi-squared distribution with degrees of freedom equal to the difference in number of free parameters between the alternate and null hypotheses. This probability distribution can then be used to determine an upper limit with a specified confidence level.

Using a Chi-squared distribution with 1 degree of freedom, the significance σ of observing a decrease in likelihood $\Delta\mathcal{L}$ can be found by

$$\sqrt{2\,\Delta\mathcal{L}} = \sigma \,. \tag{6.24}$$

An upper limit based on this significance can be calculated by

$$\sigma = \sqrt{2}\ \text{erf}^{-1}(\alpha) \,, \tag{6.25}$$

where α is the desired confidence level as a fraction of 1 (i.e. $95\% : \alpha = 0.95$) [197, 203]. The erf^{-1} is the inverse error function, an integration of a Gaussian probability distribution. This

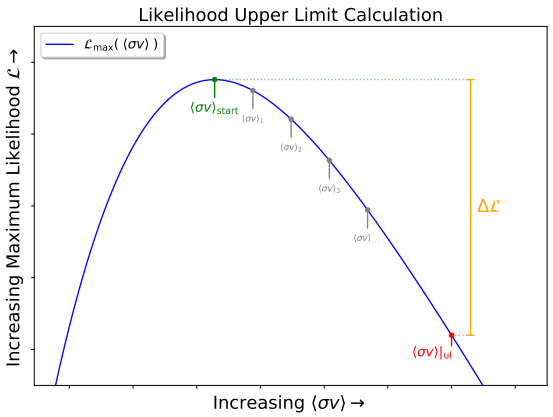

Figure 6.22: An example likelihood profile as the $\langle\sigma v\rangle$ is varied (blue line). The procedure starts at parameter $\langle\sigma v\rangle_{\text{start}}$, and $\langle\sigma v\rangle$ is increased until the likelihood has decreased by $\Delta\mathcal{L}$.

results in a likelihood decrease of

$$\Delta\mathcal{L} = \text{erf}^{-1}(\alpha)^2 \,. \tag{6.26}$$

Therefore, an upper limit on $\langle\sigma v\rangle$ can then be found by increasing $\langle\sigma v\rangle$ to the point where the likelihood has decreased by $\Delta\mathcal{L}$.

From the nine WIMP masses tested in Section 6.5, the calculated upper limits are shown in Figure 6.23 as dark blue points with error bars. Several other upper limits from previous studies are also shown for comparison. The orange upper limit is from 216 hours of VERITAS observations of several dwarf spheroidal galaxies, stacked into a single likelihood analysis [204]. The dark green upper limit is from 254 hours of H.E.S.S. observations of the Galactic Center [205]. The red upper limit is from a combined Fermi-MAGIC likelihood analysis using observations from several dwarf satellite galaxies [206]. Fermi and MAGIC spent a total of 6 years and 158 hours observing these galaxies, respectively. The light blue dashed line is the relic cross section [74].

These limits were calculated using a simple WIMP model, one that does not include the effect of Sommerfeld enhancement [157]. If Sommerfeld enhancement were included in the dark matter halo model, stronger limits would naively be expected.

Around the dark blue upper limit points from this work, systematic uncertainty error bars are also shown. For VERITAS, uncertainties in the energy reconstruction contribute a ~20% systematic uncertainty on the flux. While no dark matter was detected in this thesis, the upper limit calculation is influenced by this systematic uncertainty. This can be envisioned as a dark matter signal that was brighter than the upper limit in Figure 6.23, but then fluctuated

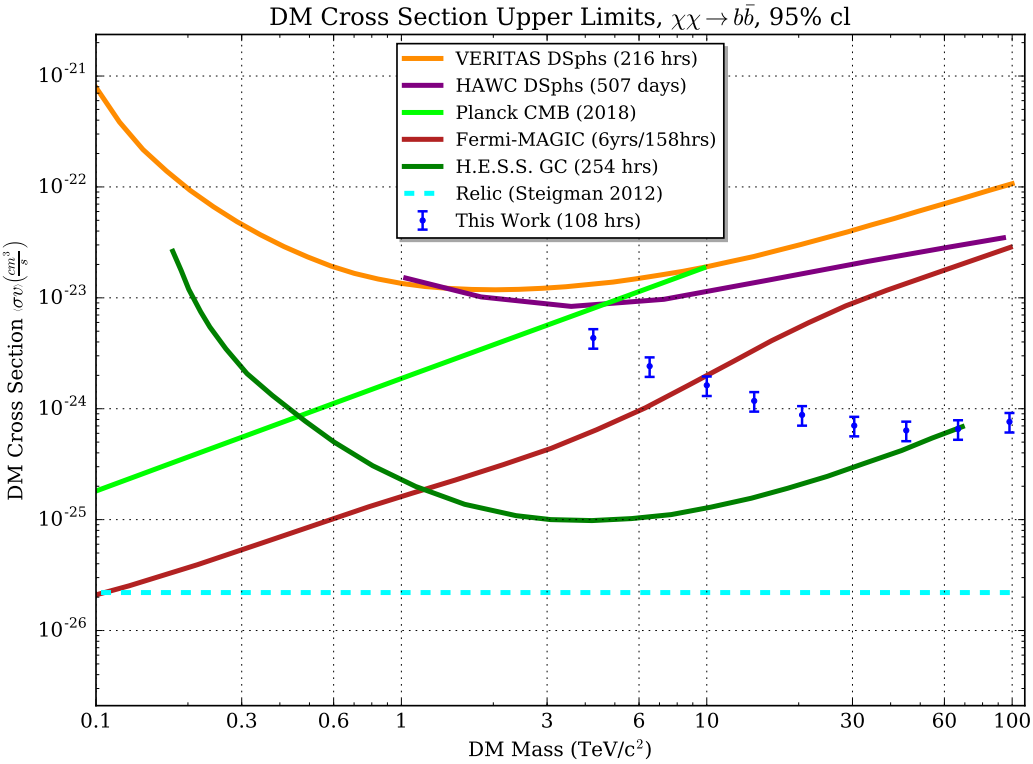

Figure 6.23: Dark matter upper limits on velocity-averaged cross sections. The results from this work are in dark blue. Orange is from a VERITAS [204] analysis of dwarf spheroidal galaxies. Dark green is from a H.E.S.S. [205] analysis of the Galactic Center. Purple is from a HAWC [207] analysis of dwarf spheroidal galaxies. Red is from a joint Fermi-MAGIC [206] analysis. Bright green is from Planck measurements of the CMB [58]. The light blue dashed line is the relic cross section [74]. Data values from this work's upper limits are in Appendix Table A.1.

downwards by 20% of its flux. Conversely, a dim dark matter signal below the upper limit could be enhanced by 20% instead. These uncertainties are reflected by the blue error bars.

6.7 Impact of Elevation Gradient

The residual map in Figure 6.19 has a visible gradient, going from the lower right to the upper left. This means that the radial camera background models are not accurately fitting the shape of the observed events. The direction of the residual gradient aligns with the elevation gradient in the camera, visible in Figures 5.19 and 5.20. To check that this elevation gradient has a negligible effect on the upper limit result in Figure 6.23, the likelihood analysis was redone with an elevation gradient.

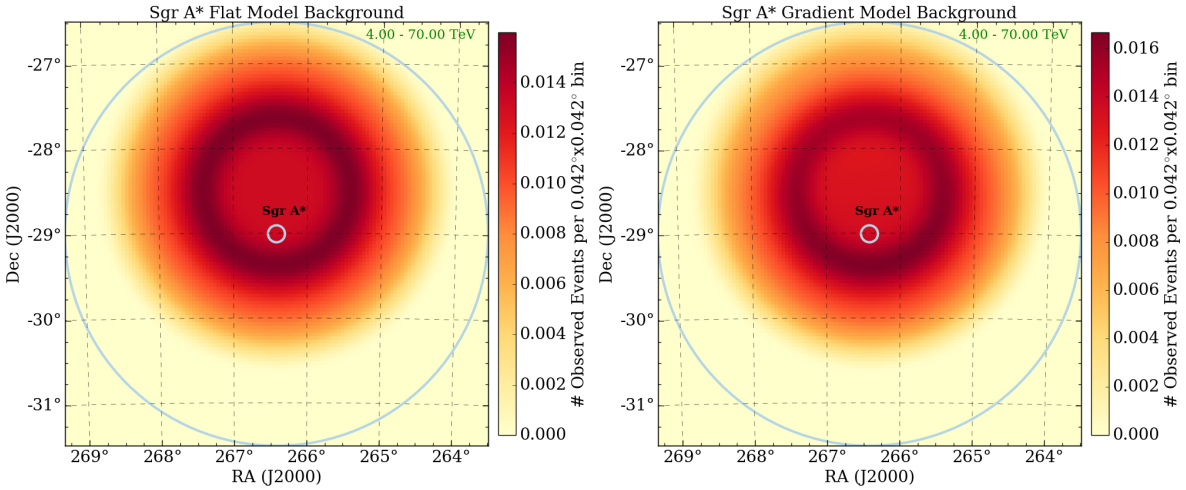

Figure 6.24: The background models for run 68348, minutes 16-24. Left is the original radial background, centered 0.5° north of the Galactic Center. Right is the same background, after applying the 5%/degree gradient along the elevation axis.

As this analysis is limited to the energy range 4–70 TeV, the elevation gradient will increase the number of events detected at the bottom of the camera, due to the thicker atmosphere providing increased interaction mass. And, since the Galactic Center is visible almost directly south at an azimuth of 193°, the elevation axis is almost parallel to the declination axis. A gradient of 5%/degree was chosen due to the relative differences between the total modeled counts and the observed counts in Figures 6.16 and 6.17. An example background is shown in Figure 6.24, before and after the gradient is applied. While faint, the difference between the two can be seen in the central dark-red ring. In the left, the ring is symmetric, while in the right, the ring is darker at the bottom than at the top.

After these were applied to all background models, the likelihood analysis was re-run for the 10 TeV WIMP mass. This can be considered representative of WIMP masses above 10 TeV, as the background does not strongly change in that range (see Figures 5.19 and 5.20). The resulting upper limit with the gradient was only 0.1% different from the upper limit with radial background models. This indicates the upper limits are not very sensitive to the background models. This likely stems from the fact that the test statistic is a ratio of the likelihoods of two model groups, both of which contain the background models. Thus, the likelihoods from both model groups changed by a similar amount, and in the same direction, partially cancelling out.

7 Conclusion

A likelihood ratio test was used with 108 hours of VERITAS data to analyze the gamma-ray emission from the Galactic Center. This test searched for a halo of WIMP dark matter particles that annihilated into $b\bar{b}$ quarks, which then cascaded into other particles, producing some gamma rays in the process. Observations were taken at an extremely low (~29°) telescope elevation. This reduced the overall sensitivity, but also shifted the sensitive energy range upwards to 4–70 TeV.

The halo model utilized in this analysis is a simple Einasto halo profile, without any core flattening. Annihilation spectra were generated for WIMPs in the 4–100 TeV mass range. The VERITAS instrument response functions were folded into the WIMP halo models, to account for dispersion in the reconstructed gamma ray position and energies. Camera background models were made using several hours of dedicated dark observations, of a region of the sky where there are no gamma-ray emitters. A low-elevation atmospheric gradient was noted in the background models, however this was found to have a negligible effect on the calculated upper limits.

No significant dark matter signal was detected in the mass range 4–100 TeV. To illuminate what WIMP candidates were ruled out by this search, cross section upper limits were calculated. Due to the VERITAS sensitivity to TeV gamma rays at low elevations, new limits were placed at very high masses. For $70\,\mathrm{TeV} < m_\chi < 100\,\mathrm{TeV}$, these upper limits exclude $\langle \sigma v \rangle_{\chi\chi \to b\bar{b}} > (6.6 - 7.6) \times 10^{-25} \frac{\mathrm{cm}^3}{\mathrm{s}}$ at the 95% confidence level. This results in an improvement over the previous Fermi-MAGIC limit by more than an order of magnitude.

This work can be expanded in several different ways. In addition to searching for different dark matter halos and annihilation spectra, the background modeling can be improved to include low-energy events, to increase the sensitivity. This may allow for new limits at a larger range of masses. Sensitivity to dark matter could be further increased by including ~800 hours of VERITAS observations of several dwarf spheroidal galaxies. The VERITAS data used here can also be combined in a joint likelihood analysis with other IACTs like H.E.S.S, MAGIC, and CTA, to perform more sensitive searches for dark matter.

Bibliography

[1] Zwicky, 1937, "On the Masses of Nebulae and of Clusters of Nebulae," *The Astrophysical Journal*, vol. 86, http://adsabs.harvard.edu/abs/1937ApJ....86..217Z.

[2] Bennett, Larson, Weiland, *et al.*, 2013, "Nine-year Wilkinson Microwave Anisotropy Probe (WMAP) Observations: Final Maps and Results," *The Astrophysical Journal Supplements*, vol. 208, http://adsabs.harvard.edu/abs/2013ApJS..208...20B.

[3] Beringer *et al.*, 2012, "Review of Particle Physics," *Physical Review D*, vol. 86, http://link.aps.org/doi/10.1103/PhysRevD.86.010001.

[4] Boehle *et al.*, 2016, "An Improved Distance and Mass Estimate for Sgr A* from a Multistar Orbit Analysis," *The Astrophysical Journal*, vol. 830, no. 1, http://stacks.iop.org/0004-637X/830/i=1/a=17.

[5] LaRosa, Kassim, Lazio, and Hyman, 2000, "A Wide-Field 90 Centimeter VLA Image of the Galactic Center Region," *The Astronomical Journal*, vol. 119, http://adsabs.harvard.edu/abs/2000AJ....119..207L.

[6] Aharonian and Neronov, 2005, "High-Energy Gamma Rays from the Massive Black Hole in the Galactic Center," *The Astrophysical Journal*, vol. 619, no. 1, http://stacks.iop.org/0004-637X/619/i=1/a=306.

[7] Ade, Aghanim, Arnaud, *et al.*, 2016, "Planck 2015 Results-XIII. Cosmological Parameters," *Astronomy & Astrophysics*, vol. 594, https://www.aanda.org/articles/aa/abs/2016/10/aa25830-15/aa25830-15.html.

[8] Prša, Harmanec, Torres, *et al.*, 2016, "Nominal Values for Selected Solar and Planetary Quantities: IAU 2015 Resolution B3," *The Astronomical Journal*, vol. 152, no. 2, http://stacks.iop.org/1538-3881/152/i=2/a=41.

[9] ESO/Digitized Sky Survey 2, "Fornax Dwarf Galaxy." Online, Accessed Sept 6, 2018, https://www.eso.org/public/images/eso1007a/.

[10] ESO, "Sculptor Dwarf Galaxy." Online, Accessed Nov 27, 2017, http://sci.esa.int/gaia/59807-sculptor-dwarf-galaxy/.

[11] Lokas, 2009, "The Mass and Velocity Anisotropy of the Carina, Fornax, Sculptor and

Sextans Dwarf Spheroidal Galaxies," *Monthly Notices of the Royal Astronomical Society: Letters*, vol. 394, no. 1, http://dx.doi.org/10.1111/j.1745-3933.2009.00620.x.

[12] Walcher, Fried, Burkert, and Klessen, 2003, "About the Morphology of Dwarf Spheroidal Galaxies and Their Dark Matter Content," *Astronomy & Astrophysics*, vol. 406, no. 3, https://doi.org/10.1051/0004-6361:20030768.

[13] Walker, Mateo, and Olszewski, 2009, "Stellar Velocities in the Carina, Fornax, Sculptor, and Sextans dSph Galaxies: Data From the Magellan/MMFS Survey," *The Astronomical Journal*, vol. 137, no. 2, http://stacks.iop.org/1538-3881/137/i=2/a=3100.

[14] Matthew *et al.*, 2007, "Velocity Dispersion Profiles of Seven Dwarf Spheroidal Galaxies," *The Astrophysical Journal Letters*, vol. 667, no. 1, http://stacks.iop.org/1538-4357/667/i=1/a=L53.

[15] Kourkchi *et al.*, 2012, "Dwarf Galaxies in the Coma Cluster - I. Velocity Dispersion Measurements," *Monthly Notices of the Royal Astronomical Society*, vol. 420, no. 4, http://mnras.oxfordjournals.org/content/420/4/2819.abstract.

[16] Binney, Tremaine, and Freeman, 2009, "Galactic Dynamics," *Physics Today*, vol. 62, no. 5, http://adsabs.harvard.edu/abs/2009PhT....62e..56B.

[17] Walker, Mateo, Olszewski, *et al.*, 2006, "Internal Kinematics of the Fornax Dwarf Spheroidal Galaxy," *The Astronomical Journal*, vol. 131, no. 4, http://stacks.iop.org/1538-3881/131/i=4/a=2114.

[18] Chiappo, Cohen-Tanugi, Conrad, *et al.*, 2017, "Dwarf Spheroidal J-factors Without Priors: A Likelihood-based Analysis for Indirect Dark Matter Searches," *Monthly Notices of the Royal Astronomical Society*, vol. 466, no. 1, http://dx.doi.org/10.1093/mnras/stw3079.

[19] Faber and Gallagher, 1979, "Masses and Mass-to-Light Ratios of Galaxies," *Annual Review of Astronomy and Astrophysics*, vol. 17, http://adsabs.harvard.edu/abs/1979ARA%26A..17..135F.

[20] Simon and Geha, 2007, "The Kinematics of the Ultra-Faint Milky Way Satellites: Solving the Missing Satellite Problem," *The Astrophysical Journal*, vol. 670, arxiv.org/abs/0706.0516.

[21] Mateo, 1998, "Dwarf Galaxies of the Local Group," *Annual Review of Astronomy and Astrophysics*, vol. 36, no. 1, https://doi.org/10.1146/annurev.astro.36.1.435.

[22] Penny, Conselice, De Rijcke, and Held, 2009, "Smooth, Undisturbed Dwarf Spheroidal Galaxies in the Perseus Cluster Core: Implications for Dark Matter Content," *Astronomische Nachrichten*, vol. 330, no. 9-10,

http://dx.doi.org/10.1002/asna.200911276.

[23] Cappellari *et al.*, 2006, "The SAURON Project-IV. The Mass-to-Light Ratio, the Virial Mass Estimator and the Fundamental Plane of Elliptical and Lenticular Galaxies," *Monthly Notices of the Royal Astronomical Society*, vol. 366, no. 4, http://mnras.oxfordjournals.org/content/366/4/1126.abstract.

[24] Sofue and Rubin, 2001, "Rotation Curves of Spiral Galaxies," *Annual Review of Astronomy and Astrophysics*, vol. 39, no. 1, https://doi.org/10.1146/annurev.astro.39.1.137.

[25] Bosma, 1978, *The Distribution and Kinematics of Neutral Hydrogen in Spiral Galaxies of Various Morphological Types*. Doctoral Thesis, http://ned.ipac.caltech.edu/level5/March05/Bosma/frames.html.

[26] Iocco, Pato, and Bertone, 2015, "Evidence for Dark Matter in the Inner Milky Way," *Nature Physics*, vol. 11, https://www.nature.com/articles/nphys3237.

[27] Corbelli and Salucci, 2000, "The Extended Rotation Curve and the Dark Matter Halo of M33," *Monthly Notices of the Royal Astronomical Society*, vol. 311, no. 2, + http://dx.doi.org/10.1046/j.1365-8711.2000.03075.x.

[28] Flynn, Holmberg, Portinari, Fuchs, and Jahreiß, 2006, "On the Mass-to-Light Ratio of the Local Galactic Disc and the Optical Luminosity of the Galaxy," *Monthly Notices of the Royal Astronomical Society*, vol. 372, no. 3, http://dx.doi.org/10.1111/j.1365-2966.2006.10911.x.

[29] Bartelmann and Schneider, 2001, "Weak Gravitational Lensing," *Physics Reports*, vol. 340, no. 4-5, http://www.sciencedirect.com/science/article/pii/S037015730000082X.

[30] Koopmans and Treu, 2003, "The Structure and Dynamics of Luminous and Dark Matter in the Early-Type Lens Galaxy of 0047–281 at z = 0.485," *The Astrophysical Journal*, vol. 583, no. 2, http://stacks.iop.org/0004-637X/583/i=2/a=606.

[31] Metcalf, Moustakas, Bunker, and Parry, 2004, "Spectroscopic Gravitational Lensing and Limits on the Dark Matter Substructure in Q2237+0305," *The Astrophysical Journal*, vol. 607, no. 1, http://stacks.iop.org/0004-637X/607/i=1/a=43.

[32] Girardi, Manzato, Mezzetti, Giuricin, and Limboz, 2002, "Observational Mass-to-Light Ratio of Galaxy Systems from Poor Groups to Rich Clusters," *The Astrophysical Journal*, vol. 569, no. 2, http://stacks.iop.org/0004-637X/569/i=2/a=720.

[33] Bergmann, Petrosian, and Lynds, 1990, "Gravitational Lens Models of Arcs in Clusters," *The Astrophysical Journal*, vol. 350, http://adsabs.harvard.edu/abs/1990ApJ...350...23B.

[34] "The Last of the Frontier Fields — Abell 370." Online, Accessed March 6, 2018,

https://www.spacetelescope.org/images/heic1711a/.

[35] Colley, Tyson, and Turner, 1996, "Unlensing Multiple Arcs in 0024+1654: Reconstruction of the Source Image," *The Astrophysical Journal Letters*, vol. 461, no. 2, http://stacks.iop.org/1538-4357/461/i=2/a=L83.

[36] Tyson, Kochanski, and Dell'Antonio, 1998, "Detailed Mass Map of CL 0024+1654 from Strong Lensing," *The Astrophysical Journal Letters*, vol. 498, no. 2, http://stacks.iop.org/1538-4357/498/i=2/a=L107.

[37] Umetsu, Medezinski, Broadhurst, *et al.*, 2010, "The Mass Structure of the Galaxy Cluster Cl0024+1654 from a Full Lensing Analysis of Joint Subaru and ACS/NIC3 Observations," *The Astrophysical Journal*, vol. 714, no. 2, http://stacks.iop.org/0004-637X/714/i=2/a=1470.

[38] Weisskopf, Brinkman, Canizares, *et al.*, 2002, "An Overview of the Performance and Scientific Results from the Chandra X-Ray Observatory," *Publications of the Astronomical Society of the Pacific*, vol. 114, no. 791, http://stacks.iop.org/1538-3873/114/i=791/a=1.

[39] Lewis, Buote, and Stocke, 2003, "Chandra Observations of A2029: The Dark Matter Profile Down to Below 0.01rvir in an Unusually Relaxed Cluster," *The Astrophysical Journal*, vol. 586, no. 1, http://stacks.iop.org/0004-637X/586/i=1/a=135.

[40] "1E 0657-56: NASA Finds Direct Proof of Dark Matter." Online, Accessed 2017-07-21, http://chandra.harvard.edu/photo/2006/1e0657/index.html.

[41] Markevitch, Gonzalez, Clowe, *et al.*, 2004, "Direct Constraints on the Dark Matter Self-Interaction Cross Section from the Merging Galaxy Cluster 1E 0657-56," *The Astrophysical Journal*, vol. 606, no. 2, http://stacks.iop.org/0004-637X/606/i=2/a=819.

[42] Markevitch, 2006, "Chandra Observation of the Most Interesting Cluster in the Universe," in *The X-ray Universe 2005* (Wilson, ed.), vol. 604 of *ESA Special Publication*, p. 723, http://adsabs.harvard.edu/abs/2006ESASP.604..723M.

[43] Clowe, Bradač, Gonzalez, *et al.*, 2006, "A Direct Empirical Proof of the Existence of Dark Matter," *The Astrophysical Journal Letters*, vol. 648, http://adsabs.harvard.edu/abs/2006ApJ...648L.109C.

[44] Clowe, Gonzalez, and Markevitch, 2004, "Weak-Lensing Mass Reconstruction of the Interacting Cluster 1E 0657-558: Direct Evidence for the Existence of Dark Matter," *The Astrophysical Journal*, vol. 604, no. 2, http://stacks.iop.org/0004-637X/604/i=2/a=596.

[45] Harvey, Massey, Kitching, Taylor, and Tittley, 2015, "The Nongravitational Interactions of Dark Matter in Colliding Galaxy Clusters," *Science*, vol. 347, no. 6229,

http://science.sciencemag.org/content/347/6229/1462.

[46] Guth, 1981, "Inflationary Universe: A Possible Solution to the Horizon and Flatness Problems," *Physical Review D*, vol. 23, https://link.aps.org/doi/10.1103/PhysRevD.23.347.

[47] Guth and Pi, 1982, "Fluctuations in the New Inflationary Universe," *Physical Review Letters*, vol. 49, https://link.aps.org/doi/10.1103/PhysRevLett.49.1110.

[48] Albrecht and Steinhardt, 1982, "Cosmology for Grand Unified Theories with Radiatively Induced Symmetry Breaking," *Physical Review Letters*, vol. 48, https://link.aps.org/doi/10.1103/PhysRevLett.48.1220.

[49] Arnison, Astbury, Aubert, *et al.*, 1983, "Experimental Observation of Lepton Pairs of Invariant Mass Around 95 GeV/c2 at the CERN SPS Collider," *Physics Letters B*, vol. 126, no. 5, http://www.sciencedirect.com/science/article/pii/0370269383901880.

[50] Affleck and Dine, 1985, "A New Mechanism for Baryogenesis," *Nuclear Physics B*, vol. 249, no. 2, http://www.sciencedirect.com/science/article/pii/0550321385900215.

[51] Cohen, Kaplan, and Nelson, 1993, "Progress in Electroweak Baryogenesis," *Annual Review of Nuclear and Particle Science*, vol. 43, no. 1, https://doi.org/10.1146/annurev.ns.43.120193.000331.

[52] Kolb and Turner, *The Early Universe*. Frontiers in Physics, Vol. 69, http://adsabs.harvard.edu/abs/1990eaun.book.....K.

[53] Hu, 2003, "CMB Temperature and Polarization Anisotropy Fundamentals," *Annals of Physics*, vol. 303, no. 1, http://www.sciencedirect.com/science/article/pii/S0003491602000222.

[54] de Bernardis, Ade, Bock, *et al.*, 2000, "A Flat Universe from High-Resolution Maps of the Cosmic Microwave Background Radiation," *Nature*, vol. 404, no. 6781,

[55] Mather, Cheng, Eplee Jr, *et al.*, 1990, "A Preliminary Measurement of the Cosmic Microwave Background Spectrum by the Cosmic Background Explorer (COBE) Satellite," *The Astrophysical Journal*, vol. 354,

[56] NASA/WMAP Science Team, "Nine Year Microwave Sky." Online, Accessed 2017-11-22, https://wmap.gsfc.nasa.gov/media/121238/index.html.

[57] Hinshaw, Larson, Komatsu, *et al.*, 2013, "Nine-year Wilkinson Microwave Anisotropy Probe (WMAP) Observations: Cosmological Parameter Results," *The Astrophysical Journal, Supplement Series*, vol. 208, no. 2, http://stacks.iop.org/0067-0049/208/i=2/a=19.

[58] Aghanim *et al.*, 2018, "Planck 2018 Results. VI. Cosmological Parameters," https://arxiv.org/abs/1807.06209.

[59] Planck Collaboration, Ade, P. A. R., Aghanim, N., *et al.*, 2014, "Planck 2013 Results. XVI. Cosmological Parameters," *Astronomy & Astrophysics*, vol. 571, https://doi.org/10.1051/0004-6361/201321591.

[60] Burles and Tytler, 1998, "The Deuterium Abundance Toward QSO 1009+2956," *The Astrophysical Journal*, vol. 507, no. 2, http://stacks.iop.org/0004-637X/507/i=2/a=732.

[61] Burles and Tytler, 1998, "The Deuterium Abundance Toward Q1937–1009," *The Astrophysical Journal*, vol. 499, no. 2, http://stacks.iop.org/0004-637X/499/i=2/a=699.

[62] Pettini, Zych, Murphy, Lewis, and Steidel, 2008, "Deuterium Abundance in the Most Metal-Poor Damped Lyman Alpha System: Converging on Ωb,0h2," *Monthly Notices of the Royal Astronomical Society*, vol. 391, no. 4, http://dx.doi.org/10.1111/j.1365-2966.2008.13921.x.

[63] Abazajian, Adelman-McCarthy, Agüeros, *et al.*, 2009, "The Seventh Data Release of the Sloan Digital Sky Survey," *The Astrophysical Journal, Supplement Series*, vol. 182, http://adsabs.harvard.edu/abs/2009ApJS..182..543A.

[64] Mann, *An Introduction to Particle Physics and the Standard Model*. Boca Raton, FL: CRC Press, 1st ed., http://inspirehep.net/record/846914.

[65] Jungman, Kamionkowski, and Griest, 1996, "Supersymmetric Dark Matter," *Physics Reports*, vol. 267, https://doi.org/10.1016/0370-1573(95)00058-5.

[66] Bond and Szalay, 1983, "The Collisionless Damping of Density Fluctuations in an Expanding Universe," *The Astrophysical Journal*, vol. 274, http://adsabs.harvard.edu/abs/1983ApJ...274..443B.

[67] Csáki, 1996, "The Minimal Supersymmetric Standard Model," *Modern Physics Letters A*, vol. 11, no. 08, http://www.worldscientific.com/doi/abs/10.1142/S021773239600062X.

[68] Chung, Everett, Kane, *et al.*, 2005, "The Soft Supersymmetry-Breaking Lagrangian: Theory and Applications," *Physics Reports*, vol. 407, no. 1, http://www.sciencedirect.com/science/article/pii/S0370157304004466.

[69] Schelke, 2004, *Supersymmetric Dark Matter: Aspects of sfermion Coannihilations*. Doctoral Thesis, http://urn.kb.se/resolve?urn=urn:nbn:se:su:diva-192.

[70] Feng, Matchev, and Wilczek, 2000, "Neutralino Dark Matter in Focus Point Supersymmetry," *Physics Letters B*, vol. 482, no. 4, http://www.sciencedirect.com/science/article/pii/S0370269300005128.

[71] Goldberg, 1983, "Constraint on the Photino Mass from Cosmology," *Physical Review Letters*, vol. 50, https://link.aps.org/doi/10.1103/PhysRevLett.50.1419.

[72] Ellis, Hagelin, Nanopoulos, Olive, and Srednicki, 1984, "Supersymmetric Relics from the Big Bang," *Nuclear Physics B*, vol. 238, no. 2, http://www.sciencedirect.com/science/article/pii/0550321384904619.

[73] Wells, 1998, "Mass Density of Neutralino Dark Matter," in *Perspectives on Supersymmetry* (Kane, ed.), vol. 18, p. 276, http://adsabs.harvard.edu/abs/1998pesu.conf..276W.

[74] Steigman, Dasgupta, and Beacom, 2012, "Precise Relic WIMP Abundance and Its Impact on Searches for Dark Matter Annihilation," *Physical Review D*, vol. 86, https://link.aps.org/doi/10.1103/PhysRevD.86.023506.

[75] Compton, 1923, "A Quantum Theory of the Scattering of X-rays by Light Elements," *Physical Review*, vol. 21, https://link.aps.org/doi/10.1103/PhysRev.21.483.

[76] Blumenthal and Gould, 1970, "Bremsstrahlung, Synchrotron Radiation, and Compton Scattering of High-Energy Electrons Traversing Dilute Gases," *Reviews of Modern Physics*, vol. 42, https://link.aps.org/doi/10.1103/RevModPhys.42.237.

[77] Rybicki and Lightman, *Radiative Processes in Astrophysics*. John Wiley & Sons, http://www.doi.org/10.1002/9783527618170.

[78] Aharonian, Akhperjanian, Anton, *et al.*, 2009, "Probing the ATIC Peak in the Cosmic-Ray Electron Spectrum with HESS," *Astronomy & Astrophysics*, vol. 508, no. 2, https://doi.org/10.1051/0004-6361/200913323.

[79] Abdo, Ackermann, Ajello, *et al.*, 2009, "Measurement of the Cosmic Ray $e^+ + e^-$ Spectrum from 20 GeV to 1 TeV with the Fermi Large Area Telescope," *Physical Review Letters*, vol. 102, https://link.aps.org/doi/10.1103/PhysRevLett.102.181101.

[80] Kerszberg, "The Cosmic-Ray Electron Spectrum Measured with H.E.S.S.." Talk presented at 35th ICRC in Busan, South Korea, 2017. https://indico.snu.ac.kr/indico/event/15/session/5/contribution/694/material/slides/0.pdf.

[81] Gaensler and Slane, 2006, "The Evolution and Structure of Pulsar Wind Nebulae," *Annual Review of Astronomy and Astrophysics*, vol. 44, no. 1, https://doi.org/10.1146/annurev.astro.44.051905.092528.

[82] Maus, Macmillan, McLean, *et al.*, 2010, "The US/UK World Magnetic Model for 2010-2015," http://nora.nerc.ac.uk/id/eprint/18737.

[83] Paul N. Arendt and Eilek, 2002, "Pair Creation in the Pulsar Magnetosphere," *The Astrophysical Journal*, vol. 581, no. 1, http://stacks.iop.org/0004-637X/581/i=1/a=451.

[84] Erber, 1966, "High-Energy Electromagnetic Conversion Processes in Intense Magnetic Fields," *Review of Modern Physics*, vol. 38, https://link.aps.org/doi/10.1103/RevModPhys.38.626.

[85] Cerutti, Uzdensky, and Begelman, 2012, "Extreme Particle Acceleration in Magnetic Reconnection Layers: Application to the Gamma-Ray Flares in the Crab Nebula," *The Astrophysical Journal*, vol. 746, no. 2, http://doi.org/10.1088/0004-637X/746/2/148.

[86] Schopper, Birk, and Lesch, 1999, "Particle Acceleration in Three-Dimensional Reconnection Regions: A New Test Particle Approach," *Physics of Plasmas*, vol. 6, no. 11, https://doi.org/10.1063/1.873696.

[87] Zweibel and Yamada, 2009, "Magnetic Reconnection in Astrophysical and Laboratory Plasmas," *Annual Review of Astronomy and Astrophysics*, vol. 47, no. 1, https://doi.org/10.1146/annurev-astro-082708-101726.

[88] Rees and Gunn, 1974, "The Origin of the Magnetic Field and Relativistic Particles in the Crab Nebula," *Monthly Notices of the Royal Astronomical Society*, vol. 167, no. 1, https://doi.org/10.1093/mnras/167.1.1.

[89] Aharonian, F., Akhperjanian, A. G., Aye, K.-M., *et al.*, 2005, "Discovery of Extended VHE Gamma-Ray Emission from the Asymmetric Pulsar Wind Nebula in MSH 15-52with HESS," *Astronomy & Astrophysics*, vol. 435, no. 1, https://doi.org/10.1051/0004-6361:200500105.

[90] Sironi and Spitkovsky, 2011, "Particle Acceleration in Relativistic Magnetized Collisionless Electron-Ion Shocks," *The Astrophysical Journal*, vol. 726, no. 2, http://stacks.iop.org/0004-637X/726/i=2/a=75.

[91] Sironi and Spitkovsky, 2014, "Relativistic Reconnection: An Efficient Source of Non-thermal Particles," *The Astrophysical Journal Letters*, vol. 783, no. 1, http://stacks.iop.org/2041-8205/783/i=1/a=L21.

[92] de Gouveia Dal Pino and Kowal, *Particle Acceleration by Magnetic Reconnection*, pp. 373–398. Berlin, Heidelberg: Springer Berlin Heidelberg, https://doi.org/10.1007/978-3-662-44625-6_13.

[93] Fermi, 1949, "On the Origin of the Cosmic Radiation," *Physical Review*, vol. 75, https://link.aps.org/doi/10.1103/PhysRev.75.1169.

[94] Aharonian, Akhperjanian, Aye, *et al.*, 2004, "High-Energy Particle Acceleration in the Shell of a Supernova Remnant," *Nature*, vol. 432, no. 7013, dx.doi.org/10.1038/nature02960.

[95] Krymskii, 1977, "A Regular Mechanism for the Acceleration of Charged Particles on the

Front of a Shock Wave," *Akademiia Nauk SSSR Doklady*, vol. 234, http://adsabs.harvard.edu/abs/1977DoSSR.234.1306K.

[96] Axford, Leer, and Skadron, 1977, "The Acceleration of Cosmic Rays by Shock Waves," *International Cosmic Ray Conference*, vol. 11, http://adsabs.harvard.edu/abs/1977ICRC...11..132A.

[97] Bell, 1978, "The Acceleration of Cosmic Rays in Shock Fronts – I," *Monthly Notices of the Royal Astronomical Society*, vol. 182, no. 2, http://dx.doi.org/10.1093/mnras/182.2.147.

[98] Blandford and Ostriker, 1978, "Particle Acceleration by Astrophysical Shocks," *The Astrophysical Journal*, vol. 221, http://adsabs.harvard.edu/abs/1978ApJ...221L..29B.

[99] Drury, 1983, "An Introduction to the Theory of Diffusive Shock Acceleration of Energetic Particles in Tenuous Plasmas," *Reports on Progress in Physics*, vol. 46, no. 8, http://stacks.iop.org/0034-4885/46/i=8/a=002.

[100] Alfvén, 1977, "Electric Currents in Cosmic Plasmas," *Reviews of Geophysics*, vol. 15, no. 3, https://agupubs.onlinelibrary.wiley.com/doi/abs/10.1029/RG015i003p00271.

[101] Blackman, 2013, "On Deriving Flux Freezing in Magnetohydrodynamics by Direct Differentiation," *European Journal of Physics*, vol. 34, no. 2, http://stacks.iop.org/0143-0807/34/i=2/a=489.

[102] Tomassetti, 2012, "Origin of the Cosmic-Ray Spectral Hardening," *The Astrophysical Journal Letters*, vol. 752, no. 1, http://stacks.iop.org/2041-8205/752/i=1/a=L13.

[103] Gabici, "The Theory of Diffusive Shock Acceleration, ISAPP 2012." https://isapp2012paris.sciencesconf.org/conference/isapp2012paris/Stefano_Gabici_three.pdf.

[104] Tavecchio, Maraschi, and Ghisellini, 1998, "Constraints on the Physical Parameters of TeV Blazars," *The Astrophysical Journal*, vol. 509, no. 2, http://stacks.iop.org/0004-637X/509/i=2/a=608.

[105] Enomoto, Tanimori, Naito, *et al.*, 2002, "The Acceleration of Cosmic-Ray Protons in the Supernova Remnant RX J1713. 7–3946," *Nature*, vol. 416, no. 6883, https://www.nature.com/articles/416823a.

[106] Pohl and Schlickeiser, 2000, "On the Conversion of Blast Wave Energy into Radiation in Active Galactic Nuclei and Gamma-ray Bursts," vol. 354, https://arxiv.org/abs/astro-ph/9911452.

[107] Dar and Laor, 1997, "Hadronic Production of TeV Gamma-Ray Flares from Blazars," *The Astrophysical Journal Letters*, vol. 478, no. 1, http://stacks.iop.org/1538-4357/478/i=1/a=L5.

[108] Stallwood, Sutton, Fields, Fox, and Kane, 1958, "Neutral Pions from Proton-Proton Collisions," *Physical Review*, vol. 109, https://link.aps.org/doi/10.1103/PhysRev.109.1716.

[109] Tuneyoshi Kamae and Niklas Karlsson and Tsunefumi Mizuno and Toshinori Abe and Tatsumi Koi, 2006, "Parameterization of γ, epm, and Neutrino Spectra Produced by p-p Interaction in Astronomical Environments," *The Astrophysical Journal*, vol. 647, no. 1, http://stacks.iop.org/0004-637X/647/i=1/a=692.

[110] Dermer, 1986, "Secondary Production of Neutral Pi-Mesons and the Diffuse Galactic Gamma Radiation," *Astronomy & Astrophysics*, vol. 157, http://adsabs.harvard.edu/abs/1986A

[111] Patrignani *et al.*, 2016 and 2017 update, "Particle Data Group," *Chinese Physics C*, vol. 40, http://pdg.lbl.gov/2017/listings/rpp2017-list-pi-zero.pdf.

[112] Strong, Moskalenko, and Reimer, 2004, "Diffuse Galactic Continuum Gamma Rays: A Model Compatible with EGRET Data and Cosmic-Ray Measurements," *The Astrophysical Journal*, vol. 613, no. 2, http://stacks.iop.org/0004-637X/613/i=2/a=962.

[113] Abraham, Abreu, Aglietta, *et al.*, 2007, "Correlation of the Highest-Energy Cosmic Rays with Nearby Extragalactic Objects," *Science*, vol. 318, no. 5852, http://science.sciencemag.org/content/318/5852/938.

[114] Akerib, Araújo, Bai, *et al.*, 2014, "First Results from the LUX Dark Matter Experiment at the Sanford Underground Research Facility," *Physical Review Letters*, vol. 112, https://link.aps.org/doi/10.1103/PhysRevLett.112.091303.

[115] Aprile, Aalbers, Agostini, *et al.*, 2017, "First Dark Matter Search Results from the XENON1T Experiment," *Physical Review Letters*, vol. 119, https://link.aps.org/doi/10.1103/PhysRevLett.119.181301.

[116] Collaboration *et al.*, 2010, "Dark Matter Search Results from the CDMS II Experiment," *Science*, vol. 327, no. 5973, http://science.sciencemag.org/content/327/5973/1619.

[117] Bernabei, Belli, Cappella, *et al.*, 2004, "Dark Matter Particles in the Galactic Halo: Results and Implications from DAMA/NaI," *International Journal of Modern Physics D*, vol. 13, no. 10, https://www.worldscientific.com/doi/abs/10.1142/S0218271804006619.

[118] Undagoitia and Rauch, 2016, "Dark Matter Direct-Detection Experiments," *Journal of Physics G: Nuclear and Particle Physics*, vol. 43, no. 1, http://stacks.iop.org/0954-3899/43/i=1/a=013001.

[119] Aharonian, F., Akhperjanian, A. G., Aye, K.-M., *et al.*, 2004, "Very High Energy Gamma Rays from the Direction of Sagittarius A*," *Astronomy & Astrophysics*, vol. 425,

no. 1, https://doi.org/10.1051/0004-6361:200400055.

[120] van Eldik, 2008, "The H.E.S.S. View of the Galactic Centre Region," *Nuclear Instruments and Methods in Physics Research Section A: Accelerators, Spectrometers, Detectors and Associated Equipment*, vol. 588, no. 1, pp. 72 – 75. http://www.sciencedirect.com/science/article/pii/S0168900208000429.

[121] Kosack, Badran, Bond, *et al.*, 2004, "TeV Gamma-Ray Observations of the Galactic Center," *The Astrophysical Journal Letters*, vol. 608, no. 2, http://stacks.iop.org/1538-4357/608/i=2/a=L97.

[122] Albert, Aliu, Anderhub, *et al.*, 2006, "Observation of Gamma Rays from the Galactic Center with the MAGIC Telescope," *The Astrophysical Journal Letters*, vol. 638, no. 2, http://stacks.iop.org/1538-4357/638/i=2/a=L101.

[123] H.E.S.S. Collaboration, Abdalla, H., Abramowski, A., *et al.*, 2018, "The H.E.S.S. Galactic Plane Survey," *A&A*, vol. 612, https://doi.org/10.1051/0004-6361/201732098.

[124] Archer, Benbow, Bird, *et al.*, 2016, "TeV Gamma-Ray Observations of the Galactic Center Ridge by VERITAS," *The Astrophysical Journal*, vol. 821, no. 2, http://stacks.iop.org/0004-637X/821/i=2/a=129.

[125] Belikov, Zaharijas, and Silk, 2012, "Study of the Gamma-ray Spectrum from the Galactic Center in view of Multi-TeV Dark Matter Candidates," *Physical Review D*, vol. 86, https://doi.org/10.1103/PhysRevD.86.083516.

[126] Cembranos, Gammaldi, and Maroto, Nov 2012, "Possible Dark Matter Origin of the Gamma Ray Emission from the Galactic Center Observed by HESS," *Physical Review D*, vol. 86, https://link.aps.org/doi/10.1103/PhysRevD.86.103506.

[127] HESS Collaboration, 2016, "Acceleration of Petaelectronvolt Protons in the Galactic Centre," *Nature*, vol. 531, https://www.nature.com/articles/nature17147.

[128] Hooper, Cholis, and Linden, 2018, "TeV Gamma Rays From Galactic Center Pulsars," *Physics of the Dark Universe*, vol. 21, https://doi.org/10.1016/j.dark.2018.05.004.

[129] Kistler, 2015, "A Tale of Two Pulsars and the Origin of TeV Gamma Rays from the Galactic Center," http://adsabs.harvard.edu/abs/2015arXiv151101159K.

[130] Hooper and Linden, 2011, "Origin of the Gamma Rays from the Galactic Center," *Physical Review D*, vol. 84, https://link.aps.org/doi/10.1103/PhysRevD.84.123005.

[131] Gordon and Macías, 2013, "Dark Matter and Pulsar Model Constraints from Galactic Center Fermi-LAT Gamma-Ray Observations," *Physical Review D*, vol. 88, https://link.aps.org/doi/10.1103/PhysRevD.88.083521.

[132] Hooper, "The Galactic Center Gamma-Ray Excess and its Interpretations." Online, TeVPA 2018, Accessed 2019-03-09, https://indico.desy.de/indico/event/18204/session/12/contribution/132.

[133] Bloemen, 1989, "Diffuse Galactic Gamma-Ray Emission," *Annual Review of Astronomy and Astrophysics*, vol. 27, no. 1, https://doi.org/10.1146/annurev.aa.27.090189.002345.

[134] Yoast-Hull, Gallagher, and Zweibel, jul 2014, "The Cosmic-Ray Population of the Galactic Central Molecular Zone," *The Astrophysical Journal*, vol. 790, https://doi.org/10.1088

[135] Abramowski, Aharonian, Ait Benkhali, *et al.*, 2014, "Diffuse Galactic Gamma-Ray Emission with H.E.S.S.," *Physical Review D*, vol. 90, https://link.aps.org/doi/10.1103/PhysRevD.90.122007.

[136] Tanabashi, Hagiwara, Hikasa, *et al.*, 2018, "Review of Particle Physics," *Physical Review D*, vol. 98, https://link.aps.org/doi/10.1103/PhysRevD.98.030001.

[137] Bonnivard, Hütten, Nezri, *et al.*, 2016, "CLUMPY: Jeans Analysis, γ-ray and ν Fluxes from Dark Matter (Sub-)Structures," *Computer Physics Communications*, vol. 200, no. Supplement C, http://www.sciencedirect.com/science/article/pii/S0010465515004348.

[138] Cirelli, Corcella, Hektor, *et al.*, 2011, "PPPC 4 DM ID: a Poor Particle Physicist Cookbook for Dark Matter Indirect Detection," *Journal of Cosmology and Astroparticle Physics*, vol. 2011, no. 3, http://stacks.iop.org/1475-7516/2011/i=03/a=051.

[139] Ciafaloni, Comelli, Riotto, *et al.*, 2011, "Weak Corrections Are Relevant for Dark Matter Indirect Detection," *Journal of Cosmology and Astroparticle Physics*, vol. 2011, no. 03, http://stacks.iop.org/1475-7516/2011/i=03/a=019.

[140] Sjöstrand, Mrenna, and Skands, 2008, "A Brief Introduction to PYTHIA 8.1," *Computer Physics Communications*, vol. 178, no. 11, http://www.sciencedirect.com/science/article/pii/S0010465508000441.

[141] Corcella, Knowles, Marchesini, *et al.*, 2001, "HERWIG 6: an Event Generator for Hadron Emission Reactions with Interfering Gluons (Including Supersymmetric Processes)," *Journal of High Energy Physics*, vol. 2001, no. 01, http://stacks.iop.org/1126-6708/2001/i=01/a=010.

[142] Bonnivard, Maurin, and Walker, 2016, "Contamination of Stellar-Kinematic Samples and Uncertainty About Dark Matter Annihilation Profiles in Ultrafaint Dwarf Galaxies: the Example of Segue I," *Monthly Notices of the Royal Astronomical Society*, vol. 462, no. 1, http://dx.doi.org/10.1093/mnras/stw1691.

[143] Springel *et al.*, 2008, "The Aquarius Project: The Subhaloes of Galactic Haloes," *Monthly Notices of the Royal Astronomical Society*, vol. 391, http://mnras.oxfordjournals.org/content/391/4/1685.full.pdf.

[144] Einasto, 1965, "Kinematics and Dynamics of Stellar Systems," *Trudy Institute Alma-Ata Conference*, vol. 5, p. 87.

[145] Navarro, Ludlow, Springel, *et al.*, 2010, "The Diversity and Similarity of Simulated Cold Dark Matter Haloes," *Monthly Notices of the Royal Astronomical Society*, vol. 402, no. 1, http://dx.doi.org/10.1111/j.1365-2966.2009.15878.x.

[146] Reid, 1993, "The Distance to the Center of the Galaxy," *Annual Review of Astronomy and Astrophysics*, vol. 31, no. 1, https://doi.org/10.1146/annurev.aa.31.090193.002021.

[147] Eisenhauer, Schödel, Genzel, *et al.*, 2003, "A Geometric Determination of the Distance to the Galactic Center," *The Astrophysical Journal Letters*, vol. 597, no. 2, http://stacks.iop.org/1538-4357/597/i=2/a=L121.

[148] Horrobin, Eisenhauer, Tecza, *et al.*, 2004, "First Results from SPIFFI. I: The Galactic Center," *Astronomische Nachrichten*, vol. 325, no. 2, http://dx.doi.org/10.1002/asna.200310181.

[149] Catena and Ullio, 2010, "A Novel Determination of the Local Dark Matter Density," *Journal of Cosmology and Astroparticle Physics*, vol. 2010, no. 08, http://stacks.iop.org/1475-7516/2010/i=08/a=004.

[150] Csáki, 1996, "The Minimal Supersymmetric Standard Model," *Modern Physics Letters A*, vol. 11, no. 08, http://www.worldscientific.com/doi/abs/10.1142/S021773239600062X.

[151] Flores and Primack, 1994, "Observational and Theoretical Constraints on Singular Dark Matter Halos," *The Astrophysical Journal*, vol. 427, http://adsabs.harvard.edu/abs/1994ApJ...427L...1F.

[152] Hui, 2001, "Unitarity Bounds and the Cuspy Halo Problem," *Physical Review Letters*, vol. 86, https://link.aps.org/doi/10.1103/PhysRevLett.86.3467.

[153] Macciò, Stinson, Brook, *et al.*, 2012, "Halo Expansion in Cosmological Hydro Simulations: Toward a Baryonic Solution of the Cusp/Core Problem in Massive Spirals," *The Astrophysical Journal Letters*, vol. 744, no. 1, http://stacks.iop.org/2041-8205/744/i=1/a=L9.

[154] Ogiya and Mori, 2014, "The Core-Cusp Problem in Cold Dark Matter Halos and Supernova Feedback: Effects of Oscillation," *The Astrophysical Journal*, vol. 793, no. 1, http://stacks.iop.org/0004-637X/793/i=1/a=46.

[155] Kamionkowski and Kinkhabwala, 1998, "Galactic Halo Models and Particle Dark-Matter

Detection," *Physical Review D*, vol. 57, https://link.aps.org/doi/10.1103/PhysRevD.57.3256.

[156] Blaauw, Gum, Pawsey, and Westerhout, 1960, "The new iau system of galactic coordinates (1958 revision)," *Monthly Notices of the Royal Astronomical Society*, vol. 121, no. 2, https://doi.org/10.1093/mnras/121.2.123.

[157] Feng, Kaplinghat, and Yu, 2010, "Sommerfeld Enhancements for Thermal Relic Dark Matter," *Physical Review D*, vol. 82, https://link.aps.org/doi/10.1103/PhysRevD.82.083525.

[158] Cherenkov, 1934, "Visible Emission of Clean Liquids by Action of γ Radiation," *Doklady Akademii Nauk SSSR*, vol. 2,

[159] Voelk and Bernloehr, 2009, "Imaging Very High Energy Gamma-Ray Telescopes," *Experimental Astronomy*, vol. 25, http://inspirehep.net/record/810115/.

[160] Frank and Tamm, 1937, "Coherent Visible Radiation of Fast Electrons Passing Through Matter," *Comptes Rendus de l'Académie des Sciences de l'URSS*, vol. 14, no. 3, pp. 109–114. http://dx.doi.org/10.1007/978-3-642-74626-0_2.

[161] Frank, 1984, "A Conceptual History of the Vavilov-Cherenkov Radiation," *Soviet Physics Uspekhi*, vol. 27, no. 5, http://stacks.iop.org/0038-5670/27/i=5/a=A04.

[162] Argonne National Laboratory, "Advanced Test Reactor Core, Idaho National Laboratory." Online, Accessed Decenber 11, 2013, https://www.flickr.com/photos/35734278@N05/3954062594.

[163] Chang and Ryskamp, 2000, "Depletion Analysis of Mixed-Oxide Fuel Pins in Light Water Reactors and the Advanced Test Reactor," *Nuclear Technology*, vol. 129, no. 3, https://doi.org/10.13182/NT00-A3065.

[164] Bethe and Heitler, 1934, "On the Stopping of Fast Particles and on the Creation of Positive Electrons," *Proceedings of the Royal Society of London A: Mathematical, Physical and Engineering Sciences*, vol. 146, no. 856, http://rspa.royalsocietypublishing.org/content/146/856/83.

[165] Klein, 1999, "Suppression of Bremsstrahlung and Pair Production Due to Environmental Factors," *Review of Modern Physics*, vol. 71, https://link.aps.org/doi/10.1103/RevModPhys.71.1501.

[166] Berger and Seltzer, 1964, "10. Tables of Energy-Losses and Ranges of Electrons and Positrons," *Studies in penetration of charged particles in matter*, no. 39,

[167] Olive *et al.*, 2014, "Review of Particle Physics," *Chinese Physics*, vol. C38, http://doi.org/10.1088/1674-1137/38/9/090001.

[168] Bernlöhr, 2008, "Simulation of Imaging Atmospheric Cherenkov Telescopes with CORSIKA and sim_telarray," *Astroparticle Physics*, vol. 30, no. 3, http://www.sciencedirect.com/science/article/pii/S0927650508000972.

[169] Holder, Acciari, Aliu, *et al.*, 2008, "Status of the VERITAS Observatory," in *AIP Conference Proceedings*, vol. 1085, pp. 657–660, AIP, https://doi.org/10.1063/1.3076760.

[170] Grube, Pandel, Gall, *et al.*, "VERITAS Pointing Monitor (VPM)." Internal VERITAS Memo, https://veritas.sao.arizona.edu/wiki/index.php/VERITAS_Memos.

[171] Davies, Cotton, 1957, "Design of the Quartermaster Solar Furnace," *Solar Energy*, vol. 1, http://www.sciencedirect.com/science/article/pii/0038092X57901160.

[172] Holder *et al.*, 2006, "The First VERITAS Telescope," *Astroparticle Physics*, vol. 25, no. 6, http://www.sciencedirect.com/science/article/pii/S092765050600051X.

[173] Roache, Irvin, Perkins, *et al.*, 2008, "Mirror Facets for the VERITAS Telescopes," *International Cosmic Ray Conference*, vol. 3, http://adsabs.harvard.edu/abs/2008ICRC....3.1397R.

[174] McCann, Hanna, Kildea, McCutcheon, 2009, "A New Mirror Alignment System for the VERITAS Telescopes," *Astroparticle Physics*, vol. 32, http://www.sciencedirect.com/science/article/pii/S0927650509001455.

[175] Lewis, 1990, "Optical characteristics of the whipple observatory tev gamma-ray imaging telescope," *Experimental Astronomy*, vol. 1, no. 4, https://doi.org/10.1007/BF00428516.

[176] Winston, 1970, "Light Collection Within the Framework of Geometrical Optics," *The Journal of the Optical Society of America*, vol. 60, no. 2, http://www.osapublishing.org/abstract.cfm?URI=josa-60-2-245.

[177] Otte, Gebremedhin, Kaplan, and Long, 2011, "The Upgrade of VERITAS with High Efficiency Photomultipliers," in *Proceedings, 32nd International Cosmic Ray Conference (ICRC 2011)*, vol. 9, p. 247, http://inspirehep.net/record/940820/files/arXiv:1110.4702.pdf.

[178] Weekes, Badran, Biller, *et al.*, 2002, "VERITAS: the Very Energetic Radiation Imaging Telescope Array System," *Astroparticle Physics*, vol. 17, no. 2, http://www.sciencedirect.com/science/article/pii/S0927650501001529.

[179] Hall, Vassiliev, Kieda, *et al.*, 2003, "Veritas CFDs," *International Cosmic Ray Conference*, vol. 5, http://adsabs.harvard.edu/abs/2003ICRC....5.2851H.

[180] Wikipedia, "Operation of a CFD." Online, Accessed 2018-01-02, https://en.wikipedia.org/wiki/File:Operation_of_a_CFD.png.

[181] Rebillot, Buckley, Dowkontt, and Kosack, 2003, "The VERITAS Flash ADC Electronics System," *International Cosmic Ray Conference*, vol. 5, http://adsabs.harvard.edu/abs/2003ICRC....5.2827B.

[182] Hanna, 2008, "Calibration of the VERITAS Gamma-ray Telescopes," in *Proceedings, 30th International Cosmic Ray Conference, Merida, Mexico*, http://indico.nucleares.unam.mx/event/4/contribution/702.

[183] Zitzer, Anderson, Byrum, *et al.*, 2012, "The Topological Trigger System for the VERITAS Upgrade," in *2012 IEEE Nuclear Science Symposium and Medical Imaging Conference Record (NSS/MIC)*, pp. 1812–1816, https://ieeexplore.ieee.org/document/6551423/.

[184] Perkens and Maier, 2009, "VERITAS Telescope 1 Relocation: Details and Improvements," http://arxiv.org/abs/0912.3841.

[185] Holder, 2005, "Exploiting VERITAS Timing Information," in *29th International Cosmic Ray Conference (ICRC 2005), Pune, India, August 3-11, 2005*, p. 383, 2005. https://arxiv.org/abs/astro-ph/0507450.

[186] Hillas, 1985, "Cerenkov Light Images of EAS Produced by Primary Gamma Rays and by Nuclei," in *Proceedings, 19th International Cosmic Ray Conference (ICRC 1985 La Jolla)*, vol. 3, p. 445, https://ntrs.nasa.gov/search.jsp?R=19850026666.

[187] Şentürk, 2011, "The Disp Method for Analysing Large Zenith Angle Gamma-Ray Data," in *Proceedings, 32nd International Cosmic Ray Conference (ICRC 2011)*, vol. 9, p. 127, 2011. http://inspirehep.net/record/929899/files/arXiv:1109.6044.pdf.

[188] Beilicke, 2012, "The Galactic Center Region Imaged by VERITAS," *Nuclear Instruments and Methods in Physics Research Section A*, vol. 692, pp. 208–211. http://www.sciencedirect.com/science/article/pii/S016890021200085X.

[189] Krawczynski, Carter-Lewis, Duke, *et al.*, 2006, "Gamma–Hadron Separation Methods for the VERITAS Array of Four Imaging Atmospheric Cherenkov Telescopes," *Astroparticle Physics*, vol. 25, no. 6, http://www.sciencedirect.com/science/article/pii/S0927650506000466.

[190] Krause, 2017, *High-sensitivity analysis of the Cygnus region observed with VERITAS*. PhD thesis, http://dx.doi.org/10.18452/17750.

[191] Knödlseder, Mayer, Deil, *et al.*, 2016, "GammaLib and ctools - A Software Framework for the Analysis of Astronomical Gamma-Ray Data," *Astronomy & Astrophysics*, vol. 593, https://doi.org/10.1051/0004-6361/201628822.

[192] Heck, Knapp, Capdevielle, Schatz, and Thouw, *CORSIKA: a Monte Carlo Code to*

Simulate Extensive Air Showers. http://adsabs.harvard.edu/abs/1998cmcc.book.....H.

[193] King, 1962, "The Structure of Star Clusters. I. an Empirical Density Law," *The Astronomical Journal*, vol. 67, http://adsabs.harvard.edu/abs/1962AJ.....67..471K.

[194] Mayer, 2015, *Pulsar Wind Nebulae at High Energies.* Doctoral Thesis, https://publishup.uni-potsdam.de/frontdoor/index/index/docId/7150.

[195] Bird, 2015, *Probing Cosmic Rays with VERITAS: Observations of M 31 and the Positron Fraction.* Doctoral Thesis, https://veritas.sao.arizona.edu/documents/Theses/RBirdThesis.pdf.

[196] Marquardt, 1963, "An Algorithm for Least-Squares Estimation of Nonlinear Parameters," *Journal of the Society for Industrial and Applied Mathematics*, vol. 11, no. 2, https://doi.org/10.1137/0111030.

[197] Wilks, 1938, "The Large-Sample Distribution of the Likelihood Ratio for Testing Composite Hypotheses," *The Annals of Mathematical Statistics*, vol. 9, no. 1, https://doi.org/10.1214/aoms/1177732360.

[198] Aharonian *et al.*, 2006, "Observations of the Crab Nebula with H.E.S.S," *Astronomy & Astrophysics*, vol. 457, www.doi.org/10.1051/0004-6361:20065351.

[199] Meagher, 2016, "Six Years of VERITAS Observations of the Crab Nebula," *Proceedings of Science*, vol. ICRC2015, https://arxiv.org/abs/1508.06442.

[200] Aleksić *et al.*, 2016, "The Major Upgrade of the MAGIC Telescopes, Part II: A Performance Study Using Observations of the Crab Nebula," *Astroparticle Physics*, vol. 72, http://inspirehep.net/record/1318574/.

[201] Maxwell, 2011, "Chi-square Intervals for a Poisson Parameter - Bayes, Classical and Structural," http://adsabs.harvard.edu/abs/2011arXiv1102.0822M.

[202] Delahaye, T., Fiasson, A., Pohl, M., and Salati, P., 2011, "The GeV-TeV Galactic Gamma-Ray Diffuse Emission - I. Uncertainties in the Predictions of the Hadronic Component," *Astronomy & Astrophysics*, vol. 531, https://doi.org/10.1051/0004-6361/201116647.

[203] Cash, 1979, "Parameter estimation in astronomy through application of the likelihood ratio," *The Astrophysical Journal*, vol. 228, http://adsabs.harvard.edu/abs/1979ApJ...228..939C.

[204] Archambault *et al.*, 2017, "Dark Matter Constraints from a Joint Analysis of Dwarf Spheroidal Galaxy Observations with VERITAS," *Physical Review*, vol. D95, no. 8, https://link.aps.org/doi/10.1103/PhysRevD.95.082001.

[205] Abdallah, Abramowski, Aharonian, *et al.*, 2016, "Search for Dark Matter Annihilations Towards the Inner Galactic Halo from 10 Years of Observations with H.E.S.S.," *Physical Review Letters*, vol. 117, https://link.aps.org/doi/10.1103/PhysRevLett.117.111301.

[206] Ahnen, Ansoldi, Antonelli, *et al.*, 2016, "Limits to Dark Matter Annihilation Cross-Section from a Combined Analysis of MAGIC and Fermi-LAT Observations of Dwarf Satellite Galaxies," *Journal of Cosmology and Astroparticle Physics*, vol. 2016, no. 02, http://stacks.iop.org/1475-7516/2016/i=02/a=039.

[207] Albert, Alfaro, Alvarez, *et al.*, 2018, "Dark Matter Limits from Dwarf Spheroidal Galaxies with the HAWC Gamma-Ray Observatory," *The Astrophysical Journal*, vol. 853, no. 2, http://stacks.iop.org/0004-637X/853/i=2/a=154.

[208] ESA, ed., *The HIPPARCOS and TYCHO Catalogues. Astrometric and Photometric Star Catalogues Derived from the ESA HIPPARCOS Space Astrometry Mission*, vol. 1200 of *ESA Special Publication*, 1997.

[209] Petrović, Serpico, and Zaharijas, 2015, "Millisecond Pulsars and the Galactic Center Gamma-ray Excess: the Importance of Luminosity Function and Secondary Emission," *Journal of Cosmology and Astroparticle Physics*, vol. 2015, no. 02, http://stacks.iop.org/1475-7516/2015/i=02/a=023.

[210] Lee, Lisanti, Safdi, Slatyer, and Xue, 2016, "Evidence for Unresolved γ-Ray Point Sources in the Inner Galaxy," *Physcal Review Letters*, vol. 116, https://link.aps.org/doi/10.1103/PhysRevLett.116.051103.

[211] Bartels, Krishnamurthy, and Weniger, 2016, "Strong Support for the Millisecond Pulsar Origin of the Galactic Center GeV Excess," *Physical Review Letters*, vol. 116, https://link.aps.org/doi/10.1103/PhysRevLett.116.051102.

[212] Daylan, Finkbeiner, Hooper, *et al.*, 2016, "The Characterization of the Gamma-Ray Signal from the Central Milky Way: A Case for Annihilating Dark Matter," *Physics of the Dark Universe*, vol. 12, http://www.sciencedirect.com/science/article/pii/S2212686416000030.

[213] Calore, Cholis, McCabe, and Weniger, 2015, "A Tale of Tails: Dark Matter Interpretations of the Fermi GeV Excess in Light of Background Model Systematics," *Physical Review D*, vol. 91, https://link.aps.org/doi/10.1103/PhysRevD.91.063003.

Appendix A

Cross Section Upper Limits

WIMP Mass	Cross Section
TeV	$\frac{\text{cm}^3}{s}$
4.250	4.347e-24
6.500	2.420e-24
10.000	1.628e-24
14.300	1.177e-24
20.512	8.795e-25
30.400	7.042e-25
45.000	6.370e-25
66.500	6.559e-25
98.000	7.627e-25

Table A.1: Mass and cross section upper limit values for Figure 6.23. Values calculated for the $b\bar{b}$ channel, using an Einasto cuspy dark matter halo and only with events with reconstructed energies between 4–70 TeV.

Appendix B

VERITAS Data Run Numbers

B.1 Crab Nebula Run Numbers

55043 55676 55677 55701 55702 55718 55746 55773 55774 55802 55932 55933 55998 55999 56226 56233 59955 59958 60165 60166 60167 61265 61293 61434 61965 65457 65555 65587 66870 66905 67142 67604 67626 67648 69974 70369 70428 70453 75815 75865 76139 76445 76898 80333 81069 81286 81337 81395 81417 81434 83525 83566

B.2 Sgr A* Run Numbers

50991 50992 50993 51016 51017 51018 51020 51064 51065 51125 51312 51313 51314 51315 51340 51341 51342 51404 51406 51427 51429 51430 51431 51454 51455 51544 51545 51561 51562 51648 51649 51684 51685 51705 51706 51726 51727 51745 51746 51748 51767 51768 51788 51789 51806 56431 56433 56434 56495 56497 56498 56499 56521 56544 56546 56599 56600 56618 56619 56620 56621 56649 56662 56696 56697 56827 56851 56852 56893 56894 56895 56917 56918 56919 57295 57296 57309 57310 57311 57327 57328 57329 57351 57352 57353 57373 57374 57376 57395 57396 57397 57398 57399 57439 57440 57441 61960 61961 61962 61963 62043 62044 62047 62048 62079 62080 62081 62084 62108 62111 62135 62138 62139 62141 62163 62184 62185 62186 62250 62251 62252 62253 62271 62272 62274 62296 62297 62319 62320 62339 62340 62341 62360 62361 62566 62567 62568 62569 62592 62593 62594 62595 62620 62621 62622 62623 62642 62643 62644 62645 62668 62669 62670 62671 62987 68348 68619 68620 68622 68623 68647 68648 68666 68667 68668 68669 68670 68684 68685 68686 68687 68727 68728 68741 68742 68765 68766 68784 68785 68801 68815 68942 69007 69020 69034 69066 69067 69085 69098 69121 69122 69134 69135 69136 69137 69138 69139 69151 69152 69153 69166 69167 69168 69185 69186 69201 69363 69365 72729 72754 72796 72845 72868 72869 72921 72969 72970 72986 72987 73140 73141 73191 73192 73211 73212 73232 73233 73253 73298 73299 73315 73316 73354 73355 73368 73369 73388 73389 73401 73402 73440 73571 73572 73573 73589 73590 73591 73605 73606 73625 73626 73665 73666 73699

73700 73701 73733 73734 73789 73792 73893 73902 73920 73937 73938 73955 73970 73971 73990 73991 73992 77478 77493 77722 77723 77739 77804 77806 77826 77827 77828 77878 77879 77880 77927 78076 78077 78078 78128 78129 78130 78160 78161 78195 78196 78197 78212 78233 82288 82421 82422 82423 82424

B.3 Sgr A* Off Run Numbers

50990 51015 51062 51063 51115 51311 51339 51403 51426 51453 51543 51560 51683 51725 51766 56496 56522 56545 56601 56826 56850 56892 56916 57294 57307 57326 57350 57372 57394 57438 61959 62042 62078 62083 62107 62182 62249 62270 62318 62359 62565 62591 62619 62641 62666 77476 77738 77803 77805 77825 77877 78075 78127 78159 78211 81928 82289

Appendix C

Effect of Stars

Understanding the camera's background is important for accurately modeling extended sources like dark matter halos. The camera's background shape is due to the performance of many individual camera pixels working together. VERITAS on-site operators had, in the past, noted that for apparent visible magnitude 6–8 stars, the camera pixels they illuminated would have a higher average current. This causes higher pedestal variations in the affected pixels, which decrease how often the pixel participated in shower images. In addition, if a star with $m_V < 6$ was in the field of view, it would cause a high enough current in the pixel to trigger a safety system that lowers its voltage to zero, to prevent it from being damaged. For particularly bright stars, such as $m_V \leq 3$, several pixels can be disabled at any given time.

Compounding this effect is that, since the telescope camera is fixed to the ground, the sky rotates around the camera center. This means that over a single 30 minute observation the field of view rotates around the camera center, and each star in view disables successive camera pixels as it passes over them. The camera rechecks these disabled pixels roughly once per minute by turning their voltage back on and monitoring the current, and resetting it to zero if the current is still above the threshold.

These effects imply that to study the effect of stars, one must study the effect of high-current and disabled camera pixels, and use this information to construct the effect of stars. In the following section, the effects of disabled camera pixels are studied.

C.1 Effects of Disabled Pixels

To examine the effects of disabled pixels, ~13 hours of Crab Nebula observations were reconstructed twice. The first analysis was with the default analysis chain settings, and the second time with a single pixel disabled in all four telescopes. This mimics the effect of having a star in the field of view that is bright enough to disable a pixel. The purpose of this study is to examine how many events are lost due to a dead pixel. If there are bright stars near the

Galactic Center, or a large number of disabled pixels in the data, the telescopes would be less sensitive to any dark matter halo.

After gamma-hadron cuts are applied to both sets of events, studies can be performed on events that only appeared in one set and not the other. Some events may only pass gamma-hadron cuts with the pixel enabled (P_e), while others only pass when the pixel is disabled (P_d). Events that are present when the pixel is both enabled and disabled can also be tested to see how far their reconstructed position moved in the camera.

In Figure C.1, the relative event rate in the camera is plotted when pixel 115 is disabled in all four telescopes. This relative event rate is calculated by binning all P_d and P_e events by their reconstructed position in camera coordinates. Then, for each camera coordinate bin, the ratio of the number of events $\frac{P_d}{P_e}$ is calculated. As seen in Figure C.1, there is a loss of events near the disabled pixel (the black circle), with a rate closer to 100% the farther one goes from the disabled pixel.

When these bins are combined radially around the disabled pixel, a clear loss of events is visible in Figure C.2. From this, it can be seen that at 0.1° from the disabled pixel, the relative event rate is almost 7% lower than when the pixel was enabled. From an area-weighted average of all bins within 0.33° of a pixel, the average event rate is approximately 3.1% lower than when the pixel is enabled. Over the entire field of view, disabling one pixel in all four telescopes resulted in 0.7% fewer events (14900 events vs 15010 per average 20 minute observation).

While this single-pixel loss-of-events effect was notable, it was also quite small. This was because for the Galactic Center analyzed in this thesis, there were relatively few disabled pixels. For the three observing targets described in Chapter 6, the amount of time pixels spent disabled was calculated. The Crab Nebula observations had a total of 2,245,377 pixel-minutes, while 37,701 pixel-minutes were lost due to pixels being disabled, about 1.68%. This 1.68% equates to a loss of 8.4 pixels (out of 499) in each telescope for the duration of an observation. For the Sgr A* Off data, the loss rate was lower at 1.17%, equivalent to losing 5.8 pixels in each telescope. For Sgr A*, 0.88% of pixel-minutes were lost, equivalent to losing 4.4 pixels in each telescope.

As these disabled pixels are mostly caused by bright stars, a search of bright stars near each observing source may shed some light on why the Crab Nebula loses 1.6% of its pixels, while Sgr A* and Sgr A* Off lose less. Table C.1 shows the brightest stars near each observing source brighter than $V_{mag} < 6.5$. While the Crab Nebula has several bright stars including HIP26451 with $V_{mag} = 2.97$, Sgr A* Off and Sgr A* only have dimmer stars (V_{mag} 4.28 and 4.53, respectively). Since one pixel disabled in all telescopes resulted in 0.7% fewer events, and the Sgr A* observations in this analysis have ~4.4 pixels disabled, a rough estimate for the events lost due to stars near Sgr A* is approximately 3%. Crab Nebula observations, with 8.4

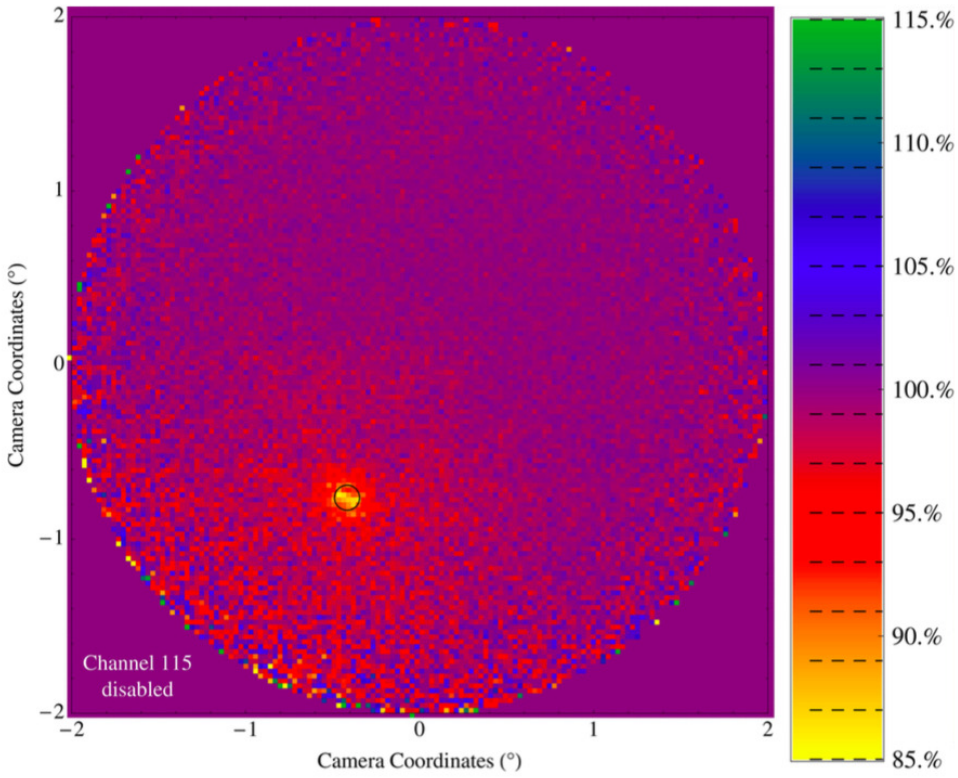

Figure C.1: Relative number of reconstructed events in the camera (squares) when pixel 115 disabled (denoted by the black circle) in all four telescopes, relative to having all pixels enabled. Camera coordinate axes are parallel to azimuth and elevation. It should be noted that squares in this plot are showing the reconstructed positions of events, which can be resolved to positions smaller than one PMT pixel.

lost pixels, lose approximately 5.9% of its events. Note however, that the majority of these event losses are not gamma rays from the observing target, but are instead lost background events near (<0.5°) the position of the stars that disabled pixels. There are several situations where a gamma ray source's flux could be underestimated due to this effect. These include:

- when a gamma-ray source transits near a visible-spectrum star, or visa versa;
- when a gamma-ray source also emits visible-spectrum photons.

Due to the scarcity of bright ($V_{mag} < 3$) visible stars and bright gamma-ray sources, this syzygy is extremely rare.

In Figure C.3, the positions of events that were rejected by cuts are shown. The white area indicates many events are lost in the area of the disabled pixel. These events would have smaller images, and would be much more susceptible to being cut.

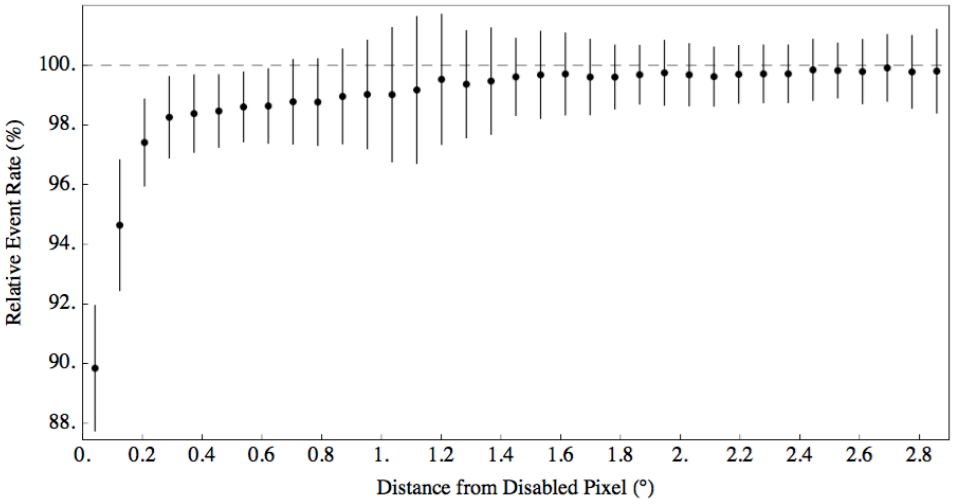

Figure C.2: Event rate in the camera with pixel 115 disabled (denoted by the black circle) in all four telescopes, relative to having all pixels enabled. The x-axis shows the angular distance from the disabled pixel.

In Figure C.4, the positions of events that are now able to pass cuts are shown. It should be noted that these are not events that were 'created' by disabling a pixel. Rather, they are events that, with the pixel enabled, did not pass cuts. Now that the pixel is disabled, they do pass cuts.

What is also noticeable is that the highest concentration of lost events was in the pixel's area, whereas the highest rate for appearing events is actually in a ring with a radius of ~1.5 pixels around the disabled pixel. This is probably due to the fact that disabling a pixel can make some images look thinner or wider, depending on where the disabled pixel is in the image. A thinner image will look more gamma-like, making it more likely to pass cuts. On the other hand, a wider image looks more hadron-like, and is less likely to pass cuts, causing some events to disappear.

In Figure C.5, the movement of gamma-like events is shown, when pixel 115 was disabled in all four telescopes. Only events which moved more than 10% of the PSF are shown. It should be noted that relatively few (0.7%, or 117 out of the 15010 events in an average 20-minute long Crab Nebula run) move more than this, and the events that do move are mostly ones with non-compact image shapes that are amputated when a pixel is disabled.

What can be learned from this is that a negligibly small number of events disappear when a pixel is disabled. Unexpectedly, disabled pixels also have an impact on events' reconstructed positions, even on the far side of the camera. This may imply that the gamma-ray PSF depends, at least to second order, on the number and pattern of disabled pixels, though no studies were

Source	**Star**	**Angle** [deg]	$\mathbf{V}_{mag}$
Crab Nebula	HIP26451	1.13	2.97
	HIP25539	1.60	4.88
	HIP26248	2.04	5.37
	HIP26072	1.55	6.19
	HIP26964	2.35	6.23
	HIP25806	0.99	6.29
	HIP26853	1.86	6.35
	HIP26616	1.17	6.42
Sgr A* Off	HIP85423	1.18	4.28
	HIP85084	0.87	5.30
	HIP85442	1.12	5.98
	HIP84445	2.08	6.20
Sgr A*	HIP87072	1.25	4.53
	HIP87836	2.60	5.76
	HIP87163	2.12	6.31
	HIP86725	1.24	6.40

Table C.1: A list of nearby stars for each observing source in this analysis. The source column is the star's closest source. The 2nd column is the star's Hipparcos catalog code. The 3rd column is the angle between the star and the source, in degrees. The 4th column is the visual magnitude, taken from Ref. [208]. Rows are sorted by source, then visual magnitude. Only stars brighter than $\mathrm{V}_{mag} = 6.5$ are shown.

done to confirm this.

As the acceptance for a particular event and the event's effective area are strongly related, the loss of acceptance also means a loss of effective area near the pixel. This can have effects on the energy reconstruction. Additionally, for CTA and its projected 7° diameter field of view, more stars will be in the field of view, implying there will be more camera pixels affected by their light.

An important concept to learn from these studies is that the PMTs in the camera work together as a whole to reconstruct events, and the loss of one PMT can affect the reconstruction of events anywhere else in the camera. These studies show the loss of a single pixel does not significantly reduce the overall event rate, but does decrease the event rate by ~3% near (<0.3°) the position of stars that are brighter than magnitude 6.5. For the Galactic Center, only 1% of the pixels are disabled, equivalent to 5 pixels in each telescope on average. Because this study indicates the number of events lost is small, and there are relatively few dead pixels in the Galactic Center's field of view, the effect of dead pixels was ignored in the dark matter search.

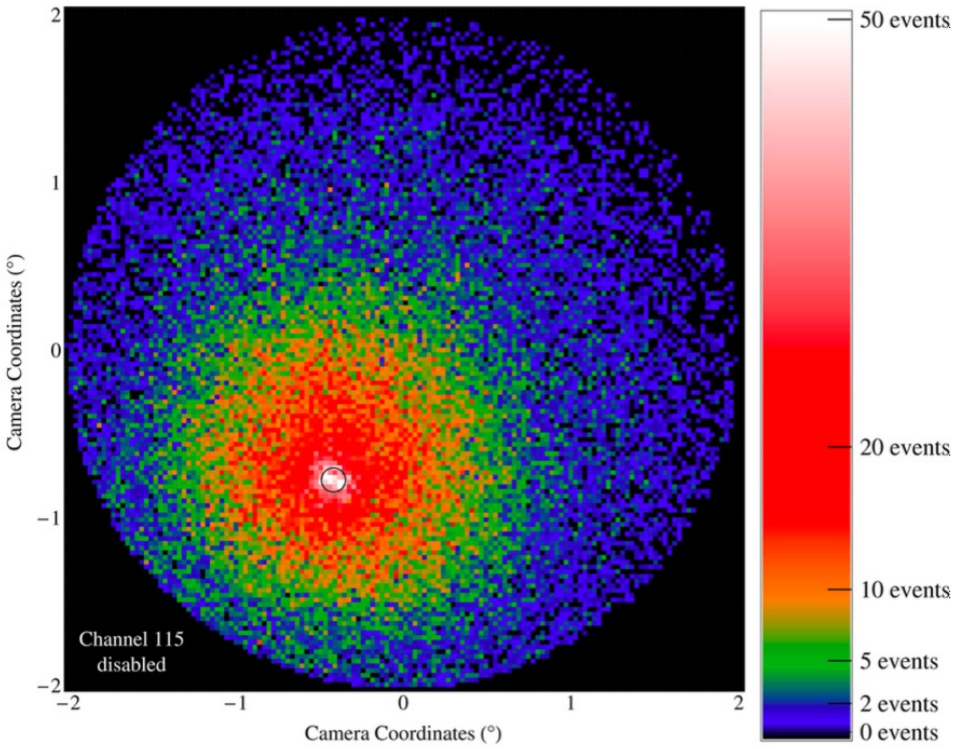

Figure C.3: Reconstructed positions of events that disappeared (squares) when pixel 115 (black circle) was disabled in all four telescopes. Positions are from their pixel-enabled reconstructed position.

Another reason these disabled pixels are not accounted for is that they are dwarfed by a much larger issue. The atmospheric gradient has a much larger effect on the background than the disabled-pixel effect. This is discussed further in Chapter 6. Future analyses may be able to account for these effects in their models of the background rates and effective areas.

Future studies could also compare how events move in energy when a pixel is disabled. Another study might investigate how the reconstructed shower-telescope distance changes, since a shower with fewer pixels will look farther away, and may be reconstructed differently. Another possibility is that, for VERITAS or future CTA observations where pixels are disabled (either due to stars or maintenance), customized background models can be constructed that account for the specific configuration of disabled pixels. Since the disabled pixel information (which pixels and the disable/enable times) is saved as part of regular observation monitoring, this can be used to apply Gaussian-shaped event-rate penalties to any background models. In general, when a pixel is disabled, it is expected that lower energy events and showers further away will be more vulnerable, and will show stronger differences than higher energy events or closer showers.

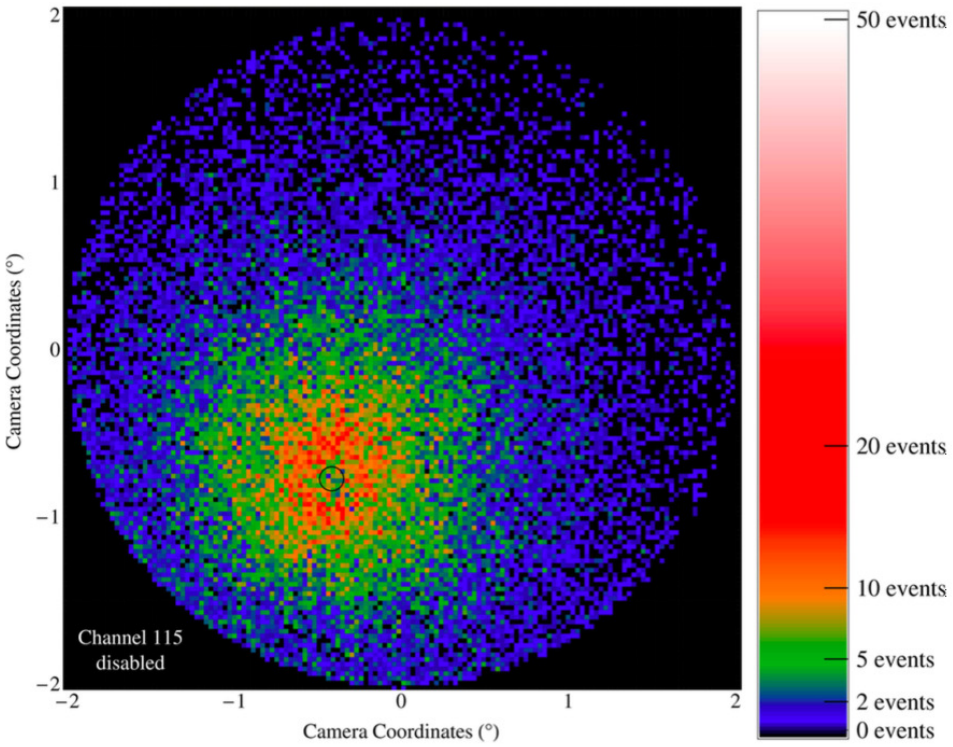

Figure C.4: Reconstructed positions of new events (squares) that appeared when pixel 115 (black circle) was disabled in all four telescopes. Positions are from their pixel-disabled reconstructed position.

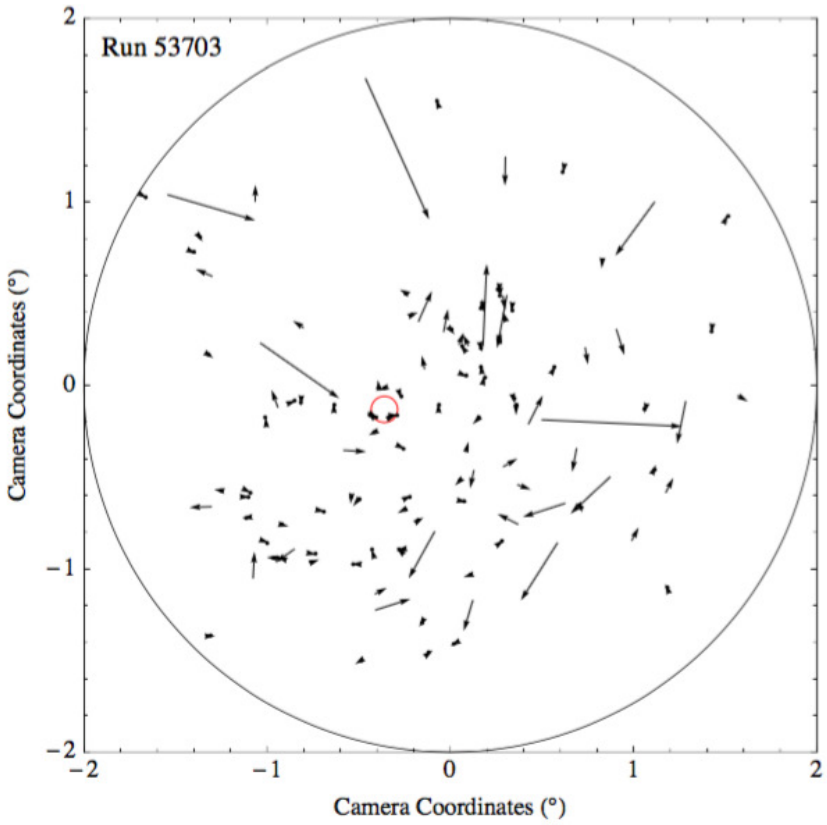

Figure C.5: Reconstructed events that moved when pixel 115 (denoted by the red circle) was disabled in all four telescopes. Arrows point from the pixel-enabled position to the pixel-disabled position.

Appendix D

Residual Sky Map Bin Significance Calculation

The likelihood analyses in Chapter 6 fit a series of models to two sets of data. The models in these analyses were chosen from using results from previous studies. However, these models may not perfectly match the sources. To check for any poorly modeled areas of the sky, the difference between the observed counts and models can be examined. While a simple residual may provide some insight, it is far better to calculate how significantly the observed counts (D) and modeled counts (M) differ in different parts of the sky.

This significance is derived through a likelihood calculation. Two hypotheses are constructed, the null and the test. The null hypothesis is that the model alone is enough to explain the number of observed events. The test hypothesis is that the number of observed events is from the model plus an unknown component. For each bin, the probability of each hypothesis is calculated with Poissonian statistics via

$$\begin{aligned} P_{\text{null}} &= \frac{M^D e^{-M}}{D!} \\ P_{\text{test}} &= \frac{D^D e^{-D}}{D!}\,. \end{aligned} \tag{D.1}$$

As this is for a single bin, the likelihood of each hypothesis is just these probabilities:

$$\begin{aligned} L_{\text{null}} &= P_{\text{null}} \\ L_{\text{test}} &= P_{\text{test}}\,. \end{aligned} \tag{D.2}$$

Then a test statistic is calculated with these two likelihood hypotheses, via

$$\begin{aligned}
\mathrm{TS} &= 2\ln\left(\frac{L_{\mathrm{test}}}{L_{\mathrm{null}}}\right) \\
&= 2\ln\left(\frac{P_{\mathrm{test}}}{P_{\mathrm{null}}}\right) \\
&= 2\ln\left(\frac{D^D e^{-D}}{D!} \times \frac{D!}{M^D e^{-M}}\right) \\
&= 2\ln\left(D^D e^{-D} M^{-D} e^{M}\right) \\
&= 2\left(\ln\left(D^D M^{-D}\right) + \ln\left(e^{-D}\right) + \ln\left(e^{M}\right)\right) \\
&= 2\left(\ln\left(\frac{D^D}{M^D}\right) - D + M\right) \\
\mathrm{TS} &= 2\left(D\ln\left(\frac{D}{M}\right) - D + M\right).
\end{aligned} \tag{D.3}$$

Then, by utilizing Wilk's theorem [197] with one extra degree of freedom, and accounting for the sign, the significance can be calculated with

$$\mathrm{Significance} = \sqrt{\mathrm{TS}} \times \mathrm{sign}\left(D - M\right). \tag{D.4}$$

This leads to the significance of a bin's residual,

$$\mathrm{Significance} = \mathrm{sign}(D - M) \times \sqrt{2\left(D\ln\left(\frac{D}{M}\right) + M - D\right)}. \tag{D.5}$$

Appendix E

Selbständigkeitserklärung

Ich erkläre, dass ich die Dissertation selbständig und nur unter Verwendung der von mir gemäß § 7 Abs. 3 der Promotionsordnung der Mathematisch-Naturwissenschaftlichen Fakultät, veröffentlicht im Amtlichen Mitteilungsblatt der HumboldtUniversität zu Berlin Nr. 17/2012 am 27.06.2012 angegebenen Hilfsmittel angefertigt habe.

31.3.2019, Nathan Kelley-Hoskins